Host-guest interactions between gaseous iodine and MOF materials : exploring dynamics and reactivity

Pedro Henrique Morais Andrade

Présenté en vue d'obtenir la grade de

Docteur de l'Université de Lille

Spécialité : Chimie théorique, physique, analytique

Thèse soutenu le 21 décembre 2023 par

Pedro Henrique Morais Andrade

École Doctorale Sciences de la Matière, du Rayonnement et de l'Environnement

Université de Lille – Sciences et Technologies

Laboratoire de Spectroscopie pour les Interactions, la Réactivité et l'Environnement (LASIRE)

Interactions Hôte-Invité entre l'Iode Gazeux et les Matériaux de Type MOF : Dynamique et Réactivité

Rapporteurs :

Bernard Humbert	Professeur, Université de Nantes, IMN
Frédéric Meunier	Directeur de recherche CNRS, Université de Lyon, IRCELYON

Examinateurs :

Isabelle Batonneau-Gener	Maître des conférences, Université de Poitiers, IC2MP
Sandrine Bourrelly	Maître des conférences, Université d'Aix-Marseille, MADIREL
Christophe Volkringer	Professeur, Centrale Lille, UCCS. Président du jury
Marco Daturi	Professeur, Université de Caen, LCS

Directeur de thèse :

Alain Moissette	Professeur, Université de Lille, LASIRE

Co-encadrant :

Matthieu Hureau	Maître des conférences, Université de Lille, LASIRE

Membres Invités :

Christophe Dujardin	Professeur, Centrale Lille, UCCS
Thierry Loiseau	Directeur de recherche CNRS, Université de Lille, UCCS

PEDRO HENRIQUE MORAIS ANDRADE

“HOST-GUEST INTERACTIONS BETWEEN GASEOUS IODINE AND MOF MATERIALS: EXPLORING DYNAMICS AND REACTIVITY"

PhD thesis presented at University of Lille (ULille), École Doctorale Sciences de la Matière, du Rayonnement et de l’Environnement (EDSMRE) as a partial requirement for obtaining the degree of Doctor of Philosophy.

Specialty: Theoretical, Physical, and Analytical Chemistry

Supervisor: Prof. Alain Moissette
Co-supervisor: Dr. Matthieu Hureau

Villeneuve d’Ascq
December 2023

Acknowledgements

I would like to thank all those who directly or indirectly collaborated in the preparation of this work and, in particular, to my family and friends for their commitment and support throughout this journey, for the moments of fraternization, and for the lightness of spirit. To my thesis supervisor Prof. Alain Moissette, to my co-supervisor Dr. Matthieu Hureau for their friendship, support, and availability during all my formation. These feelings extend towards the collaborators of this project, Prof. Christophe Volkringer and Dr. Thierry Loiseau, whose cooperation and supply of materials and space were fundamental in the execution of this thesis. I also thank the reviewers, Prof. Bernard Humbert, and Dr. Frederic Meunier, for their willingness to contribute and evaluate this work. Dr. Sandrine Bourrelly and Dr. Isabelle Batonneau-Gener are accredited for their availability to be a part of this thesis' jury and for her constructive criticism. Prof. Marco Daturi, and Prof. Christophe Dujardin are warmly thanked for examining this work and for their constant presence across the last two years, always providing valuable insights that were fundamental for the development of this research. I express gratitude to the other professors, engineers, and doctors from Université de Lille, Centrale Lille, and UFMG (*Universidade Federal de Minas Gerais*), who were of fundamental importance during my academic formation: Prof. Eduardo Nunes, Prof. Manuel Houmard, Dr. Jérémy Dhainault, Dr. Sylvain Duval, Dr. Aurelien Moncomble, Dr. Natacha Henry, Dr. Isabelle De Waele, Dr. Vincent De Waele, Dr. Hervé Vezin, Dr. Karima Meziane, Dr. Hania Ahouari, Dr. Alexandre Legrand, Myriam Moreau, Jérémy Gaillard, and Philippe Devaux. Dr. Antonio Tejeda is recognized for its collaboration. I also thank the ULille (*Université de Lille*), especially LASIRE (*LAboratoire de Spectroscopie pour les Interactions, la Réactivité et l'Environnement*), the EC-Lille (*École Centrale de Lille*), especially UCCS (*Unité de Catalyse et Chimie du Solide*), the UFMG, especially DEMET (*Departamento de Engenharia Metalúrgica e de Materiais*) and DQ (*Departamento de Química*), the EDSMRE (*École Doctorale Sciences de la Matière, du Rayonnement et de l'Environnement*), and CNRS (*Centre National de la Recherche Scientifique*) for the provision of resources, spaces, materials and financial assistance during the realization of this research. The FEDER (*Fonds Européen de Développement Régional*), the *Région Hauts de France*, and the *Ministère de l'Éducation Nationale de l'Enseignement Supérieur et de la Recherche* are acknowledged for the funding of X-ray diffractometers from the Chevreul Institute platform. The PMEL (*Plateforme de Microscopie Électronique de Lille*) is acknowledged for the support provided in the SEM and EDS techniques. I also recognize the characterization platform for the vibrational spectroscopy facilities of LASIRE. Finally, I would like to thank the ULille for the PhD grant.

Table of Contents

List of Abbreviations and Acronyms

1,4-ndc	1,4- naphthalenedicarboxylate
AC	Activated Carbon
apy	aminopyridine
ATH	Anthracene
ATR	Attenuated Total Reflectance
BDC	benzene-dicarboxylate
BET	Brunauer, Emmett, and Teller
bpe	1,2-bis(4-pyridyl)ethene
bpy	4,4′-bipyridine
BSE	backscattered electrons
BSSE	Basis Set Superposition Error
CB	Conduction Band
CBM	Conduction Band Minimum
CNRS	Centre National de la Recherche Scientifique
COFs	Covalent Organic Frameworks
CTCs	Charge Transfer Complexes
CUM	Coordinative Unsaturated Metal
DEMET	Departamento de Engenharia Metalúrgica e de Materiais
DFT	Density Functional Theory
DMF	dimethylformamide
DOS	Density of States
DQ	Departamento de Química
DR	Diffuse Reflectance
DSC	Differential Scanning Calorimetry
EC-Lille	École Centrale de Lille
EDA	Electron Donor-Acceptor
EDS	Energy-dispersive X-ray Spectroscopy
EDSMRE	Ecole Doctorale Sciences de la Matière, du Rayonnement et de l'Environnement
EFA	Evolving Factor Analysis
EPR	Electron Paramagnetic Resonance
fcu	Face-centered unity
FEDER	Fonds Européen de Développement Régional
FEG	Field Emission Gun
FL	Fluorescence
fnnls	fast non-negative least squares
FT	Fourrier Transformed
FTAS	Femtosecond Transient Absorption Spectroscopy
FTIR	Fourier Transformed Infrared Spectroscopy

GAC	Granular Activated Carbon
GHCT	Guest-to-Host Charge Transfer
GNRs	Gold Nanorods
H_2BDC	1,4-benzenedicarboxylic acid
HAXPES	Hard X-rays Photoelectron Spectroscopy
hcp	Hexagonal close-packed
HER	Hydrogen Evolution Reactions
HGCT	Host-to-Guest Charge Transfer
HHTN	2,3,8,9,14,15-hexahydroxytrinaphthylene
HOCO	Highest Occupied Crystalline Orbital
HOMO	Highest Occupied Molecular Orbital
HSAB	Hard Soft Acid Base
HSB-2	1,2-bis(4'-pyridylmethylamino)-ethane
HT-PXRD	High Temperature Powder X-Ray Diffraction
ICP-MS	Inductively Coupled Plasma Mass Spectroscopy
ICP-OES	Inductively Coupled Plasma - Optical Emission Spectrometry
IE	Isoreticular Expansion
IL	Ionic Liquid
ina	isonicotinate
IPES	Inverse Photoelectron Spectroscopy
IR	Infrared
IUPAC	International Union of Pure and Applied Chemistry
K-K	Kramers-Kronig
K-M	Kubelka-Munk
LASIRE	Laboratoire de Spectroscopie pour les Interactions, la Réactivité et l'Environnement
LBT	Linker-Based Transition
LDF	Linear Driving Force
LLCT	Linker-to-Linker Charge Transfer
LMCT	Linker-to-Metal Charge Transfer
LUCO	Lowest Unoccupied Crystalline Orbital
LUMO	Lowest Unoccupied Molecular Orbital
m-DOBDC	4,6-dioxo-1,3-benzenedicarboxylate
MBT	Metal-Based Transition
MCR-ALS	Multivariate Curve Resolution-Alternating Least Squares
MeOH	methanol
MLCT	Metal-to-Linker Charge Transfer
MMCT	Metal-to-Metal Charge Transfer
MOC	Metal-Organic Channel
MOFs	Metal Organic Frameworks
MOR	Mordenite
MRI	Magnetic Resonance Imaging

NEXAFS	Near-Edge X-ray Absorption Fine Structure
NH_2–BDC	aminobenzene-1,4-dicarboxylate
NH_2–BPDC	2-amino-[1,1'-biphenyl]-4,4'-dicarboxylate
NH_2–H_2BDC	aminobenzene-1,4-dicarboxylic acid
NH_2–H_2BPDC	2-amino-[1,1'-biphenyl]-4,4'-dicarboxylic acid
NMR	Nuclear Magnetic Resonance
ODB	4,4'-oxydibenzoate
OER	Oxygen Evolution Reactions
p-DOBDC	2,5-dioxo-1,4-benzenedicarboxylate
PAC	Powdered Activated Carbon
PBU	Primary Building Units
PDOS	Partial Density of States
PESA	Photoelectron Spectroscopy in Air
PL	Photoluminescence
PMEL	Plateforme de Microscopie Électronique de Lille
POPs	Porous Organic Polymers
PSM	Post-Synthetic Modification
PTC	3,4,9,10-perylenetetracarboxylate
PXRD	Powder X-Ray Diffraction
QD	Quantum Dot
RT	Room Temperature
SBU	Secondary Building Units
SC-XRD	Single Crystal X-Ray Diffraction
SEM	Scanning Electron Microscopy
SNF	Spent Nuclear Fuel
SSAs	Specific Surface Areas
SSE	Steady-State Emission
SVD	Singular Value Decomposition
TADS	Terephthalic Acid Disodium Salt
TAS	Transient Absorption Spectroscopy
TCPB	1,2,4,5-tetrakis(4-carboxyphenyl)benzene
TCSPC	Time-Correlated Single Photon Counting
TDOS	Total Density of States
TEM	Transmission Electron Microscopy
TGA	Thermogravimetric Analysis
TPT	2,4,6-tris(4-pyridyl)-1,3,5-triazine)
tptc	triphenyl-3,3'',5,5''-tetracarboxylate
TRE	Time Resolved Emission
TSBDC	trans-stilbene-4,4-dicarboxylate
TTF	tetrathiafulvalene
TTFDC	tetrathiafulvalene-dicarboxylate

TTIP	titanium tetraisopropoxide
UCCS	Unité de Catalyse et Chimie du Solide
UFMG	Universidade Federal de Minas Gerais
ULille	Université de Lille
UNF	Used Nuclear Fuel
UPS	Ultraviolet Photoelectron Spectroscopy
USI	Universal Salt Iodization
UV-vis	Ultraviolet-Visible
VB	Valence Band
VBM	Valence Band Maximum
VL	Vacuum Level
XPS	X-ray Photoinduced Spectroscopy
XRD	X-Ray Diffraction

Introduction

The release of radioactive iodine into the atmosphere has become an issue of great concern from the scientific community in the last century. Throughout the last 40 years, the world witnessed at least two major nuclear plant accidents, the first one in Chernobyl, on April 1986, and the second one in Fukushima, on March 2011 [1,2]. These accidental events, together with the reprocessing of Spent Nuclear Fuel (SNF) release harmful gaseous species such as radioactive isotopes of H, C, Xe, Kr, Cl, and I into the atmosphere. These spills can cause great damage to fauna and to flora as they can also impact water bodies and soil [1–4]. The radioactive iodine is often released in its gaseous form (I_2) and also as organic-iodine compounds (CH_3I) [5], in which the main radioactive isotopes present are found to be ^{129}I and ^{131}I. For instance, ^{129}I raises concern due to its long half-life time ($t_{1/2} = 1.6 \times 10^7$ years) [4] and high mobility in most geological environments [4]. On the other hand, iodine-131 presents high activity (4.59×10^{15} $Bq.g^{-1}$) and have high potential to be captured by the thyroid and incorporated into human metabolic processes, causing cancer, metabolism dysfunctions and a profound impact on growth [4,6]. The capture of iodine poses several challenges since it is a highly flowing gas with a great oxidation capacity. At the same time, iodine can be easily dissolved in water and spread throughout different ecosystems [7].

Several classes of materials have been used for trapping gaseous iodine such as activated carbon [8], zeolites [4], aerogels [9], covalent organic frameworks (COFs) [10], and porous organic polymers (POPs) [11]. However, these compounds can present numerous problems as some of them are hazardous to the environment, others are expensive or amorphous, and some of them present risk of explosion in the desired work conditions [4,8,12–15]. Aiming to address these problems, metal-organic frameworks (MOFs) have been widely investigated for their properties as iodine adsorbents [12,13,16,17]. These hybrid materials are formed by inorganic polyoxo clusters that are connected to each other by organic linkers, forming organized and open crystalline networks [18,19]. Due to the various combinations of diverse metal sites and organic linkers, numerous MOF structures with different properties can be obtained using different synthesis approaches [20]. MOFs are known for their high specific surface areas (SSAs), permanent porous structure, and for the possibility of being chemically modified – by functionalizing their pores, by replacing their metal contents, and/or by modifying their organic linkers [21,22]. Actually, there are procedures reported in the literature that can be used to modify these materials through post-synthetic modifications (PSM), which allow the development of many structures that

cannot be obtained by direct solvothermal routes [23]. In fact, the optimization of MOF materials for trapping iodine can be achieved by several means such as introducing functional groups, shaping their porosity, using redox metal centers, and doping with metals or active molecules [15]. For instance, since I_2 is known to be an electron acceptor, frameworks with electron donor groups can improve the iodine uptake [12]. Tailoring the size of the pores by using series of iso-reticular MOFs is also an interesting approach for capturing I_2 [15]. However, although the adsorption of iodine using MOFs was already subject of several studies, it lacks information about the interactions between iodine species and the crystalline network of these materials [7,12,13]. Therefore, to address the points raised in the introduction, this manuscript is composed by six chapters.

Chapter I consists of a bibliographic review that presents the context of the study and couples the state of the art over the iodine chemistry, its capture using MOF materials, and the photoreactivity and confinement effect that generates different charge transfer complexes (CTCs).

Chapter II provides an in-depth description of the materials and methods used during this work, including the syntheses of the compounds, the characterization techniques, and the iodine sorption tests.

Chapter III extensively discuss how to access the band gap type and energy of semiconductor materials by simply using diffuse reflectance UV-Vis data. Indeed, the effects of band gap and CTCs seem to be closely related to the iodine adsorption and evolution within the porous structure of MOF compounds.

Chapter IV reports an experimental study over the iodine capture and evolution using UiO-66 to unravel the influence of the metal contents. The series of Zr-based UiO-66 MOFs used in this study stands out by its thermal and chemical stability as well as by its facility to be functionalized, either by replacing the organic linker on its structure or also by changing the metal content within the inorganic cluster [12,13]. In particular, several studies were already conducted using such family of MOFs, highlighting the capacity of this material to retain I_2 under conditions that simulates a nuclear accident, and also demonstrating the influence of the organic linker over the iodine capture [12,24,25]. In this context, the effect of the gradual substitution of zirconium by hafnium on the iodine trapping is investigated.

Chapter V proposes a methodology to follow the iodine diffusion over single crystal materials using Raman mapping spectroscopy. This approach is applied on UiO-67_NH_2 with different metal contents (zirconium and hafnium). In this case, this class of MOFs stands out by its ability to form single crystals with more than 40 μm in size.

Chapter VI shows experiments that were carried out to compare the metal effect over the CTCs in titanium-based MOFs and its influence over the iodine capture and stabilization. Indeed, because of their enhanced photocatalytic properties, high acidity, low toxicity, and potential to form linker-to-metal charge transfer (LMCT) complexes, the use of titanium-based MOFs can be particularly interesting for trapping iodine [26,27]. The MIL-125 MOF material used here has a similar structure to that of UiO-66 and therefore, is interesting for comparative purposes.

Chapter I: Bibliographic Review

1.1. Context of the study

The contamination of the atmosphere, soil, and waterways with materials that are harmful to fauna and flora is one of the most problematic issues nowadays all around the world. These contaminants can be divided in two classes: the hazardous materials that occur by nature, and those occurring due to human activity (anthropogenic). The first consist in pollutants such as minerals, soil, and organic compounds that can be naturally found in the environment; while the second generally come from combustion, chemical reactions or from the unsecured effluent of toxic materials. The anthropogenic pollution has been accelerated in the last few centuries due to the exponential growth of the industrial production and global consumption, which increases the interest on methods for the capture and degradation of these pollutants [20].

Among the hazardous materials found in the environment, some raise more interest, either due to their high toxicity and difficulty of treatment or because of the enormous quantity in which these contaminants are emitted. Among those, it is worth mentioning the greenhouse gases (CO_2, CH_4, O_3, N_2O), volatile organic compounds (toluene, benzene, phenols, xylenes), polycyclic aromatic compounds (naphthalene, anthracene, benzopyrenes), and radioactive contaminants (^{129}I, ^{131}I, ^{134}Cs, ^{137}Cs) [20]. One of the scenarios that contributes for increasing the release of these species into the atmosphere is the rising demand for energy worldwide, which is being supplied mainly by fossil fuels (Figure 1.1) [28]. However, some countries present a specific energetic matrix that is mainly composed by other energy sources. This is notably the case of France, which holds the highest share of nuclear energy in the world, with 71% of its supply dependent on nuclear power plants, followed by hydropower (11%), and other fossil fuels (8%) (Figure 1.1) [29]. In this case, the main source of atmospheric pollution comes from nuclear accidents and during the reprocessing of Used Nuclear Fuel (UNF) [4,30].

Several methods have been applied for the removal and degradation of these atmospheric pollutants such as biodegradation [31], chemical degradation [32], adsorption [25], and photocatalysis [33]. Among those, adsorption and photocatalysis pose a significant advantage over other techniques for their low-cost, high efficiency, low environmental impact, ease of operation, and the possibility of reuse the materials [34]. In this case, seeking to improve the efficiency of the materials used, it is of great interest to understand the reactions mechanisms and also the physicochemical phenomena that are behind them. Therefore, this study aims at characterizing the interactions and the degradation mechanisms that can occur between

nanoporous host materials and molecular air pollutants trapped on their surface or adsorbed in their pores.

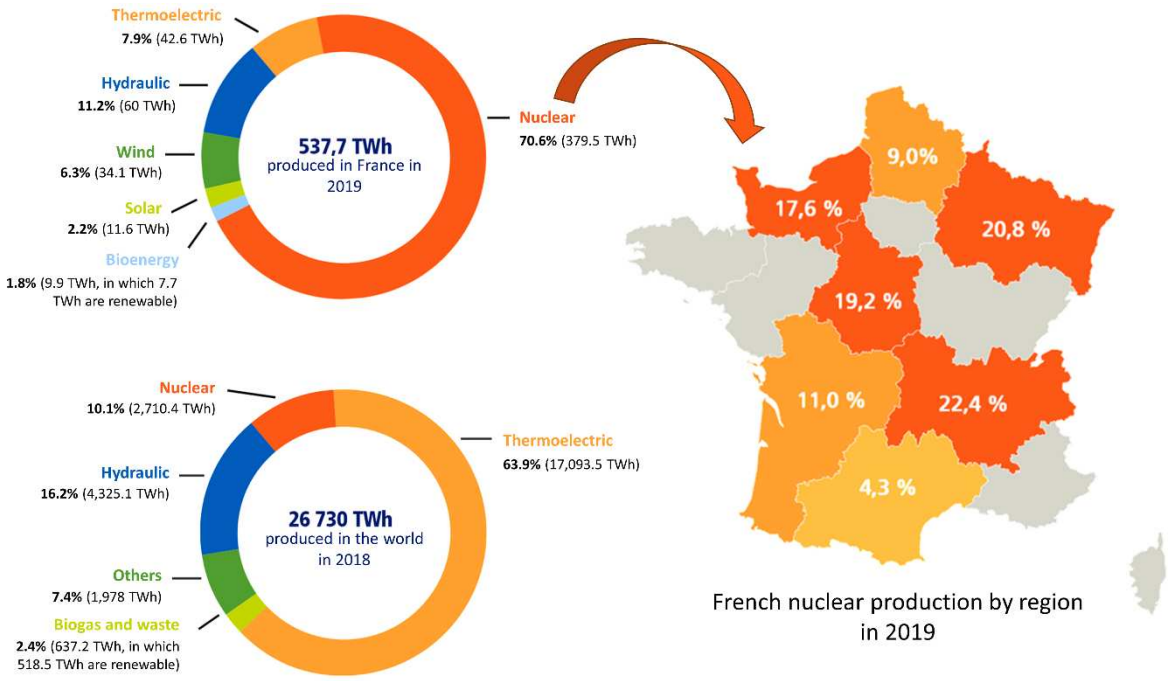

Figure 1.1: On the left side: data on the distribution of the electricity production in France (2019) and worldwide (2018). On the right side: France map showing the nuclear energy production by region in 2019. [29]

1.1.1. Radioactive pollutants

Natural levels of background radiation from radionuclides vary by more than two orders of magnitude across the terrestrial globe. Areas showing high levels of natural radioactivity are present in China, India, Iran, Kenya, Namibia, France, Brazil, and many other countries [3]. However, due to the increase of nuclear energy production in the last century, the immobilization of radioactive contaminants has become crucial nowadays. Even though a great part of these radionuclides are released during fuel reprocessing in nuclear units, nuclear spills and major accidents also contributes to this scenario [21].

In the last 40 years, the world witnessed at least two massive nuclear accidents: the first one in Chernobyl (Ukraine), on April 1986; and the second one in Fukushima (Japan), on March 2011 [30]. In Chernobyl, a nuclear reactor exploded during the test of a cooling system in its reactor core. As consequence, a vast amount of radioactive material was released over an area of 200,000 km² in Eastern and central Europe, over a 10-day period. Millions of people were exposed to measurable levels of radioactive fallout [35]. It has been reported that the explosion

was about 400 times stronger in terms of the radiation released than the one observed in Hiroshima (Japan), during the World War II, on August 1945 [36]. On the other hand, the nuclear facility in Fukushima was damaged due to an earthquake of 9.0 magnitude (Richter scale) followed by a tsunami on the East coast of Japan. During this accident, radioactive material was released not only in the atmosphere, but also into waterbodies. The accident, 25 years after Chernobyl, rekindled the public concern on radiological health and environmental problems caused by nuclear accidents [37]. For instance, following the Fukushima nuclear accident, it was estimated that 1 PBq (Peta Becquerel) of ^{131}I was released as well as 8.06 GBq (Giga Becquerel) of ^{129}I. In this case, although radioactive iodine species were detected in raw water in Fukushima, the atmospheric pathway played the most significant role for spreading these species [2]. Back there, a few days after the accident, the radioactive cloud formed in Japan was detected in all continents of the globe, with greater intensity in Asia, North America, and Europe (Figure 1.2) [38].

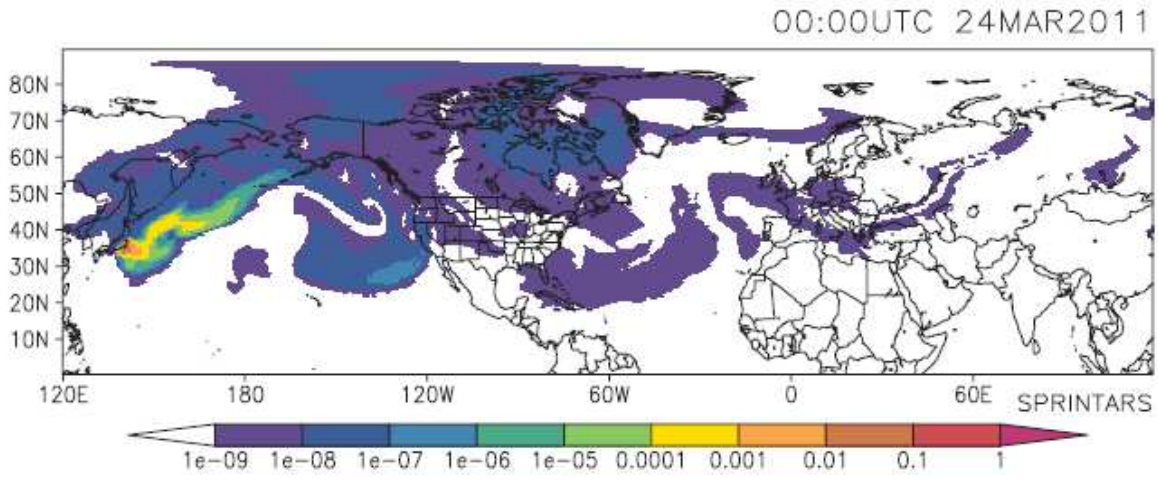

Figure 1.2: Simulation demonstrating the mass concentration of radioactive particles released continuously from Fukushima that are near the earth's surface on March 24, 2011. Each color represents the variation of one order of magnitude. Image obtained from Takemura *et al*. [5]

Among the many fission products formed in accidental situations, some are volatile under the surrounding temperature and pressure conditions, which may engender high spreading and significant danger to fauna and flora. The fission process during energy production generates some particular species such as radioisotopes of iodine, which are co-products of ^{235}U. Among those, the ^{129}I and ^{131}I are the most common isotopes released during UNF reprocessing and also in nuclear accidents. The former raises concerns due to its long half-

life ($t_{1/2}$ = 1.57 × 10^7 years) in addition to its high mobility in most geological environments, reason why it is further studied during waste reprocessing and UNF treatment [4]. The latter presents high activity (4.59 × 10^{15} Bq.g^{-1}) and potential to be incorporated into human metabolic processes [6]. For this reason, radiation protection institutes are particularly interested in ^{131}I releases in the event of a nuclear accident [39]. Moreover, iodine is mainly released in its gaseous form (I_2 and organic R–I, where R is a carbon chain) or in the form of aerosols, which are harder to deal with due to its high capacity to spread into the atmosphere [5].

1.2. The chemistry of iodine

Iodine is a chemical element (atomic number 53) that is part of the halogen family (column 7A in the periodic table) and presents one stable isotope (^{127}I) in addition to several radioactive ones. Table 1 shows the different iodine species as well as their half-life time and decay mode.

Table 1.1: Atomic mass, half-life time, and decay mode of different iodine isotopes.

Notation	Atomic mass	Half-life time	Decay mode
^{123}I	123	13 hours	β^+, γ
^{124}I	124	4 days	β^+
^{125}I	125	59 days	β^+
^{127}I	**127**	**Stable**	***NA**
^{129}I	129	1.57 × 10^7 years	β^-
^{131}I	131	8 days	β^-, γ
^{135}I	135	7 hours	β^-

*NA: non-applicable

The stable iodine is commonly used in different applications, worth citing the medical and chemical sectors. For instance, iodine is commonly applied as a contrast in X-ray imaging exams due to its opacity to this radiation [40]. It is also used for threating thyroid cancer since I_2 can react in the human body and form a molecule, derived from iodolactone, and a radical, both of which slow down the proliferation and induce apoptosis of the cancerous cell [41]. In catalysis, iodine is present in different organic synthesis such as Diels-Alder reactions, esterification, and Michael Additions [42]. Finally, iodine is also widely used in the agricultural industry. For

instance, the Universal Salt Iodization (USI) is an effective strategy used in nearly all countries worldwide countries for preventing iodine deficiency in the human diet [43].

It is worth mentioning that iodine can present several oxidation states (-1, +1, +3, +5, +7) and a great number of volatile species. For instance, neutral iodine presents itself as I_2, which is a greyish solid at room temperature with melting point T_F = 113.7 ºC and boiling point T_E = 184.4 ºC. Being extremely volatile, I_2 is easily sublimated into purple vapors that can be highly reactive due to the elevated electronegativity of iodine, which makes it a great oxidant. In the atmosphere, I_2 can be transformed to several species worth mentioning CH_3I, and other oxidized species such as IO, IO_2 and I_2O [44]. Moreover, iodine has a weak solubility in water (which can be improved by adding KI or by increasing the pH) where it can form other species such as I_3^- and IO_3^-. However, I_2 is highly soluble in several organic solvents such as ethanol and acetone.

Due to its high electronegativity, the interactions between iodine and other elements can be predicted by the "Hard Soft Acid Base" (HSAB) theory. In this case, it relates the acid-base reactivity of two different species to the polarizability of their orbitals. Hard acids are electron acceptors that are highly positively charged and exhibit small sizes, whereas soft acids present the opposites properties. On the other hand, soft bases are electron donors with orbitals that are easily polarized, whereas hard bases are not. Moreover, the interaction between hard-hard or soft-soft acid-bases are more intense than the hard-soft association [45]. Following this principle, iodide (I^-) is considered to be a soft base since it presents a relatively high ionic radius and a small charge and, therefore, an easily polarizable orbital. Also, according to the theory, it is supposed to present high affinity for other soft acids, notably the monovalent metal ions – i.e., Cu^+, Ag^+, Au^+, Hg^+. However, I_2 is considered to be a soft acid since the I–I bond is easily polarizable in the presence of an electron donor species – i.e., oxygen, nitrogen, benzene [39].

The stable iodine is an element of great importance for several metabolic processes in the human body. In fact, it interferes in the synthesis of different thyroid hormones, such as thyroxine and triiodothyronine [46]. Its deficiency in early stages of life can impairs cognition and growth [47]. In addition, severe iodine deficiency can cause hypothyroidism, whereas a sudden increase in its uptake is related to transient hyperthyroidism and autoimmune thyroid disease [48].

On the other hand, the continuous exposure to radioactive iodine can give rise to several problems in fauna, and flora [49]. For instance, an epidemic of childhood thyroid cancer appeared years later following the Chernobyl nuclear power plant accident, and it was related to the exposure to ^{131}I [50]. Other consequences were also found in the population exposed to radioactive iodine, such as atrophy of the thyroid gland, hypothyroidism, benign adenomatous nodules, injuries in the salivary gland, and chromosome aberrations [51–53]. In these cases, the injection of KI has proven to be an effective method for protection against irradiation of the thyroid after exposure to radioactive iodine [54].

1.2.1. Methods used to trap iodine

The methods used to trap iodine can be separated into two major classes: wet and dry processes. Caustic scrubbing, mercurex and iodox process, and fluorocarbon absorption are examples of wet processes that were already applied with such purpose [8]. In these cases, a solvent (whose selection depends on the applied method) is generally used to separate the I_2 from the gas phase. Briefly, alkaline scrubbing process uses NaOH (1–2 M) as solvent to react with both organic and nonorganic iodine species, forming new sodium-iodide compounds (NaI). One of the drawbacks of this process is the precipitation of sodium carbonate that may occur if the solubility is exceeded [8]. The Mercurex and Iodox processes remove organic and elemental iodine from gas stream by adsorbing the iodine in a nitric acid solution containing mercury. However, the Hg must be separated from the iodine and the resulting precipitant is conditioned for storage, which introduces another step and increases the complexity of this method [8]. Finally, fluorocarbon absorption is carried out using a packed column with dichlorodifluoromethane. In this case, the high cost of the distillation process is a downside for employing this technique [8].

On the other hand, dry processes are basically related to adsorption processes, as it is one of the most effective unit operations to capture the volatile radioactive contaminants from gas streams [46]. In fact, adsorption is a well-established technique, and it is more powerful and advantageous than most wet processes due to its simplicity, reliability, non-corrosive nature, simple design, low maintenance, and low operating costs [46]. Moreover, the waste product obtained at the end is in a dry form, which makes it easier to handle. However, this method still presents some major challenges related to its cost and to the preparation of an effective solid

sorbent – which must be selective to the species of interest and stable under the desired work conditions [8,55].

One of the solid sorbents that has been widely studied for iodine removal due to its high surface area and pore size is the Activated Carbon (AC) [8,56]. It can be subdivided into two main categories namely Granular Activated Carbon (GAC), with larger particles, and Powdered Activated Carbon (PAC), with thinner particles. Several variables influence the adsorption of radioactive iodine from gas streams worth mentioning: iodine concentration, relative humidity, bed temperature, service time, radiation, impregnation, manufacture, particle size, and gas velocity through the filter [57]. The total removal capacity can be improved by several techniques, such as the selection of raw materials, the method of preparation, and the impregnation of other compounds [58]. One can cite, for example, the use of $ZnCl_2$ as activator agent, which improved the iodine uptake capacity from 0.6 $mg.g^{-1}$ to 2.4 $g.g^{-1}$ in static adsorption conditions [59]. On the other hand, the bamboo charcoal (raw material) presented 70% of iodine removal efficiency in single pass [60]. In fact, its SSA is higher when compared to other sorbent such as anthracite and commercial coconut AC. This feature was ascribed to the expressive fraction of micropores that would be effective in adsorption of small nonpolar gaseous ^{131}I molecules [61]. However, although AC has been successfully used in power plants, it exhibits a relatively low ignition point and can lead to the formation of explosive compounds within the filter bed [57]. Moreover, the presence of nitrogen oxides in the UNF off-gas stream adversely affects the material's performance. Therefore, AC has been employed as a potential sorbent for iodine entrapment, but it brings several issues as the capacity decrease over time and the possibility of explosion, for example. For these reasons, other porous sorbents have been widely investigated [12–14].

Alternatively, zeolites are often employed to trap iodine. They are aluminosilicate minerals that can be naturally found in nature or synthetically produced [62]. Their porous structure allows the adsorption of a great amount of gases, radionuclides and stable cations (Na^+, Ca^{2+}, Mg^{2+}, Ba^{2+}) [63]. In fact, due to their low permeability, sorption characteristics, thermal and chemical stability, they have several industrial applications [64,65]. Moreover, their strong framework structure, which contains cations and enclosing cavities, allows the stability of ordered micropores, normally with diameters below 2 nm [66]. One class of zeolites that is well known for the capture of gaseous radioiodine is the silver-containing mordenite (Ag-MOR). They have been employed for several decades in reprocessing plant operations to

transform gaseous I_2 and/or CH_3I into nonvolatile AgI [4]. Commonly, the Ag-exchanged MOR is reduced before use and the unreduced Ag-MOR is readily available through treatment in a H_2 stream, as shown in Figure 1.3 [67]. It was reported that the maximum iodine loading for the reduced Ag-MOR lies between 3.3 and 17 g of iodine/100g material [8]. However, Ag-based zeolites pose several problems since the trapped AgI can be thermally decomposed, thus releasing the iodine and rendering the Ag-sorbent less useful [4]. Moreover, silver is a very expensive material (>2000 €/kg) and it is hazardous to the environment [8].

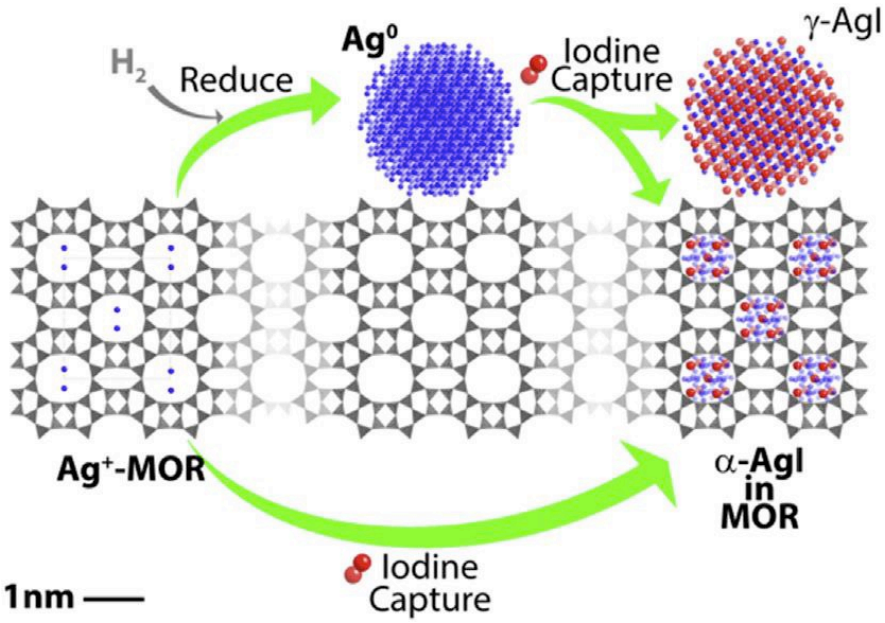

Figure 1.3: Scheme obtained from Chapman *et al.* [67] demonstrating the iodine capture by silver-containing Ag-MOR. While pre-reducing the silver mordenite (MOR) yields a mixture of γ-AgI nanoparticles and subnanometer α-AgI, direct iodine uptake by silver-exchanged MOR produces exclusively subnanometer α-AgI.

Another class of materials widely used to capture I_2 are the aerogels. They are basically a type of low-density and mesoporous materials with a gel-like structure [15]. For instance, chalcogenide aerogels stand out due to their high affinity with soft binding sites, which can, in some cases, capture up to 2.39 $g.g^{-1}$ of iodine [9]. Another advantage of aerogels is the possibility of loading them with nanoparticles. In fact, Riley *et al.* [68] improved by four times the iodine capture capacity of aluminosilicate aerogels when loading them with silver. However, the study of guest-host interactions in aerogels is of great challenge because of their amorphous structures [15].

Covalent Organic Frameworks (COFs) were also in-depth evaluated for trapping iodine. They are a class of porous polymers formed by strong covalent bonds between organic building

blocks, creating materials with 2D or 3D open structures [15]. For instance, an imine-based COF with hexagonal-shaped channels showed extremely high iodine adsorption (6.26 $g.g^{-1}$) and great recyclability upon five cycles of adsorption/desorption [10]. Actually, some studies have demonstrated the impact of the CTCs in the iodine binding within the COFs (Figure 1.4), while others highlighted the necessity of tailoring the pore size of the compounds to optimize the iodine capture [69,70]. Finally, Porous Organic Polymers (POPs) are a class of materials which are built exclusively through covalent bonds of organic molecules. They are usually amorphous materials that can present high iodine uptakes. Contrary to COFs (which are basically constructed from reversible condensation reactions), their syntheses tend to involve polycondensation, click-type reactions, trimerizations, or Friedel-Crafts couplings [15]. For instance, a new triazine-based POP was designed using cyanuric chloride as the backbone and exhibited a high iodine adsorption capacity (4.9 $g.g^{-1}$) [11]. However, as with aerogels, the main challenge in using COFs and POPs to adsorb I_2 is their low crystallinity, which makes it difficult to study the host-guest binding mechanism experimentally [15].

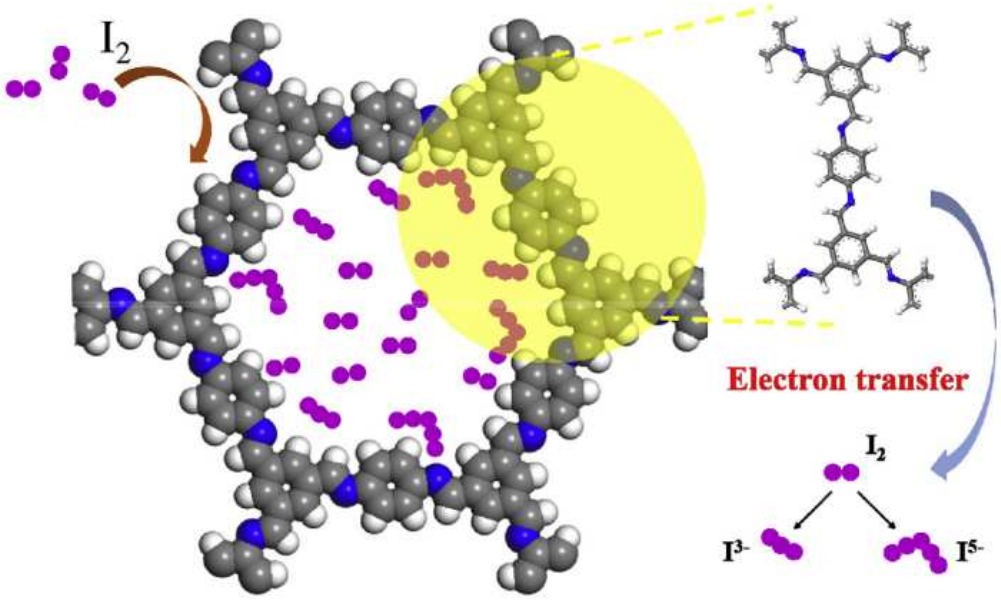

Figure 1.4: Schematic illustration obtained from Yang *et al.* [71] of the iodine uptake mechanism in COF-LZU1s. In blue: nitrogen; in gray: carbon, in white: hydrogen.

In that context and aiming to address these problems, MOFs have been widely studied for adsorbing iodine [16,17]. These hybrid, crystalline, porous materials possess high surface areas, tunable structures, and can achieve high chemical stability, which makes them great

candidates for capturing I_2 [15]. Several methodologies can be applied for optimizing their capacity of adsorbing iodine, such as: introduction of functional groups, shaping their porosity, presence of redox metal centers, doping with metals and molecules, pressure-induced amorphization, and glass sintering [15]. Those features will be further discussed in section 1.3.2 (Iodine confinement using MOFs).

1.2.2. Iodine speciation using spectroscopy

The major challenges when characterizing the different iodine species are related to their great oxidation capacity and high molecular weight. In fact, most techniques that require a secondary vacuum such as Scanning Electron Microscopy (SEM), Transmission Electron Microscopy (TEM), gas sorption tests, and X-ray Photoinduced Spectroscopy (XPS), should be avoided due to the high volatility of I_2 [39]. Moreover, in Nuclear Magnetic Resonance (NMR), the stable isotope ^{127}I has a quadripolar moment which produces signals very large to be observed using a high resolution NMR spectrometer [39]. Furthermore, since ^{127}I is considered as a heavy element, the X-Ray Diffraction (XRD) analysis are also arduous, especially when iodine species are inserted inside a non-dense porous material, as in the case of MOFs [39]. Other techniques such as the Inductively Coupled Plasma Mass Spectroscopy (ICP-MS) can be used for quantifying I_2 but is useless to determine the different species that are present in the sample. In other cases, such as Electron Paramagnetic Resonance (EPR), the iodine paramagnetic species are known for their high *g*-factor anisotropy and therefore, when combined to the fast electron spin relaxation caused by the large spin-orbit interaction of the iodine atoms, makes their signals hardly observable [72]. Finally, Fourier Transformed Infrared Spectroscopy (FTIR) cannot identify the presence of I_2 because the molecule is symmetrical and hence, does not exhibit any active vibrational mode in FTIR [39].

With that in view, the most promising techniques to characterize the different species of iodine are the Ultraviolet-Visible (UV-vis) absorption, and the Raman scattering spectroscopies. For instance, UV-Vis allows the study of electronic transitions between the ground state to the excited states of the different species present in the sample. In the case of the diiodide (I_2), the main transition occurs between the π_g^* and the σ_u^* molecular orbitals [73,74]. When I_2 is in solution, the position of the UV-Vis absorption bands depends on the polar character of the solvent. For instance, in absence of interactions – as in the case of

tetrachloromethane or dichloromethane – the bands are observed at 290 and 510 nm [75]. However, polar solvents such as ethanol or pyridine can deform the electric cloud of the I_2 molecule and form a CTC with the guest material, creating a blueshift in their UV-Vis absorption bands [76]. In fact, in the presence of pyridine, a new CTC band is formed at about 235 nm, whereas the iodine contribution at 520 nm shifts to 422 nm [76]. Nevertheless, some nonpolar solvents – such as benzene – can create π bonds with the I_2 molecules, generating signatures between 400 – 500 nm [77,78]. Finally, the I_3^- species – which is normally formed in aqueous solution – exhibits bands situating around 290 and 360 nm [79].

As mentioned before, iodine is not infrared active because it is a linear molecule that belongs to the $D_{\infty h}$ point group and exhibits a single vibrational mode (symmetrical I–I stretching) without any change of dipolar moment during vibration. Furthermore, even in the case of symmetry lowering due to the interaction of I_2 with the environment and therefore, the breaking of selection rules, the vibrational modes expected for I_2 species (below 250 cm^{-1}) are not observable using IR spectroscopy, as this technique does not allow access to a spectral range below 400 cm^{-1}. However, this vibrational mode can be observed by Raman spectroscopy, for which the selection rules depend on changes in polarizability during vibration. Thus, Raman scattering has proved to be the method of choice for studying I_2 and its different possible form of interaction. In that context, Table 1.2 reports various characteristic Raman bands between 100 and 300 cm^{-1} already observed in previous works for different iodine species.

Table 1.2: Active iodine vibrations in Raman spectroscopy

Iodine species	Raman shift (cm^{-1})	Comments	References
Solid I_2	180	Stretching vibration	[80]
Gaseous I_2	215	Stretching vibration	[81]
"free" I_2	200 – 209	Low interaction with a solid	[12,13,82,83]
"perturbed" I_2	150 – 180	Perturbed by a CTC	[12,13,83,84]
I_2 in solution	200 – 215	Depends on the solvent polarity	[81]
$I_2^{\bullet-}$	114	Same position as $\nu_s(I_3^-)$	[85]
I_3^- symmetric	105 – 115	Stretching vibration ν_{s1}	[83–90]
I_3^- asymmetric	130 – 165	Stretching vibration ν_{as1}	[83–90]
I_5^- linear	104, 160	Linear $[I_2 \cdots I^- \cdots I_2]$	[89,90]
I_5^- V-shaped	114, 131, 167	V-shaped $[I_2 \cdots I^- \cdots I_2]$	[89,90]
I_5^- L-shaped	106, 135, 164	L-shaped $[I_3^- \cdots I_2]$	[89,90]
I_7^-	175	$[I_2 \cdots I_3^- \cdots I_2]$	[85]

Indeed, particular attention must be paid to vibration modes that are related to species confined in porous solids, such as "free" I_2, "perturbed" I_2, $I_2^{\bullet-}$, and I_n^- (n = 3, 5, 7, …). For instance, the "free" I_2 species is related to iodine molecules that have none or very low interaction with a solid porous network [12,13,82,83]. The adsorbed I_2, here named "perturbed" I_2, is characterized by the formation of a CTC with a strong electron donor material, which perturbs the I–I bond and reduces its size. In fact, Deplano *et al.* [84] proposed an empirical relation between the length of the I–I bond and the interaction force between the iodine molecule and the electron donor element, according to the Equation (1.1). Here, d is the length of the I–I bond, d_0 is the length of the I–I bond in the solid state I_2, c is an empirical constant, and n is the CTC force. In this case, when n is higher than 0.6, the I_2 molecule is considered to be simply perturbed by an electron donor element. In the other hand, when n is less than 0.6, the interaction is considered to be strong enough to create a trinuclear entity [84].

$$\mathbf{d = d_0 - c \cdot \log (n)} \qquad (1.1)$$

Polyiodides are also commonly described in the literature. They constitute a class of polyhalogeno anions composed entirely of iodine atoms [91]. Its most common and simplest member is the triiodide ion (I_3^-), but there are larger entities that are frequently mentioned, such as in I_{2n}^{2-} (n = 4, 6, 8, …) and I_n^- (n = 5, 7, 9, …) [83–90]. I_3^- exhibits three vibrational modes: symmetric stretching (ν_s), asymmetric stretching (ν_{as}), and bending (δ). It is worth mentioning that its asymmetric stretching vibration is not supposed to be active in Raman spectroscopy. Nevertheless, the confinement of such species inside porous materials creates a small deformation on the I_3^- structure, which lowers its symmetry and makes the ν_{as} vibration mode optically active [85].

1.3. Metal Organic Frameworks

Nanoporous materials are outspread across the society nowadays due to their enormous applications in several fields such as chemistry, engineering, medicine, energy, and agriculture [92,93]. MOFs are one of its classes that has been of growing interest in the last few decades. These crystalline solids are formed by the connection of metal clusters and organic linkers, producing highly organized and porous structures (up to 90% free volume) [94]. The geometry of these linkers, combined with the coordination modes of the inorganic parts, produces frameworks with different structures that can be designed to target selected applications such

as catalysis, drug delivery, gas storage, and removal of pollutants [95]. The most noticeable characteristic of these materials is, undoubtedly, their high SSA, which can achieve values of up to 7,000 $m^2.g^{-1}$ and has a direct influence on their properties and applications [96]. In fact, the main features that contribute to their enormous relevance in the scientific community nowadays are: (I) the precise control over structures types by using different topologies based on the connectivity and shape of the molecular building blocks; (II) their exceptional porosity and tunable pore size; (III) the possibility of being post-synthetically modified and also chemically functionalized; (IV) the presence of multivariate structures with different metals and/or organic linkers which enables the creation of heterogeneity order within the pores; (V) the facility of being characterized by commonly used techniques such as XRD, FTIR, Raman, UV-Vis, EPR, and NMR spectroscopies; and (VI) their straightforward scalable synthesis (Figure 1.5) [18,97,98]. However, MOF materials also present some inconveniences such as their low thermal stabilities (normally between 300 and 400 ºC), high cost of production, and use of organic solvents, which makes their use a challenge in some applications [99].

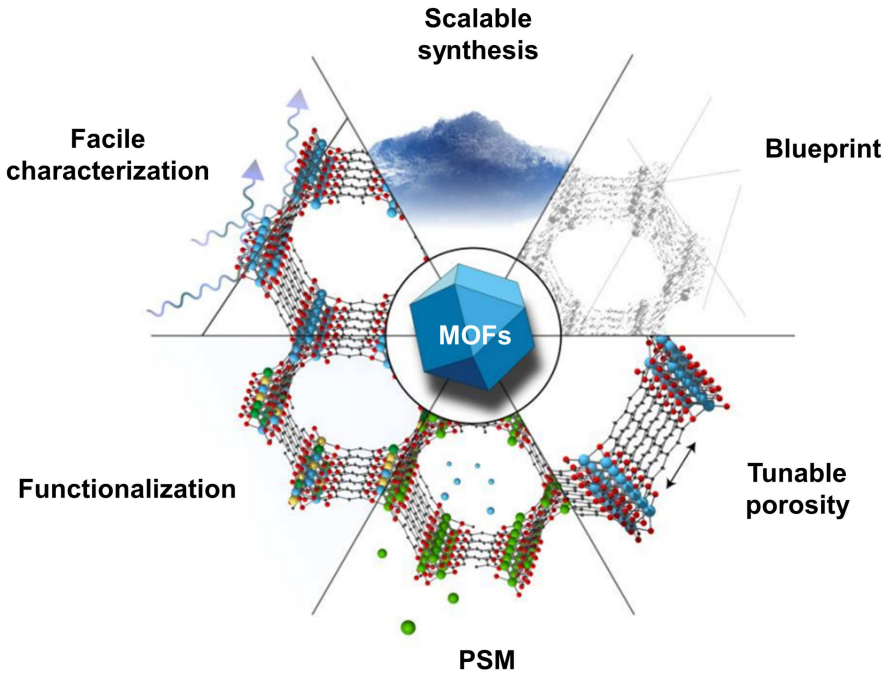

Figure 1.5: Scheme obtained from Freund *et al*. [98] illustrating the main characteristics of MOF materials that contribute to their scientific relevance in several fields.

The MOFs structure can be described as a hybrid framework, which is very similar to a classical inorganic porous solid as both of them have a three-dimensional skeleton, which is formed by the association of secondary building units (SBU). In inorganic SBU, there is only inorganic parts (e.g., SiO_4, PO_4, AsO_4, SO_4, associated with metallic cations in four, five or six-coordination), while in hybrid SBU, the anionic species are replaced by organic linkers [18]. The properties displayed by MOFs caused some ambiguity or confusion along the years with the term "coordination polymer". However, there are some major differences between these two types of materials. In comparison, MOFs usually exhibit higher thermal stability, permanent porosity and structural robustness [100]. They can present subnetworks formally described as clusters (0D), chains (1D), layers (2D) or frameworks (3D). These structures can be modulated by making different combinations of metals with organic linkers, which leads to infinite possibilities of architectures, topology, size, shape and rigidity [18,100].

In 2000, O'Keeffe *et al.* [101] and Férey [102] observed that some structures of MOFs corresponded to extended versions of simpler materials, such as diamonds and sodalites. After that, a real structural prediction was able to be made taking into account a careful selection of primary building units (PBU), the spatial organization, the local minima of the "energy" landscape, and the possible structures [18,95,100]. This prediction is commonly made by computer simulation, which provides a list of hybrid candidates (existing or not yet synthesized structures), with their space group, cell parameters, and atomic positions [18]. The final structure and properties of the MOFs are controlled by these parameters, but also by other synthesis constraints such as pressure, solvent, modulator, pH, reaction time, and temperature [100].

As mentioned before, some of the most desirable characteristics of MOFs are their permanent porosity and ultrahigh surface areas. Therefore, the possibility to tailor these properties without changing their fundamental topology is of major importance. One can cite the Isoreticular Expansion (IE), which is an important process that allows the control of pore size by varying the length and/or type of the organic linker (Figure 1.6). [103].

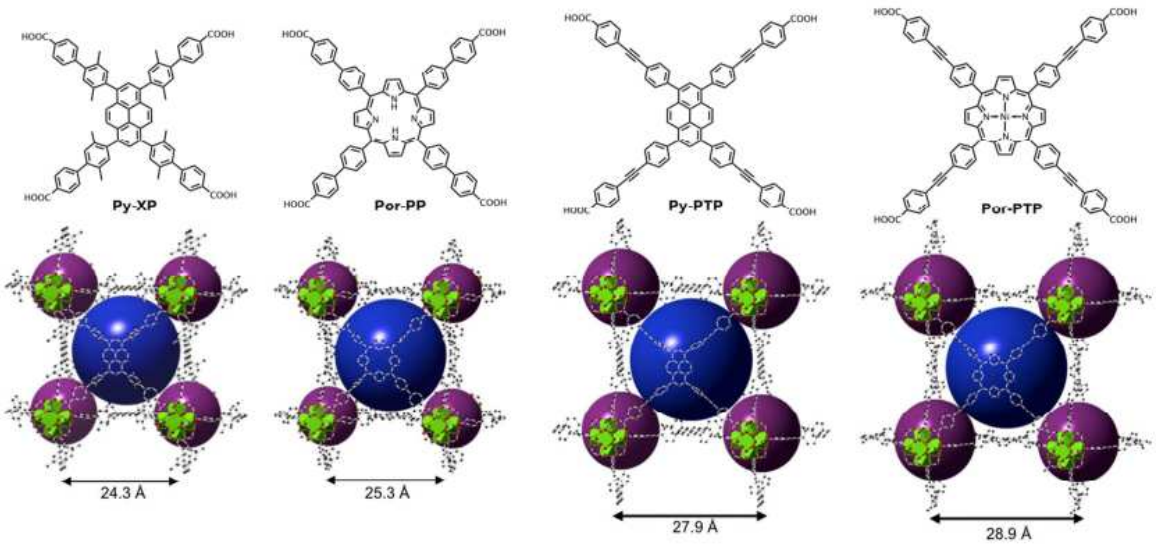

Figure 1.6: Scheme obtained from of Wang *et al.* [103] showing tetravalent organic linkers of Py-XP^{4-}, Por-PP^{4-}, Py-PTP^{4-}, and Por-PTP^{4-} used for constructing NU-1101, NU-1102, NU-1103 and NU-1104, respectively. The increasing dimensions of the organic linkers result in the isoreticular expansion of the MOF structures, with surface areas of 4422, 4712, 5646, and 5290 $m^2.g^{-1}$, respectively.

For instance, NU-1101, which is one of the most successful examples of IE strategy in a Zr-MOFs series, is synthetized using Py-XP^{4-} as the organic linker. This linker can be replaced by a longer one, such as Py-PTP^{4-}, which produces an isoreticular structure to NU-1101, but with a larger pore size and higher SSA (Figure 1.6). Usually, these properties have a proportional relationship between them. Indeed, Wang *et al.* reported NU-1101 showing a specific surface area of 4,422 $m^2.g^{-1}$, while NU-1103 have a specific surface area of 5,646 $m^2.g^{-1}$ and a pore volume of 2.91 $cm^3.g^{-1}$ [103]. Since the variation of linkers or functional groups does not affect the isoreticular nature of MOFs structures, this process has proved to be an efficient method to increase their efficiency for certain applications, such as CO_2, H_2, and I_2 adsorption [12,95].

The PSM is another chemical route used to change the functionality of MOFs. The main advantage of this technique is the possibility to obtain structures that cannot be otherwise achieved through direct synthesis (Figure 1.7). For this specific process, Zr-MOFs have been extensively researched due to their high stabilities in water, acid, and basic media [99]. For instance, Kim *et al.* [23] obtained Ti-containing UiO-66 MOFs by an approach associated with the substitution of central metal ion.

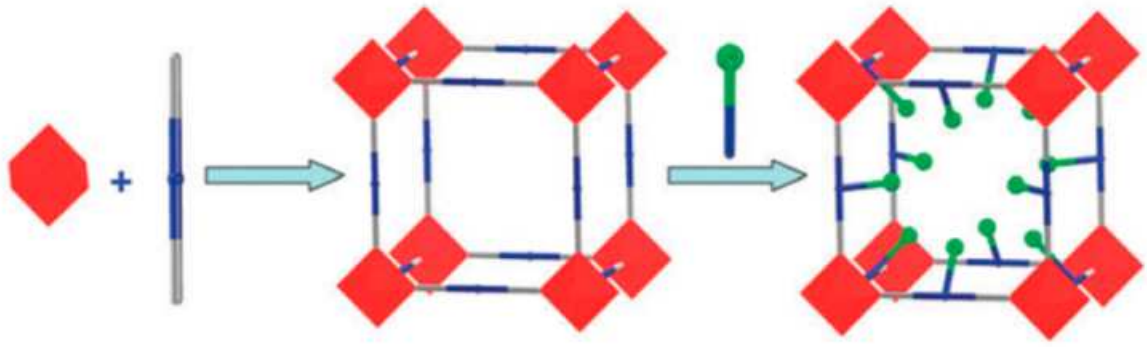

Figure 1.7: Scheme illustrating the principle of Post-Synthetic Modification in MOFs. Obtained from Wang and Astruc [104].

1.3.1. Different applications for MOF materials

Studies have been performed for the application of MOFs in several areas such as catalysis, adsorption, separation and storage of gases, liquids, and molecular species (i.e., H_2, CO_2 and CH_4), drug delivery, nanoreactors and nanomoulds for nanoscience, applied physics, and energy (Figure 1.8) [98,104]. However, some other features such as conductivity, magnetic and optical properties still lack deeper investigation [105].

One of the most important uses of MOFs is in the catalysis field. In this case, five types of systems or actives sites can be utilized: (a) homochiral metal-organic frameworks, (b) metal ions or linkers in the metal-organic frameworks, (c) coordinative unsaturated metal (CUM) centers, (d) metal complexes in supramolecular porous frameworks, (e) highly dispersed metal or metal oxide nanoparticles loaded onto porous MOF host lattices [18]. Several reactions can be catalyzed by such materials, worth mentioning hydrogen evolution, hydrogenation, Fischer-Tropsch synthesis, reduction of inorganic and organic compounds, and oxidation of different molecules such as olefins, alcohols, carbon monoxide, and sulfur derivatives [104]. Finally, electrocatalysis and photocatalysis deserve special attention due to recent advances in the field. While several reactions of great industrial interest – such as Hydrogen Evolution Reactions (HER) and Oxygen Evolution Reactions (OER) – were improved using MOF-derived electrocatalysts, the photodegradation of organic contaminants was improved using TiO_2@MOF composites [106–108].

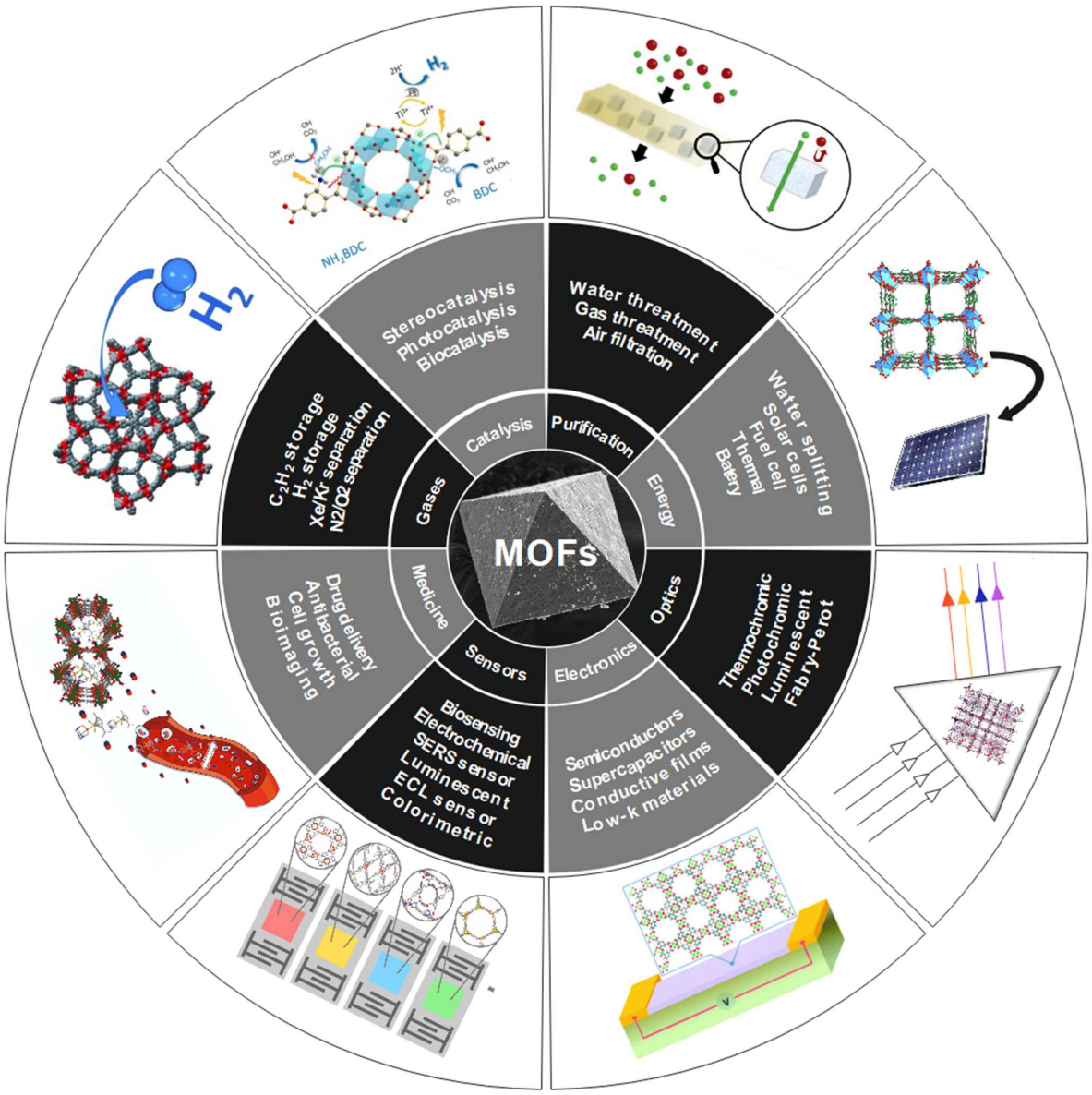

Figure 1.8: Scheme displaying the different applications for MOF materials.

MOFs are also extensively applied for gas storage and are in the top of the energy and environmental field. In fact, they can be applied for the removal of gaseous pollutants, such as CO_2 and ^{131}I, which are deeply related to anthropogenic atmospheric pollution [16,104]. They can also be used for hydrogen storage, which represents one of the major challenges for hydrogen energy and fuel cells in the automobile sector [109]. Despite hydrides seem to be an attractive option for such purpose, they have high densities which leads to low weight-based storage [18]. MOFs, on the other hand, do not have these limitations as their density is very low (below 1

g.cm^{-3}) [18]. Because of that, several MOF materials have displayed promising capacities for hydrogen storage at 77 K, such as MOF-5, HKUST-1, and MIL-53(Al) [110].

Other fields such as biomedical applications, chemical sensing, and electronic conduction also have MOFs as frontline materials [98]. For instance, they can be used in magnetic resonance imaging (MRI) as contrast agents or as a platform for adsorbing clinically approved contrast agents in theragnostic treatments [98,111]. Moreover, in the sensor field, the PSM of Mg-MOF-74 films with ethylenediamine increases the selectivity of on-chip CO_2 sensors [112]. Finally, an iron-tetrazolate MOF showing tunable electrical conductivity was reported to achieve a conductivity exceeding 1 S.cm^{-1}, which is a record in the field [113].

1.3.2. Charge transfer in MOFs

Charge transfer plays a key role for understanding the mechanisms behind several of these applications based on MOF materials. The electronic structure of isolated atoms or molecules – as in a perfect gas, for example – are mainly consisted of allowed energy levels. As the atoms become closer, the interaction between those levels starts to form continuous bands, as demonstrated in Figure 1.9 [114–117]. In this case, the Valence Band (VB) is composed of bonding orbitals filled with electrons, whereas the Conduction Band (CB) is mainly formed by empty antibonding orbitals [118,119]. Those bands can overlap (in the case of conductors) or be spaced (as in semiconductors and insulators) by an energy value also known as band gap (E_g) [117]. It is worth mentioning that, in all cases, the electron mobility in crystalline materials depends on the possibility of an electron to hop from the VB to the CB [120]. For instance, in conductors, the electrons have free mobility because both bands are naturally overlapped. Even so, in materials exhibiting band gaps, the CB can be populated if the electrons absorb a sufficient amount of energy ($> E_g$) to jump from the VB to the CB [120,121]. Actually, electron excitation can only occur following these principles. Nevertheless, when a guest species is introduced into the system and interacts with the compound, the electronic structure of the ensemble must be considered. In this case, if the spatial and energetic requirements are suitable, the charge carriers (electrons and holes) can move between the host material and the guest molecule.

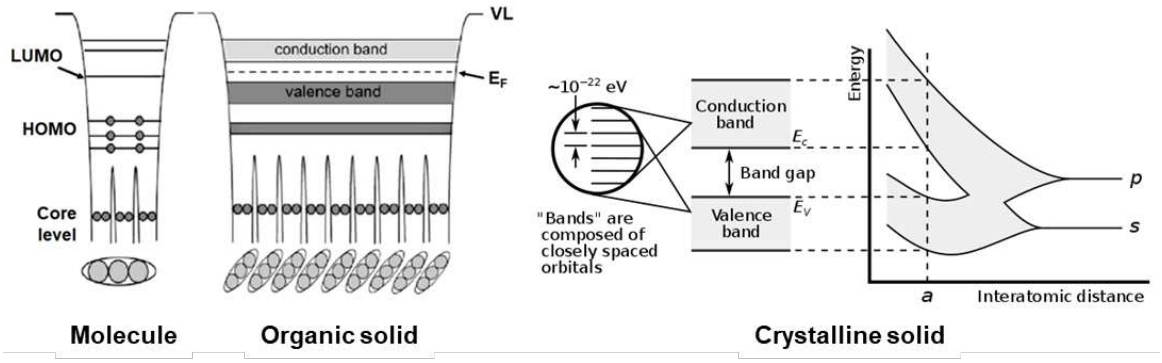

Figure 1.9: Electronic energy structure for an isolated molecule and a crystalline solid. When the interatomic distance reduces, the molecular orbitals (here represented by the *s* and *p* orbitals) start to form bands composed of closely spaced orbitals ($\Delta E \approx 10^{-22}$ eV). VL = vacuum level; E_F = Fermi level; E_V = valence band energy; E_C = conduction band energy; LUMO = Lowest Unoccupied Molecular Orbital; HOMO = Highest Occupied Molecular Orbital; a = lattice parameter.

Several CTC were already described in MOF materials and their presence influence the dynamics and reactivity of MOF-based systems. This behavior is related to the enormous range of structures that can be obtained by replacing the MOFs linkers and metal sites, by introducing molecules and/or nanoparticles inside their framework, by creating defects on their structure, and even by forming composites with other materials. The main CTCs exhibited by MOF materials are the Linker-Based Transition (LBT) [13,27], the Metal-Based Transition (MBT) [122], the Metal-to-Linker Charge Transfer (MLCT) [123], the Linker-to-Metal Charge Transfer (LMCT) [27], the Linker-to-Linker Charge Transfer (LLCT) [124], and the Metal-to-Metal Charge Transfer (MMCT) [125]. A scheme representing these types of CTCs observed in metal complexes is highlighted in Figure 1.10. Here, it is important to notice that, aiming to facilitate the comprehension, the electronic structure was represented as molecular orbitals of metal complexes in Figure 1.10, even though it is actually composed by MOFs bands, as mentioned before (Figure 1.9).

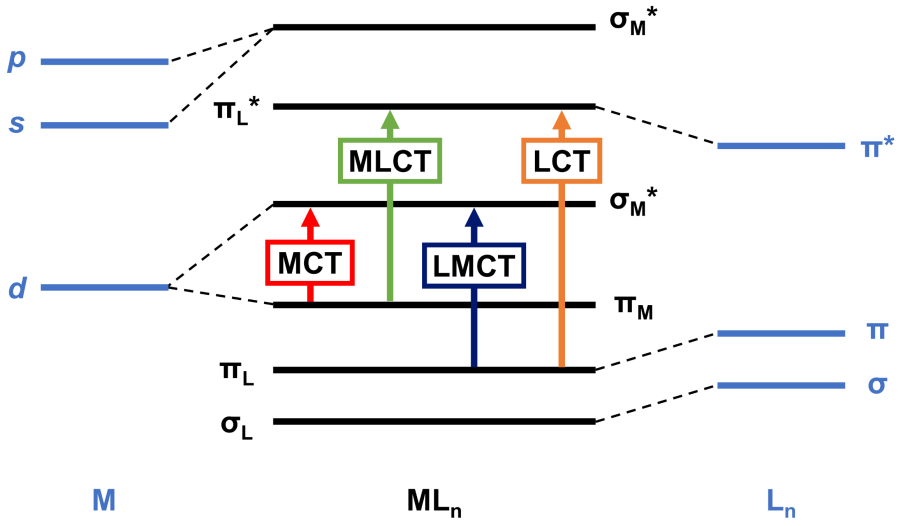

Figure 1.10: Molecular orbitals scheme and possible charge transfer in MOFs, here represented as metal complexes (ML_n). The LLCT and MMCT transitions are similar to those of LCT and MCT, respectively, but in a presence of a second linker or metal.

Both the VB and CB are formed by linker orbitals in the LBT, whereas in the MBT they are composed by metal orbitals. For instance, to build a MOF with a pure linker emission, a fluorescent or phosphorescent linker can be chosen [122]. An example is the UiO-66_NH_2 system, which exhibits a LBT related to its amino-terephthalate linkers, as demonstrated by Nasalevich *et al.* [27] (Figure 1.11). In this case, the authors demonstrated that the d^0 orbitals of the $Zr^{(IV)}$ cations are too close to the vacuum level and thus, they do not overlap with the π^* orbitals of the benzene-dicarboxylate (BDC) linker, despite the suitable geometry. This feature was confirmed by the absence of EPR signal related to $Zr^{(III)}$ cations, as observed in Figure 1.11. In the other hand, an MBT is predominately found in MOFs containing lanthanide or actinide cations, even though it also occurs in transition and *p*-block metals. One example is the $[Eu_2L_3(H_2O)_4]\cdot 3DMF$ (L = 2',5'-bis(methoxy-methyl)-[1,1':4',1''-terphenyl]-4,4''-dicarboxylate), in which the emission is related to the presence of Eu^{3+} cations, which excites electrons from its *d* to *f*-orbitals [126].

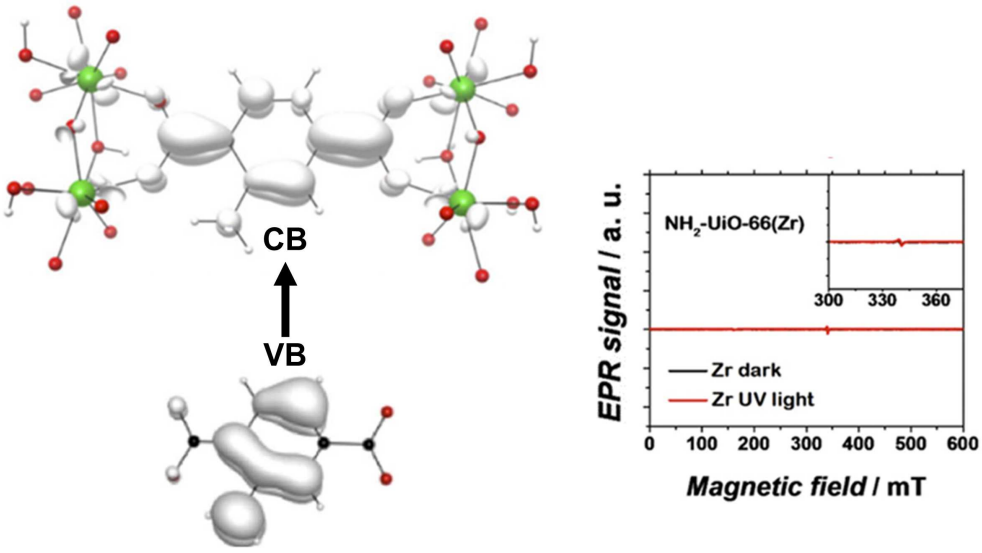

Figure 1.11: In the left: **s**cheme illustrating the LBT in in UiO-66_NH_2. The VB and CB contributions are both related to the linker. In the right: EPR signal showing that no paramagnetic species such as Zr^{3+} are formed upon excitation in the inorganic cluster, which rules out the possibility of a LMCT. Modified from Nasalevich *et al.* [27].

The CT can also be formed between the organic and inorganic parts of the MOF. In this case, the direction of the electron dictates their nomenclature. For instance, a LMCT is observed when the VB and the CB are located in the organic and inorganic parts of the MOF, respectively. This type of CT is typically found in MOFs containing transition metal cations and suitable organic linkers [122]. In fact, metals with high oxidation states (good candidates are cations with closed *d*-shells, such as d^0 and d^{10}) may be reduced in combination with linkers that can be partially oxidized. Indeed, contrary to what was found for UiO-66_NH_2, Nasalevich *et al.* [27] demonstrated that a LMCT is present in MIL-125_NH_2 materials. In this case, because the MOF is formed by $Ti^{(IV)}$ cations, the d^0 orbitals of the metal sites have both the energetic and geometric requirements to overlap with the π* orbitals of the BDC linker. This feature results in a CB that is localized over the inorganic part of the MOF, which was confirmed by a $Ti^{(III)}$ signal observed in EPR spectroscopy (Figure 1.12).

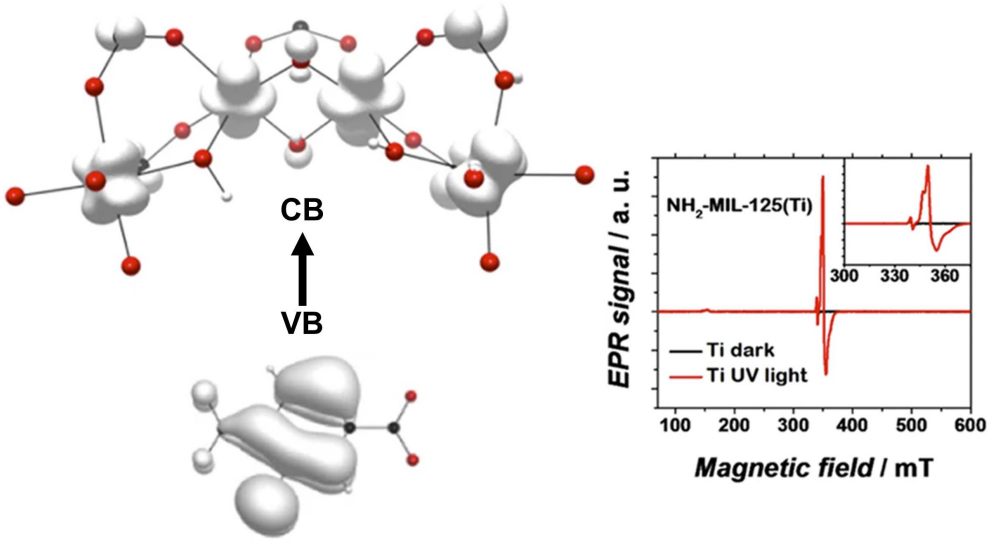

Figure 1.12: In the left: **s**cheme illustrating the LMCT in in MIL-125_NH_2. The VB and CB contributions are related to the linker and titanium cluster, respectively. In the right: EPR signal showing the presence of a Ti^{3+} paramagnetic species upon excitation in the inorganic cluster, which confirms the LMCT. Modified from Nasalevich *et al.* [27].

Similarly, the MLCT is observed between the inorganic and organic parts of the MOF. However, in this case, the VB and the CB are located over the metal and linker, respectively. This type of CT is commonly observed in MOFs with metal cations presenting a d^6, d^8 and d^{10} electron configurations concomitantly to *p*-acceptor linkers [122]. For instance, Kent *et al.* [123] observed a long lived triplet MLCT excited state in a $[ZnL_1]\cdot 2DMF\cdot 4H_2O$, where L_1 = $\{Ru[4,4'\text{-}(CO_2)_2\text{-}bpy)]_2(bpy)\}^{2-}$ and in a $[ZnL_2H_2]\cdot 3H_2O$, where L_2 = $\{Ru[4,4'\text{-}(CO_2)_2\text{-}bpy)]_2(CN)_2\}^{4-}$ MOFs (bpy = 4,4′-bipyridine). Also, another Zn-based MOF was found to transfer energy from the d^{10} molecular orbital of the Zn^{2+} to the LUMO+3 of the K_4PTC (PTC = 3,4,9,10-perylenetetracarboxylate) linker, creating a strong luminescence effect (Figure 1.13) [127].

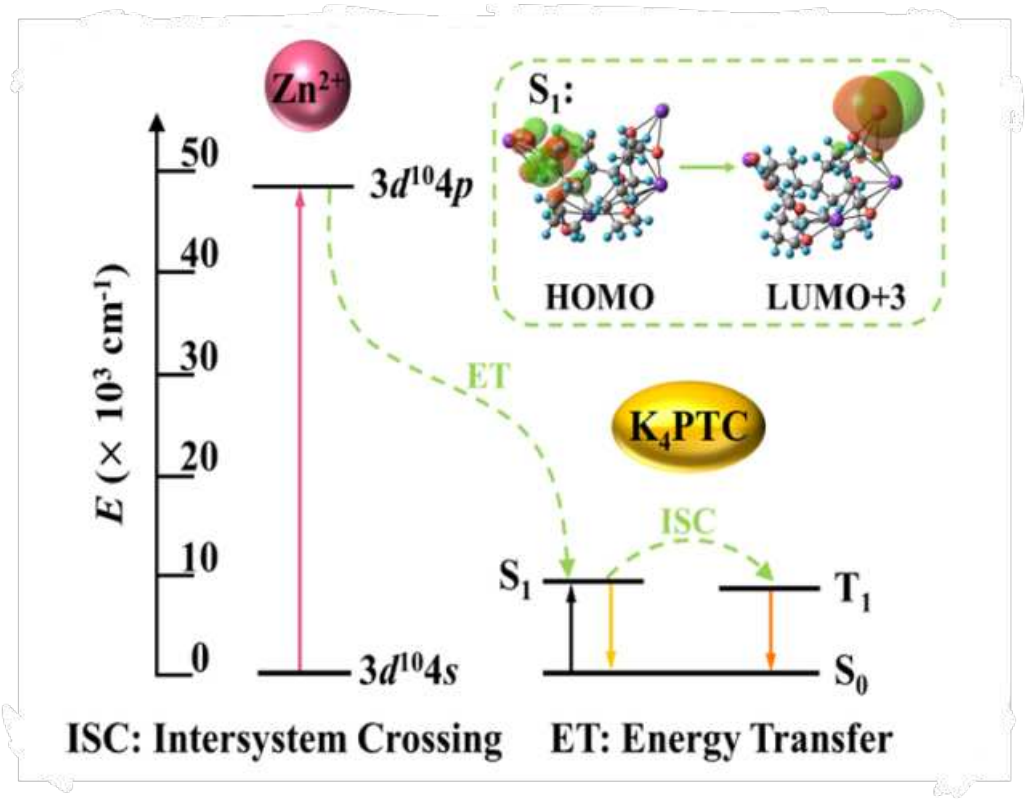

Figure 1.13: Scheme obtained from Song *et al.* [127] showing the MLCT from the d^0 orbitals from the Zn^{2+} cations to the LUMO+3 of the K_4PTC

The charge transfer process can also occur between different linkers in the same structure, which is the case of the Linker-to-Linker Charge Transfer (LLCT). For engineering MOFs with such behavior, it is necessary to build structure with two types of linkers: a strong electron-donor, and a strong electron-acceptor. For instance, Huo *et al.* [124] verified this type of CTC in three different manganese-based MOFs by using tetrathiafulvalene-dicarboxylate as the electron-donor linker, and different conjugated bipyridines as electron-acceptor sites (Figure 1.14).

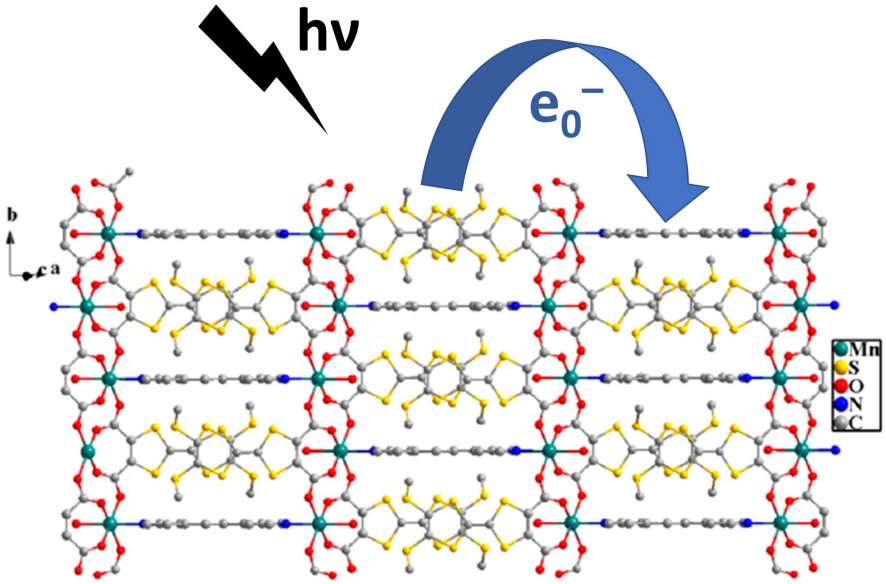

Figure 1.14: Scheme adapted from Huo *et al.* [124] demonstrating the LLCT between two TTF-dicarboxylate and 1,2-bis(4-pyridyl)ethene (bpe) linkers [bpe = 1,2-bis(4-pyridyl)ethene]. In this case, the electrons move from the TTF-dicarboxylate to the bpe linker.

Contrary to the LLCT, in the Metal-to-Metal Charge Transfer (MMCT) the electron excitation occurs between two metal sites. In fact, at least two different metal sites must be present in the same MOF compound for this CTC to be observed. For instance, Deneff *et al.*[128] verified a MMCT using a family of heterometallic rare-earth MOFs based on the 1,2,4,5-tetrakis(4-carboxyphenyl)benzene (TCPB) organic linker and containing different metal ratios of $Eu^{(III)}$, $Nd^{(III)}$, and $Yb^{(III)}$. They demonstrated that the incorporation of multiple metals into the MOFs structures had direct effects on their photoluminescence properties. First, upon excitation, a LMCT was formed between the TCBP linker and the Eu^{3+} inorganic cluster. Then, a metal-to-metal energy transfer took place from the long-lived Eu^{3+} to the Nd^{3+} and Yb^{3+} cations, which improved the emission features of the material (Figure 1.15).

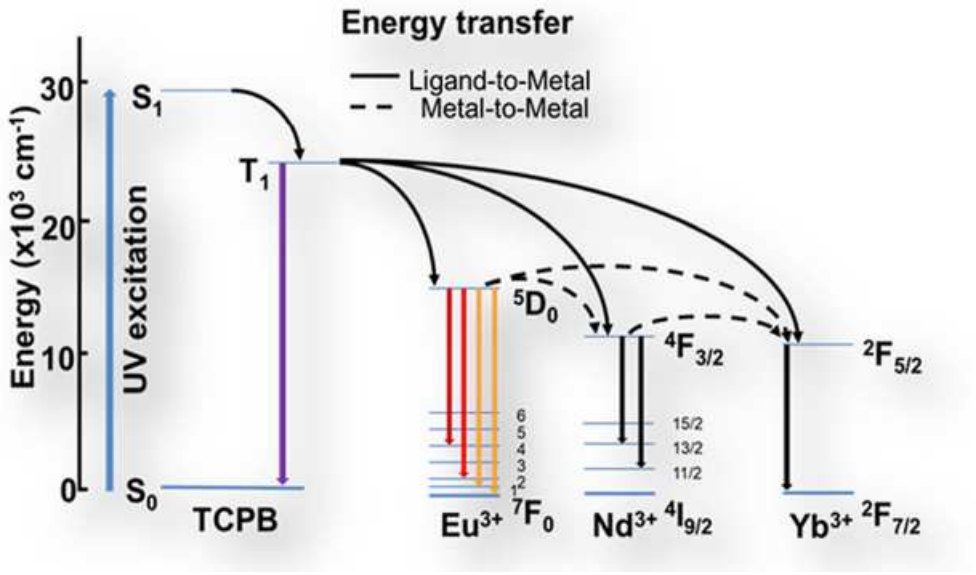

Figure 1.15: Scheme obtained from Deneff *et al.*[128] showing the MMCT between the Eu^{3+} and the Nd^{3+} and Yb^{3+} cations.

Finally, these interactions can also be present between the MOFs lattice and guest molecules or particles. In such cases, the CTC is often named depending on the nature of the involved species (i.e.: MMCT if both the host and guest entities are metals). Nevertheless, these effects should be distinguished from the CTCs that happens exclusively between structural components of the MOF (linkers and metals from the lattice). Therefore, they are also called Host-to-Guest Charge Transfer (HGCT) or Guest-to-Host Charge Transfer (GHCT), depending on the direction of the excited electron (similarly to what happens in LMCT and MLCT). For instance, there are systems where the electron transfer occurs from the VB of the MOF material towards the CB of a guest molecule, which is indicative of a HGCT. This is the case of the I_2 reduction into I_3^- observed in several I_2@MOF systems, such as in I_2@BOF-1 [129], I_2@MFM-300(V^{III}) [130], I_2@{$[(ZnI_2)_3(TPT)_2]\cdot 5.5(C_6H_5NO_2)\}_n$ (TPT = 2,4,6-tris(4-pyridyl)-1,3,5-triazine) [131], I_2@Th-BPYDC [132], I_2@CAU-21-ODB (ODB = 4,4'-oxydibenzoate) [133], I_2@-Cu_3(HHTN)$_2$ (HHTN = 2,3,8,9,14,15- hexahydroxytrinaphthylene) [134], I_2@Co_2(*m*-DOBDC) (*m*-DOBDC = 4,6-dioxo-1,3-benzenedicarboxylate) [135], I_2@HSB-W8 and I_2@HSB-W9 [136].

For instance, a HGCT was observed in two Cd-based MOFs named HSB-W8 and HSB-W9, which exhibits 2D and twofold interpenetrated 3D structures, respectively [136]. They were built using hydrogenated Schiff linkers – 1,2-bis(4'-pyridylmethylamino)-ethane (HSB-2) and trans-stilbene-4,4-dicarboxylate (TSBDC) – and $Cd(NO_3)_2$ using a diffusion method. The π-

electron-rich stilbene moieties were found to form a CTC with I_2 molecules, alluding to a chemisorption process. Also, the electron transfer from the MOF towards the iodine was able to reduce the I_2 species into I_3^- and other polyiodide anions.

Interestingly, a similar feature was observed in previous works with I_2@UiO-66(Zr) and I_2@UiO-6*x*(Zr)_NH_2 systems (*x* = 6 or 7) [12]. This study revealed, using EPR spectroscopy, that the metal center of UiO-6*x* materials (Zr^{4+}) cannot be oxidized nor reduced, even upon UV light irradiation ($\lambda < 420$ nm) [12,13]. Also, there were no evidences of a C–I bond formation in these compounds [12]. Yet, the I_2 into I_3^- redox conversion was verified in both I_2@UiO-66(Zr) and I_2@UiO-6*x*(Zr)_NH_2 materials through Raman spectroscopy [12]. In these cases, a CTC between the BDC linkers and the I_2 molecule was responsible for generating $BDC^{\bullet+}$ radicals and I_3^- species [13]. On the other hand, the I_3^- formation on the I_2-loaded Co_2(*m*-DOBDC) MOF was ascribed to an electrophilic aromatic substitution caused by the activation of the C–H bond at the electron-rich carbon (C5) of *m*-$DOBDC^{4-}$ [135]. The reaction forms an aryl C–I bond and I^- or I_3^- that coordinate to unsaturated open Co sites.

Finally, when the VB is located in the guest species and the CB is related to the MOF lattice, the CTC is named GHCT. This is the case of a HKUST-1 decorated with palladium nanocubes (Pd@HKUST-1). Here, Chen *et al.* [137] observed – by means of Hard X-rays Photoelectron Spectroscopy (HAXPES) – an electron transfer from the *d*-orbitals of the palladium to the *d*-orbitals of the copper cations in HKUST-1, as highlighted in Figure 1.16. Their results were confirmed by interfacial and internal Density of States (DOS) calculated using the density functional theory (DFT) method.

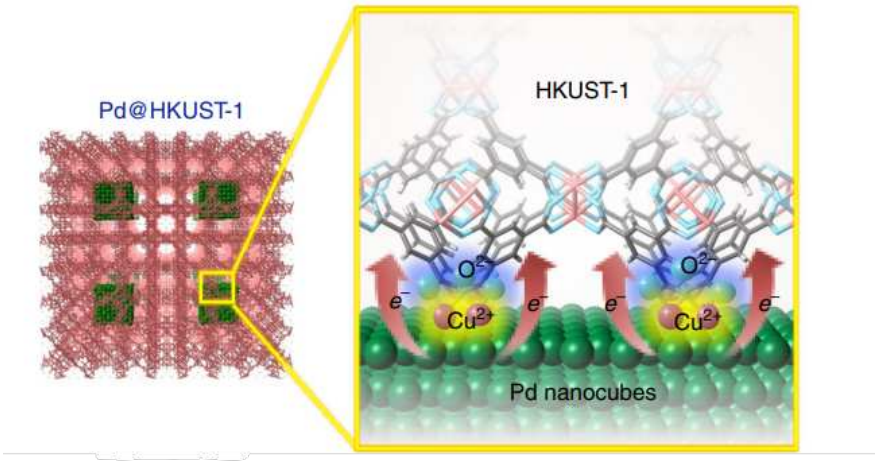

Figure 1.16: Schematic obtained from Chen *et al.* [137] showing the GHCT from Pd nanocubes to HKUST-1 at the interface.

1.4. Confinement and reactivity

As discussed above, porous materials that present well-ordered channels or cavities such as zeolites, MOFs, and COFs are commonly applied in several confinement applications such as size-selective confined space functions, molecular containers, molecular conduits, catalysts, chemical recognizers, adsorbent materials, drying agents, delivery systems, ion-exchange, sensing, nuclear waste storage, solar cells, photoluminescent solar concentrators, guest-conformation tuning, guest preorganization, color changing media, scavenger, and biomedical systems [138–145]. Therefore, the interactions between confined species and host materials are of great interest for the scientific community, specially due to the possibility of controlling different parameters of the guest-host system such as hydrophilicity, surface area, and chirality [146,147].

For instance, Yanai *et al.* [148] observed structural transformations of a crystalline host framework triggered by structural changes in a guest molecule. By using a Metal-Organic Channel (MOC) composed of [Zn_2(terephthalate)$_2$(triethylenediamine)], the authors verified a *cis*/*trans* isomerization of the guest azobenzene molecule upon light irradiation or heat treatment. This effect was accompanied by an enormous increase in the gas adsorption properties of the material, as demonstrated in Figure 1.17. Indeed, the initial *trans*-azobenzene@MOC compound exhibited negligible N_2 adsorption. In contrast, the *cis*-azobenzene@MOC exhibited a N_2 gas uptake about 8 times higher in comparison.

This type of host-guest chemistry is deeply related to the confinement effect of different molecules. In fact, studies regarding stimulus-responsive MOF materials suggest that several strategies can be applied to synthesize compounds with such characteristics, worth mentioning: (I) use of responsive building unities; (II) guest exchange; (III) linker exchange; (IV) metal exchange; (V) covalent modification or functionalization; and (VI) core-shell structures [149].

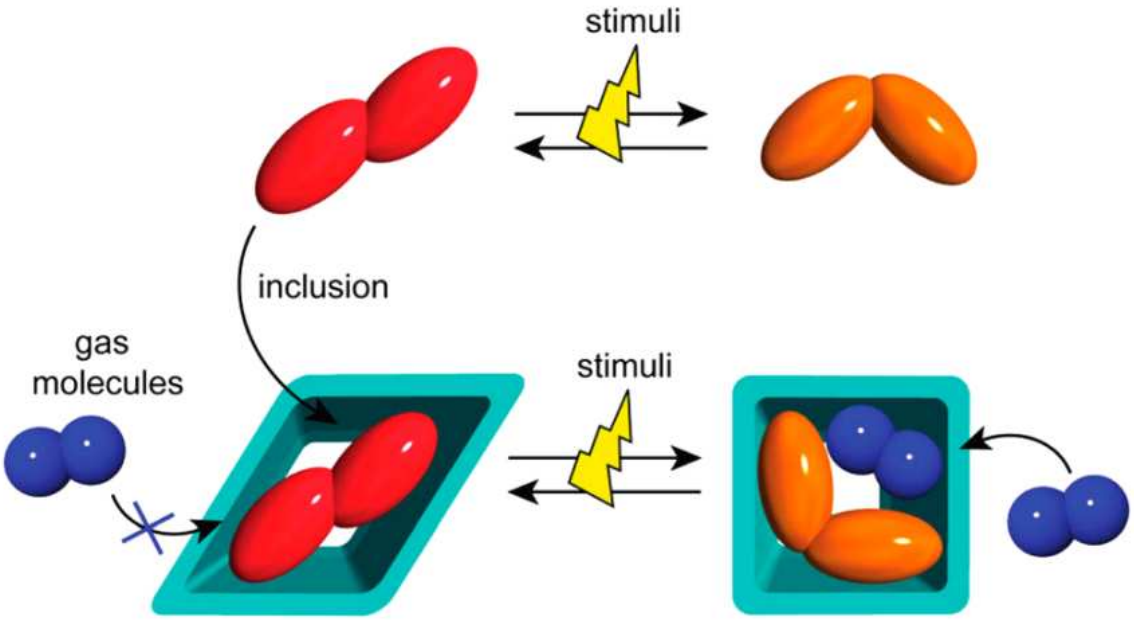

Figure 1.17: Schematic illustration obtained from Yanai *et al.* [148] demonstrating the concept of guest-to-host structural transmission. The red and orange objects represent *trans*-azobenzene and *cis*-azobenzene, respectively.

For instance, Zheng *et al.* [150] demonstrated a correlation between the topology of MOF frameworks and trapped metal species that may be exploited to create a large family of zeolite-type MOFs with channels modified by metal ions and clusters. Other applications such as solid-state reversible photo-switching were observed in anthracene@ZIF-8 materials [151]. In this case, the anthracene (ATH) molecules were found to be ordered in two pairs with a partial overlapping geometry in the cages of ZIF-8. This first conformation gave rise to a yellow excimer emission, in which, upon UV light excitation, ATH molecules are photodimerized to form a non-fluorescent photodimer (with a purple monomer emission). This effect was reversible upon thermal dissociation of ATH and further reorganization into ordered pairs [151]. Another interesting confinement effect in MOFs was reported by Khaletskaya *et al.* [152] by using a core-shell GNRs-[Al(OH)(1,4-ndc)] (1,4-ndc = 1,4- naphthalenedicarboxylate; GNRs = gold nanorods) composite. In fact, the authors demonstrated that the GNRs have the ability to act as an optical switch to induce the release of loaded ATH upon light excitation. In this case, the photothermal conversion of the GNRs entities upon near-infrared light excitation increased the molecular mobility of the guest molecules (in this case, ATH) and triggered their remote release (Figure 1.18).

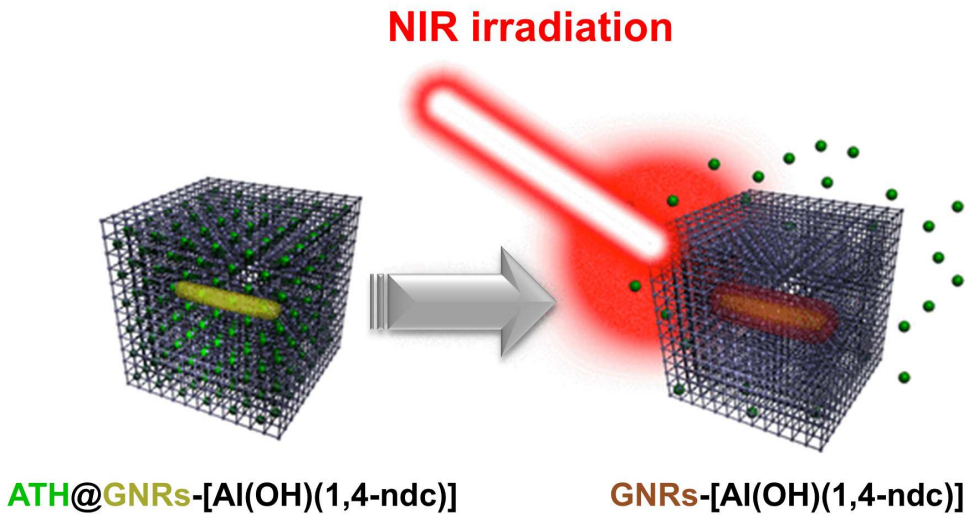

Figure 1.18: Scheme obtained from Khaletskaya *et al*. [152] showing the light-induced molecular release of ATH using a GNR-[Al(OH)(1,4-ndc)] compound as an optical switch with sensibility to near-infrared radiation.

1.4.1. Iodine confinement using MOFs

The capture of iodine using MOFs can be achieved via adsorption from solution or vapor diffusion [15]. Because one of the major health issues associated to nuclear contamination is related to the spread of gaseous iodine in the atmosphere, this section deals specifically with the capture of iodine in gaseous phase. Considering this, a resume of the state-of-the-art for the best MOFs used to trap gaseous iodine is highlighted in Table 1.3.

Table 1.3: State-of-the-art for the best MOF sorbents used for capturing gaseous iodine.

Adsorbent	Iodine uptake ($g.g^{-1}$)	Conditions	Ref.
UiO-67(NH_2)$_2$	1.21	gaseous I_2 flow (0.08 $mg.h^{-1}$); T = RT	[12]
HKUST-1	1.75	I_2 vapor; T = 75 ºC	[153]
ZIF-8	1.25	I_2 vapor; T = 77 ºC	[154]
PCN-333(Al)	4.42	I_2 vapor; T = 75 ºC	[155]
IL@PCN-333(Al)	7.35	I_2 vapor; T = 75 ºC	[155]
MOF-808	2.18	I_2 vapor; T = 80 ºC	[156]
NU-1000	1.45	I_2 vapor; T = 80 ºC	[156]
Zn_2(tptc)(apy)	2.16	I_2 vapor; T = 75 ºC	[157]
$Zr_6O_4(OH)_4(L^4)_6$	1.07	I_2 vapor; T = RT	[158]
$Zr_6O_4(OH)_4(L^5)_6$	1.80	I_2 vapor; T = RT	[158]
$Zr_6O_4(OH)_4(L^6)_6$	1.80	I_2 vapor; T = RT	[158]
$Zr_6O_4(OH)_4(L^7)_6$	2.79	I_2 vapor; T = RT	[158]
MFM-300(Sc)	1.54	I_2 vapor; T = 80 ºC	[159]
MFM-300(In)	1.16	I_2 vapor; T = 80 ºC	[159]
MFM-300(Fe)	1.29	I_2 vapor; T = 80 ºC	[159]
MFM-300(V^{III})	1.42	I_2 vapor; T = 70 ºC	[130]
MFM-300(V^{IV})	1.25	I_2 vapor; T = 70 ºC	[130]
UPC-158	1.78	I_2 vapor; T = 70 ºC	[160]
UPC-158-HF	2.19	I_2 vapor; T = 70 ºC	[160]
UPC-158-HCl	2.92	I_2 vapor; T = 70 ºC	[160]
UPC-158-HBr	2.75	I_2 vapor; T = 70 ºC	[160]
UiO-66	1.17	I_2 vapor; T = 80 ºC	[161]
UiO-66-FA	2.25	I_2 vapor; T = 80 ºC	[161]
Co_2(*m*-DOBDC)	2.02	I_2 vapor; T = 75 ºC	[135]
Co_2(*p*-DOBDC)	2.15	I_2 vapor; T = 75 ºC	[135]
HSB-W8	2.32	I_2 vapor; T = RT	[136]
HSB-W9	1.92	I_2 vapor; T = RT	[136]
Th-BPYDC	2.23	I_2 vapor	[162]

L^4 = 4,40-stilbene-dibenzoate; L^5 = 4,40-(ethyne-1,2-diyl)-dibenzoate; L^6 = 4,40-(buta-1,3-diyne-1,4-diyl)-dibenzoate; L^7 = 4,40-[1,4-phenylenebis(ethyne-2,1-diyl)]-dibenzoate; *m*-DOBDC = 4,6-dioxo-1,3-benzenedicarboxylate; *p*-DOBDC = 2,5-dioxo-1,4-benzenedicarboxylate.

Falaise *et al.* [25] investigated the I_2 kinetic adsorption within aluminum-based MOF compounds. In this case, MIL-101_NH_2 shows the best I_2 adsorption kinetics for removing iodine from a cyclohexane solution, with 90% of initial molecular iodine removed after 30 hours (Figure 1.19) [25]. It is worth mentioning that the authors observed that the level of iodine uptake is not directly associated with the MOF surface area. Instead, it is correlated to the characteristics of the pendant group. In fact, among groups such as methyl, chloride, and carboxylic acid, amine proves a much higher removal efficiency. A comparison between MIL-101_NH_2 and MIL-100, two MOFs with similar surfaces and topologies, shows this more

clearly. Iodine uptake by MIL-101-NH_2 is seven times greater than in the case of MIL-100 [25]. In this case, the increase in the I_2 adsorption capacity was attributed to the amine functional group, which is a strong electron donor and has the ability to form strong CTC with iodine. This enables a higher uptake of I_2 by the MOF framework and highlights the importance of the amino group for the trapping and immobilization of iodine. More recently, a thiol-functionalized MIL-53(Al) also exhibited a notable improvement compared to the pristine MOF when trapping iodine (0.33 $g.g^{-1}$) [163].

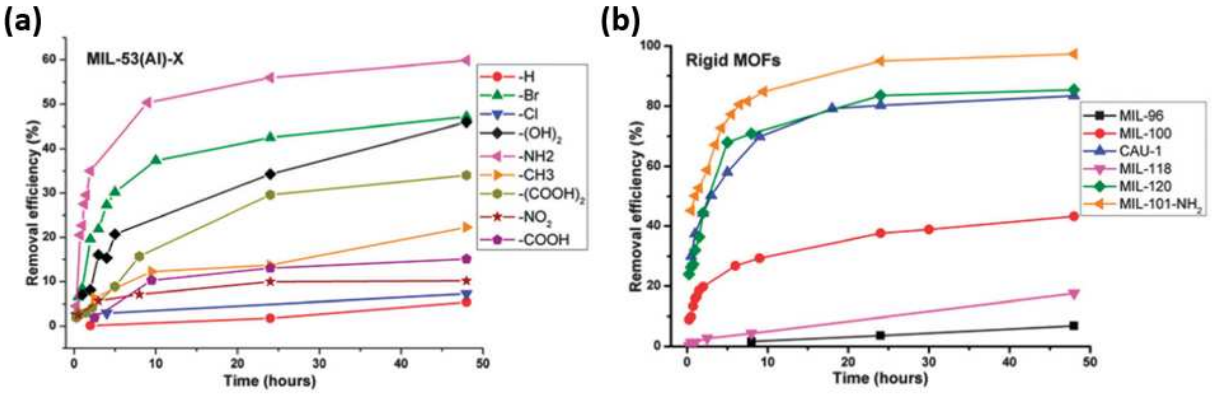

Figure 1.19: Iodine adsorption kinetics of (a) flexible and (b) rigid Al-based MOF compounds (RT). Obtained from Falaise *et al.* [25].

Zr-based UiO-66 MOFs that were elongated using linkers containing unsaturated alkene and alkyne as bridges also exhibits improved iodine uptakes by providing sites for the halogenation of their unsaturated C–C bonds [15,158]. Indeed, UiO family of MOFs bearing zirconium stands out in this vast class of crystalline solids due to its thermal and chemical stability as well as its facility to be functionalized, either by replacing the organic linker on its structure or also by changing the metal content within the inorganic cluster [12,13] . Several studies were already conducted using such family of MOFs, highlighting the capacity of this material to retain I_2 under conditions that simulates a nuclear accident (^{131}I leaking with steam at 120 ºC and up to 2 MGy γ radiation from ^{60}Co source) [16] and also the influence of the organic linker over the iodine capture [12,24,25]. The authors confirmed the affinity of the –NH_2 group towards the iodine molecule, as the amino-functionalized MOFs exhibited an enormous improvement on the iodine removal capacity – from 0.22 $g.g^{-1}$ in the pristine UiO-67 against 1.21 $g.g^{-1}$ in UiO-67(NH_2)$_2$ – during 48 h of contact with the gas stream (Figure 1.20). Moreover, the presence of –NH_2 groups also improved the iodine capture by a 2.7 factor in

UiO-66 [12]. Similarly, other functional groups such as –OH and –COOH also favorized the I_2 capture [24]. These results confirm that electron-donating groups can improve the CTCs between the MOFs and the I_2 molecules.

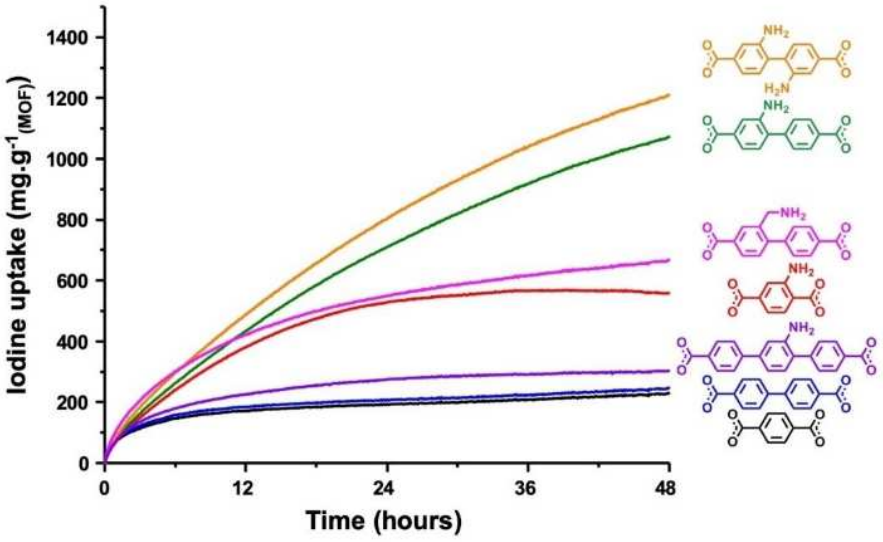

Figure 1.20: Kinetic curves obtained from Leloire *et al.* [12] of gaseous iodine adsorption in UiO-67 and UiO-68 derivative compounds at room temperature compared to that of UiO-66-H. Adsorption was carried out at room temperature and ambient pressure for an exposure time of up to t=48 h.

Another interesting method to improve the I_2 capture is to introduce iodine containing groups to the MOF linker. For instance, the complex $[Tb(Cu_4I_4)(ina)_3(DMF)]\cdot 1.5I_2$ (ina = isonicotinate) incorporates $[Cu_4I_4]$ moieties and possesses channels of 9.4 – 9.7 Å diameter [164]. The interaction between the iodine molecules and the $[Cu_4I_4]$ groups form tetraiodide anions (I_4^{2-}) with $[I^- \cdots I_2 \cdots I^-]$ interactions in a short intermolecular distance (3.34 Å), as demonstrated in Figure 1.21 [165]. A similar feature was also observed by Brunet *et al.* [131] for a $[(ZnI_2)_3(TPT)_2]$ (TPT = 2,4,6-tris(4-pyridyl)-1,3,5-triazine) upon exposure to iodine vapor. In this case, the I_4^{2-} species were later converted into I_3^- after increasing the iodine loading in the material (up to 1.73 $g.g^{-1}$).

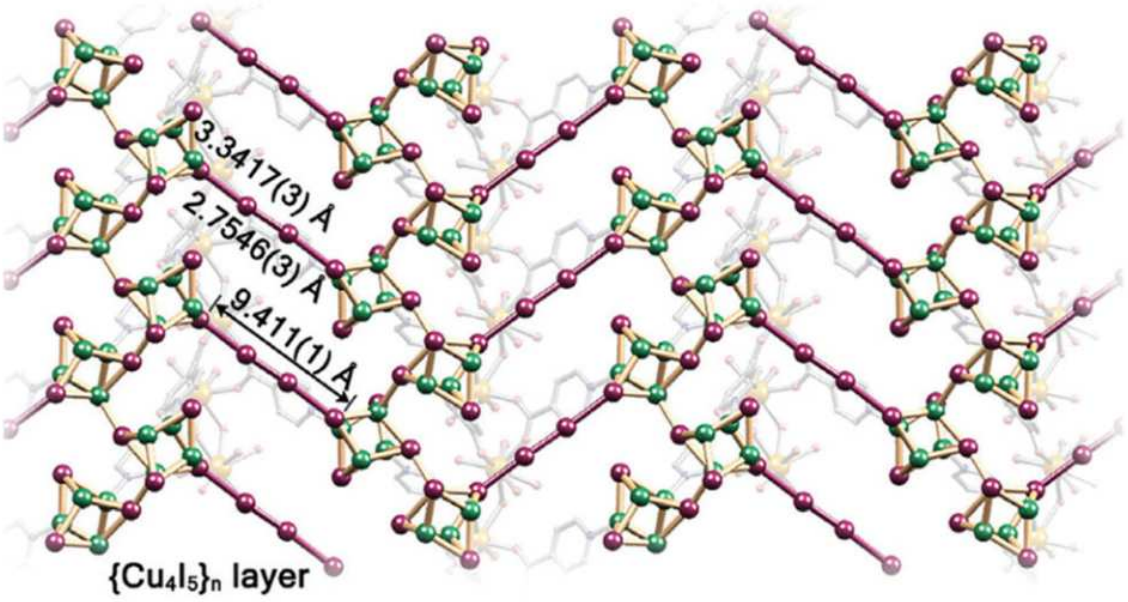

Figure 1.21: View of the linear I_4^{2-} bridge constructed in $[Tb(Cu_4I_4)(ina)_3]$ [165].

Shaping porosity is also an important feature when improving the I_2 capture by MOF materials. Recently, Marshall *et al.* [158] synthesized a series of Zr-based isoreticular MOFs using the extended form of UiO-66, where the elongated linkers exhibit unsaturated carbon chains such as alkenes, alkynes, and units as bridges, as demonstrated in Figure 1.22. The authors were able to achieve SSAs ranging between 2650 – 3850 $m^2.g^{-1}$ and iodine uptakes of 1.1 – 2.8 $g.g^{-1}$. The increase in the I_2 uptake for structures with bigger linkers was related to the higher density of aromatic groups in the structure [158]. Similarly, Leloire *et al.* [12] also evaluated the pore size influence on the iodine capture when increasing the length of the linker in a series of amino-functionalized UiO materials (Figure 1.20). These authors showed that an increase in the pore size favorizes the iodine capture – UiO-66_NH_2 can trap 0.56 $g.g^{-1}$, whereas UiO-67_NH_2 can reach values of 1.07 $g.g^{-1}$ for a pore volume of 0.31 and 0.83 $cm^3.g^{-1}$, respectively [12]. However, if the pores are too large – as in the case of UiO-68_NH_2 – the iodine molecules will not be retained inside the structure; instead, they will pass through the sample without having a significative interaction with the material's framework. This effect reduces the iodine trapping capacity to 0.30 $g.g^{-1}$ in UiO-68_NH_2 [12]. These results demonstrate that there is an optimum pore size for trapping iodine. Indeed, if the pores are too small, the molecule will not enter into the framework cages while if they are too large, the molecules will pass through the MOFs lattice without being captured. In fact, high surface areas and porosity are not the only

prerequisites for high iodine uptake in MOFs. Some other factors such as pore geometry and shape can also significantly influence adsorption [15]. A good example is the complex [Zn_2(tptc)(apy)] (tptc = triphenyl-3,3'',5,5''-tetracarboxylate; apy = aminopyridine) which presented a high iodine uptake (2.16 $g.g^{-1}$) even though it has a relative low SSA (168 $m^2.g^{-1}$) and pore volume (0.46 $cm^3.g^{-1}$) [157]. In this case, the great capacity to retain iodine was ascribed to effects of the conjugated π-electron aromatic system, halogen bonding, and presence of amino groups [157]. That being said, there are still some correlations between high SSA, pore volume, and iodine trapping capacity, especially considering gas diffusion experiments [15].

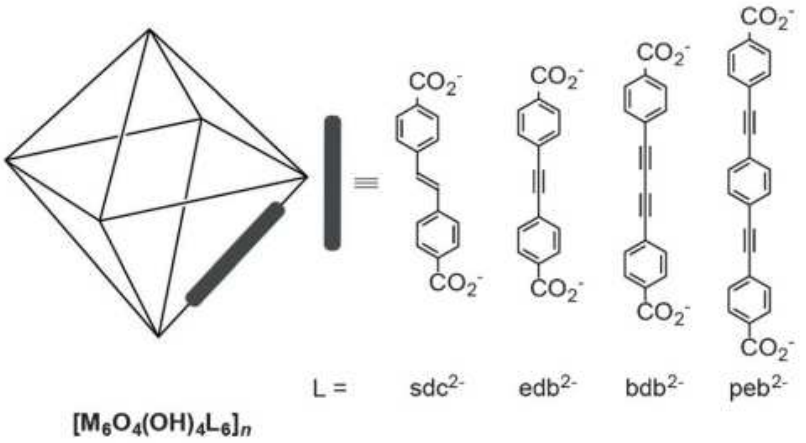

Figure 1.22: Scheme of the linkers used by Marshall *et al*. [158] to produce a series of Zr-based isoreticular UiO-66 MOFs.

The presence of redox metal centers can also influence the iodine trapping capacity in MOF materials. For instance, redox-active centers were observed in MFM-300(V^{III}), which showed a reversible iodine uptake of 1.42 $g.g^{-1}$ followed by a significant enhancement of the electrical conductivity (Figure 1.23) [130]. Again, the oxidation of V^{3+} into V^{4+} was responsible for the formation of the I_3^- species within the pores of the MOF, which was verified by XPS and Raman spectroscopies [130]. Here, it is worth mentioning that the adsorbed I_2/I_3^- molecules reduced the conductivity of the material by a magnitude of 10^6, making MFM-300(V^{III}) a great candidate for detecting iodine [130].

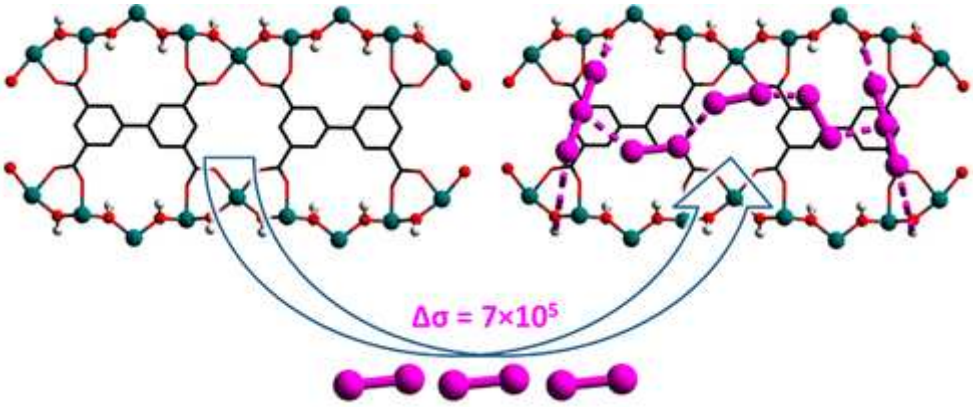

Figure 1.23: Scheme obtained from Zhang *et al.* [130] representing the iodine adsorption in MFM-300(V^{III}) followed by an increase of the electrical conductivity of about 10^5 times.

Another interesting approach to improve the iodine capture is to dope the MOF materials with active metal sites and/or molecules. For instance, the formation of metal iodides (similar to that observed for aerogels) was observed in MIL-101 doped with Ag^{2+} ions [166]. The authors demonstrated that, when MIL-101 is doped with Ag^{2+}, its capacity to retain iodine is multiplied by 12 (up to 0.24 $g.g^{-1}$). Similarly, Bingbing *et al.* [167] improved MIL-101 adsorption capacity towards iodine by incorporating copper nanoparticles. In this case the iodine uptake achieved 3.42 $g.g^{-1}$. Using a different approach, Meng *et al.* [134] synthesized a new *d*–π conjugated 2D Cu_3(HHTN) MOF (HHTN = 2,3,8,9,14,15-hexahydroxytrinaphthylene) doped with I_2 molecules. The I_2 doping process involved partial oxidation of both the linker and metal sites concomitantly to the formation of I_3^- species, as demonstrated using XPS analysis. This procedure was able to improve the conductivity of the Cu_3(HHTN) compound by 360 times, demonstrating other applications for trapping iodine in MOF materials. Moreover, ionic liquids (IL) can also improve the I_2 capture, as demonstrated by Tang *et al.* [155] using PCN-333(Al). In fact, the pristine PCN-333(Al) achieved an I_2 retention of 3.40 $g.g^{-1}$, whereas the IL@PCN-333(Al) trapped 7.35 $g.g^{-1}$ of gaseous iodine [155]. This result is the highest recorded I_2 uptake from gas diffusion and originates from interactions between iodine and halides – in this case, bromide present in the ionic liquid located inside the pores of the MOF (Figure 1.24) [155]. The same technique was also applied to MIL-101(Cr) to increase the I_2 uptake from 0.39 to 0.96 $g.g^{-1}$ after doping with an ionic liquid.

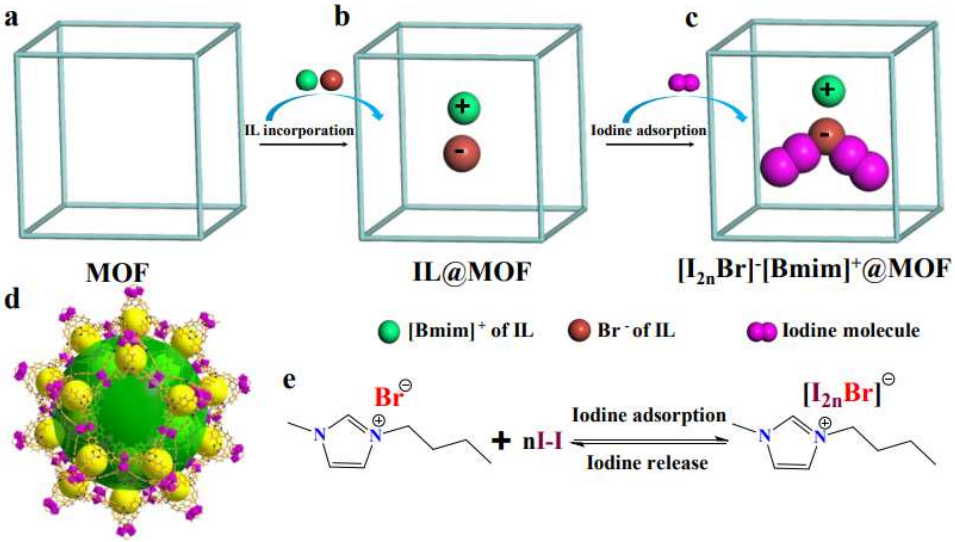

Figure 1.24: Scheme obtained from Tang *et al.* [155] illustrating the iodine adsorption by a MOF impregnated with an ionic liquid. (a) pristine MOF, (b) MOF with incorporated IL, (c) IL-induced dynamic ionization of I_2 molecule in IL@MOF, (d) the structure of PCN-333(Al), and (e) the mechanism of dynamic oligoiodide chain-formation in IL@MOF.

Some studies also highlighted the influence of defects in the MOFs structures when capturing iodine. For instance, Guan *et al.* [168] used a defect-containing hafnium-based UiO-66 to adsorb iodine from a cyclohexane solution. The authors observed a controlled formation of defect sites in the UiO-66(Hf) sample by simple acid treatment, which improved the iodine capture by 44%. This increase was ascribed to the iodine adsorption at the defective sites, as schematized in Figure 1.25. Similarly, Maddock *et al.* [161] also demonstrated a better iodine gas uptake in the defect-containing UiO-66(Zr) material. In this case, the defects were attributed to missing clusters in the framework and were found to improve the I_2 adsorption capacity from 1.17 to 2.25 $g.g^{-1}$.

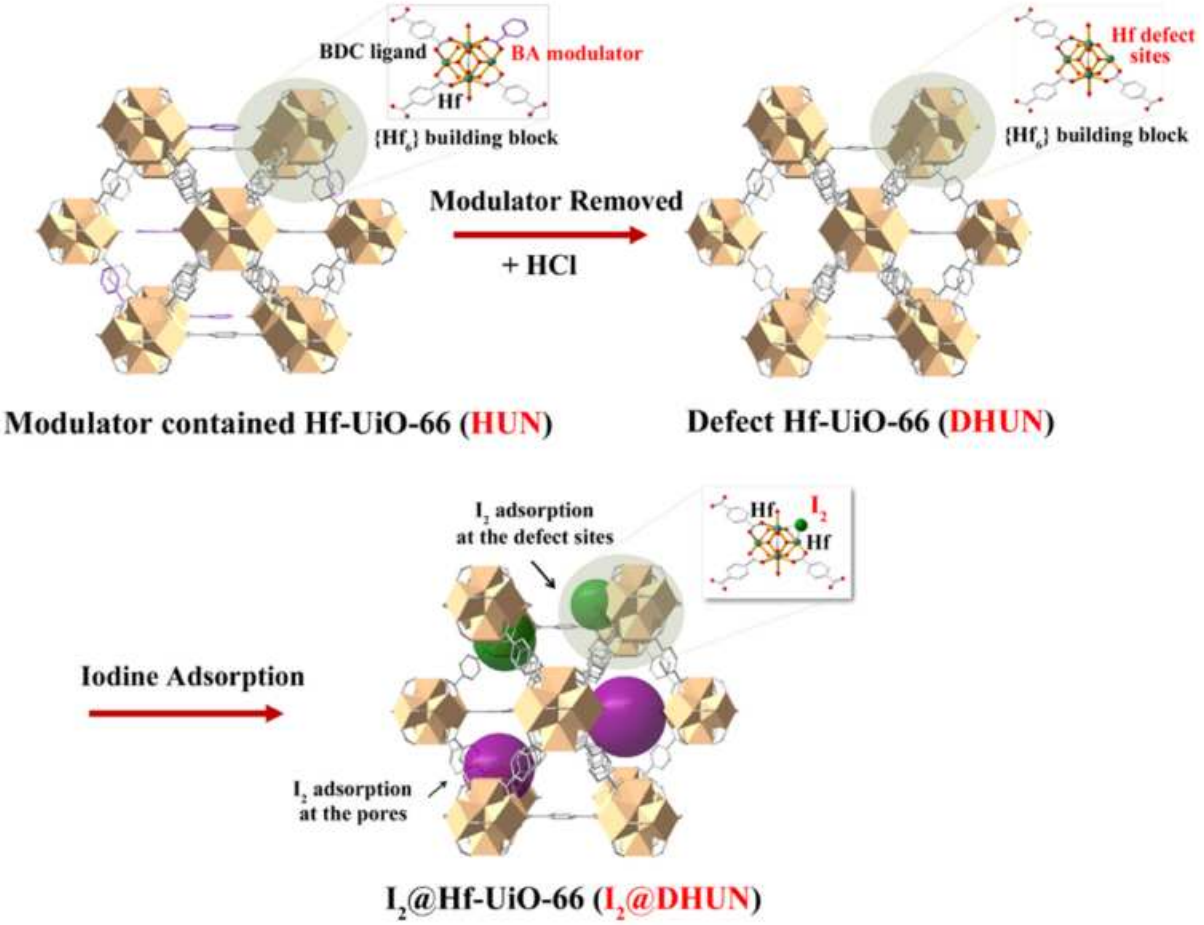

Figure 1.25: Diagram obtained from Guan *et al.* [168] illustrating the iodine adsorption in defect-containing UiO-66(Hf).

In another study, Lee *et al.* [135] obtained a Co_2(*m*-DOBDC) (*m*-DOBDC = 4,6-dioxo-1,3-benzenedicarboxylate) MOF with increased capacity to retain iodine (up to 78% of removal efficiency from a cyclohexane solution within 30 minutes). In this case, the C–H bond at the electron-rich carbon of the *m*-DOBDC organic linker was responsible to induce an electrophilic aromatic substitution, creating an aryl C–I bond and I^- or I_3^- that coordinate to unsaturated open Co sites. Using SC-XRD analysis, the authors were able to crystallographically visualize the I_2 binding sites and also the I^- and I_3^- formation, whereas the presence of the I_3^- was also confirmed by Raman spectroscopy (Figure 1.26).

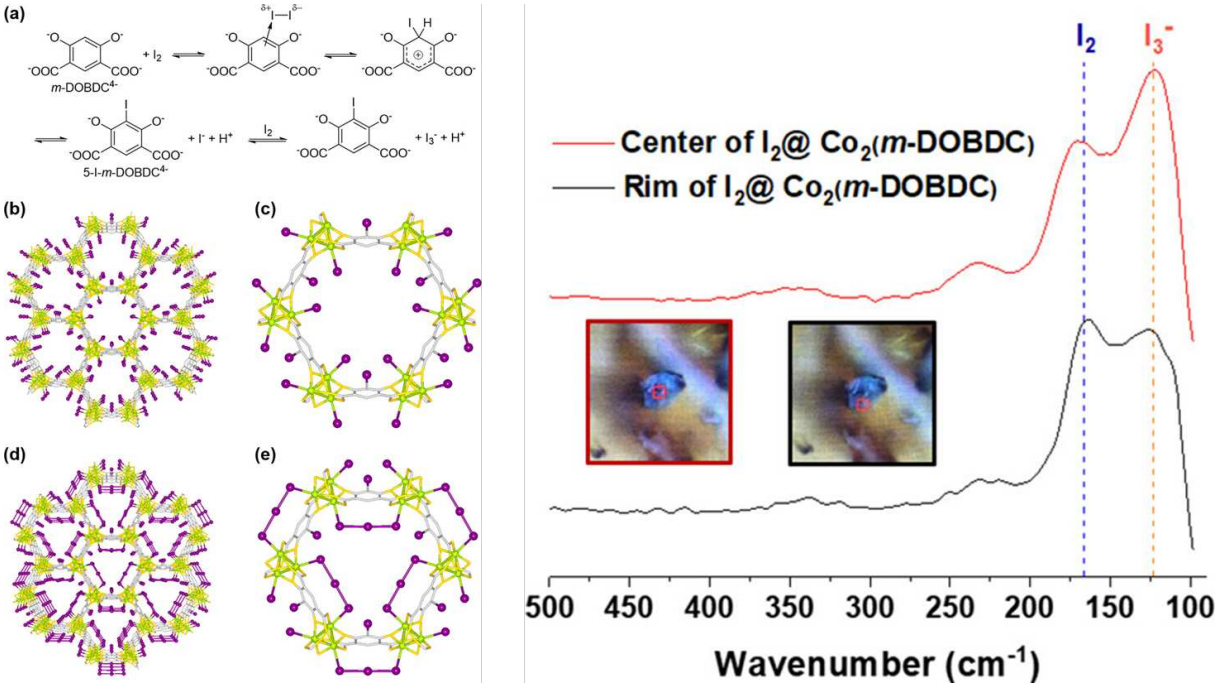

Figure 1.26: (a) Proposed mechanism for the iodine substitution and I^-/I_3^- formation in *m*-$DOBDC^{4-}$ organic linker. Crystal structures of Co_2(*m*-DOBDC) with I_2 loadings of (b, c) 10 wt.% and (d, e) 100 wt.%. On the right side: Raman spectra from the center (red) and rim (black) of the cross-section of I_2(50 wt.%)@Co_2(*m*-DOBDC) single crystals. Image modified from Lee *et al* [135]

Chapman *et al.* [169] developed a method named "pressure-induced squeezing" that seeks to increase the retention of iodine molecules by distorting the morphology of the MOF material, as highlighted in Figure 1.27. In this case, the authors used ZIF-8 to capture iodine (with an I_2 trapping capacity of 1.25 $g.g^{-1}$) and compressed the I_2-loaded material into extruded pellets under a pressure of 1.2 GPa. The process amorphized the material and was sufficient to retain the trapped iodine within its structure – as verified by thermogravimetric analysis (TGA) [169]. Similar studies were conducted for a series of ZIFs (ZIF-4, ZIF-69, and ZIF-mnIm) and confirmed a similar amorphization upon ball-milling [170]. Finally, glass sintering can also be used for the disposal of radioactive iodine. In fact, a combination of ZIF-8 and HKUST-1 with sintered glass and metallic silver flakes has been converted into a glass-composite material for iodine capture [171]. The produced composite did not show any loss of iodine uptake and presented great thermal and chemical stability, which demonstrates the potential of immobilizing radioactive iodine in MOF materials for safe transport and storage.

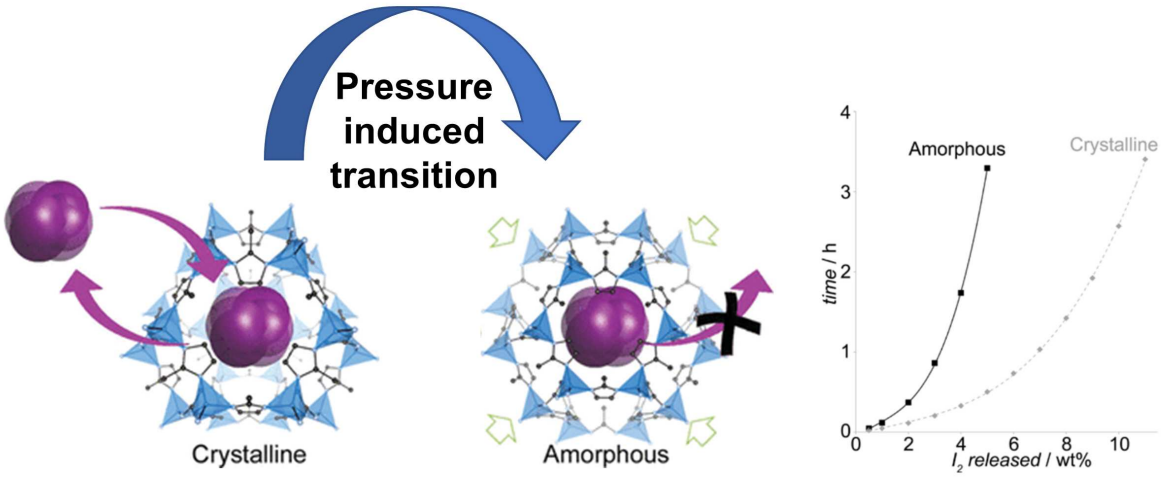

Figure 1.27: Scheme obtained from Chapman *et al.* [169] demonstrating the effect of the pressure-induced squeezing over the amount of iodine released from the ZIF-8 material.

As mentioned above, MOFs must also show stability under ionizing radiation produced by radioactive decay to be effectively used in nuclear clean-up processes. Considering that, Volkringer *et al.* [172] investigated this property using different types of MOFs submitted to different gamma radiation levels (which was chosen as it can penetrate deeper into materials than alpha and beta radiation). In this case, the MOFs studied had different metal nodes and oxidation states: ZIF-8 (Zn^{2+}), HKUST-1 (Cu^{2+}), MILs (Al^{3+}) and UiO-66 (Zr^{4+}). Their study demonstrated the extreme stability of Al-MOFs under gamma irradiation proportional to the radioactive conditions experienced for at least 8 days following a nuclear accident [172]. In another study, Leloire *et al.* [16] demonstrated the stability of spherical UiO-66_NH_2 granules loaded with ^{131}I under steam at 120 ºC during 7 days and after the exposure to 2 MGy of γ radiation obtained from a ^{60}Co source, as highlighted in Figure 1.28. The authors simulated nuclear accident conditions by placing the granules over a filtration line with 3.5 bars of absolute pressure, and with 20 % of relative humidity for 30 h. Even in such conditions, the system did not demonstrate any loss of iodine from the bench, nor the material exhibited any structural damage to the granules [16].

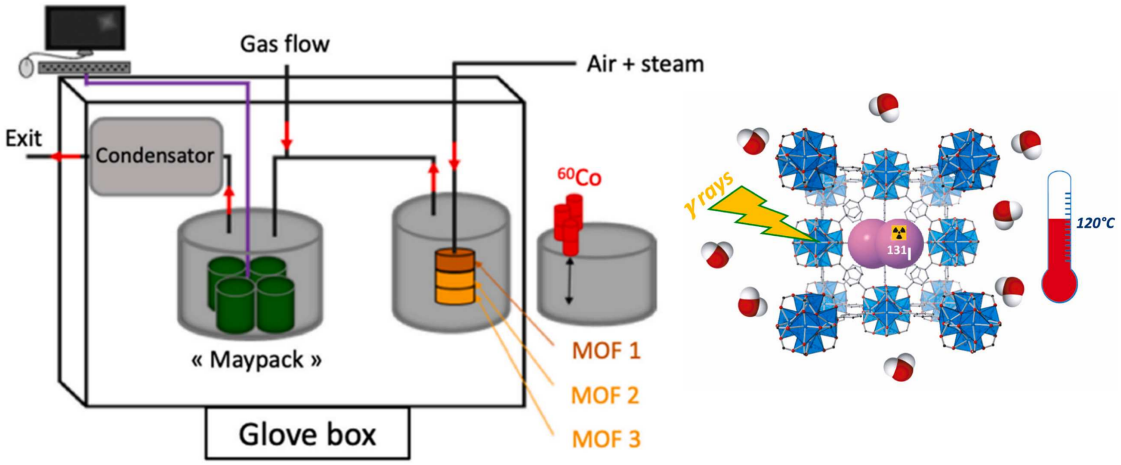

Figure 1.28: Scheme obtained from Leloire *et al*. [16] showing the ^{131}I adsorption in MOF compounds simulating the conditions of a nuclear accident (120 ºC, 2 MGy of γ radiation, 3.5 bars of absolute pressure, and 20% humidity).

1.4.2. Spectroscopy as a tool for understanding reactivity in MOF materials

Several techniques can be used for evaluating the different charge transfer process in MOF materials. This section deals specifically with the most current spectroscopy techniques used to better understand these phenomena. With that in mind, Table 1.4 displays different spectroscopy methods already applied in MOF systems to evaluate their CTC characteristics.

As mentioned before, a LBT was observed in an amino-functionalized UiO-66 MOF by Nasalevich *et al*.[27]. The authors evaluated the band gap of the synthesized materials by using the Tauc plot of the Kubelka-Munk function and considered the materials as presenting a direct allowed transition. The attribution of the LBT in UiO-66_NH_2 was conducted using DFT calculations, EPR and FTAS spectroscopies, which demonstrated that the VB and CB are both located over the organic linker (Figure 1.11) [27]. On the other hand, the MBT observed in $[Eu_2L_3(H_2O)_4]\cdot{}_3DMF$ was mainly verified by Photoluminescence (PL) measurements [126]. In this case, the authors collected spectra before and after exposure to DMF and observed a huge increase in the signal related to the Eu^{3+} cations, which was attributed to an MBT between the *d* and *f*-orbitals.

Table 1.4: Different spectroscopy techniques used for evaluating the CT types in several MOF materials.

MOF	CTC	Spectroscopy techniques applied	References
MOF-5	LMCT	DR UV-Vis; PL; Raman	[173]
MIL-125(NH_2)	LMCT	DR UV-Vis; EPR; FTAS	[27]
UiO-66(NH_2)	LBT	DR UV-Vis; EPR; FTAS	[27]
$[Eu_2L_3(H_2O)_4]\cdot_3DMF$	MBT	PL	[126]
$[ZnL_1]\cdot2DMF\cdot4H_2O$	MLCT	SSE; TRE; UV-vis; TCSPC	[123]
$[ZnL_2H_2]\cdot3H_2O$	MLCT	SSE; TRE; UV-vis; TCSPC	[123]
Zn-PTC	MLCT	UV-Vis; FL	[127]
Mn(TTFDC)(4,4′-bpy)-$(H_2O)]_n\cdot_nCH_3CN$	LLCT	DR UV-Vis; EPR	[124]
[Mn(TTFDC) $(bpe)_{0.5}(DMF)]_n\cdot2_nH_2O$	LLCT	DR UV-Vis; EPR	[124]
[Mn(TTFDC) $(bpa)(H_2O)]_n\cdot2_nH_2O$	LLCT	DR UV-Vis; EPR	[124]
Nd-Yb-Eu-TCPB	MMCT	PL	[128]
I_2@MFM-300(V^{III})	HGCT	XPS; Raman; EPR	[130]
Pd@HKUST-1	GHCT	HAXPES; NEXAFS	[137]

DRS = Diffuse Reflectance; EPR = Electron Paramagnetic Resonance; PL = Photoluminescence; DFT = Density Functional Theory; FTAS = Femtosecond Transient Absorption Spectroscopy; SSE = Steady-State Emission; TRE = Time Resolved Emission; TCSPC = Time-Correlated Single Photon Counting; FL = Fluorescence; HAXPES = Hard X-rays Photo-Electron Spectroscopy; NEXAFS = Near-Edge X-ray Absorption Fine Structure; XPS = X-ray Photoelectron Spectroscopy; L_1 = $\{Ru[4,4'\text{-}(CO_2)_2\text{-}bpy)]_2(bpy)\}^2$; L_2 = $\{Ru[4,4'\text{-}(CO_2)_2\text{-}bpy)]_2(CN)_2\}^{4-}$; L_3 = 2',5'-bis(methoxy-methyl)-[1,1':4',1''-terphenyl]-4,4''-dicarboxylate; PTC = 3,4,9,10-perylenetetracarboxylate; TTFDC = tetrathiafulvalene-dicarboxylate; bpy = 4,4′-bipyridine; bpe = 1,2-bis(4-pyridyl)ethene; bpa = 1,2-bis(4-pyridyl)ethane; TCPB = 1,2,4,5-tetrakis(4-carboxyphenyl)benzene

Moreover, Bordiga *et al*. [173] observed that the Zn_4O_{13} cluster in MOF-5 behaves as a quantum dot (QD), whereas the organic part acts as a photon antenna able to transfer the energy to the inorganic ZnO-like QD part. This effect, generated by a LMCT between the BDC linker and the Zn-based inorganic cluster, was observed using diffuse reflectance (DR) UV-Vis and PL spectroscopies combined with Raman spectroscopy. By acquiring DR UV-vis spectra of a ZnO powder (which was compared to the inorganic part of the MOF) and of a terephthalic acid disodium salt (TADS) (which was compared to the organic linker of the MOF), the authors were able to relate their absorption bands to the signal obtained for the MOF-5 (Figure 1.29). Indeed, they demonstrated that the VB and CB of ZnO are related to O(2*p*) and Zn(4*s*) orbitals, respectively, and that the corresponding transition was responsible for the DR UV-vis signal with an edge in the near UV region at 380 nm [173]. In addition, the signals recorded for the TADS were ascribed to a $\pi \rightarrow \pi^*$ transition of its aromatic ring and started at 322 nm, extending over the UV region. [173]. However, this $\pi \rightarrow \pi^*$ transition was found to exhibit a redshift in

MOF-5 spectrum, which was ascribed to the interaction with two carboxylate groups [173]. Furthermore, the authors showed that the MOF-5 spectrum does not correspond to a simple superimposition of the ZnO and TADS signals. Instead, a maximum band centered at 290 nm (related to the organic part) with an edge at 350 nm (due to the inorganic part) was observed. The edge at 350 nm was assigned to a LMCT ($O^{2-}Zn^{2+} \rightarrow O^{-}Zn^{+}$), similarly to that observed for ZnO but blue shifted due to confinement effects [173]. This attribution was confirmed by the PL measurements, as shown in Figure 1.29b. Here, the excitation and emission scans of the three components (MOF-5, ZnO, and TADS) were also compared. Bordiga *et al*. [173] showed that the MOF-5 excitation spectrum is observed at the same position as that of TADS, whereas the emission spectrum is at the same position as that of ZnO, but with much higher intensity. This feature reveals that the energy transfer occurs from the organic part of the MOF towards the Zn_4O_{13} and confirms the presence of a LMCT.

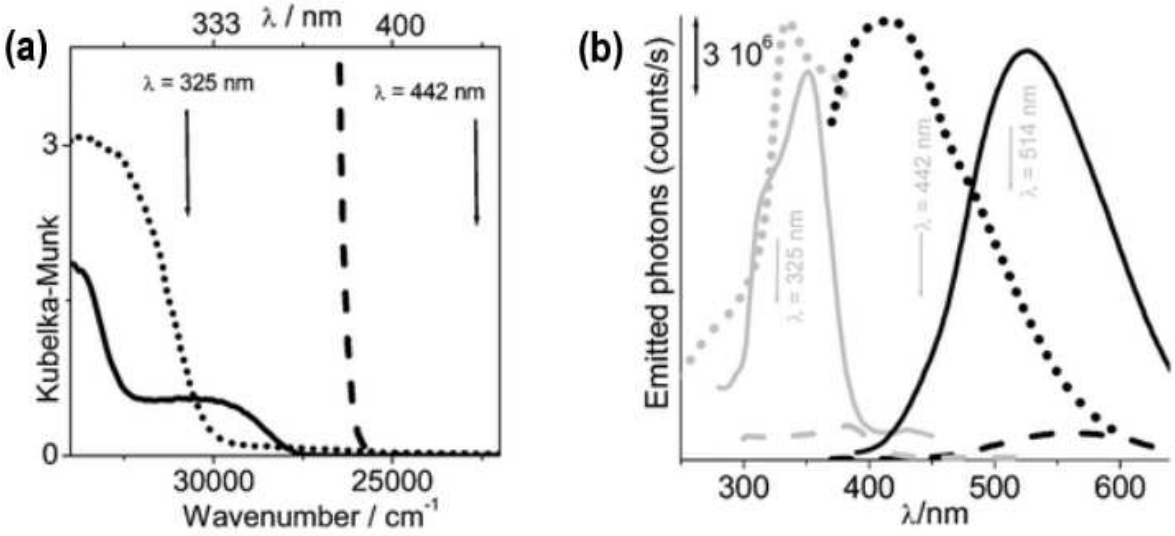

Figure 1.29: Optical properties of MOF-5 obtained from Bordiga *et al*.[173] (a) UV–Vis spectra of ZnO (dashed), TADS (dotted) and MOF-5 (solid). Arrows indicate Raman lasers. (b) PL spectra. Grey curves (excitation scans), black curves (emission scans). MOF-5 (solid, λ_{emis} = 518 nm and λ_{ex} = 350 nm); TADS (dotted, λ_{emis} = 418 nm and λ_{ex} = 335 nm); ZnO (dashed, λ_{emis} = 560 nm and λ_{ex} = 380 nm).

Furthermore, in the $[ZnL_1]\cdot 2DMF\cdot 4H_2O$ (L_1 = $\{Ru[4,4'\text{-}(CO_2)_2\text{-bpy})]_2(bpy)\}^{2}$) and $[ZnL_2H_2]\cdot 3H_2O$ (L_2 = $\{Ru[4,4'\text{-}(CO_2)_2\text{-bpy})]_2(CN)_2\}^{4-}$) an absorption band was observed using UV-Vis spectroscopy at 550–750 nm, which is characteristic of a MLCT signal related to spin–orbit coupling [123]. This attribution was confirmed by adding quenchers to the system and by fitting the emission decays of the signals. Also, a modified Stern–Volmer lifetime analysis was performed on the MOFs to determine the relative rates of energy transfer. Similarly, the MLCT

in a Zn-PTC (PTC = 3,4,9,10-perylenetetracarboxylate) based MOF was demonstrated by Song *et al.* [127] by coupling UV-Vis and Fluorescence (FL) spectroscopies, as shown in Figure 1.30. Indeed, the authors observed two new absorption bands at 356 and 504 nm in the UV-Vis spectrum of Zn-PTC compared to that of the K_4PTC linker. In addition, the FL emission bands of Zn-PTC (at 428, 462, 645, and 693 nm) were the same as those obtained for the K_4PTC linker, demonstrating that the excited state is composed of PTC orbitals. Thus, when combining the two techniques, the authors were able to attribute a MLCT to the Zn-PTC MOF [127].

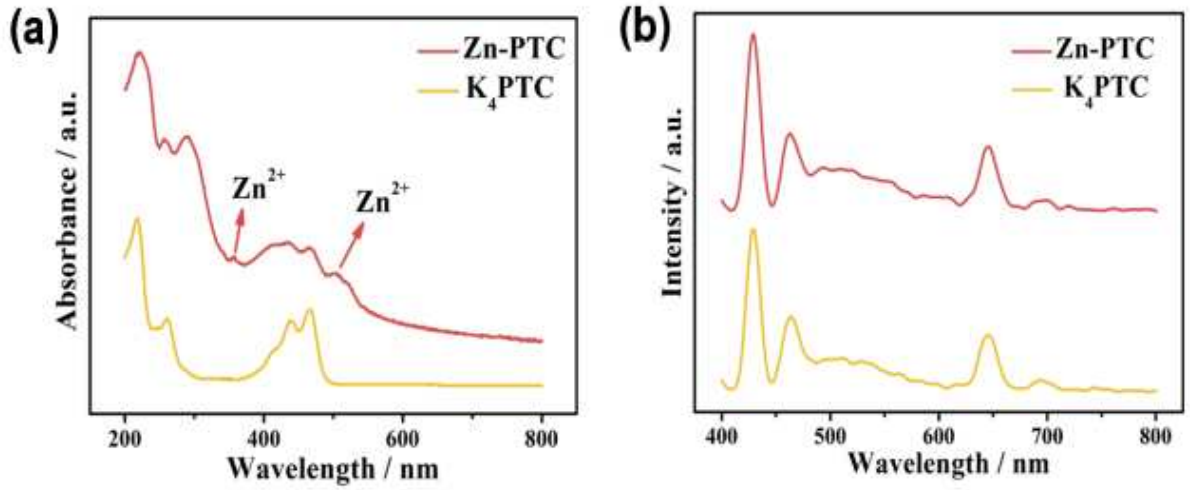

Figure 1.30: (a) UV−vis and (b) FL spectra of Zn-PTC and K_4PTC obtained from Song *et al.* [127].

In the case of the MMCT observed in Nd-Yb-Eu-TCPB, the authors defined the CTC by using PL spectroscopy [128]. They acquired spectra for the single-metal Nd-TCPB and Eu-TCPB, as well as for the bimetallic and trimetallic compounds (Figure 1.31). When evaluating the effect of adding other metals in the MOF structure, they detected new signals which were not present in the monometallic materials. Such behavior was then assigned to a CTC between the different metals in the Nd-Yb-Eu-TCPB structure. In the other hand, the LLCT mechanism in Mn-TTFDC-(bipyridine) compounds was elucidated through DR UV-Vis and EPR spectroscopies coupled with DFT calculations [124]. Actually, Huo *et al.* [124] attributed the UV-Vis absorption bands between 498 and 582 nm to the (TTF)-to-linker (bipyridine) charge transfer (LLCT). The EPR spectra of the MOFs also revealed a signal related to the presence of $TTF^{\bullet+}$ paramagnetic species, which is in accord with the LLCT phenomenon.

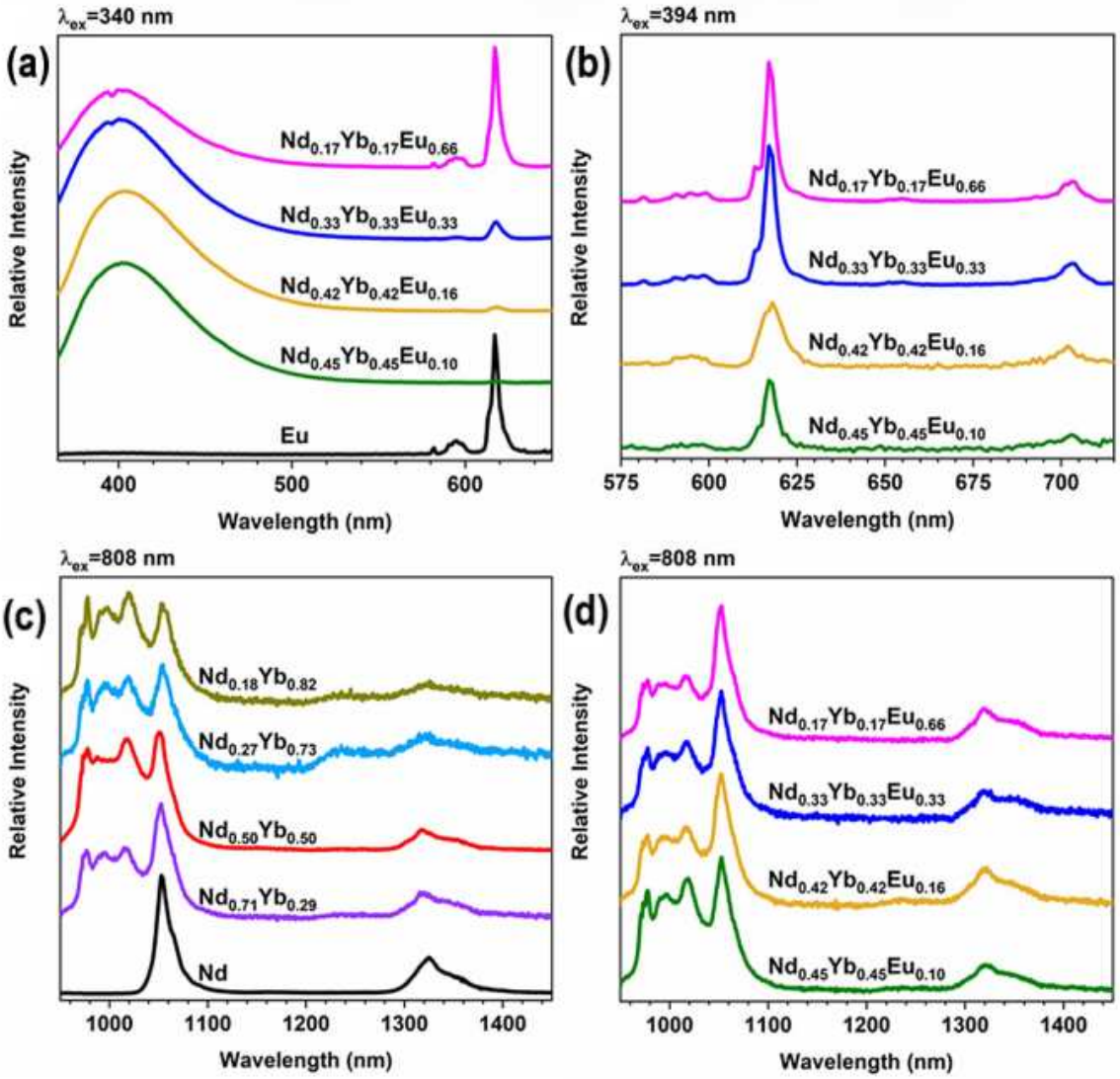

Figure 1.31: Photoluminescence spectra for single-metal Nd-TCPB and Eu-TCPB compounds (black), the bimetallic compounds Nd-Yb-TCPB (red, purple, light blue, and brown), and the trimetallic Nd-Yb-Eu-TCPB compounds (blue, green, yellow, and pink). Obtained from Deneff *et al.* [128].

Spectroscopy characterizations can also be applied to host and guest interactions. For instance, the HGCT in I_2@BOF-1 system was observed using UV-Vis and EPR spectroscopies. In particular, EPR spectroscopy confirmed the partial oxidation of Ni^{2+} into Ni^{3+}, while UV-Vis and single crystal XRD confirmed the presence of I_3^- anions in the channels of the MOF [129]. Finally, the GHCT in Pd@HKUST-1 was observed using Hard X-rays Photo- Electron Spectroscopy (HAXPES) and Near-Edge X-ray Absorption Fine Structure (NEXAFS) coupled to DFT calculations. Indeed, the HAXPES valence band spectrum of the Pd nanoparticles showed a very similar signal to that of the Pd@HKUST-1. On the other hand, the NEXAFS spectra of HKUST-1 and Pd@HKUST-1 revealed the role of the oxygen and copper in the CTC

between the Pd nanoparticle and the MOF structure. Actually, the coexistence of Cu^{+} and Cu^{2+} sites in Pd@HKUST-1 was shown by the presence of a peak at 931.9 eV, which was confirmed by another signal related to the Cu^{+}–O species at 532.9 eV (Figure 1.32). Those features established the presence of a GHCT in the Pd@HKUST-1 system.

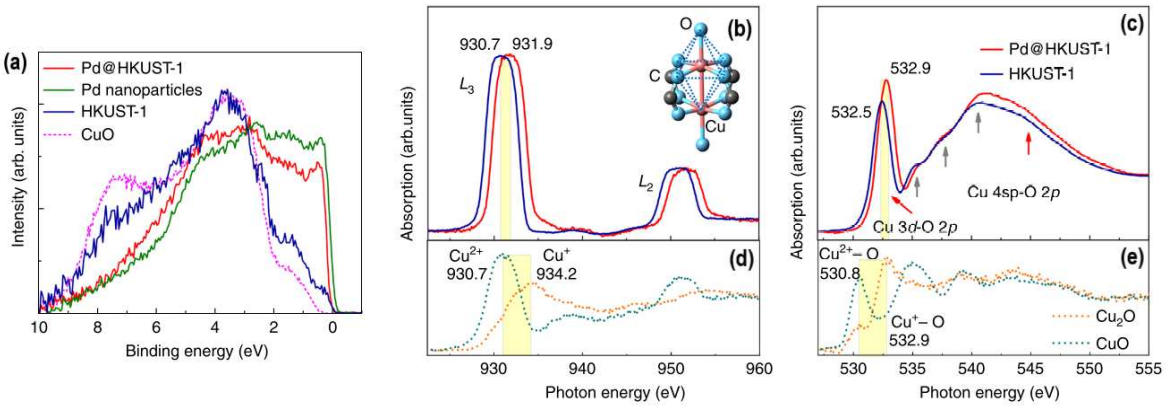

Figure 1.32: (a) Normalized HAXPES valence-band (VB) spectra of Pd nanocubes (green solid line), HKUST-1 (blue solid line) and Pd@HKUST-1 (red solid line) referring to CuO (violet dashed line) at an incident energy of 5.95 keV, which show the Pd 4*d* states in Pd nanocubes and Cu 3*d* states in HKUST-1. (b) Cu conduction band observed by NEXAFS showing Cu L edge. (c) O K edge NEXAFS spectra of HKUST-1 and Pd@HKUST-1. (d) Cu L edge of the CuO and Cu_2O powder and (e) O K edge of the CuO and Cu_2O powder. The inset of (b) shows the atomic structure related to Cu, O and C atoms of HKUST-1. Figure modified from Chen *et al.* [137].

Chapter II: Materials and Methods

2.1. Syntheses of the MOF compounds

All the compounds used in this work were synthesized and activated before being characterized and employed for capturing iodine. These procedures are thoroughly described below.

2.1.1. Syntheses of the UiO-66 compounds

UiO-66(Zr): UiO-66(Zr) was prepared by solvothermal treatment as follows: zirconium chloride ($ZrCl_4$, Sigma Aldrich 99.9%, 2.0 g, 8.58 mmol), terephthalic acid ($(COOH)_2C_6H_4$, Sigma Aldrich, 98%, 2.8 g, 16.85 mmol), formic acid (HCOOH, 32.5 mL) and *N,N*-dimethylformamide (DMF, 163 mL) were initially added in a 250 mL glass bottle, which was then placed in an oven. After raising temperature for 1 h, the system was kept at 120 ºC for 24 h. A white solid was recovered by centrifugation after natural cooling of the bottle. Then, it was washed three times with fresh DMF and three times with fresh ethanol. Finally, it was calcined in air at 100 ºC for 1 h and then 150 ºC for 18 h for the activation step. After the last stage, 2.5 g of UiO-66(Zr) were collected and kept in a flask under Ar atmosphere in a glovebox (JACOMEX, GP Campus series).

UiO-66(Hf): UiO-66(Hf) was solvothermally prepared as well. Hafnium chloride ($HfCl_4$, Sigma Aldrich 99.9%, 2.75 g, 8.58 mmol), terephthalic acid ($(COOH)_2C_6H_4$, Sigma Aldrich, 98%, 2.8 g, 16.85 mmol), formic acid (HCOOH, 32.5 mL) and dimethylformamide (DMF, 163 mL) were initially added in a 250 mL glass bottle and the following procedure is identical to that described above for UiO-66(Zr). After the last stage, 2.5 g of UiO-66(Hf) were collected and kept in a flask under Ar atmosphere.

UiO-66(Hf,Zr): The other three samples of UiO-66(Hf/Zr) series followed the same synthesis procedure while respecting the desired Hf/Zr molar ratio. Shortly, the $HfCl_4$ and $ZrCl_4$ salts were pre-mixed in molar proportions of 1:3, 1:1, and 3:1, based on a total 8.58 mmol for $HfCl_4$ + $ZrCl_4$. The molar ratio between the total amount of metal precursors and the other reactants was maintained in all syntheses. The other stages followed as previously described. The mass of solid collected after drying was about 2.5 g for each Hf/Zr composition and it was kept in glass flasks under Ar atmosphere. It is worth mentioning that the percentages of Hf and Zr presented in this work are always only related to the metal atoms (i.e., the UiO-66(25% Hf)

presents 19% Hf and 81% Zr over a total of 100% metal atoms). Also, the UiO-66 structure is exhibited in Figure 2.1, as well as their main cavities.

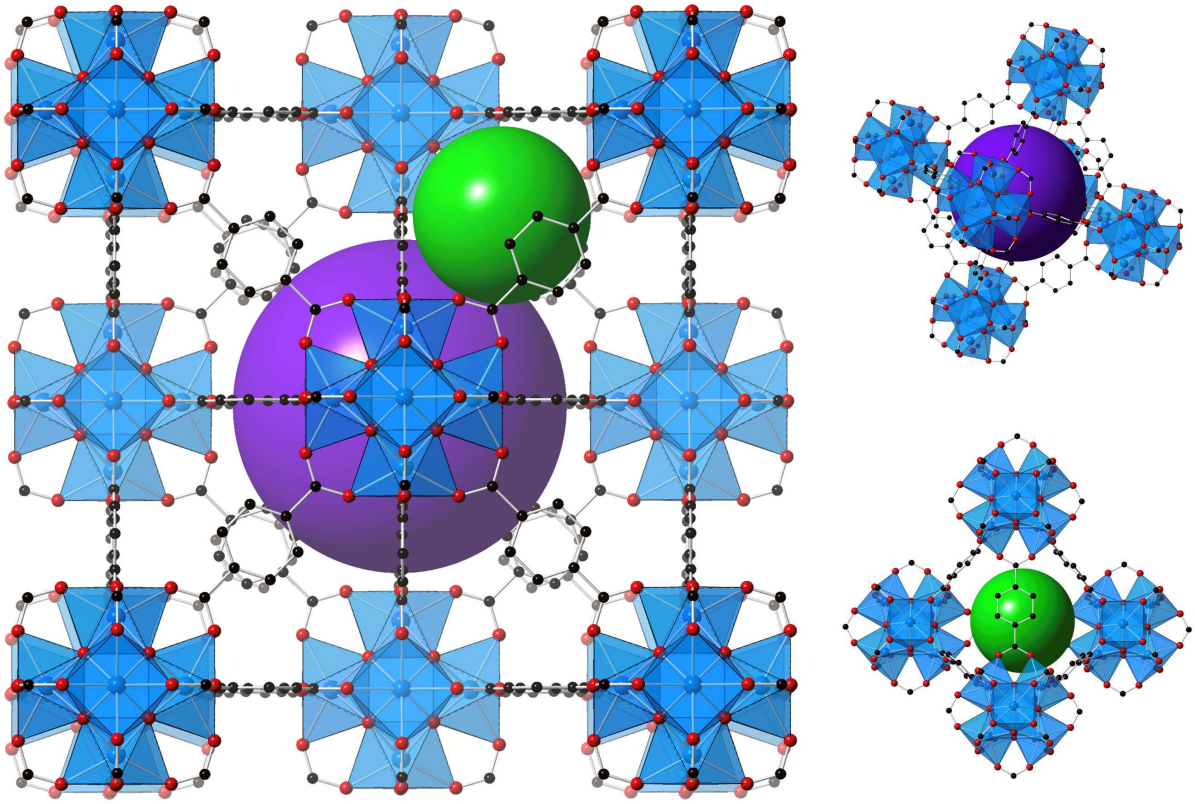

Figure 2.1: Structure of UiO-66 showing the inorganic clusters (blue), the octahedral cages (one of them is highlighted in purple) and the tetrahedral cages (one of them is highlighted in green). Carbon and oxygen atoms are shown in black and red, respectively. The hydrogens are not exhibited for better clarity.

2.1.2. Syntheses of the UiO-67_NH_2 compounds

Organic linker: $(COOH)_2(NH_2)C_{12}H_8$ was synthesized as schematized in Figure 2.2. First, [1,1'-biphenyl]-4,4'-dimethyl-dicarboxylate (5 g, 18.5 mmol, 1 eq) was completely dissolved in nitric acid (35%, 1.28 mL, 18.5 mmol, 1 eq) and then, sulfuric acid (95%, 0.78 mL) was added over 45 minutes, at 0°C, under magnetic stirring. The reaction was kept stirring at room temperature for 5 more minutes. The resulting mixture was poured into 100 mL of ice-cold water, followed by the formation of a white precipitate of pasty texture, which was then dissolved in ethyl acetate. The organic phase was washed 3 times with water (30 mL), twice with saturated sodium bicarbonate solution ($NaHCO_3$, 30 mL) and twice with saturated sodium chloride solution (NaCl, 30 mL). It was then dried over magnesium sulfate ($MgSO_4$). At this

point, the organic phase was evaporated on a rotary evaporator. The solution was recovered, treated with 25 mL of acetonitrile, and filtered to remove unreacted reagent. The product (2-nitro-[1,1'-biphenyl]-4,4'-dimethyl-dicarboxylate), labeled as "molecule 1" (Figure 2.2) was purified by a routine flash purification using a puriFlash XS520Plus apparatus (15 mL.min^{-1} flow rate) with petroleum ether/ethyl acetate (90/10) as eluent. At the end of this process, 2.92 g of 2-nitro-[1,1'-biphenyl]-4,4'-dimethyl-dicarboxylate was obtained.

Afterwards, the "molecule 1" (2.92 g, 9.24 mmol, 1 eq) was dissolved in methanol (80 mL, 1.97 mol) and heated under reflux (70°C). After that, dihydrate tin(II) chloride (10.42 g, 46.2 mmol, 5 eq) was slowly added under magnetic stirring. When the addition was complete, the solution was heated under reflux for 6 h. It was cooled to room temperature and then placed in the refrigerator overnight to promote the recrystallization of the "molecule 2" (2-amino-[1,1'-biphenyl]-4,4'-dimethyl-dicarboxylate) (Figure 2.2). Finally, the solid was filtered off and washed with 50 mL of methanol. At this point, 2.0 g of 2-amino-[1,1'-biphenyl]-4,4'-dimethyl-dicarboxylate was recovered.

Finally, the "molecule 2" (2 g, 7 mmol, 1 eq) was taken up in methanol (25 mL) using a 2M potassium hydroxide solution (25 mL, 910 mmol). This solution was heated under reflux (70°C) for 24 h with magnetic stirring. Then, 25 mL of water was added to the system and then, 6M hydrochloric acid was added dropwise until a precipitate was formed. The solid was recovered by filtration and washed with 300 mL of water. The final product (2-amino-[1,1'-biphenyl]-4,4'-dicarboxylic acid) was labeled as "molecule 3" and was then placed in an oven (70°C for 4 hours). At the end of this process, 1.65 g of product was attained. The chemical formula, mass of product obtained, reaction yield, and NMR spectra data are summarized in the Annex file (Table A1).

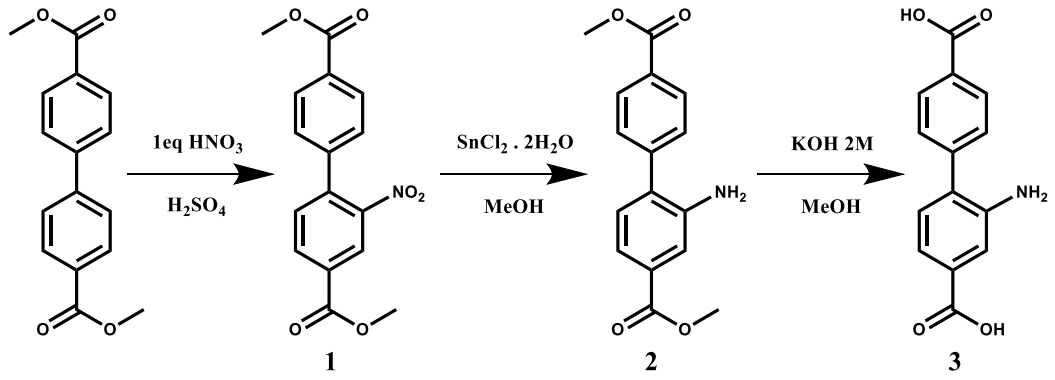

Figure 2.2: Schematic for the synthesis of 2-amino-[1,1'-biphenyl]-4,4'-dicarboxylic acid (NH_2-H_2BPDC).

UiO-67(Zr)_NH_2: UiO-67(Zr)_NH_2 was typically prepared by a solvothermal treatment. In a 20 mL glass flask, zirconium chloride ($ZrCl_4$, Sigma Aldrich 99.9%, 100 mg, 0.429 mmol) was first dissolved in dimethylformamide (DMF, Sigma Aldrich, anhydrous 99.8%, 10 mL) under magnetic stirring for approximately 5 minutes. Then, NH_2-H_2BPDC linker ($(COOH)_2C_{12}H_7NH_2$, 220 mg, 0.855 mmol) was added to the solution, which was kept stirring for another 10 minutes. Finally, benzoic acid (C_6H_5COOH, Sigma Aldrich, ≥ 99.5%, 1.5 g, 0.12 mol) was added and the solution was maintained under stirring until complete dissolution of the precursors. The flask was placed inside an oven at 130 ºC for 48 h. After natural cooling, the crystals attached to the glass were gently pushed to the solution with the aid of a spatula. They were washed three times with fresh DMF (15 mL) and three times with fresh chloroform ($CHCl_3$, 15 mL Sigma Aldrich, ≥ 99.8%). The powder was activated under primary vacuum at 100 ºC for 1 h and finally, the solid was collected and kept in a flask under argon atmosphere.

UiO-67(Hf)_NH_2: UiO-67(Hf)_NH_2 was solvothermally prepared as well. Hafnium chloride ($HfCl_4$, Sigma Aldrich 99.9%, 196 mg, 0.429 mmol), NH_2-H_2BPDC ($(COOH)_2C_{12}H_7$-NH_2, 220 mg, 0.855 mmol), benzoic acid (C_6H_5COOH, Sigma Aldrich, ≥ 99.5%, 1.5 g, 0.12 mol) and dimethylformamide (DMF, Sigma Aldrich, anhydrous 99.8%, 10 mL) were initially added in a 20 mL glass flask following a procedure that is identical to that described above for UiO-67(Zr)_NH_2. The collected solid was kept in a flask under argon atmosphere.

UiO-67(Zr/Hf)_NH_2: UiO-67(Zr/Hf)_NH_2 followed the same synthesis procedure while respecting the desired Zr/Hf molar ratio. Shortly, the $HfCl_4$ and $ZrCl_4$ salts were pre-mixed in molar proportions of 1:1, based on a total 0.429 mmol for $HfCl_4$ + $ZrCl_4$. The molar ratio between the total amount of metal precursors and the other reactants was maintained constant.

2.1.3. Syntheses of the MIL-125(Ti), MIL-125(Ti)_NH_2 and CAU-1(Al)_NH_2 compounds

MIL-125(Ti): MIL-125(Ti) was synthesized from a solution containing dimethylformamide (DMF, Sigma Aldrich, anhydrous 99.8%, 4.5 mL) and methanol (MeOH, Sigma Aldrich, anhydrous 99.8%, 0.5 mL) was prepared under Ar atmosphere inside a glovebox (JACOMEX, GP Campus series). Then, titanium tetraisopropoxide (TTIP, Sigma Aldrich, 97%, 300 µL) and butyric acid (C_3H_7COOH, Sigma Aldrich, ≥ 99%, 459 µL) were

added into the previous solution and kept under magnetic stirring during five minutes. At that moment, terephthalic acid ($(COOH)_2C_6H_4$, Sigma Aldrich, 98%, 250 mg) was added and kept stirring for ten minutes. The mixture was placed in a 25 mL stainless steel autoclave under autogenous pressure at 120 ºC for 24 h. A white powder was recovered by centrifugation, washed three times with fresh anhydrous DMF and three times with fresh anhydrous MeOH. Finally, it was calcinated in air at 200 ºC for 12 h. After this stage, the solid was collected and kept in a closed flask under Ar atmosphere. The structure of the MIL-125 compound is represented in Figure 2.3.

MIL-125(Ti)_NH_2: MIL-125(Ti)_NH_2 was prepared by solvothermal treatment as follows. A solution containing dimethylformamide (DMF, Sigma Aldrich, anhydrous 99.8%, 4.5 mL) and methanol (MeOH, Sigma Aldrich, anhydrous 99.8%, 0.5 mL) was prepared under Ar atmosphere inside a glovebox. Then, titanium tetraisopropoxide (TTIP, Sigma Aldrich, 97%, 300 µL) was added dropwise and kept under magnetic stirring for five minutes. At that moment, 2-aminoterephthalic acid ($(COOH)_2C_6H_4NH_2$, Sigma Aldrich, 99%, 418 mg) was added and kept stirring for ten minutes. At the end, methanol (MeOH, Sigma Aldrich, anhydrous 99.8%, 4.0 mL) was once more added into the mixture. It was then placed inside a 25 mL stainless steel autoclave under autogenous pressure at 150 ºC for 16 h. A yellow powder was recovered by centrifugation, washed three times with fresh anhydrous DMF and three times with fresh anhydrous MeOH. Finally, it was calcinated in air at 100 ºC for 12 h. After this stage, the solid was collected and kept in a closed flask under Ar atmosphere.

CAU-1(Al)_NH_2: CAU-1(Al)_NH_2 was synthesized by solvothermal treatment. First, 2-aminoterephthalic acid ($(COOH)_2C_6H_4NH_2$, Sigma Aldrich, 99%, 1.12 g, 6.2 mmol) and aluminum chloride hexahydrate ($AlCl_3 \cdot 6H_2O$, Sigma Aldrich, 99%, 4.45 g, 18.4 mmol) were suspended in methanol (MeOH, Sigma Aldrich, anhydrous 99.8%, 59 mL). The resulting dispersion was heated at 125 ºC for 5h. The yellow solid was recovered by centrifugation and washed three times with deionized water for three days. The powder was isolated and dried at room temperature in air. After this stage, the solid was collected and kept in a closed flask under Ar atmosphere.

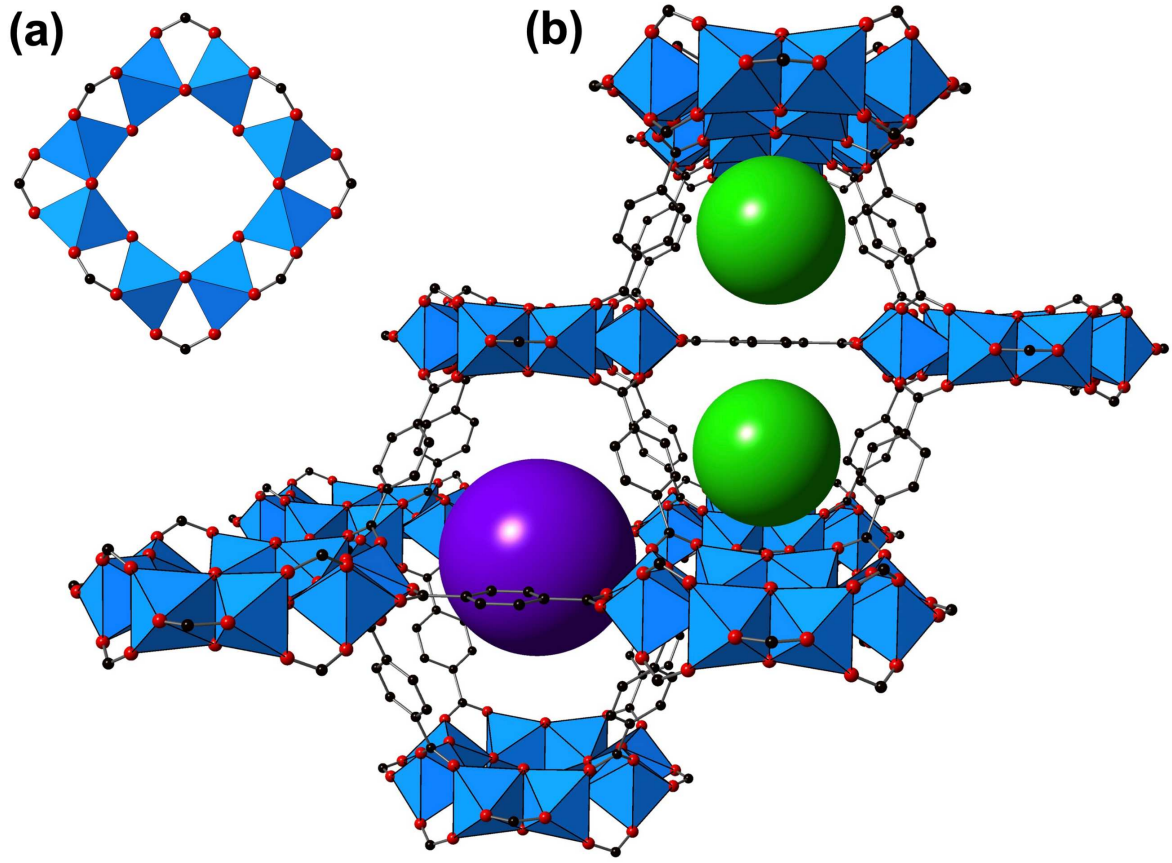

Figure 2.3: Structure of MIL-125(Ti) showing (a) the 8-membered ring of Ti-oxo/hydroxy cluster and (b) the distorted tetrahedral (green) and octahedral cages (purple). Titanium cations are presented as blue polyhedra, oxygen and carbon atoms are represented in red and black, respectively, and hydrogens were concealed for better aesthetics. Both MIL-125(Ti)_NH_2 and CAU-1(Al)_NH_2 have the same isoreticular arrangement than MIL-125(Ti) and therefore, they all exhibit identical crystal structures. Their composition only differs from MIL-125(Ti) due to the presence of $–NH_2$ groups on the position-2 of the terephthalate organic linker. In addition, the hydroxyl groups on the MIL-125(Ti) and MIL-125(Ti)_NH_2 inorganic cluster are replaced by methoxy ($–OCH_3$) groups in CAU-1(Al)_NH_2 to balance the Al^{3+} charge.

2.2. Characterization techniques

The characterization techniques used to evaluate the different properties of the materials are described in depth below. They are: XRD, Inductively Coupled Plasma - Optical Emission Spectrometry (ICP-OES), N_2 sorption tests, SEM, Energy-dispersive X-ray Spectroscopy (EDS), FTIR, Raman spectroscopy, Diffuse Reflectance UV-vis Spectroscopy, EPR, NMR, band gap evaluation, chemometrics, and TGA.

2.2.1. X-Ray Diffraction

XRD is a common technique used to identify the different phases and properties of crystalline materials. Briefly, when a crystal with an interplanar spacing *d* is irradiated by X-ray beam with a comparable wavelength λ, the constructive interference between elastically scattered X-ray beams can be observed at specific 2θ angles when the Bragg's Law is satisfied (Figure A1). In this work, three different XRD techniques were applied depending on the sample: Single Crystal X-Ray Diffraction (SC-XRD), and Powder X-Ray Diffraction (PXRD) using capillaries, and High Temperature Powder X-Ray Diffraction (HT-PXRD). These diffractometers can operate in different geometries depending on their principles. For instance, the PXRD using capillaries are constructed following the Debye-Scherrer geometry (transmission), while the HT-PXRD usually uses the Bragg-Brentano geometry (Figure A2). In the former case, the X-ray beam is focused using a primary monochromator before passing through the sample (which is usually placed in a capillary) and it is then collected by the detector that moves in a 2θ angle (Figure A2). On the latter, the primary X-ray beam is irradiated on the sample which is placed in a flat surface. The beam is then diffracted and collected by the detector. This geometry can exhibit both the X-ray tube and the detector moving in a theta-theta (θ-θ) angle, or only the detector moves in a 2θ angle (Figure A2).

PXRD – capillaries: PXRD experiments using capillaries were conducted in parallel transmission (Debye-Scherrer) geometry for the UiO-66(Zr,Hf) samples. The powdered samples were placed inside WJM-Glass Müller GmbH borosilicate capillaries (Φ = 0.7 mm), which were then sealed with Sader Invisible epoxy resin. The analyses were conducted in a SmartLab Rigaku diffractometer equipped with a 9 kW rotating anode X-ray generator (Cu $K\alpha_1$ = 1.5418 Å), endowed with a HyPix-3000 hybrid multi-dimensional pixel detector (Figure A3). The 2θ scans were performed in the range 5-70°, with a step size of 0.01° and a speed of 3°/min.

SC-XRD: SC-XRD experiments were done for the three UiO-67(Zr,Hf)_NH_2 samples using a Bruker DUO-APEX2 diffractometer equipped with a two-dimensional CCD 4K detector and 2 m-sources generating Mo-Kα (λ = 0.71073 Å) and Cu-Kα (λ = 1.54178 Å) radiations (Figure A4). The diffractograms were collected at room temperature under air atmosphere. The structure refinement was conducted using the JANA software.

HT-PXRD: HT-PXRD analysis was conducted for the MIL-125(Ti), MIL-125(Ti)_NH2 and CAU-1(Al)_NH2. The patterns were recorded in reflection mode using an

HTK1200 Bruker diffractometer with a Bragg-Brentano theta-theta (θ-θ) geometry (Figure A5). The instrument is dedicated to the study of polycrystalline samples at high temperature (up to 1200 °C), under different atmospheric conditions (in this case, the measurements were conducted under air flow), using a HT chamber of the Anton Paar HTK1200N type. The apparatus includes a copper anticathode (λCuKα = 1.5406 Å) and is equipped with a fast LynxEye detector. During the data acquisition, the compounds were heated in an alumina support at 5º/min up to 800 ºC using temperature plateaus each 20 ºC. Diffractograms were collected in the 6-80° 2θ-range with a step size of 0.02° and a speed of 2.4°/min.

2.2.2. Inductively Coupled Plasma – Optical Emission Spectroscopy

ICP-OES is an analytical technique used for the detection of chemical elements. It is a type of emission spectroscopy that generates excited atoms and ions that emit electromagnetic radiation at wavelengths specific to a particular element using an inductively coupled plasma (Figure A6). The ionized gas source is produced at high temperatures in the plasma and a peristaltic pump delivers an aqueous or organic sample into an analytical nebulizer. The sample is changed into mist and introduced directly inside the plasma flame where it is broken down into charged ions after colliding with the plasma. The respective atoms lose electrons and recombine repeatedly in the plasma, emitting radiation at the characteristic wavelengths of the elements involved. Finally, the intensity of the emissions from various wavelengths are proportional to the concentrations of the elements within the sample.

The ICP-OES experiments were conducted using an Agilent 5110 ICP-OES spectrometer in radial sighting mode (Figure A7). The mineralization of the samples was performed using 100 mg for the activated UiO-66(Zr,Hf) and 10 mg for the activated UiO-67(Zr,Hf)_NH_2 compounds. First, the samples were digested using a solution containing 10 mL of HF and 5 mL of HNO_3 and then they were heated to 140 ºC for 48 h, followed by a dry evaporation step. Next, they were etched with aqua regia (HNO_3:HCl 3:6 mL), heated to 120 ºC for 24 h and dried to a residue of 0.5 mL Finally, 9.5 mL of water was added, and the solution was diluted at 1/100 after filtration before being analysed using the 264.141 and 343.823 nm emission lines of hafnium and zirconium, respectively.

2.2.3. N_2 sorption tests

N_2 sorption tests are often conducted in microporous materials to estimate different textural properties such as SSAs and pore size distribution. The most popular model applied to evaluate the SSA of different materials is the BET (Brunauer, Emmett, and Teller) theory [174]. The BET is considered as an extension of the Langmuir theory [175], which only considers a monolayer molecular adsorption. Therefore, the BET model follows some hypotheses such as:

- gas molecules are adsorbed on a solid in infinite layers,
- those molecules only interact with adjacent layers,
- the Langmuir theory can be applied to each layer,
- the enthalpy of adsorption for the first layer is constant and higher than the second,
- the enthalpy of the second layer is the same as the enthalpy of liquefaction.

In addition, it is not required for a layer to be complete before an upper layer formation starts. The BET equation considers the equilibrium and saturation pressure of adsorbates at the temperature of adsorption, the quantity of adsorbed gas, and the monolayer volume.

In a practical sense, the sample is first degassed inside a glass tube to remove any adsorbate molecules. Then, after the tube is filled with an inert gas (often N_2) the mass of the dried material is acquired (by subtraction between the mass of the empty tube and the final mass), and the tube is putted into the analysis chamber. The apparatus increases the gas pressure inside the tube until there is no considerable variation in the partial pressure p/p_0. Then, a point is collected and plotted in a graph where the *y*-axis is the "quantity of adsorbed gas" and the *x*-axis is the p/p_0. This process is repeated up to $p/p_0 = 1$ before the sample is degassed by gradually reducing the gas pressure. At the end, a characteristic isotherm is obtained and compared with different models provided by the IUPAC (Figure A8) [176]. The format of the isotherm, especially considering the possible hysteresis formed between the adsorption and desorption regimes (which are related to pore blocking and delayed condensation caused by capillarity), contain information about the adsorbent (microporous, mesoporous, weak substrate) and the adsorbate (monolayer, multilayer). Finally, by applying the BET equation to the $0.015 \leq p/p_0 \leq 0.3$ region, the SSA value is obtained considering the quantity of monolayer adsorbed gas, the BET constant *c*, the molar volume of the gas, and the Avogrado number.

In this work, the N_2 sorption was performed at liquid nitrogen temperature (77 K) in a Micromeritics ASAP2020 apparatus (Figure A9) using samples previously degassed under vacuum at 80 ºC for UiO-67(Zr,Hf)_NH_2 materials, at 100 ºC for MIL-125(Ti)_NH_2 and CAU-

1(Al)_NH_2, at 150 °C for UiO-66(Zr,Hf) compounds, and at 200 ºC for MIL-125(Ti). The specific surface area and pore size distribution of the examined samples were evaluated by the multipoint BET model in the 0.015-0.3 p/p_0 range.

2.2.4. Scanning Electron Microscopy

SEM is a technique used to scan the surface of a sample using a focused beam of electrons. The interaction between the electrons and the atoms from the sample generates signals that contain information about the surface topography but also the chemical composition of the material. The apparatus is composed of an electron source – which can be composed of tungsten cathode, lanthanum hexaboride (LaB_6) cathode, or field emission gun (FEG) –, an anode, a set of magnetic lens and deflection coils, a vacuum pump, and different detectors – the detector for backscattered and secondary electrons being the most common (Figure A10). The SEM samples must be either conductive so they can withstand the high vacuum and energy of the electron beam without creating charge effects. In the case of powdered samples, they are often deposited over a carbon tape and then coated with a conductive element such as carbon, gold, palladium, chromium, platinum, iridium, tungsten, or osmium.

Once placed on the specimen stage, a high vacuum is applied, and the electron beam is turned on. The interaction between the electrons and the sample creates a teardrop-shaped interaction volume which extends to few micrometers into the surface. For topographic information, the most used signal is that collected from the secondary electrons, which are basically ejected from the conduction or valence band of the sample through inelastic scattering with the beam (Figure A10). Because these electrons have low energy (< 50 eV) they can only penetrate a few nanometers below the surface. Therefore, it provides information about topological characteristics of the substrate, where the brightness of the signal is related to the number of electrons that reaches the detector. Hence, steep surfaces and edges tend to be brighter than flat surfaces, resulting in well-defined 3D images. On the other hand, the backscattered electrons (BSE) consist of high-energy electrons originating in the electron beam that are reflected through elastic scattering with the specimen atoms (Figure A10). Therefore, BSE provides information related to the chemical composition of the sample, as heavy elements backscatter electrons more strongly than light elements and consequentially, appear brighter in the image.

In this work, the SEM was conducted on a FEG microscope (Hitachi SU 5000) at an accelerating voltage of 5 kV, using samples previously sputter-coated with carbon (Figure A11).

2.2.5. Energy-Dispersive x-ray Spectroscopy

EDS is an analytical technique that is usually coupled to electron microscopes (in transmission of scanning configurations) and allows the obtention of chemical information coupled with imaging. Basically, the target sample is stimulated by an electron or an X-ray beam, which excites electrons from an inner shell of the atoms, creating holes (Figure A12). Then, an electron from an outer, higher-energy shell fills this hole and emits radiation in the form of X-rays with characteristic energy values that depend on the element and on the transition – i.e., the difference between the energies of the outer and inner shells.

The EDS analyses were conducted on a FEG microscope (Hitachi SU 5000) at an accelerating voltage between 5 and 10 kV, depending on the necessary energy to observe the transitions of different elements. This microscope is equipped with a Si(Li) EDS detector (AZtec from the Oxford Instruments) with a 60 mm^2 window.

2.2.6. Fourier Transformed Infrared Spectroscopy

FTIR spectroscopy is particularly suitable to identify structural features and adsorption sites in porous materials by means of unique transmittance patterns, which are associated with the vibrational frequencies of chemical bonds in stretching and bending modes. Basically, a light beam in the infrared region (780 nm $\leq \lambda \leq$ 1 mm) is irradiated into the target sample, which absorbs a part of the radiation to produce transition between energy levels related to the vibrations of chemical bonds (Figure A13). Different vibrations have different associated energies, which are related to several parameters such as the mass of the involved atoms, the type of vibration (i.e., stretching, bending), the symmetry, and the environment of the compound. Considering adsorption and emission, the transitional moment of the entity (which depends on the dipole moment) must be non-null, so the probability of a given transition to happen is not zero. Therefore, diatomic homonuclear molecules (like I_2) do not have spectral signatures in infrared spectroscopy.

In this work, FTIR was performed on a Perkin Elmer Spectrum 2 using an attenuated total reflectance (ATR) accessory and a diamond crystal as the reflective element (Figure A14). The spectra were recorded using a resolution of 4 cm^{-1} and 128 scans. The ATR-FTIR technique allows to examine a liquid or solid sample without further preparation. Basically, the infrared light passes through the ATR crystal in such a way that it reflects on the internal surface, which is in contact with the sample, creating an evanescent wave (Figure A14). The light undergoes multiple internal reflections in the crystal depending on the angle of incidence and is then collected by a detector as it exits the crystal.

2.2.7. Raman spectroscopy

Raman spectroscopy is another vibrational spectroscopy technique that typically yields similar yet complementary information to that obtained with infrared spectroscopy. However, while the infrared spectroscopy relies upon the excitation of the ground state of the sample up to a vibrational state, Raman spectroscopy excite the system into virtual levels which then decay into different vibrational states. The technique relies on the inelastic scattering of photons (Raman scattering) by irradiating the sample with a monochromatic light source, usually from a laser in the visible, near infrared, or near ultraviolet regions. The laser interaction with the sample makes it possible to observe vibrations of the chemical bonds as the energy of the molecule is shifted up (Stokes Raman scattering) or down (Anti-Stokes Raman scattering) upon irradiation (Figure A15). In addition, there is a part of the irradiation that is elastically scattered (Rayleigh scattering) and therefore, it must be filtered while the rest of the light is collected by a detector. It is worth mentioning that, when a vibrational mode is active in both Raman and infrared spectroscopies, it is theoretically expected at the same position on the spectra.

In this work two different Raman techniques were used: FT-Raman and micro-Raman. In the former case, a near-IR laser (λ_{ex} = 1064 nm) is used, and the Fourier transform converts the interferogram signal into the desired spectra, similarly to the FTIR technique. In the latter case, three different laser wavelengths are available (515, 633, and 785 nm) and the spectra are obtained using dispersive single-stage spectrographs paired with charge-coupled device detectors.

UiO-66, MIL-125, MIL-125_NH_2, and CAU-1_NH_2 compounds were analyzed using a Bruker RFS 100/S FT-Raman with a CW Nd:YAG laser (λ_{ex} = 1064 nm) as excitation source

(Figure A16). A laser power of 50 mW was used, the spectra were measured in the region 50 – 4000 cm^{-1} with a resolution of 2 cm^{-1} and were accumulated over 1000 scans. For the iodine evolution analysis in UiO-66(Zr,Hf), the Raman spectra were taken every one hour for 24 hours, every two hours for the next 24 hours, and every four hours for the last 24 hours (three days spectra collection in total). To follow the iodine adsorption process, in-situ Raman experiments were conducted for the I_2@MIL-125 and I_2@CAU-1 compound, with spectra taken every hour for five days in total. Briefly, a homemade filtration bench supplied with non-radioactive iodine (more details in section 2.3) was coupled with the FT-Raman spectrometer by placing the quartz cell containing the MOF in the optical trajectory of the Raman laser. The parameters of the spectrometer were the same for the other experiments described above.

Micro-Raman Analyses were performed for the UiO-67_NH_2 compounds and for the desorption experiments using MIL-125 and MIL-125_NH_2 materials. The analyses were conducted on a LabRam HR-Evolution (Horiba scientific) microspectrometer using a 50X 0.9 NA Olympus objective (Figure A16). The spectrometer is equipped with a 600 lines/mm grating. In the case of UiO-67_NH_2 materials, a Raman mapping was also carried out using different excitation sources (515, 633, and 785 nm) and a spatial resolution of 1 µm. To evaluate only the thermodynamic aspect of the iodine distribution inside the pores (without any influence of kinetic phenomena) all the samples were kept sealed under argon atmosphere for one week after the contact with gaseous I_2. Also, to evaluate the kinetic of iodine diffusion, the spectra were collected in two different conditions: after 16 and 48 h of contact between the UiO-67_NH_2 solids and the iodine gas. The in-situ Raman desorption experiments were performed for I_2@MIL-125 and I_2@MIL-125_NH_2 materials using the same configurations and a 785 nm excitation source. The samples were heated at 100 ºC.min^{-1} up to different temperatures (40, 50, 60, 70, 80, 90, 100, 110, and 120 ºC) using a TMS 94 Ramp Temperature Programmer. The powdered samples were always replaced after one temperature cycle. Spectra were acquired each five minutes for 19 hours and data processing was performed using LabSpec6 software.

2.2.8. Ultraviolet-Visible spectroscopy

UV-Vis spectroscopy uses a part of the ultraviolet, the entire visible, and adjacent infrared regions of the light spectrum to produce electronic transitions in different systems. Basically, upon UV-Vis irradiation, the electrons absorb photon energy giving rise to an excited

state (Figure A17). For instance, organic chromophores have characteristic colors due to different transitions in the UV-Vis region, such as π–π*, n–π*, σ–σ*, and n–σ*. On the other hand, transition metal complexes are often colored because of their incompletely filled *d* orbitals allowing multiple electronic transitions. Although UV-Vis spectroscopy is often applied to solutions, diffuse-reflectance UV-Vis allows the obtention of data using solid-state samples. Briefly, when light is irradiated on a body several phenomena may occur such as absorption, transmission, refraction, and reflection. In the last case, the light can reflect in a specular or diffuse manner (which is the case of irregular surfaces and therefore, most materials). Thus, a diffuse-reflectance UV-Vis spectrometer works with a detector in the form of an integration sphere that detects the light diffused in every direction (Figure A17). Through the difference between the measurement of the reference sample (usually barium sulphate) and the target sample, the diffuse-reflectance spectrum is obtained. Then, different methods are available to transform this data into an absorbance spectrum, which is further detailed in Chapter III.

In this work, the diffuse reflectance UV-Vis experiments were carried out on a Varian Cary 5000 spectrometer using Praying Mantis™ Diffuse Reflection Accessory adapted for the characterization of powder samples. The spectra were recorded in the 200-800 nm spectral range with a resolution of 1 nm and were plotted using the Kubelka-Munk function [177].

2.2.9. Electron Paramagnetic Resonance

EPR is a spectroscopy technique used to identify the presence of paramagnetic species which are related to materials with unpaired electrons. The method is based on the creation of an external magnetic field that aligns the magnetic moment of the electrons in the system in a parallel or antiparallel fashion, each alignment having a specific energy due to the Zeeman effect. The energy difference between the lower and upper state for unpaired electrons is in the order of microwave radiation (Figure A18). Basically, an EPR test operates under a constant microwave irradiation and varies the magnetic field. When the energy provided by the microwave light equals to the split between the two energetic states, a transition occurs, and an absorption phenomenon is observed – EPR spectra is often represented as the first derivative of the absorption spectra. Because the energy of the transition is proportional to the so-called *g*-

factor, this is one of the most important values for identifying the paramagnetic species that are present in the system (i.e., g = 2.0023 for free electrons).

Here, the EPR spectra were recorded using a Bruker ELEXYS E580 operating at 9.6 GHz. All spectra were recorded at both room temperature and 120 K with 1.0 G modulation amplitude and different microwave power (Figure A18). In situ irradiation of samples was performed with an LC8 Hamamatsu lamp using either its full spectrum or the UV region between 240 and 400 nm. Spectra simulation were conducted using the EasySpin software with pepper function and the experimental data were refined using internal esfit function [178].

2.2.10. Nuclear Magnetic Resonance

NMR spectroscopy is a spectroscopic technique used to observe atoms with non-null magnetic moment in their nuclei. Its principle is very similar to that of EPR spectroscopy, as it is based on the formation of different energy levels (in the order of radio frequency, roughly from 4 to 900 MHz) under the influence of an external magnetic field (Figure A19). NMR spectroscopy gives information about both the electronic structure and individual functional groups of the system. Although NMR spectroscopy is deeply used for liquid samples, the magic-angle spinning technique allowed its application for solid-state materials. Basically, the rotation of the sample at the magic angle (θ_m = 54.74° with respect to the direction of the magnetic field) allows to improve the resolution of the solid-state NMR spectra by reducing the anisotropy of the sample. In fact, liquid NMR spectra are characterized by fine absorption lines, whereas solid-state NMR often exhibits very broad signals because of the orientation dependance of the chemical shift (resonant frequency of an atomic nucleus relative to a standard in a magnetic field).

This work used only liquid ^{1}H NMR spectroscopy which was performed in a Bruker AVANCE III HD 300 MHz spectrometer via a 60-position Sample Xpress autosampler. The chemical shifts were referenced by the external resonance of the tetramethylsilane. The sample digestion was performed using 10 mg of solid material by soaking it into 1 mL of a 4M NaOD/D_2O solution before sonicating the mixture for 15 minutes. Then, 0.6 mL of the liquid was recovered by filtration and placed into a 5 mm NMR tube before being analysed at 8 scans.

2.2.11. Thermogravimetric Analysis

TGA is a method of thermal analysis used to measure the mass of the sample over time as temperature changes. This measurement provides information about different physical phenomena such as adsorption, desorption, phase transition, thermal decomposition, oxidation, and reduction (Figure A20). Basically, the instrumentation consists of a precision balance with a sample pan that is located in an oven. The analysis can be conducted in different atmospheres and pressures depending on the equipment (nitrogen, air, vacuum, argon, carburizing gases, high pressure, corrosive gases)

Here, the TGA analysis were conducted in a Mettler Toledo TGA/DSC 3+ instrument for the MIL-125(Ti) and MIL-125(Ti)_NH_2. The data was acquired under an 80 $mL.min^{-1}$ air flow using alumina crucibles. Initially, the samples were heated at 5 $ºC.min^{-1}$ starting from room temperature up to 800 ºC. Then, in a second moment, the iodine-loaded compounds were heated at 100 $ºC.min^{-1}$ and kept 20 hours in different temperatures (40, 60, 80, 100, and 120 ºC).

2.2.12. Chemometrics

Chemometric is defined as the science of extracting information from chemical system by data analysis means. In this work, it was carried out using the Raman spectra obtained during the course of the iodine sorption in UiO-66 materials. For that, the Multivariate Curve Resolution-Alternating Least Squares (MCR-ALS) algorithm was applied (Figure A21) [179]. This method is focused on extracting relevant information of the single components in a mixture system through a bilinear model decomposition of the experimental data matrix (D) into a product of matrices C and S^T that contain pure profiles of components linked to the row mode (usually concentrations or peak profiles) and the column mode (usually spectra).

The experimental data matrix (D) was obtained by loading the Raman spectra of the I_2@MOFs. The number of components of the system was evaluated by the Singular Value Decomposition (SVD) algorithm. The initial estimation of the factor matrix was obtained by the Evolving Factor Analysis (EFA). Non-negativity constraints were applied to all species of the spectra (S^T) and concentrations (C) matrices by using the fast non-negative least squares (fnnls) algorithm [179]. Unimodality constraints were also imposed to all species of the concentrations matrix (C) based on the same algorithm. The spectra were divided by the Euclidean norm, the maximum number of interactions was set to 500 and the convergence criterion to 0.1.

2.2.13. Computational modeling

All the computations were carried out using the Gaussian 16 suite of programs. The energies were computed out using DFT-based methods, more specifically the PBE0 global hybrid functional, which was augmented with an empirical correction for the dispersion (GD3). The Kohn-Sham wave-functions were described using the 6-311++G(d,p) basis set on all the atoms but iodine. This latter atom was described using the Stuttgart-Dresden ECP and the associated basis set. The geometry of organic molecules was optimized using the standard algorithms implemented in Gaussian 16 and the nature of the obtained was checked by the computations of the harmonic frequencies.

2.3. Iodine adsorption tests

A home-made filtration bench supplied with non-radioactive iodine (^{127}I) was used in order to evaluate the evolution of iodine content trapped within MOF materials (Figure 2.4). Briefly, the gaseous iodine is generated using a permeation oven (VICI Metronics Dynacalibrator® Model 150) heated to 100 °C and containing permeation tubes with solid-state iodine crystals. This heating allows the sublimation of iodine and its vapors (0.8 $mg.h^{-1}$) are entrained by an argon flow at a flow rate of 10 $L.h^{-1}$, controlled by a flowmeter (Bronkhorst High-tech E-Flow), providing an iodine concentration of 0.08 $mg.L^{-1}$. Then, the gas flow reaches a filtration cell which contains a frit of porosity 2, adapted to the width of the tube (4 mm). The MOF powdered sample is placed over the frit, allowing the gaseous iodine to pass through it at room temperature. The amount of I_2 molecules that have not been trapped within the MOF is captured in a two-liter bottle, filled with a 0.1 M potassium iodide solution. This solution makes it possible to chemically transform the I_2 into I_3^- according to the Equation (2.1).

$$I_2 + I^- \leftrightarrow I_3^- \qquad (2.1)$$

Magnetic stirring is applied to ensure constant agitation and homogeneity of the solution. Using a peristaltic pump (Cole-Parmer Masterflex L/S Model 77201-60), the I_3^- solution is continuously dosed by a Shimadzu UV1800 UV-vis spectrometer. In parallel, a blank solution of KI (0.1 M) is pumped into the spectrometer in order to have a continuous reference. The wavelength is set to 352 nm during the analysis, corresponding to the main absorption band of the I_3^- aqueous species. UV-vis measurements are then collected every four

minutes over a period of 16 hours. For each sample analyzed, two measurements are prepared: the first corresponds to a blank that is applied in order to obtain the iodine flux delivered by the assembly during the experiment without filter solid; the second is the actual test carried out in the presence of a MOF sample. Once the two measurements are done, the difference between them generates a third curve, which corresponds to the theoretical absorbance associated with the iodine trapped inside the pores of the MOF. Thanks to a preliminary calibration, it is possible to measure the mass of iodine trapped per quantity of MOF. The kinetics of adsorption for the different materials was evaluated using the Linear Driving Force (LDF) model [180], which was already successfully applied in very similar systems containing UiO-66 and I_2 [12]. The LDF model is represented by the Equation (2.2), where *F(t)* is the fractional uptake (m_t/m_{tf}) – m_t is the uptake mass at a given time and m_{tf} is the uptake mass at the final time –, k_{LDF} is the effective mass transfer coefficient (h^{-1}) at given temperature and pressure, and *t* is the time in hours.

$$F(t) = 1 - e^{-k_{LDF}\, t} \tag{2.2}$$

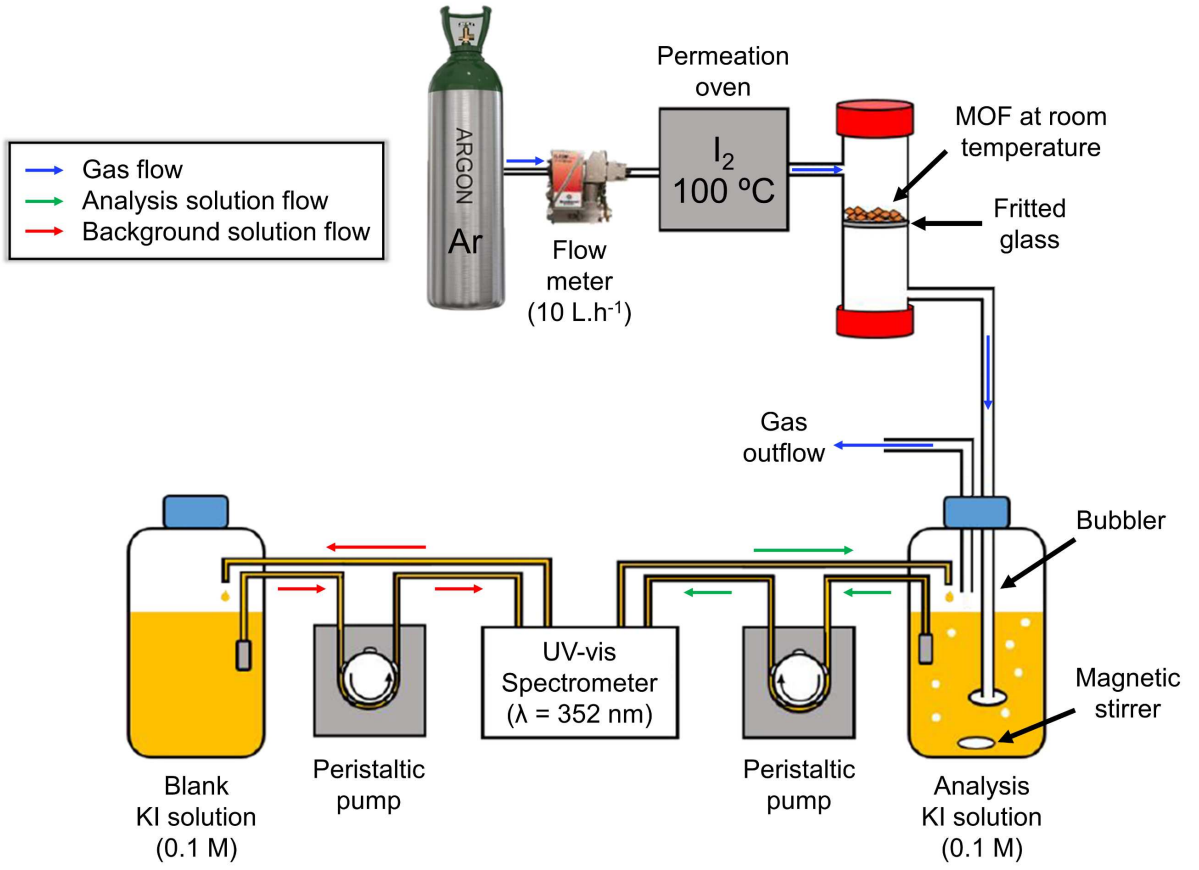

Figure 2.4: Scheme of the filtration bench used during the iodine evolution tests. The I_2 adsorption and the UV-Vis spectra were conducted at room temperature.

Chapter III: How to Correctly Determine the Band Gap Type and Energies from Diffuse Reflectance UV-Vis Data

3.1. Introduction

Heterogeneous photocatalysis has become a field of great interest since its early development back in the 70's [181]. Since then, it has become a multidisciplinary area that incorporates semiconductor physics, surface sciences, physical chemistry, materials science, biology, and chemical engineering [182,183]. After the demonstration of the water photolysis in the presence of TiO_2 by Fujishima and Honda in 1972 [181], different types of semiconductors have been extensively evaluated according to their photocatalytic properties in liquid and gaseous mixtures, worth mentioning TiO_2, ZnO, Fe_2O_3, ZnS, and CdS [182,184]. Later on, many other materials and heterojunctions have been developed for photocatalytic applications, such as polymers [185], MOFs [186], and MOFs-TiO_2 heterojunctions [108]. The properties of those materials – e.g., porosity, SSAs, particle size, and electronic structure – have been continuously improved over the years due to the extensive research in this field [187–189]. When considering the most common inorganic semiconductors, their main properties (such as electronic structure, band gap energies and types) are already thoroughly known, mainly due to the large number of experimental and theoretical data that have already been collected. On the other hand, due to the great number of MOFs that already exist and that are discovered daily (there are more than 90,000 MOF-structures documented in the Cambridge Structural Database and more than 500,000 have been predicted) [190,191], theoretical studies that normally take several months to be conducted cannot keep up with the speed in which new structures are discovered. Moreover, these hybrid, crystalline, porous materials have characteristics that are, in some areas, gathered between semiconductor physics and homogeneous photocatalysis [105]. In fact, these materials can be considered as solids with well-defined boundaries with the solution, but also as infinite quasi-molecules. Therefore, it is rather unusual how concepts of coordination chemistry are often mixed with those of semiconductor physics in MOF literature [105].

One of the most important characteristics of a semiconductor is its optical band gap. For inorganic semiconductors, this feature is frequently obtained using the Tauc plot applied to the UV-Vis data [192]. However, approaches based purely on this method are not accurate in a general sense, especially for distinguishing direct and indirect band gaps. For dealing with this limitation, researchers often combine other experimental techniques to obtain this information, such as XPS, ultraviolet photoelectron spectroscopy (UPS), and inverse photoelectron spectroscopy (IPES) [193]. Nevertheless, these techniques are not always of easy access, which hinders a more complete and accurate analysis. For such reason, this chapter draws attention to

various studies that have been conducted over the last few decades for assessing the electronic structure of MOFs. It also discusses the reliability of the obtained results, proposing a combination of methodologies for determining band gap energies and types purely from diffuse-reflectance UV-Vis data, which should reduce the gap between experiment and theory in the MOF realm. Also, by providing a concise methodology for assessing these energies, this work expects to diminish the discrepancies in optical band gap values obtained from different sources.

3.2. The band gap theory in UV-vis spectroscopy

The study of the interaction between light and matter has been deeply intensified since the postulation of the photoelectric effect by Heinrich Hertz in 1887 [194]. Afterward, through the contributions of Max Planck [195] and Albert Einstein [196], the energy carried by light was found to be composed by discrete quantized packets also known as quanta. Einstein predicted that the energy of these packets increases linearly with the frequency of the light and it is independent of its intensity ($E = h\nu$), which was later confirmed by Millikan [197] through an experimental determination of the Plank constant h. Later on, in 1931, Alan Herries Wilson [118,119] introduced the concept of band gap in semiconductors through its conduction band theory. Essentially, different classes of materials such as metals, semiconductors, and insulators can be distinguished by the energy distribution of their electronic states near the Fermi level E_F. In metals and other conductive materials, the Fermi level lies inside at least one band whereas in semiconductors and insulators it is situated in an energy range where no electronic state can exist [198]. This region, commonly known as band gap (E_g), refers to the energy difference (usually in eV) between the valence band maximum (VBM) and the conduction band minimum (CBM). In other words, it represents the minimum energy necessary ($E \geq E_g$) to promote an electron bounded to an atom to a conduction electron, which is free to move through the material lattice, serving as charge carrier.

For instance, semiconductors have the capacity to absorb photons with a certain amount of energy $h\nu \geq E_g$ and to use them to excite electrons from the VB to the CB [199]. It should also be noted that an increase in temperature upsurges the concentration of charge carriers in the CB of semiconductors and thus, improves its conductivity [120]. After the proof of the relationship between the photon energy and the band gap of these materials, several studies were conducted

aiming to obtain compounds with narrower band gaps, which allows the excitation of electrons within the visible light and near-IR region [200–203]. This feature is greatly desired for the environmental remediation of different pollutants since those materials can be photoactive under solar light, which guarantees a better reaction yield for compounds with reduced E_g [204]. However, wider band gaps are also envisaged in other applications, such as optoelectronic and energy harvesting [205]. For these reasons, the assessment of the band gap energy of semiconductors is crucial to the study of such materials.

The optical absorption of crystalline semiconductors is often evaluated by semi-classical models in which the electrons receive a quantum mechanics approach, whereas the electromagnetic waves receive a classical approach [206]. These optical transitions can present changes in the electron wave-vector $(\vec{k})$ or not. Indeed, direct and indirect transitions are characterized by the momentum difference in the Brillouin zone between the minimal-energy state in the CB and the maximal-energy state in the VB (Figure 3.1) [207]. If those states occur in different k-vectors, the material has an indirect band gap and the transition is labeled as "phonon assisted", since almost all the change in the momentum of the system is transferred from a phonon [207]. On the other hand, if the momentum of the charge carriers is preserved, a direct band gap is ascribed to the compound and only photons are involved in the transition [207]. According to some selection rules [208,209], optical transitions can be allowed (higher probability) or forbidden (lower probability), which affects the measurements for quantifying E_g.

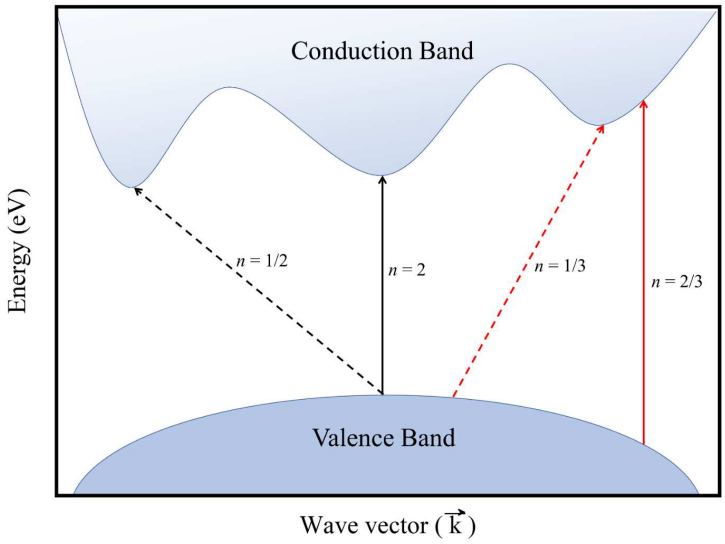

Figure 3.1: Scheme showing the different types of optical transitions between the valence band and the conduction band in a semiconductor. In black: allowed transitions. In red: forbidden transitions. Solid arrows represent direct transitions and dotted arrows represent indirect ones. The coefficient *n* depends on the electron transition exhibited by the material – e.g., indirect allowed transition (n = 1/2), direct allowed transition (n = 2), indirect forbidden transition (n = 1/3), and direct forbidden transition (n = 2/3).

In an ideal scenario, at absolute zero temperature, no phonons are available for being absorbed. Therefore, the optical absorption plotted against the photon energy has a different behavior for crystals with direct and indirect gaps, as demonstrated in Figure 3.2 [210]. At first, in materials with direct gaps, the band edge determines the gap energy as there is no significant change of $\vec{k}$ and therefore, $E_g = h\nu$ [210]. However, in indirect band gap materials, the band edges of the VB and CB are widely separated in the $\vec{k}$ space. For this reason, a phonon with energy $\hbar\Omega$ and wavevector $\vec{k}$ has to be emitted for the transition to take place. As a consequence, the optical absorption is weaker near the band edge [210]. In such systems, the energy necessary for the indirect process to occur is greater than the true band gap – as it needs to be partially used to emit a phonon – and the absorption threshold for the indirect transition between the VB and the CB is at $h\nu = E_g + \hbar\Omega$ (Figure 3.2) [210]. Finally, at higher temperatures, if a phonon is absorbed along with a photon, the transition may also take place at $h\nu = E_g - \hbar\Omega$ [210].

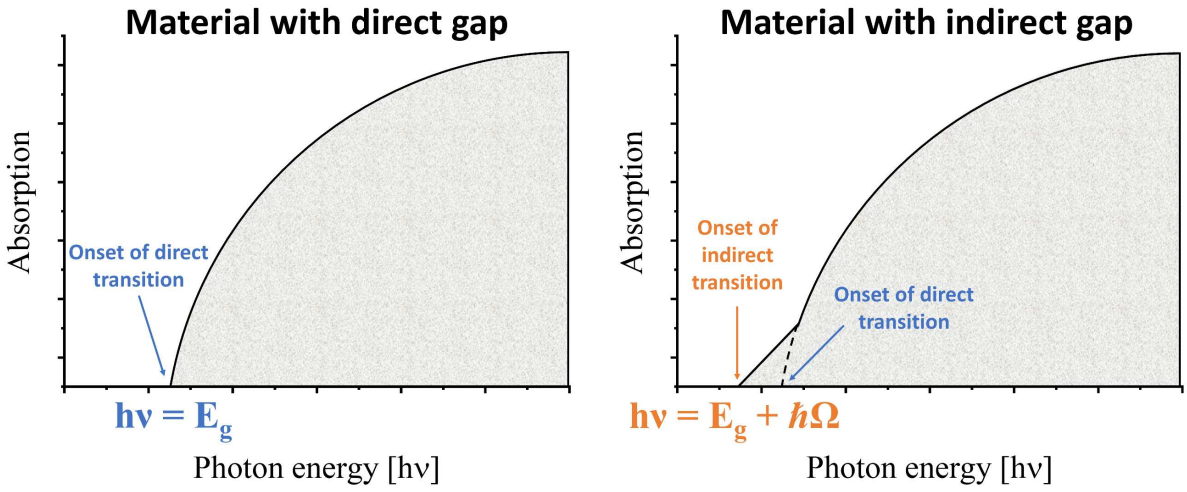

Figure 3.2: Scheme representing the optical absorption spectra at 0 K for a crystalline material with direct (left) and indirect gaps (right). The energy for the onset of the direct transition is displayed in blue and for the indirect transition, in orange. Adapted from Kittel [210].

In both the direct and indirect transitions, the absorption coefficient *α(E)* is expected to be zero for energy values smaller than the band gap of the material, as indicated in Equation (3.1). In case of energy values equal or higher than the band gap, there are significative differences in the relation between *α(E)* and E_g for direct and indirect band gaps, as highlighted in Equations (3.2) and (3.3), respectively, where $\hbar\Omega$ represents the energy of a phonon.

$$\alpha(E < E_g) = 0 \tag{3.1}$$

$$\alpha_{direct}(E \geq E_g) \propto (E - E_g)^{1/2} \tag{3.2}$$

$$\alpha_{indirect}(E \geq E_g) \propto (E + \hbar\Omega - E_g)^2 \tag{3.3}$$

Due to these relationships, the band gaps can be determined by measuring the absorption coefficient. If the gap is direct, the E_g values can be assessed through the extrapolation of the linear least squares fit of α^2 in a "α^2 versus $h\nu$" plot that intercepts the *x-axis* [206]. Similarly, if the gap is indirect, E_g can be obtained by the extrapolation of the linear least squares fit of $\alpha^{1/2}$ to zero, in a "$\alpha^{1/2}$ versus $h\nu$" plot [206]. However, this semi-classical approach presents some failures at low temperatures (since no Coulomb attraction is taken into account), in materials presenting defects and impurities (due to extrinsic absorption), and for energies $E \gg E_g$ [206]. Also, some other effects such as local temperature [211], external strong electric or magnetic fields [212,213], and doping-alloying effects should be considered as they can influence the *α(E)* profiles [206].

When structural-electronic disorder is present (for amorphous semiconductors, for example), the determination of the band gap from optical absorption requires other methodology, especially due to the presence of tail states nearby the VB and the CB [206]. Such approach was first proposed by Tauc [214] by imposing some restrictions to the optical absorption processes, such as considering an absence of k-vector conservation, a constant momentum transition matrix element, and a density of electron states close to the VB and CB that is proportional to the square root of the photon energy. During the study, Tauc [214] evaluated the optical properties and the electronic structures of amorphous germanium, and showed that there are regions in which $\hbar\omega\sqrt{\varepsilon_2}$ is linearly dependent on the photon energy ($\hbar\omega$), where $\hbar$ is the reduced Plank constant (6.582×10^{-16} eV·s), ω is the photon angular frequency (rad.s^{-1}), and ε_2 is the imaginary part of the relative permittivity. ε_2 is defined according to the Equation (3.4), in which n is the refractive index and κ is the extinction coefficient. In this context, Tauc *et al.* [214] verified an absorption band represented by a straight line where $\omega^2\varepsilon_2 \approx (\hbar\omega - E_g)^2$. They demonstrated that the band gap of the material can be obtained through the intercept between the extrapolation of this line and the photon-energy axis. The authors also verified that, in this case, only the energy is conserved (electron and photon) but not the momentum (k-vector), which is indicative of an indirect transition [214].

$$\varepsilon_2 = 2n\kappa \tag{3.4}$$

The optical and electronic properties of amorphous semiconductors were further investigated by Davis and Mott in more general systems [215]. They proposed a relationship that offered the best fit to the optical absorption edge by considering the conductivity σ at a certain angular frequency ω, according to the Equation (3.5). Then, from the plot of $(\alpha\hbar\omega)^2$ against the photon energy $\hbar\omega$, where α is the absorption coefficient (cm^{-1}), a linear region was obtained and extrapolated to the abscissa axis to assess the E_g value.

$$\sigma(\omega) = \frac{\sigma_0\left(\hbar\omega - E_g\right)^2}{\hbar\omega} \tag{3.5}$$

A relation was further stablished between the measured absorbance and the energy, showing that the optical absorption strength depends on the difference between the photon and the band gap energy as represented in Equation (3.6) [216]. In this case, h is the Plank constant (4.1357×10^{-15} eV.s), v is the photon frequency (Hz), A is the slope of the Tauc plot in the linear region, and n depends on the electron transition exhibited by the material (Figure 3.1) – *e.g.,* indirect allowed transition (n = 1/2), direct allowed transition (n = 2), indirect forbidden transition (1/3), and direct forbidden transition (2/3).

$$(\alpha h\nu)^n = A(h\nu - E_g) \tag{3.6}$$

Although the Tauc method was originally developed for the evaluation of absorption in amorphous semiconductors, it is extensively applied for assessing the band gap of crystalline thin films [216] and nowadays, it is commonly used for other types of crystalline materials as well – such as powdered TiO_2 and ZnO [217–219]. Dolgonos, Mason, and Poeppelmeier [220] emphasized that the Tauc plot is only applicable to materials in which a localization of energy states can be assumed (which is the case of amorphous materials and nanoparticles), indicating that the method is inappropriate to deal with crystalline and/or highly-doped semiconductors. However, a recent study demonstrated that the linearity of the Tauc plot obtained for nanocrystals is not as significant when compared to that of bulk materials [217]. This last feature was ascribed to the discretization and blueshift of the energy spectrum from the electronic states, but also to the relaxation of the momentum selection rule which cannot be considered for crystals with considerably small size [217]

The usual procedure for a Tauc analysis consists in acquiring optical absorbance data and plotting $(\alpha h\nu)^n$ versus $h\nu$, while testing the n-values (n = 2 or ½) until the best fit is obtained for the absorption edge, allowing to assign the correct type of the optical transition to the

material [216]. This analysis is not always obvious. The assignment is often difficult for materials with flat bands and, even sometimes for materials with dispersing bands [221]. In addition, some compounds present a pre-edge absorption in their UV-Vis spectra, which can influence the interpretation and the accuracy of the band gap estimation [222]. Also, Coulter and Birnie [216] highlighted that materials that exhibit indirect band gaps may also present direct transitions at higher energies, which would justify the acquisition of both E_g values (for n = 2 and ½). This means that both direct and indirect transitions can happen in semiconductor materials if the energetic conditions are favorable.

In view of all the previously mentioned situations that lead to deviations from the Tauc theory, other methodologies have been proposed for assessing the band gap energies from UV-Vis data. For instance, Cody *et al.* [223] adopted a methodology that assumes a constant dipole transition matrix element, where E_g is obtained from the extrapolation of the linear least squares fit of $(\alpha/h\nu)^{1/2}$ to zero in a "$(\alpha/h\nu)^{1/2}$ versus $h\nu$" plot (normally, $E_{Tauc} > E_{Cody}$). Another approach was proposed by Zanatta [206], which reported a method to obtain accurate E_g values by fitting a sigmoid (Boltzmann) function to the corresponding optical absorption spectra of crystalline (plate-like and powdered samples) and amorphous Ge, Si, and GaAs compounds. In that study it was concluded that, regardless of the method, the absorption coefficient (α) is one of the most important physical parameters for evaluating the band gap. Table 3.1 shows different models for obtaining the absorption coefficient.

Table 3.1: Methods applied for obtain the absorption coefficient (α) using UV-Vis data according to Zanatta [206]. d is the thickness of the sample, T is the transmittance, R is the reflectance, $\boldsymbol{R}_\infty$ is the diffuse reflectivity of a non-absorbing material, K and S are the Kubelka-Munk absorption and scattering coefficients, respectively.

Method	Formula	Considerations
Bouger-Lambert-Beer [224–226]	$\alpha_{BLB}(E) = \frac{1}{d}\ln\left(\frac{1}{T}\right)$	Does not consider the reflectance
Pankove [227]	$\alpha_P(E) = \frac{1}{d}\ln\left[\frac{(1-R)^2}{T}\right]$	Considers that the product αd is large
Pankove-Vahalová [227,228]	$\alpha_{PV}(E) = \frac{1}{d}\ln\left[\frac{(1-R)^2}{T} + \sqrt{\frac{(1-R)^4}{4T^2}} + R^2\right]$	Includes internal reflections for small values of αd
Kubelka-Munk [177]	$\alpha_{KM}(E) \cong F(R) = \frac{(1-R_\infty)^2}{2R_\infty} = \frac{K}{S}$	Considers a two-flux radiation model

Other techniques can be also combined for evaluating the band gap of semiconductors [105]. For instance, the VBM can be obtained by combining XPS, UPS, and photoelectron spectroscopy in air (PESA); while the CBM can be assessed through IPES [193,229–232].

3.3. The link between absorption and diffuse reflectance UV-vis data

Although UV-Vis spectroscopy is often applied to the band gap determination, diffuse-reflectance UV-Vis also allows its assessment from the absorption coefficient in solid-state samples. Briefly, when light is irradiated on a body several phenomena may occur, such as absorption, transmission, refraction, and reflection. In the last case, the light can reflect in a specular or diffuse manner (which is the case of irregular surfaces and therefore, most solid materials). Diffuse-reflectance UV-Vis spectrometers collect this diffused light in an integration sphere. Through the difference between a reference spectrum (usually from barium sulphate) and that of the target sample, the required diffuse-reflectance spectrum is obtained. Then, different methods allow to derive the absorbance spectrum, as detailed below.

Back in 1931, Paul Kubelka and Franz Munk [177] published the theory to obtain the absorbance spectra from diffuse reflectance. Their theory is based on a model in which the radiation field inside a light-scattering sample is represented by two fluxes that cross an arbitrary section (dx) within the coating layer. The first flux – $i(x)$ – travels through the illuminated surface, whereas the second – $j(x)$ – flows in the opposite way (Figure 3.3) [233]. In this case, the incident light on the substrate's surface has intensity I, of which the portion $RI = J$ is reflected (R represents the total reflectance of the coating). It is worth mentioning that, in order to avoid misinterpretation of the variables, the equations presented in this work have the same mathematical form as in the original paper, but with modified symbolism. Furthermore, even though a more modern four-flux model has already been reported in the literature [234], the Kubelka-Munk (K-M) two-flux method is still a valid approach when the system does not absorb light and if only the film and the substrate are considered [234].

P. Kubelka and F. Munk [177] considered a substrate in optical contact with a background with known reflectance (R_g), transmittance (T_g), and absorbance (A_g), as highlighted in Figure 3.3.

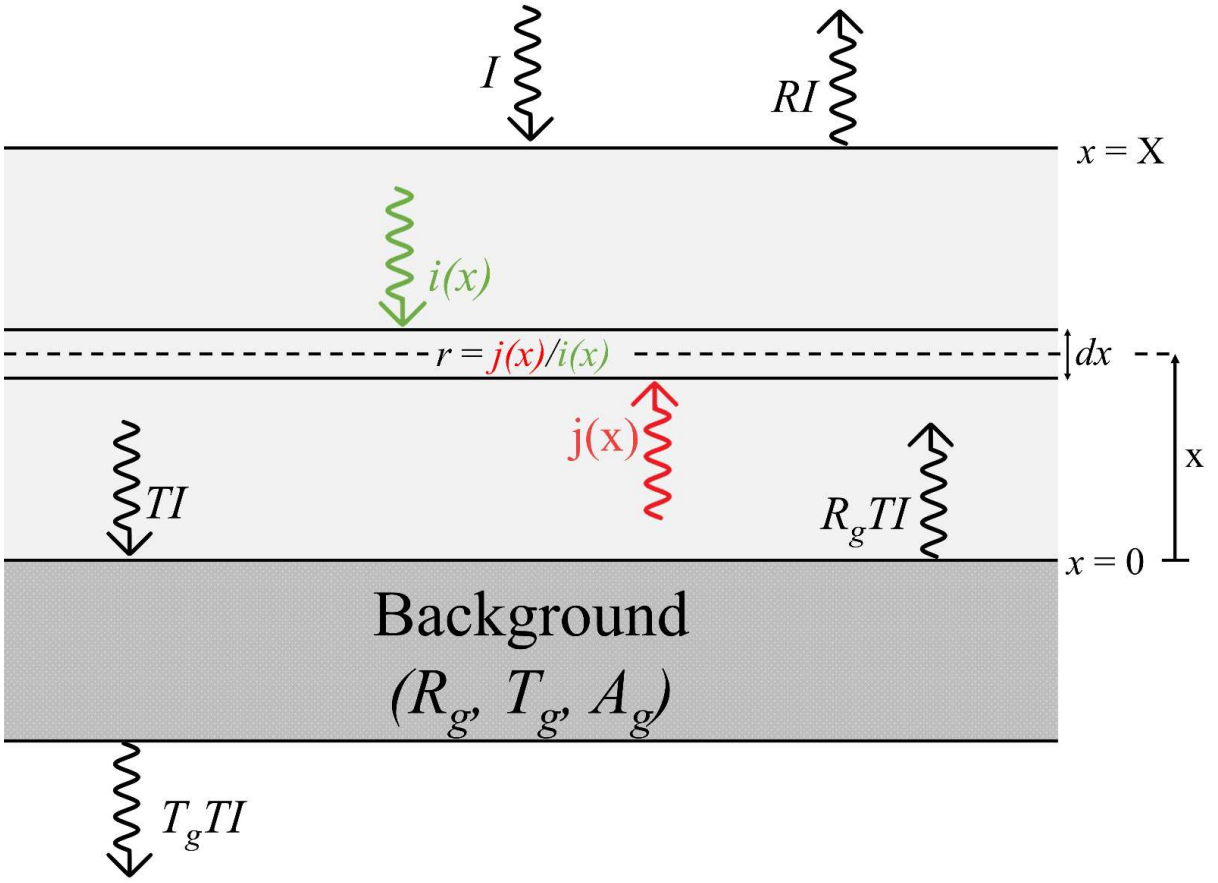

Figure 3.3: Scheme of the Kubelka-Munk model for the reflectance and transmittance of a finite thick plane-parallel light-scattering specimen (thickness ≡ X) placed in contact with a background substrate with known reflectance (R_g), transmittance (T_g) and absorbance ($A_g = 1 - T_g - R_g$). *I* is the intensity of the incident radiation, *i(x)* is the light flux that flows through the illuminated surface, *j(x)* is the light flux flowing back to the illuminated surface, *T* is the fraction of the incident light transmitted by the substrate, and *R* is the total reflectance of the system. This scheme was adapted from Hecht [235].

In such case, the components *i(x)* and *j(x)* are described by the Equations (3.7) and (3.8), where *S* and *K* are the scattering and absorption coefficients ($K \equiv \alpha$), respectively [234,235].

$$di(x) = -(S + K)i(x)dx + Si(x)dx \tag{3.7}$$

$$dj(x) = (S + K)i(x)dx - Si(x)dx \tag{3.8}$$

Considering that $a \equiv (S+K)/S$ and that $r \equiv j(x)/i(x)$ (analogous to $RI = J$), the equations (3.7) and (3.8) can be combined into a single differential equation or into an integral, as represented in Equations (3.9) and (3.10), respectively.

$$\frac{dr}{Sdx} = r^2 - 2ar + 1 \tag{3.9}$$

$$\int \frac{dr}{r^2 - 2ar + 1} = S \int dx \tag{3.10}$$

In order to solve this integral, the authors first evaluated a specific case, the "albedo of an infinitely thick coating", which is related to a layer so thick (X → ∞) that any further increase in its thickness does not alter the total reflectance of the system (*R*) [177]. Here, it is worth emphasizing that "albedo" stands for the ratio between the radiation reflected and incident on a surface ($R = J/I$) – it goes from zero to one, where zero is a black body that absorbs all incident radiation, and one is a body that reflects all radiation [233]. In this case, the Equation (3.10) can be integrated over the entire thickness of the infinite layer (X → ∞), resulting in the Equation (3.11), where R_∞ is the reflectance in an infinite thick coating layer [177].

$$\lim_{X \to \infty} r \equiv R_\infty = 1 + \frac{K}{S} - \sqrt{\left(\frac{K}{S}\right)^2 + 2\frac{K}{S}} \tag{3.11}$$

Later on, D. R. Duncan [236] demonstrated back in 1940 that the colors produced by a mixture of pigments can also be deduced by an expression considering the two coefficients (*K* and *S*), which are dependent on the wavelength of the incident light. These constants may be assessed by two measurements: first, by evaluating the reflectance of the pigments' mixture in different wavelengths; second, by obtaining the same values but for another blend containing one of the initial pigments mixed to a standard dye [236]. Duncan confirmed the "albedo of an infinitely thick coating" condition proposed by Kubelka and Munk by evaluating the variation of R_∞ when adding to the system a fraction of a compound that modifies both the *K* and *S* of the pigments [236]. This was the first time that the Equation (3.11) was reduced to the well-known K-M function, first called "reflectivity function" by Duncan – $F(R_\infty)$ – which is represented in Equation (3.12) [236].

$$F(R_\infty) = \frac{(1 - R_\infty)^2}{2R_\infty} = \frac{K}{S} \tag{3.12}$$

Duncan also demonstrated that, when the contribution of *K* and *S* are separately evaluated for each *i* component of concentration c_i in the system, the Equation (3.12) takes the form of Equation (3.13) [236].

$$F(R_\infty) = \frac{K}{S} = \frac{\sum(c_i K_i)}{\sum(c_i S_i)} \tag{3.13}$$

When considering small amount of pigments, the scatter coefficient (*S*) is dominated by the base material and therefore, it is assumed to be constant. In such case, Equation (3.13) is replaced by Equation (3.14), which is a linear function of the substrate concentration [236].

$$F(R_\infty) = \frac{\sum(c_i K_i)}{\sum(c_i S_i)} \approx \frac{\sum(c_i K_i)}{S} \tag{3.14}$$

The Kubelka-Munk transform is regularly used in solid-state spectroscopy measurements as, in this case, the samples are often opaque and therefore, can be considered as an infinitely thick coating (and the Equations (3.12) and (3.13) are both suitable) [237,238]. For instance, in infrared spectroscopy it is common to prepare solid samples by grinding them and mixing with KBr. In this case, the assumption that the analyte has low effect on the scattering coefficient (*S*) of the mixture is valid and therefore, it can be considered as a constant (Equation (3.14) is appropriate) [236]. However, for diffuse reflectance UV-Vis spectroscopy and near-infrared spectroscopy, the samples are regularly measured in their natural particulate state. Thus, this previous assumption becomes incorrect and higher deviations from linearity are observed [239]. This arises from the fact that the K-M model considers the samples as homogeneous and infinitesimal media and consequently, the method becomes valid only for very thin layers of small particles with low absorption [240]. In fact, the K-M theory exhibits high deviations from experimental data when the reflectance values are below 60% ($K/S > 0.13$) [241]. The criteria used to define if the K-M approach is reasonable consists in verifying the linearity of the curve when plotting *F(R)* versus the concentration of the absorber [240]. However, in several cases, researchers use the *log(1/R)* function as an empirical pretreatment to the data in order to normalize it [239]. At this point, it is worth mentioning that even though the Kubelka-Munk model gives a way to determine the ratio between the absorption and the scattering coefficients, it does not provide the values of *S* and *K* separately [239].

In 1999, trying to address these failures, D. Dahm [240] developed a more general equation. This author defined the absorption/remission function, *A(r,t)*, highlighted in Equation (3.15), where *r*, and *t* are the fraction of light remitted, and transmitted in one layer of material, respectively.

$$A(r,t) = \frac{[(1-r)^2 - t^2]}{r} \tag{3.15}$$

The equation can be related to the K-M function when considering a layer so thick that $t \rightarrow 0$ and then, $A(R,0) = 2F(R)$. In a more general case, the total reflectance of the material (R) can be assessed by combining the equations of Benford [242] and the absorption/remission function $A(r,t)$, giving rise to the Dahm equation [240], as demonstrated in Equation (3.16). Here, A is the fraction of incident light that is absorbed, R is the fraction remitted, and T is the fraction transmitted by a substrate of any thickness. Note that the Dahm equation is not suitable for powdered samples, as the transmittance values cannot be obtained through diffuse reflectance UV-Vis data.

$$A(R_d, T_d) = \frac{(1 - R_d)^2 - {T_d}^2}{R_d} = \frac{(2 - a - 2r)a}{r} \tag{3.16}$$

The failure of continuous models applied in diffuse reflectance data can be therefore ascribed to several factors. In the case of the Kubelka-Munk theory, the limitations related to the use of highly absorbent materials were often identified as the main problem, as discussed above [241]. The fact that the K-M theory is simply based on a two-flux approach of the radiation field was also mentioned and it was assumed in the past that adding additional directions (four-flux model) would fix the problem [234]. However, other limitations were also highlighted, such as the particular specular reflection in diffuse reflectance FTIR data, and the fact that the sample must be thick, densely-packed, and constituted by particles with random shapes whose size approximates to the wavelength of the incident radiation [206,243]. For instance, Landi *et al* [244] demonstrated that a thickness of about 0.5 mm is not sufficient for applying the K-M function in diffuse reflectance UV-Vis data acquired for TiO_2 nanoparticles. The K-M approach also considers that the material's absorption coefficient (S) should be constant and that it must not emit light within the measured spectral range [206]. Donald and Kevin Dahm [245] demonstrated that the failures in the K-M model are intrinsic to continuous models and also to the fact that they fail to predict simultaneously the fractions of light that are transmitted and diffused, reason why discontinuous models can be a tool for improving these theories. Nevertheless, the Dahm equation cannot predict the fractions of incident light that are directly transmitted and therefore, it can be inferred that the K and S coefficients are not proportional to those of the Bouger-Lambert-Beer law [239]. This last feature presents a great challenge when dealing with diffuse reflectance data since, in general, spectroscopists are mostly interested in evaluating the absorption coefficient of the substrate due to its strong correlation to the concentration of the absorbing species in the system [239,240]. However, even though the Kubelka-Munk theory is

considered as a pseudo-absorption function [206], it is widely accepted nowadays for evaluating the band gap energies of most semiconductor materials through diffuse reflectance UV-Vis measurements [237].

3.4. Assessing the band gap energies in MOFs

One of the most interesting features of MOFs is the possibility of chemically modifying them, either by decorating their pores with nanoparticles, by functionalizing their linkers with different organic groups, by replacing their metal sites, or even by creating defects on their structures [18]. These characteristics, coupled with the enormous possibilities of combining different organic linkers and metal sites, allow the formation of several structures with distinct CTCs upon UV-Vis excitation – considering the inorganic cluster, the organic linker, and other guest species. The different types of CTC that can be envisaged for MOFs were described in Chapter 1 and are summarized below: the Linker-Based Transition (LBT) [13,27], the Metal-Based Transition (MBT) [122], the Linker-to-Linker Charge Transfer (LLCT) [124], the Metal-to-Metal Charge Transfer (MMCT) [125], the Metal-to-Linker Charge Transfer (MLCT) [123], and the Linker-to-Metal Charge Transfer (LMCT) [27].

When dealing with these hybrid materials in photocatalysis, the concepts between semiconductor physics and homogeneous photocatalysis are often mixed [105]. Kolobov, Goesten, and Gascon [105] highlighted how unusual it is to mix coordination chemistry notions (such as LMCT) to others from semiconductors physics (such as conduction band) as it happens in MOFs literature. However, this happens because of the dual character of these hybrid materials. For instance, the alignment of the electronic bands in MOFs (semiconductor physics) can be manipulated by functionalizing their linkers (coordination chemistry), similarly to what occurs in solution [246]. The proximity of the MOFs from the solution state lies specially on the fact that these materials have a great volume of pores which are, routinely, filled with solvent molecules [105]. However, in some cases, they can also behave like nonmolecular semiconductors in photovoltaics, especially when considering their curvature maxima (VBM and CBM) and also their conductivity, even though this last feature is not much explored in the field of MOFs photocatalysis [105]. Due to the wealth of structures and electronic structures in MOFs, they are particularly well-adapted compounds to study the procedures for determining band gaps.

3.5. Results and discussion

For evaluating the optical properties of these hybrid materials, several MOFs were synthesized – UiO-66(Zr), UiO-66(Hf), UiO-66(Zr/Ti), UiO-66(Hf/Ti), UiO-67(Zr)_NH_2, UiO-67(Hf)_NH_2, UiO-67(Zr/Hf)_NH_2, MIL-125(Ti), and MIL-125(Ti)_NH_2 – and characterized by XRD and diffuse reflectance UV-Vis spectroscopy. The band gap energies were assessed by different methods and the obtained results were further compared with other reports found in the literature.

3.5.1. Diffuse reflectance UV-Vis spectroscopy

The quality of the synthesized MOFs was characterized by their PXRD patterns (Figure 3.4) and SC-XRD data (Table A3, Table A4, and Table A5), which are all in agreement with the literature.

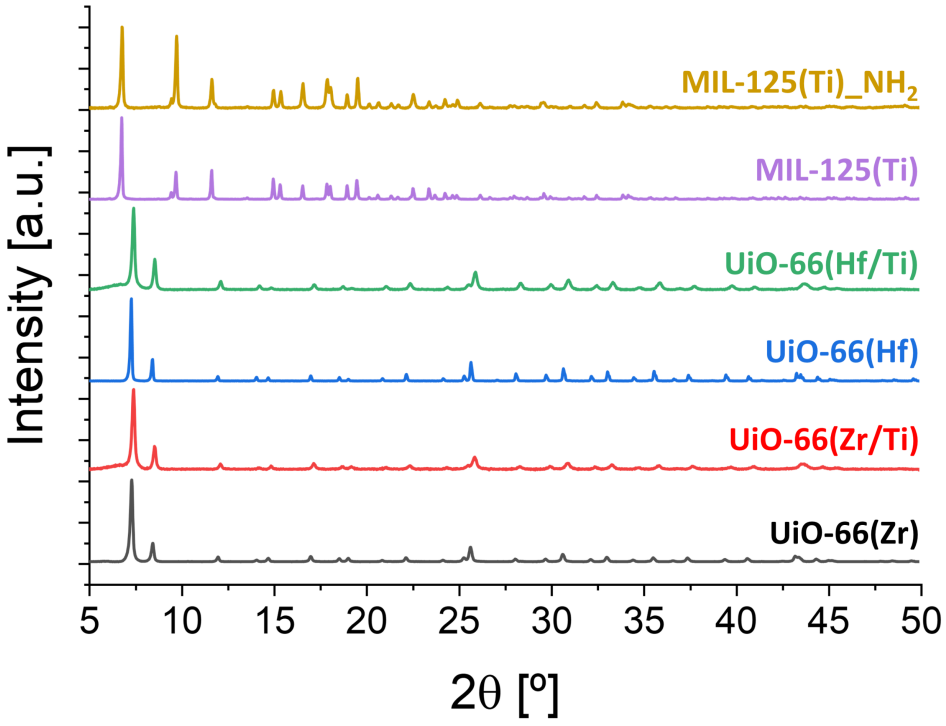

Figure 3.4: Powder X-ray diffraction patterns for UiO-66(Zr) (black), UiO-66(Ti/Zr) (red), UiO-66(Hf) (blue), UiO-66(Ti/Hf) (green), MIL-125 (purple), and MIL-125_NH_2 (yellow brown) obtained at $\lambda_{CuK\alpha1}$ = 1.5418 Å.

Their diffuse reflectance UV-Vis spectra are displayed in Figure 3.5, alongside the *log(1/R)* and the Kubelka-Munk representation. All the spectra were normalized from 0 to 100 for comparative purposes. The differences when evaluating the diffuse reflectance spectra using the K-M approach (F(R) for ordinate axis) and the *log(1/R)* are clearly visible (Figure 3.5).

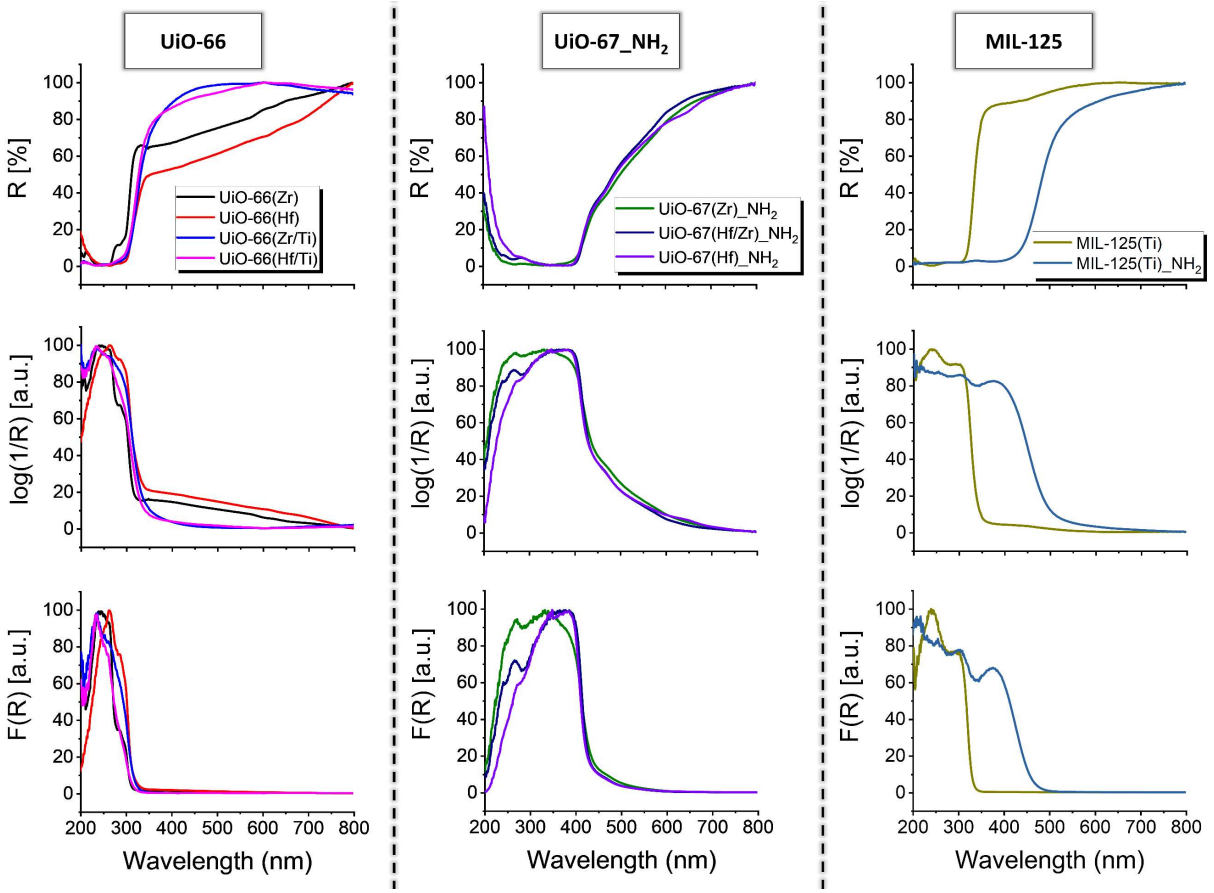

Figure 3.5: Diffuse reflectance UV-Vis spectra presented in reflectance R(%), log(1/R), and using Kubelka-Munk units (F(R)) obtained for UiO-66, UiO-67_NH_2, and MIL-125 compounds. The log(1/R) and the F(R) spectra were normalized to 100 for comparative purposes.

For instance, regarding the UiO-66 family, the K-M values present a thinner absorption band (between 200 and 320 nm) and a greater slope near its absorption tail when compared to the *log(1/R)* data. A similar feature is also present in the spectra of the UiO-67_NH_2, and MIL-125 compounds. This simple difference can, by itself, be a source of misevaluation of the materials' band gaps, as the extrapolation of these curves to zero (R, F(R), and *log(1/R)* versus *hv*) intercepts the abscissa axis in different *hv* values. Moreover, it seems that the K-M method led to spectra that are more consistent when considering their absorption band edges, which are better delimited than those obtained by using the *log(1/R)* data. Nevertheless, because it is not

possible to acquire absorption and transmission UV-Vis data for powdered samples without pre-treatment, the K-M and the *log(1/R)* approaches are the best possible approximations for the *α(E)* in this work. For this reason, the Dahm equation [240] was not considered in this study.

The spectra of the UiO-66 compounds exhibit absorptions in the UV domain between 200 and 320 nm regardless the nature of the metal site (zirconium, hafnium, or titanium-doped) (Figure 3.5), which is in agreement with other works [12,13,247]. The absorption maximum of this band is located at 243 nm for UiO-66(Zr), at 263 nm for UiO-66(Hf), and at 236 nm for the titanium-doped UiO-66(M/Ti) (M = Zr or Hf). This contribution is attributed to linker-based HOCO (Highest Occupied Crystalline Orbital) – LUCO (Lowest Unoccupied Crystalline Orbital) transitions [13]. It is worth mentioning that these orbitals (HOCO and LUCO) have been introduced to combine the concepts of both molecular (HOMO and LUMO) and bulk chemistry (VBM and CBM) realms, as mentioned before by Kolobov, Goesten and Gascon [105]. Furthermore, the spectrum of the Zr-based UiO-66 exhibits a shoulder at 292 nm that increases in intensity when replacing the zirconium by hafnium. This feature was ascribed to the different molar extinction coefficients of zirconium and hafnium, since there is no wavelength shift regarding the position of this shoulder from UiO-66(Zr) to UiO-66(Hf) [248]. Finally, the titanium-doped UiO-66(M/Ti) (M = Zr or Hf) does not exhibit any shoulder (Figure 3.5), which should be ascribed to the different CTCs upon photoexcitation exhibited by this material – LMCT in UiO-66(M/Ti) against LBT in UiO-66(M).

Several computational studies regarding the electronic structure of UiO-66 materials were already reported in the literature. For instance, as demonstrated by Yasin *et al.* [249] using a DFT approach, the presence of $–NH_2$ groups in the UiO-66 family enriches mostly the valence band density of states, not altering the energies of the metal cations. Their study also revealed that the total density of states (TDOS) of the molecular orbitals in UiO-66(Ti) reduces the position of the CBM, at the same time that it increases the position of the VBM [249]. In this case, when looking deeper into the partial density of states (PDOS) of UiO-66(Ti), these authors showed that the reduction in the CBM position is related to the inorganic part of the MOF, whereas the increase in the VBM is associated to carbon and oxygen atoms [249]. In fact, in their study, the DFT approach was coupled with experimental data of a titanium-doped UiO-66(Zr/Ti)_NH_2, which revealed that the presence of Ti creates a PDOS related to the inorganic cluster on the CBM of the material [249].

In UiO-67_NH_2 compounds, the addition of another aromatic cycle and the –NH_2 functionalization of the linker lead to the broadening of the absorption bands (Figure 3.5), which changes from 200-320 nm in UiO-66 to 200-450 nm in UiO-67_NH_2, with a tail that continues up to 600 nm. This feature was related to the enrichment of the valence band DOS caused by the presence of the amino group and of the extra aromatic cycle [249]. However, this aspect does not cause an alteration of the CTC upon excitation when compared to UiO-66, as both materials exhibit a LBT [27,249,250]. In fact, the PDOS calculated for UiO-67(Zr) and UiO-67(Hf) reveals that the VBM and CBM are located on the organic linker, mainly in the *p*-orbitals of carbon and oxygen atoms. Upon addition of –NH_2, this behavior is not expected to change even with the presence of the nitrogen *p*-orbitals and therefore, the position of the VBM and CBM bands is still assumed to be bound to the organic linker [250].

Finally, the spectrum of MIL-125(Ti) shows an absorption band extending from 200 to 350 nm, which is consistent with other reports from the literature (Figure 3.5) [202,246,251]. The maximum absorption is observed at 240 nm with a shoulder at 300 nm, similar to that found for UiO-66(Zr) [13,27]. Nevertheless, studies have shown that the charge transfer in MIL-125(Ti) is not similar to that of UiO-66 materials [246]. Indeed, the π–π stacking – which is observed in the UiO-66 compounds and enables the LBT complex in such materials – is not possible in MIL-125(Ti) due to the long distance between its BDC linkers, which are about 7 Å apart [246,252]. That being said, the absorption signal in the UV-vis spectra of MIL-125(Ti) was ascribed to the octahedral coordination in titanium species [251,253]. In fact, Hendon *et al.* [202] demonstrated that a LMCT is present in MIL-125(Ti) (contrary to UiO-66 materials, which exhibits LBT complexes). Actually, the valence band of MIL-125(Ti) was found to be mainly composed of BDC aromatic *2p*-orbitals, whereas the conduction band is related to titanium *d*-orbitals and oxygen *p*-orbitals [202]. The same behavior was verified by Dan-Hardi *et al.* [26], who observed that the photogenerated electrons in MIL-125(Ti) are trapped by the Ti^{4+} cations, forming Ti^{3+}.

When introducing the –NH_2 in MIL-125(Ti), the spectrum of the formed MIL-125(Ti)_NH_2 compound exhibited significant broadening of the absorption band, up to 500 nm. This feature was also in accord with other reports from the literature [202,251,254]. In this case, the spectrum seems to be composed of two contributions: the first one is analogous to that of MIL-125(Ti), and the second one is characterized by an absorption band with a maximum value at 377 nm [202,251,254,255]. Likewise, the absorption band in MIL-125(Ti)_NH_2 was related to the LMCT between the NH_2-BDC linker and the inorganic oxo/hydroxo cluster [202,251,254,255].

Previous studies have also shown that the charge separation in the amino-functionalized MIL-125(Ti)_NH_2 can stabilize the electrons in the titanium inorganic cluster, while the holes are trapped by the organic linker (either on the carboxylate or on the amino groups) [256,257]. In fact, it was demonstrated that the –NH_2 group can act as an "antenna" that stabilizes the holes, which prolongs the lifetime of the photoexcited state when compared to that of MIL-125(Ti) compound [256]. This phenomenon suggests that the LMCT must take place between the N or O atoms into Ti^{4+} cations [258]. In an analogous way to that observed for the UiO-6*x* (*x* = 6 or 7) family, other previous works have proven that the amino functionalization can rise up the VB energy in MIL-125(Ti)_NH_2 materials by introducing mid-gap states related to the –NH_2 groups [249,258,259]. This behavior was explained by the strong electron donor character of aromatic amines, even though they have no influence over the CB positions [258].

3.5.2. Band gap evaluation: Cody, Tauc, and direct/indirect methods

When evaluating the UV-vis spectra of different semiconductors, it is common to come across materials that exhibit a sub-band gap energy – especially in the case of defected, doped, bulk or surface modified materials. These modifications create intra-band gap states that reflect in their absorption spectra by forming an Urbach-like tail, which influences the band gap assessment by different methods [222]. In these cases, the curves need a baseline correction before being evaluated at the *x*-axis intercept point, as discussed before by Makuła, Pacia, and Macyk [222]. This conclusion was reached by studying a dye modified TiO_2 semiconductor, where the system was measured by placing barium sulfate mixtures grounded separately with titania and methyl orange [222]. In a first step, these mixtures were placed side by side in the holder and then, in a second step, they were mixed and evaluated in a system where both components can interact. In this last case, the authors showed that the resulting spectrum is not a simple sum of the individual spectra, but a linear combination of both [222]. This result can be extrapolated to hybrid materials as their different components (in this case, the inorganic clusters, and the organic linkers) can lead to a spectrum whose contributions cannot be fully resolved. Hence, a pre-treatment must be conducted in the cases where the compound presents a pre-absorption edge, as represented in Figure 3.6. Here, the Tauc plots obtained from UiO-67(Zr)_NH_2 absorption band exhibit a linear region when considering both indirect (Figure 3.6a) and direct (Figure 3.6b) band gaps. However, to guarantee a better fitting of the Tauc function, it should be noted that a baseline correction is required before the extrapolation of the

curve in the case of indirect band gap. This correction is also needed for the Cody band gap and for the direct [$F(R)^2$] and indirect [$F(R)^{1/2}$] methods.

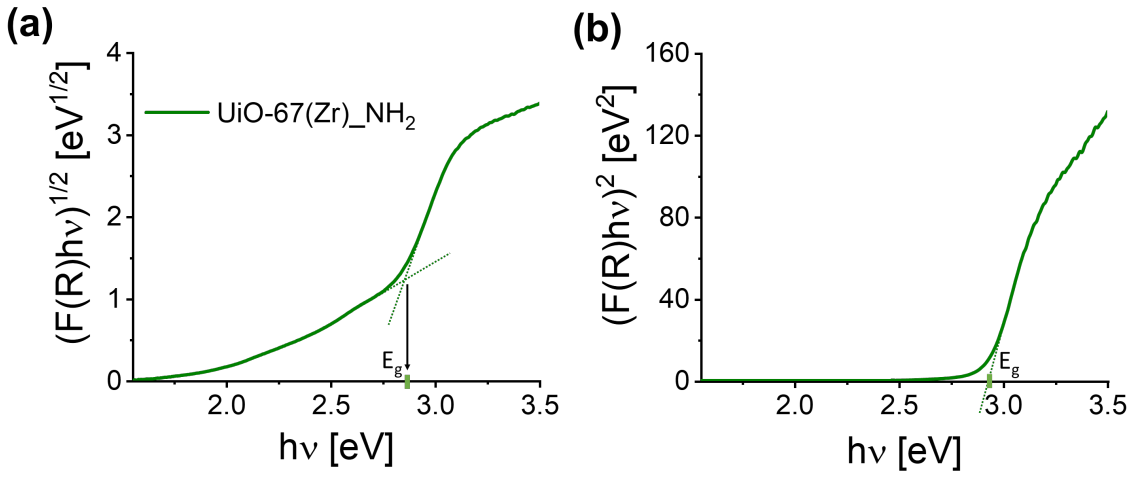

Figure 3.6: Demonstration of how to assess the band gap value using the extrapolation of the curve obtained from the absorption band recorded for UiO-67(Zr)_NH_2. (a) indirect band gap with baseline correction; (b) direct band gap without baseline correction.

To determine if a compound has a direct or an indirect band gap in the absence of calculations, it is recommended to plot both the direct and indirect band gaps as a function of the photon energy. The plot exhibiting a clear linear region should be considered as the best fitting and therefore, is presumed to be the correct band gap type [206]. Optical absorption spectra may also report if a material displays a direct or an indirect gap. In direct gaps, there is a sudden step rise in absorption (see spectra of UiO-66 compounds in Figure 3.5), whereas for indirect gaps there is first a small gradual rise in a frequency range followed by a sudden rise in absorption (see spectra of MIL-125(Ti)_NH_2 in Figure 3.5) [260]. In this last case, the frequency at which the absorption coefficient starts rising gradually is the measure of the indirect gap [260]. However, this determination is not as simple as it seems. For instance, the electronic structure of the UiO-66 compound has been deeply evaluated in different works and it was concluded the presence of a direct band gap for UiO-66(Zr) [250,261]. This observation was further confirmed by Yasin *et al.* [249], who found by DFT calculations and experiments that substituting zirconium by hafnium in UiO-66 does not change the band gap type, which is direct regardless the metal. Still, it is possible to find several studies that consider the UiO-66 materials as presenting an indirect band gap [262,263]. These controversies are especially common in the realm

of MOFs, since most of these compounds exhibit linear regions regardless the type of plot (direct or indirect) that is considered (Figure 3.7).

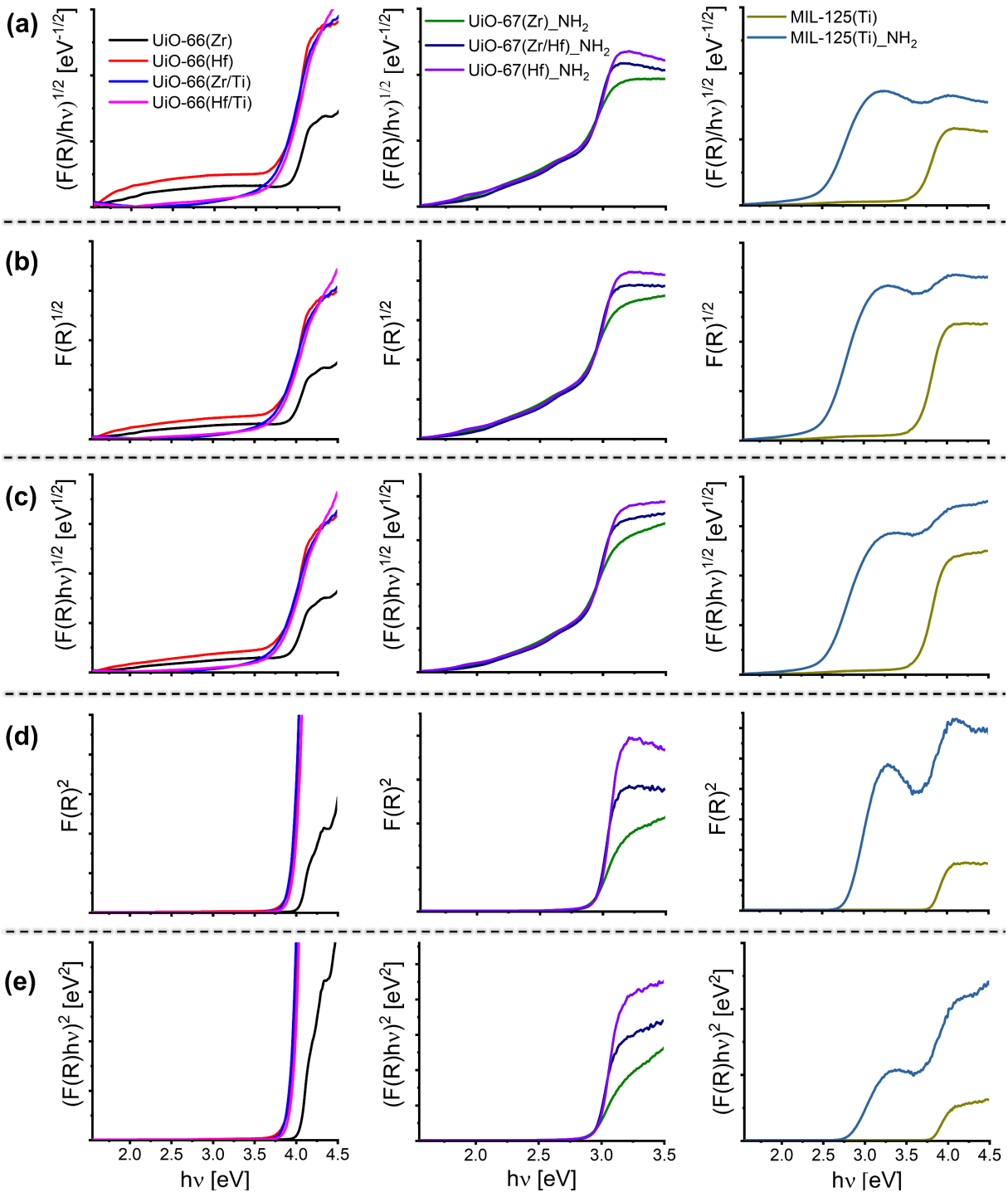

Figure 3.7: Band gap energies assessment using the Kubelka-Munk function for UiO-66, UiO-67_NH_2, and MIL-125 materials. (a) Cody band gap; (b) indirect band gap; (c) Tauc indirect band gap; (d) direct band gap; (e) Tauc direct band gap.

This feature demonstrates the necessity to consolidate a method to determine if a material has a direct or an indirect band gap only by means of experiments. Aiming to address this issue, the band gap energies of the MOFs synthesized here were assessed using different approaches by means of the Kubelka-Munk function (Table 3.2 and Figure 3.7).

Table 3.2: Band gap values (eV) assessed through the plot of R, F(R), $(F(R)/h\nu)^{1/2}$, $F(R)^{1/2}$, $(F(R)h\nu)^{1/2}$, $F(R)^2$, and $(F(R)h\nu)^2$ against the photon energy hν.

Method	UiO-66				UiO-67_NH_2			MIL-125	
	Zr	Hf	Zr/Ti	Hf/Ti	Zr	Zr/Hf	Hf	H	NH_2
R	4.20	4.14	4.09	3.97	3.08	3.04	3.08	3.88	3.00
F(R)	3.98	3.93	3.89	3.94	2.83	2.88	2.90	3.75	2.69
$(F(R)/h\nu)^{1/2}$	3.95	3.88	3.74	3.74	2.84	2.89	2.92	3.67	2.54
$F(R)^{1/2}$	3.96	3.89	3.78	3.79	2.85	2.92	2.90	3.67	2.52
$(F(R)h\nu)^{1/2}$	3.96	3.90	3.79	3.82	2.85	2.91	2.92	3.67	2.53
$F(R)^2$	4.05	4.04	4.00	4.04	2.92	2.95	2.98	3.82	2.80
$(F(R)h\nu)^2$	4.06	4.03	4.02	4.05	2.93	2.96	2.98	3.81	2.80

It is reasonable to assume that the first electronic transition observed in a UV-vis spectrum starting from lower to higher energies (in other words, from higher to lower wavelengths) corresponds to the HOCO – LUCO transition in crystalline materials [27]. For this reason, it is possible to extrapolate the tangent line to the absorption band edge until it intercepts the abscissa axis and then, transform the wavelength value to electron-volts to find the E_g value for the material. This result is highlighted in Table 3.2 as F(R) method ($E_{g[F(R)]}$). This approach was conducted elsewhere for MIL-100(Al), and the band gap type was found to be indirect due to the proximity between the $E_{g[F(R)]}$ and the $E_{g(ind)}$ values [108]. In MOF systems, this is a more accurate approach than the others presented before, as it relies only on the experimental data and not on partial assumptions (i.e., the best linearity or different step rise in absorption UV-vis data). Interestingly, these $E_{g[F(R)]}$ values are in between the indirect and the direct band gaps values for all the compounds studied here (i.e., $E_{g[F(R)]\_MIL\text{-}125(Ti)}$ = 3.75 eV, $E_{g(dir)\_MIL\text{-}125(Ti)}$ = 3.67 eV and $E_{g(ind)\_MIL\text{-}125(Ti)}$ = 3.82 eV) [250]. This finding may indicate that $E_{g[F(R)]}$ provides an "average" energy value for the optical band gap, considering the probability of both direct and indirect transitions to occur, as discussed in section 3.2.

When considering the band gap for UiO-66 samples, all methods end up generating plots with linear regions between 3.5 and 4.5 eV. The values obtained using the Cody, the indirect,

and the Tauc indirect methods exhibit a pre-absorption edge and therefore, must be corrected by a baseline – which is also the case for UiO-67_NH_2 and MIL-125 compounds (Figure 3.7). As mentioned before, some works in the literature consider that UiO-66 exhibits a direct band gap, while others assume that it behaves as an indirect semiconductor. Indeed, the Tauc direct band gap value for UiO-66(Zr) (4.06 eV, see Table 3.2) matches to that obtained from DFT simulations (4.07 eV) [250] and also from experimental data (4.07 eV) from other works [264]. On the other hand, the UiO-66(Zr) Tauc indirect band gap (3.96 eV, see Table 3.2) is also similar to that found through experimental UV-Vis data elsewhere [263].

Other works already demonstrated that the presence of hafnium and/or titanium reduce the band gap of the UiO-66 materials [13,262]. However, in their presence, DFT simulations are not as accurate as for the zirconium-based material. In fact, the Tauc direct E_g found for the hafnium-based UiO-66(Hf) using computational data (3.74 eV) [250] is smaller than that obtained from diffuse reflectance UV-Vis spectroscopy in this work (4.03 eV) and also in previous studies [13]. This feature demonstrates how theoretical band gaps can considerably differ from experimental data in many compounds. For instance, the predicted band gap value for a 100 at.% titanium-based UiO-66(Ti) was found to be 3.64 eV [250], which is smaller than the energies obtained in this study using the Tauc method considering an indirect band gap: UiO-66(Zr/Ti) = 3.79 eV and UiO-66(Hf/Ti) = 3.82 eV. Other works also reported similar experimental values for the band gap of UiO-66(Zr/Ti) [263].

UiO-67 is another compound that has been found as direct or indirect semiconductor in different studies [265,266]. It is also a good example of how the Tauc plot can provide a different evaluation of the band gap than other methods. For example, if the baseline correction is not applied to the indirect Tauc plot data[265], the band gap is found to be around 2.0 eV for UiO-67, which is very different from the predicted value using computational simulation (~ 3.7 eV) [250,267] and also from the experimental one (3.68 eV) [268]. Wang *et al.* [269] assessed the experimental band gaps for a series of zirconium-based UiO-6*x*_NH_2 (x = 6, 7, or 8) and using the Tauc plot found a direct band gap of 2.76 eV for UiO-67(Zr)_NH_2, which is close to the value obtained here (2.93 eV, see Table 3.2). Contrary to what was observed for UiO-66 [13], the presence of hafnium does not have a great influence on the calculated band gap values for the UiO-67_NH_2 samples, which can even increase from 2.93 to 2.98 eV when replacing zirconium by hafnium (Table 3.2). This different behavior is ascribed to a change on the valence band electronic states caused by the presence of the amino group [249]. In fact, replacing Zr by

Hf cations can increase the value of the VBM by adding energy states in the conduction band of UiO-66, which are related to oxygen atoms [249]. However, this effect is not observed in UiO-67_NH_2 because the amino group creates mid-gap states that influences the band gap energies, reducing the influence of the metal on the VBM position. This feature was highlighted by Yasin *et al.* [249] through the plot of the PDOS of the molecular orbitals for UiO-66 and UiO-66_NH_2 considering both zirconium and hafnium metals.

Finally, the MIL-125(Ti) has an indirect Tauc band gap that reduces from 3.67 to 2.53 eV after the amino functionalization (Table 3.2). This result is comparable to that obtained elsewhere [202] and should be related to the same phenomenon as in the case of functionalizing UiO-6*x* samples (*x* = 6 or 7) with –NH_2 groups. Here, it is clear that the direct and indirect Tauc band gaps are quite similar for both MIL-125 ($E_{g(ind)\_MIL\text{-}125(Ti)}$ = 3.67 eV, $E_{g(dir)\_MIL\text{-}125(Ti)}$ = 3.81 eV) and its amino functionalized version ($E_{g(ind)\_MIL\text{-}125(Ti)\_NH2}$ = 2.53 eV, $E_{g(dir)\_MIL\text{-}125(Ti)\_NH2}$ = 2.80 eV). Moreover, the E_g value obtained directly from the Kubelka-Munk UV-Vis spectrum is in between both these direct and indirect values: 3.75 and 2.69 eV for MIL-125(Ti) and MIL-125(Ti)_NH_2, respectively. For this reason, both values should be acquired and mentioned when describing the electronic structure of such materials, as discussed before [216].

The *log(1/R)* data was also applied to access the band gap energies for the different MOFs and the results demonstrate linear regions in which the E_g values can be properly extracted (Figure A23). However, the obtained results seem to be less accurate when compared to those reported in the literature for all MOFs samples (Table A1) [202,250,262,263,267–269]. This can be ascribed to the fact that most works dealing with powdered samples use the Kubelka-Munk model to acquire the UV-Vis spectra that is further analyzed to obtain the band gap of the samples. Also, it is clear that the edges of the absorption bands are better defined using the K-M approach than the *log(1/R)* data (Figure 3.5), which can be another source of error.

3.5.3. Band gap evaluation: the Boltzmann regression

A more recent method for assessing the band gap of semiconductor materials was proposed by Zanatta [206], which evaluated the reliability of the sigmoid-Boltzmann function represented in Equation (3.17) by fitting collected data from the $\alpha_{PV}(E)$ spectra (Table 3.1). Here, α_{max} and α_{min} are the maximum and minimum absorption coefficients, E_0^{Boltz} is the

energy coordinate (abscissa axis) in which the absorption coefficient is in halfway between α_{max} and α_{min}, and δE is related to the slope of the sigmoid curve.

$$\alpha(E) = \alpha_{max} + \frac{\alpha_{min} - \alpha_{max}}{1 + exp\left(\frac{E - E_0^{Boltz}}{\delta E}\right)} \quad (3.17)$$

It was suggested that the E_0^{Boltz} value can be understood as a central energy around which most optical transitions take place (depending on the nature of the band gaps and on the presence of disorders) [206]. For such reason, the band gap energy values should be presented by a Gaussian-like distribution with average energy E_0^{Boltz}, standard deviation ∂E, and Boltzmann factor n_{type}, according to Equation (3.18). n_{type} is obtained from the histogram corresponding to an extensive data collection considering standard deviations of 0.1 or 0.2 and is highly influenced by the type of transition exhibited by the material [206].

$$E_g^{Boltz} = E_0^{Boltz} - n_{type} \times \partial E \quad (3.18)$$

Following this reasoning, the fitting of the Boltzmann function was applied to the Kubelka-Munk (Figure 3.8) and also to the log(*1/R*) data (Figure A24) of the different compounds synthesized in this work. When using the Kubelka-Munk function, the obtained correlation coefficients (R^2) values for the Boltzmann regression are all above 0.99, showing the good agreement between the experimental K-M data and the empirical method. However, the fit of the Boltzmann regression for the log(*1/R*) data exhibited lower coefficient of correlation for most compounds, which is ascribed to the inferior accuracy of this approach when dealing with diffuse reflectance UV-Vis data.

After fitting the diffuse reflectance UV-Vis data using the Boltzmann function, the E_0^{Boltz} was obtained for each compound considering the Kubelka-Munk function (Table 3.3) and the log(*1/R*) data (Table A7). In its original work, Zanatta [206] verified that the value obtained for E_0^{Boltz} is independent of the applied methodology for assessing the absorption coefficient $\alpha(E)$ – i.e., $\alpha_{BLB}(E)$, $\alpha_P(E)$, $\alpha_{PV}(E)$ – revealing that it should be also unaffected by measurements or data treatment details such as different spectra correction. This result was found to be inaccurate in the case of MOFs, as the E_0^{Boltz} values obtained from the Kubelka-Munk differ from those found using the log(*1/R*) approach (Table 3.3 and Table A7).

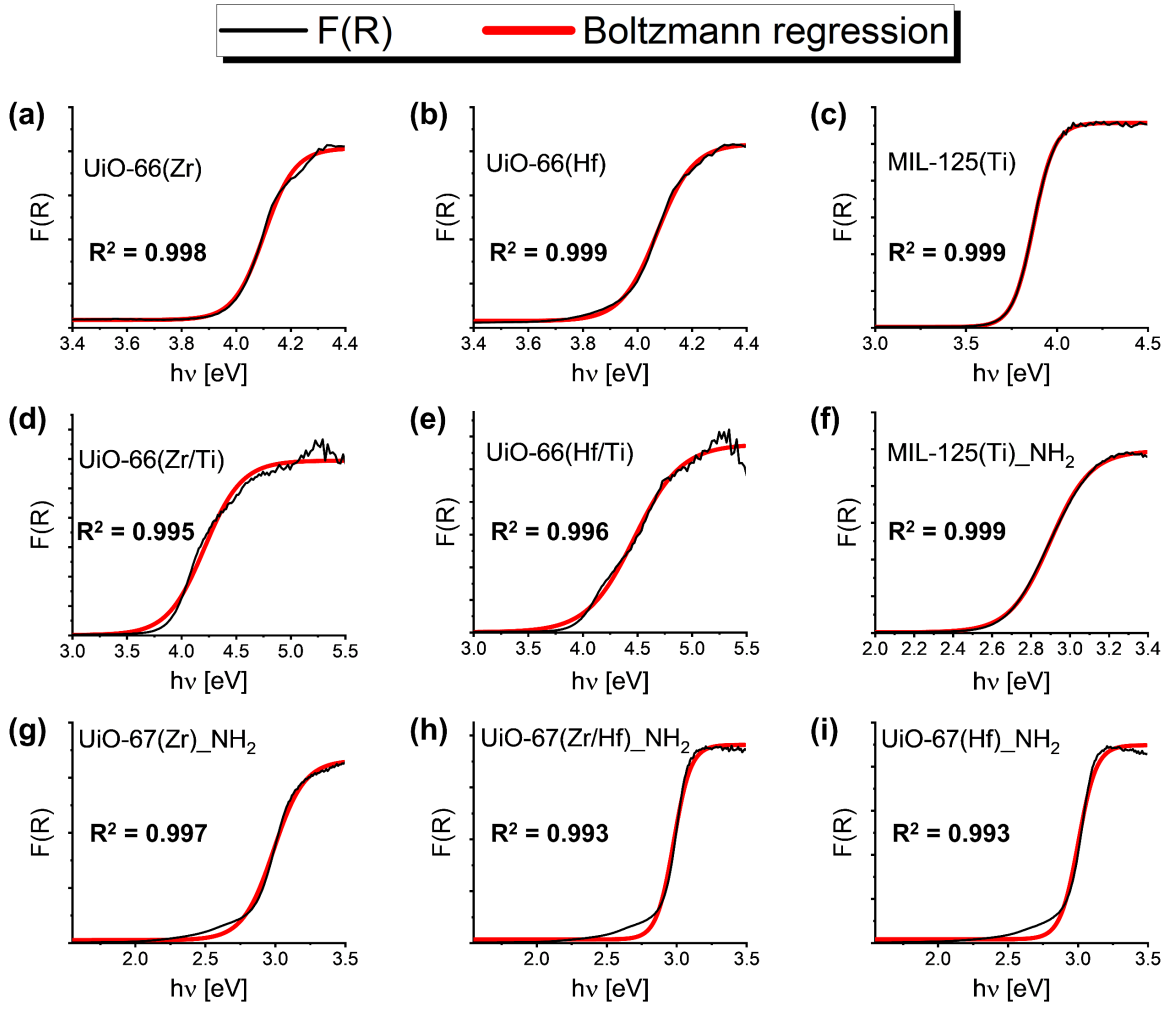

Figure 3.8: Optical band gap energies calculated using the Boltzmann regression according to the Equation (3.17) by means of the Kubelka-Munk data for (a) UiO-66(Zr), (b) UiO-66(Hf), (c) MIL-125(Ti), (d) UiO-66(Zr/Ti), (e) UiO-66(Hf/Ti), (f) MIL-125(Ti)_NH_2, (g) UiO-67(Zr)_NH_2, (h) UiO-67(Zr/Hf)_NH_2, and (i) UiO-67(Hf)_NH_2. The black lines represent the Kubelka-Munk (F(R)) data obtained for the MOFs and the red lines are the Boltzmann regression.

Table 3.3: Band gap energies (eV) calculated from Equation (3.18) considering the E_0^{Boltz} values obtained from the K-M function and using $n_{dir}^{Boltz} \approx 0.9$ and $n_{ind}^{Boltz} \approx 3.5$.

Method	UiO-66				UiO-67_NH_2			MIL-125	
	Zr	Hf	Zr/Ti	Hf/Ti	Zr	Zr/Hf	Hf	H	NH_2
E_0^{Boltz}	4.11	4.07	4.18	4.49	2.99	2.98	3.01	3.87	2.90
δE	0.056	0.067	0.171	0.215	0.111	0.061	0.065	0.058	0.103
$E_{g(dir)}^{Boltz}$	4.06	4.01	4.03	4.30	2.89	2.93	2.95	3.82	2.81
$E_{g(ind)}^{Boltz}$	3.91	3.84	3.58	3.74	2.61	2.77	2.78	3.67	2.54

The band gap energies obtained by the different methods for all the MOFs investigated can be separated into groups with similar values depending on the type of the transition (Figure 3.9 and Figure A25). Note that the energies obtained by the Cody band gap were always closer to the indirect band gap energies (when comparing to the indirect Tauc method), and the raw diffuse reflectance data (*R*) overestimated the E_g values in most cases. Also, the direct and indirect band gaps are closer in the case of UiO-67_NH_2 when comparing to the other compounds. The E_0^{Boltz} energies evaluated using the K-M data were also overestimated and are closer to the direct band gap energies for all the compounds, as demonstrated in Figure 3.9. This parameter was also preserved for most of the compounds when using the *log(1/R)* data with the exception of the UiO-67_NH_2 materials (Figure A25). This is ascribed to the worse fit of the Boltzmann function, as verified by the inferior correlation coefficient in these cases (Figure A24). Finally, in order to verify if the gap in these MOF systems can be evaluated similarly to other semiconductors as proposed by Zanatta [206], the $E_{g(dir)}^{Boltz}$ and $E_{g(ind)}^{Boltz}$ values were calculated according to the Equation (3.18). The empiric n^{Boltz} values were obtained from a large data collection considering powdered samples with direct ($n_{dir}^{Boltz} \approx 0.9$) and indirect ($n_{ind}^{Boltz} \approx 3.5$) band gaps [206]. The δE values were extracted from the fitting of the Boltzmann function to the experimental data. The obtained values are displayed in Table 3.3 and Table A7.

When analyzing the calculated $E_{g(dir)}^{Boltz}$ and $E_{g(ind)}^{Boltz}$ and comparing them to the other methods, four different scenarios were identified. In the first one, there is a match only between the $E_{g(dir)}^{Boltz}$ values and the direct band gaps – i.e., UiO-66(Zr), UiO-66(Hf), and UiO-66(Zr/Ti). In the second case, only the $E_{g(ind)}^{Boltz}$ corresponds to the experimental values, as for the UiO-66(Hf/Ti) material. In the third situation, none of the groups matches the Boltzmann regression, but the $E_{g(dir)}^{Boltz}$ lies in between the two regions (direct and indirect), as observed for the entire UiO-67_NH_2 series. Finally, in the fourth scenario, for MIL-125(Ti) and MIL-125(Ti)_NH_2 compounds, both the $E_{g(dir)}^{Boltz}$ and $E_{g(ind)}^{Boltz}$ are close to the direct and indirect band gap regions, respectively. These different behaviors provide first evidence for determining the type of optical transition exhibited by these materials.

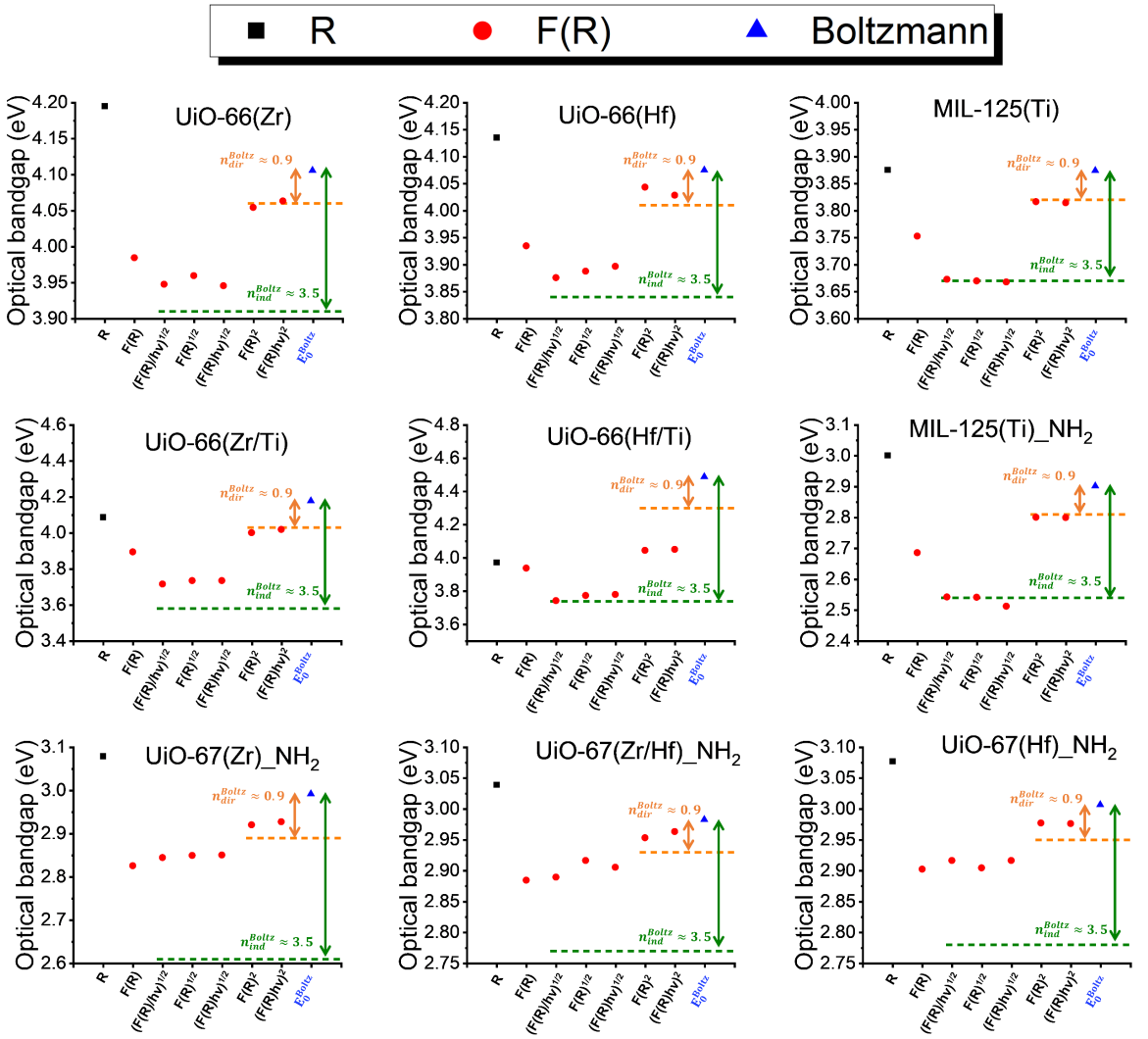

Figure 3.9: Optical band gap energies obtained using different methods: extrapolation of the reflectance curve (R), extrapolation of the Kubelka-Munk curve F(R), Cody's band gap [$(F(R)/h\nu)^{1/2}$], indirect band gap [$(F(R)^{1/2}$], Tauc indirect band gap [$(F(R)h\nu)^{1/2}$], direct band gap [$F(R)^2$], Tauc direct band gap [$(F(R)h\nu)^2$], and Boltzmann fit of the F(R) spectra E_0^{Boltz}. The horizontal lines represent values obtained for the $E_{g(dir)}^{Boltz}$ (orange) and for the $E_{g(ind)}^{Boltz}$ (green) when considering $n_{dir}^{Boltz} = 0.9$ and $n_{ind}^{Boltz} = 3.5$, respectively. The vertical arrows represent the distance between E_0^{Boltz} and $E_{g(dir)}^{Boltz}$ (orange) and $E_{g(ind)}^{Boltz}$ (green).

For instance, in the case of the UiO-66(Zr) and UiO-66(Hf), the proximity of the $E_{g(dir)}^{Boltz}$ energies to those obtained by using the $F(R)^2$ and $(F(R)h\nu)^2$ plots (Figure 3.9) supports the statement that UiO-66(M) (M = Zr or Hf) has a direct band gap, which is consistent with other reports and computational simulations [250,264]. Then, after introducing titanium, the values acquired for the UiO-66(Zr/Ti) direct band gap follow better the Boltzmann regression (Figure 3.9), even though the indirect values are closer to that reported in the literature [250]. This discrepancy is ascribed to the use of the Tauc plot (with different *n* coefficients: $n = 2$ or $n = ½$) without a previous consideration of the band gap transition type, which highlights the

importance of obtaining such information from experimental data. On the other hand, the presence of titanium in UiO-66(Hf/Ti) seems to modify the type of band gap observed for the UiO-66 materials from direct to indirect. In fact, there is a better agreement between the $E_{g(ind)}^{Boltz}$ and the $(F(R)h\nu)^{1/2}$ plot for this compound, inferring that the Ti-doping can alter the band gap type observed for the UiO-66 materials from direct to indirect in some cases, as mentioned before [262,263]. Similarly, when considering the UiO-67_NH_2 compounds, the $E_{g(dir)}^{Boltz}$ was found to be closer to the values obtained for direct band gaps, which is also a signal that these materials exhibit direct electronic transition upon excitation. Finally, for MIL-125(Ti) and MIL-125(Ti)_NH_2, both the $E_{g(dir)}^{Boltz}$ and the $E_{g(ind)}^{Boltz}$ values agree with the energies obtained from other methods. MIL-125(Ti) exhibited an $E_{g(dir)}^{Boltz}$ = 3.85 eV that compares to $E_{g(dir)}^{Tauc}$ = 3.81 eV, and $E_{g(ind)}^{Boltz}$ = 3.62 eV compares to $E_{g(ind)}^{Tauc}$ = 3.67 eV; whereas MIL-125(Ti)_NH_2 presented an $E_{g(dir)}^{Boltz}$ = 2.87 eV while $E_{g(dir)}^{Tauc}$ = 2.80 eV, and $E_{g(ind)}^{Boltz}$ = 2.46 eV while $E_{g(ind)}^{Tauc}$ = 2.53 eV. Therefore, it is not possible to infer whether these materials present a direct or indirect band gap based only on the energies obtained by the Boltzmann regression, which accentuates the necessity to acquire both values in this case.

3.5.4. Band gap evaluation: complex dielectric function and the Kramers-Kronig transformation

The band gap assessment by the different methods presented above (Tauc, Cody, and Boltzmann) takes into consideration the density of states of the material and relies on some assumptions [270,271]. For instance, the Cody band gap considers that the dipole elements in the optical matrix are independent of the photon energy [223]. On the other hand, the Tauc model considers that the momentum is independent of the photon energy in the adsorption edge [272], which provides information about the E_g. However, there is another method (Kramers-Kronig) that uses a dielectric transformation, where the optical constants – refractive index (n), extinction coefficient (κ), and reflectivity (R) – are expressed as functions of the real and imaginary parts of the complex dielectric function (ε), as represented in Equation (3.19) [273].

$$\varepsilon_{complex} = \varepsilon_{real} - i\varepsilon_{imaginary} \quad (3.19)$$

In this case, because the bulk material is spatially independent, it is possible to compare the values obtained to those of classical dipole oscillator models [272,274]. In fact, several attempts

to correlate empirical data between band gap energies and resonance frequency of oscillators can be found in the literature [275,276]. For instance, T. S. Moss [276] related the refractive index to the band gap energy and was able to fit an empirical law for an enormous range of materials. Other variations of the model were also discussed in the literature, as it is the case of the Ravindra and Reddy's relationships [277]. In this case, a relationship between the band gap and the refractive index was proposed for semiconductors. It can also be mentioned the atomic approach of Moss [276], the nearly free electron model of Penn [278], the oscillator concept of Wemple [279], and the optical polarizability approach of Finkenrath [275]. Finally, Hervé and Vandamme [274] further expanded the Penn model based on covalent and ionic bonds within the semiconductor material, creating a mathematical basis for the above mentioned models.

The real and imaginary parts of the dielectric function allow the determination of the macroscopic optical parameters (such as reflectivity, absorption coefficient, refractive index, and penetration depth) [112]. They can be related to the extinction coefficient (κ) and the refractive index (n), which are functions of the frequency ν – according to the Equations (3.20) and (3.21).

$$\varepsilon_{\text{real}} = \text{n}(\nu)^2 - \kappa(\nu)^2 \tag{3.20}$$

$$\varepsilon_{\text{imaginary}} = 2\text{n}(\nu)\kappa(\nu) \tag{3.21}$$

In order to describe the spatial independence, the complex transformation of the dielectric function is conducted in a polar coordinate system. It is then possible to express the Penn model with only two parameters with spatial independence (i.e., an infinite inhomogeneous medium), as in Equation [280].

$$\Phi = tan^{-1}\left(\frac{\varepsilon_{imaginary}}{\varepsilon_{real}}\right) = tan^{-1}\left(\frac{2n(\nu)\kappa(\nu)}{n(\nu)^2 - \kappa(\nu)^2}\right) \tag{3.22}$$

The Kramers-Kronig [281,282] transformation (K-K transformation) is of an extremely importance at this point, as it can be used to obtain the extinction coefficient (κ) and the refractive index (n) of the material through diffuse reflectance spectra, as highlighted in Equations (3.23) and (3.24) [283]. Here, R is the diffuse reflectance data (normalized from 0 to 1).

$$n(\nu) = \frac{1 - R(\nu)}{1 + R(\nu) - 2cos\theta(\nu)\sqrt{R(\nu)}} \tag{3.23}$$

$$\kappa(\nu) = \frac{-2sin\theta(\nu)\sqrt{R(\nu)}}{1 + R(\nu) - 2cos\theta(\nu)\sqrt{R(\nu)}} \tag{3.24}$$

In this case, the phase shift angle of the sample (θ) is given by Equation (3.25), where ν_m is the medium frequency on the range of the collected spectra [283].

$$\theta(\nu) = \frac{2\nu_m}{\pi} \int_0^\infty \frac{ln\sqrt{R(\nu)}}{\nu^2 - \nu_m^2} d\nu \tag{3.25}$$

The dispersion-dissipation – $\log(\varepsilon_{complex})$ and Φ – plotted against the photon energy ($h\nu$) characterizes the optical properties of the material since $n(\nu) - \kappa(\nu) \rightarrow 0$ in the region where $\Phi \rightarrow {}^{-\pi}/_{2}$ [283]. In fact, for semiconductor materials, the Φ vs ($h\nu$) plot exhibits a discontinuity and a 180º phase shift when $\Phi \rightarrow 90º$, as reported elsewhere [283]. This effect was attributed to a polarization effect in semiconductors and insulators [284]. The presence of discontinuities in the Φ vs ($h\nu$) plot for the MOF materials confirms therefore their semiconductor character (Figure 3.10).

Finally, combining Equations (3.20) to (3.25) and the Tauc method –Equation (3.6) – Equation (3.26) can be derived, which relates the band gap energies (E_g) to the refractive index $n(\nu)$ and to the photon energy $h\nu$. In this case, μ_0 is the vaccum permeability [283].

$$(h\nu)^{-1} = -\mu_0 n(\nu)^2 + (E_g)^{-1} \tag{3.26}$$

At this point, a plot of $(h\nu)^{-1}$ (the inverse of the photon energy [eV^{-1}]) in the y-axis versus $n(\nu)^2$ on the x-axis makes explicit a linear regime region which denotates the onset of absorption [283]. The extrapolation of this curve into the y-axis corresponds to the inverse of the band gap energy of the material $(E_g)^{-1}$, as demonstrated in Figure 3.11.

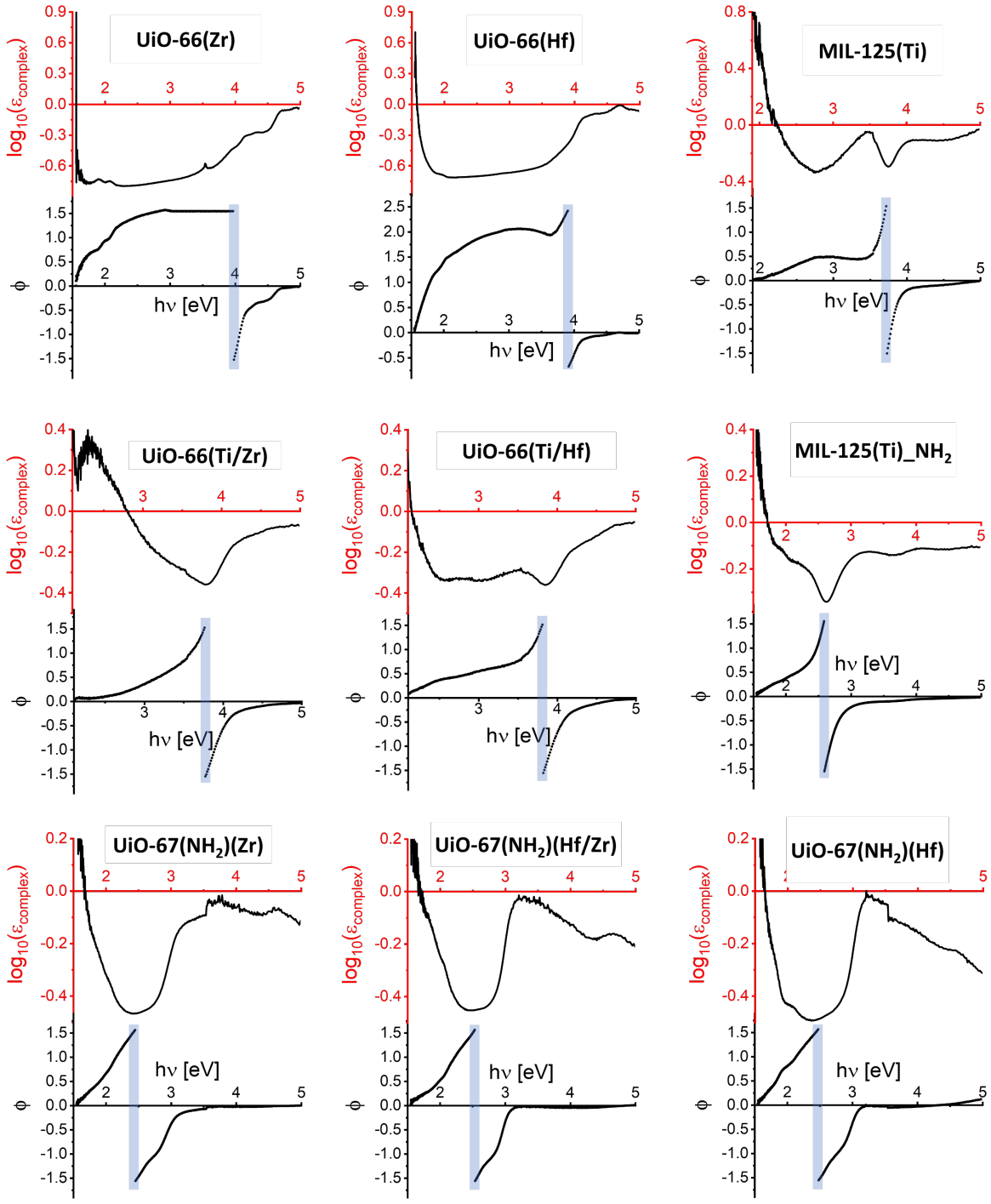

Figure 3.10: Dispersion-dissipation versus energy plots for UiO-66, UiO-67_NH_2 and MIL-125 materials. The absorption edge corresponding to the discontinuity at $\Phi \rightarrow 90^{o}$ is represented as a blue region.

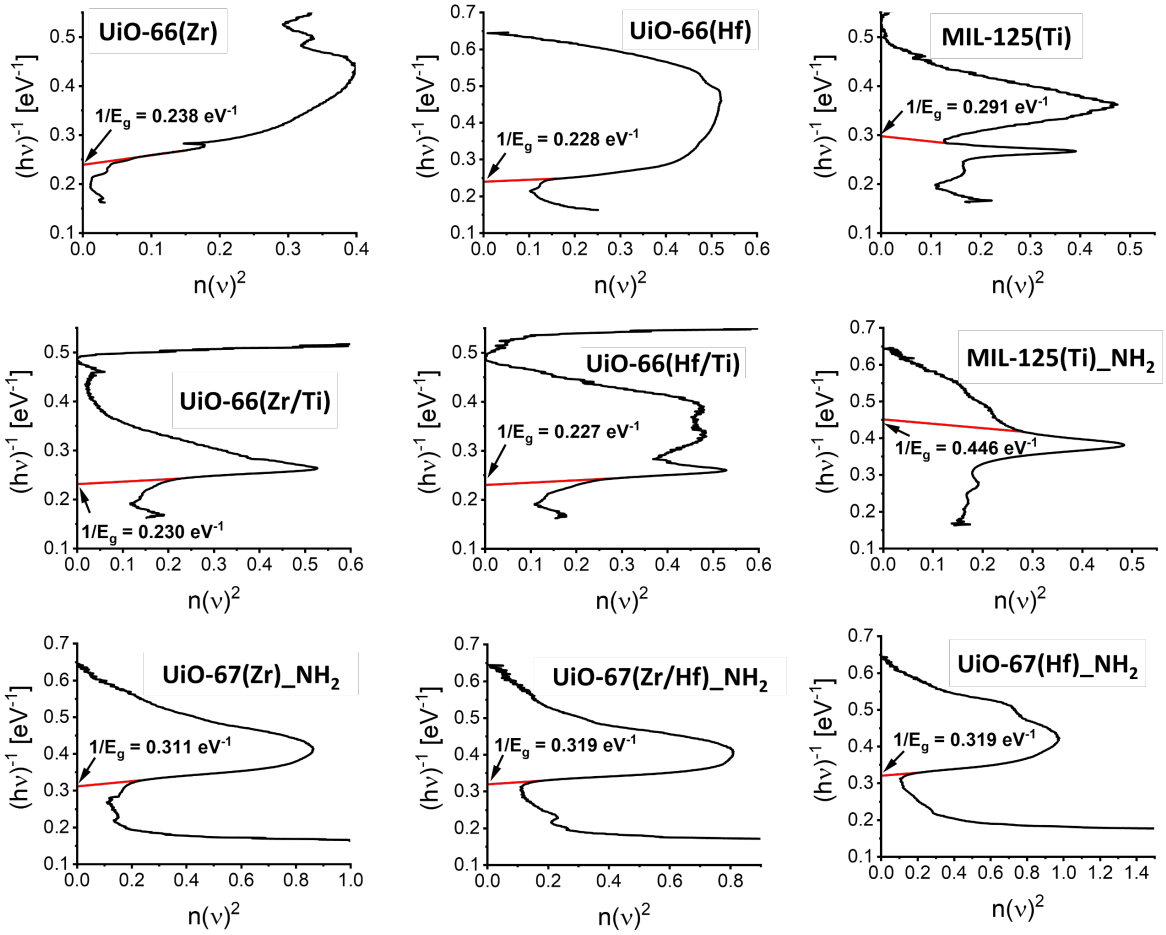

Figure 3.11: Band gap energies calculated for UiO-66, UiO-67_NH_2, and MIL-125 compounds by using the Kramers-Kronig transformation through the plot of $(h\nu)^{-1}$ versus $n(\nu)^2$. The red line highlights the position where the E_g^{-1} values were assessed. This line has a positive slope for direct band gaps and a negative slope for indirect band gaps.

The band gap values obtained through the K-K transformation (E_g^{K-K}) are shown in Table 3.4, alongside the average values for the direct (Tauc direct, Boltzmann direct, and pure direct) and indirect (Tauc indirect, Cody, Boltzmann indirect, and pure indirect) methods, and an error between the E_g^{K-K} and each band gap type (direct or indirect). Interesting information can be obtained when analyzing the band gap and the error values between the band gap energies obtained using the K-K transform and the average value from Tauc, Cody, and Boltzmann methods. First, the Kramers-Kronig approach overestimates the optical band gap for most compounds, except for MIL-125(Ti) and MIL-125(Ti)_NH_2.

Table 3.4: Band gap energies calculated using the Kramers-Kronig transformation, comparison with the average for direct and indirect values $\overline{E_g}$, and percentage of error between E_g^{K-K} and $\overline{E_g}$.

MOF	E_g^{K-K}	$\overline{E_g}$		$\left\|\frac{E_g^{K-K} - \overline{E_g}}{\overline{E_g}}\right\|$	
		Direct	Indirect	$\overline{E_g}$ direct	$\overline{E_g}$ indirect
	[eV]	[eV]	[eV]	[%]	[%]
UiO-66(Zr)	4.20	4.07	3.94	**3.2**	6.6
UiO-66(Hf)	4.39	4.04	3.86	**8.6**	13.7
UiO-66(Zr/Ti)	4.35	4.05	3.69	**7.4**	17.9
UiO-66(Hf/Ti)	4.41	4.17	3.73	**5.8**	18.2
UiO-67(Zr)_NH_2	3.22	2.93	2.76	**9.9**	16.7
UiO-67(Zr/Hf)_NH_2	3.13	2.96	2.86	**5.7**	9.4
UiO-67(Hf)_NH_2	3.13	2.98	2.87	**5.0**	9.1
MIL-125(Ti)	3.44	3.83	3.66	10.2	**6.0**
MIL-125(Ti)_NH_2	2.24	2.82	2.51	20.6	**10.8**

* Direct values were obtained considering the average between the Tauc direct, the pure direct, and the Boltzmann direct band gaps. Indirect values were obtained considering the average between the Cody, Tauc indirect, pure indirect, and Boltzmann indirect band gaps.

It is clear that the discrepancies observed are closely related to the type of transition, as the values of E_g^{K-K} and $\overline{E_g}$ can vary by up to an order of magnitude considering the same sample. In general, the E_g^{K-K} energies obtained for the UiO-6*x* series were closer to the average values of direct transitions, suggesting that this family of materials exhibits a direct band gap, in agreement with what was observed using the Boltzmann regression results (Figure 3.9 and Figure A25). However, UiO-66(Hf/Ti) is an exception. It appears to exhibit an indirect band gap when considering the proximity of the $E_{g(ind)}^{Boltz}$, but is closer to the direct average when considering the E_g^{K-K} (Table 3.2, Table 3.3, and Table 3.4). Finally, MIL-125(Ti) and MIL-125(Ti)_NH_2 shows a smaller error for the indirect band gap, indicating that this type of transition is favored in these materials. In contrast, using the Boltzmann regression, both direct and indirect band gaps assumptions are reasonable for these two materials.

At this point, it is worth mentioning that the use of the complex dielectric function to assess band gap energies of semiconductors must be applied carefully. In fact, since the method

considers the inverse plot of energy ($1/E_g$ against $n(\nu)^2$), any variation in the position of the interception line can impact enormously the results – i.e.: for $1/E_g = 0.40$ eV^{-1} → $E_g = 2.50$ eV; whereas $1/E_g = 0.43$ eV^{-1} → $E_g = 2.33$ eV. Moreover, there are several different regions that present a linear behavior when plotting $1/E_g$ against $n(\nu)^2$ (Figure 3.11). Therefore, there are several places where the tangent connecting the curve to the *y*-axis can be plotted (as in the Tauc plot for the tangent extrapolated to the *x*-axis, as discussed above), potentially favoring enormous error in the E_g determination using the K-K transform. Nevertheless, the method is very attractive to confirm the band gap type for different materials. It can confirm results from other methods, such as the Tauc plot (direct and indirect), the Cody (indirect), the pure direct, and the pure indirect approaches.

Finally, the average energy grouping the regions of direct (pure direct, and Tauc direct) and indirect (pure indirect, Tauc indirect, and Cody band gap) transitions were calculated using the Kubelka-Munk model and were compared to other methods (Boltzmann and Kramers-Kronig) for determining the optical band gap type of MOF (Table 3.5).

Table 3.5: Optical band gap transitions attributions (direct or indirect) considering the average energy values calculated from the Kubelka-Munk transformed UV-Vis spectra. Direct transitions considered for the average: "pure" direct and Tauc direct. Indirect transitions considered for the average: "pure" indirect, Tauc indirect, and Cody band gap. The values were compared to the energies calculated using the Boltzmann regression ($E_{g(dir)}^{Boltz}$ and $E_{g(ind)}^{Boltz}$) and the Kramers-Kronig (E_g^{K-K}) transformation.

MOF	$\overline{E_{g(dir)}}$ [eV]	$\overline{E_{g(ind)}}$ [eV]	$E_{g(dir)}^{Boltz}$ [eV]	$E_{g(ind)}^{Boltz}$ [eV]	Boltzmann attribution	E_g^{K-K} [eV]	K-K attribution	Conclusion
UiO-66(Zr)	4.06	3.96	**4.06**	3.91	Direct	4.20	Direct	Direct
UiO-66(Hf)	4.04	3.89	**4.01**	3.84	Direct	4.39	Direct	Direct
UiO-66(Zr/Ti)	4.01	3.77	**4.03**	3.58	Direct	4.35	Direct	Direct
UiO-66(Hf/Ti)	4.05	3.78	4.30	**3.74**	Indirect	4.41	Direct	Inconclusive
UiO-67(Zr)_NH_2	2.93	2.85	**2.89**	2.61	Direct	3.22	Direct	Direct
UiO-67(Zr/Hf)_NH_2	2.96	2.91	**2.93**	2.77	Direct	3.13	Direct	Direct
UiO-67(Hf)_NH_2	2.98	2.91	**2.95**	2.78	Direct	3.13	Direct	Direct
MIL-125(Ti)	3.82	3.67	**3.82**	**3.67**	Direct/indirect	3.44	Indirect	Indirect
MIL-125(Ti)_NH_2	2.80	2.53	**2.81**	**2.54**	Direct/indirect	2.24	Indirect	Indirect

Both Boltzmann and Kramers-Kronig attributions converge for most materials. In fact, the entire UiO-6*x* series is found to present direct band gap transitions, with the exception of UiO-66(Hf/Ti), where the analysis was inconclusive (Boltzmann: indirect; K-K: direct). In contrast, both transition types were assigned to MIL-125(Ti) and MIL-125(Ti)_NH_2 considering the Boltzmann regression, while the Kramers-Kronig model was closer to the average energies of the indirect optical band gap. Therefore, the interface between the two methods indicate that these materials exhibit indirect transitions. Finally, it is worth mentioning that the tangent line connecting the $(h\nu)^{-1}$ curve to the *y*-axis in the Kramers-Kronig plot has a negative slope for MIL-125(Ti) and MIL-125(Ti)_NH_2 (Figure 3.11). This slope is positive for all the other MOF compounds, indicating that it can also be a tool for determining the band gap transition type: for positive slopes, the band gap is direct; for negative slopes, the band gap is indirect.

3.6. Conclusions

This work evaluated the different methods to access the band gap of powdered and single-crystal MOF materials by means of diffuse reflectance UV-vis data. The results have been extensively compared to the literature. The Kubelka-Munk approach and the log(*1/R*) were individually considered when treating the diffuse reflectance data. The results demonstrate that, although the Kubelka-Munk method presents some constraints regarding high absorbent samples, it is more suitable than the log(*1/R*) approach because it provides spectra with sharper absorption edges, which facilitates the further interpretation and characterization of the band gaps. Several methods were applied to obtain the E_g values of the different materials, worth mentioning the band gap obtained directly from the diffuse reflectance data, from the Kubelka-Munk data, from the log(*1/R*) data, the Cody band gap $[(\alpha/h\nu)^{1/2}]$, the indirect band gap $(\alpha^{1/2})$, the Tauc indirect band gap $[(\alpha h\nu)^{1/2}]$, the direct band gap (α^2), the Tauc direct band gap $[(\alpha h\nu)^2]$, the Boltzmann band gap, and the Kramers-Kronig band gap. These different approaches were compared with both experimental and computational data from the literature and the limitations of some procedures were emphasized. The influence of pre-data treatment and baseline correction were also highlighted in cases where a pre-absorption edge is present, which can lead to a misevaluation of the band gap. Moreover, for some materials such as MIL-125(Ti) and MIL-125(Ti)_NH_2, the need of acquiring both the indirect and direct band gap values was also discussed. A comparative method was proposed for determining the type of band gap exhibited

by the different materials without needing computer simulations. Basically, the Boltzmann regression coupled to the Kramers-Kronig transformation offers a solid base for determining either if a material has a direct or an indirect gap by only comparing the obtained $E_{g(dir/ind)}^{Boltz}$ and E_g^{K-K} results with those from the other methodologies (i.e., Tauc direct and indirect band gaps). In other words, a complete methodology for determining band gap types by using diffuse reflectance UV-vis spectroscopy in powdered semiconductor materials is proposed (Figure 3.12). This work should contribute to determine band gaps more accurately, leading to more reliability in different areas of chemistry, physics, and materials engineering, where these gaps are of importance.

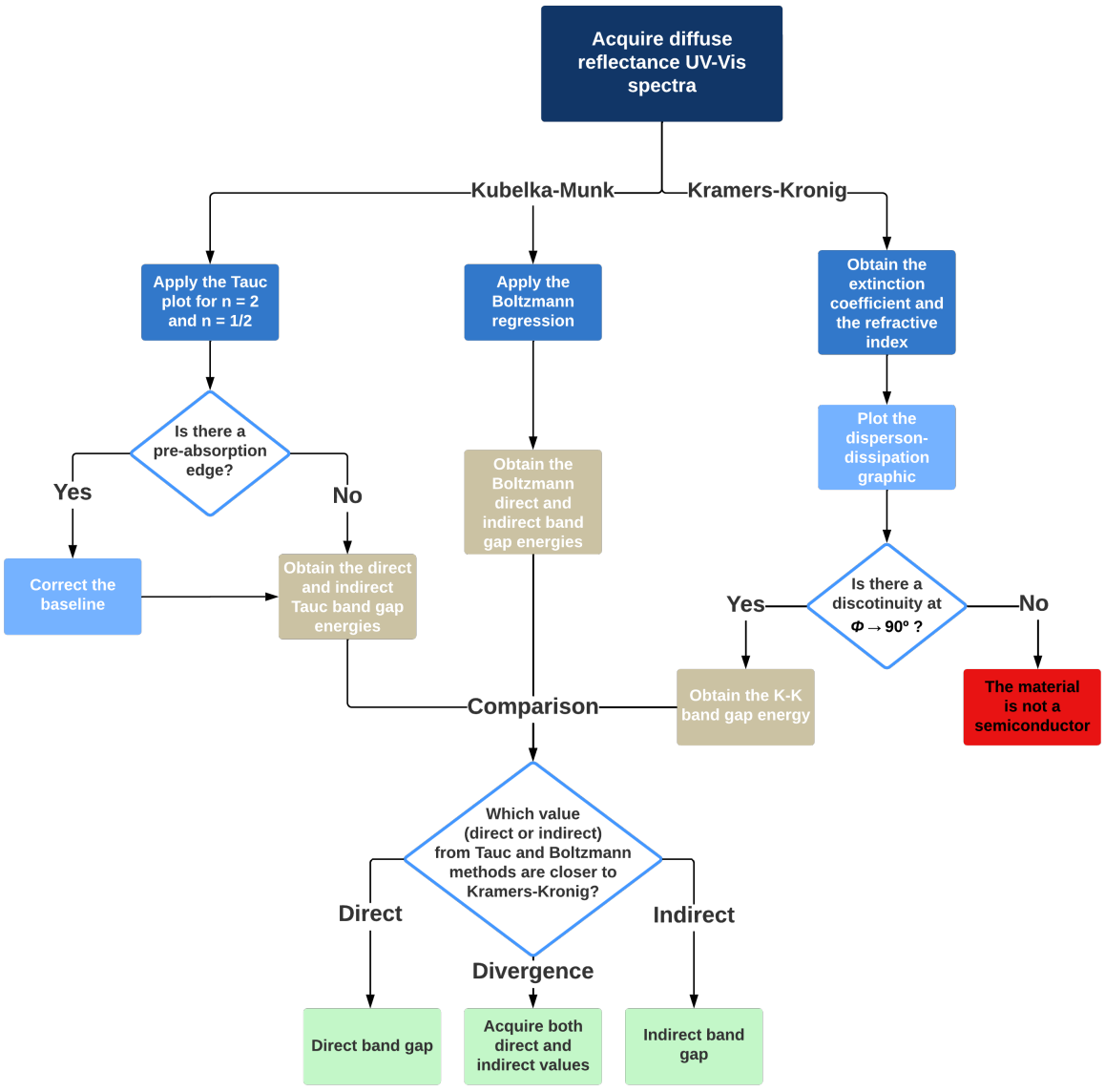

Figure 3.12: Flowchart demonstrating the methodology for determining whether a material has a direct or indirect band gap transition.

Chapter IV: Unraveling the Metal Influence Over the Iodine Evolution in UiO-66 Materials

4.1. Introduction

Zirconium-based MOFs are widely studied due to their high stability in severe chemical environments, such as acid and basic media [95]. One can cite the topology UiO-66, which is synthesized from the mixture of $ZrCl_4$ and 1,4-benzenedicarboxylic acid (H_2BDC, also known as terephthalic acid) in *N,N*-dimethylformamide solvent [264]. It presents a three-dimensional framework defining a face centered cubic unit that consists of inorganic $Zr_6O_4(OH)_4$ bricks, 12-fold connected to the lattice through the BDC linkers to the Zr-nodes [285]. A parent structure from UiO-66(Zr) is also reported in the literature and can be obtained by changing the metal precursor to $HfCl_4$ [286]. Finally, bimetallic UiO-66 materials were also reported elsewhere with composition variation $\{Zr_xHf_{6-x}\}$ for the inorganic core [287]. UiO-66(Hf) exhibits similar physical-chemical properties to those of UiO-66(Zr) since both metals – zirconium and hafnium – are part of the same group elements (column IV of the periodic table) with the same tetravalent oxidation state. However, it is expected that Hf-based MOFs offer higher acidic behavior than their isostructural Zr-based MOFs, since the dissociation enthalpies of Hf–O bonds are higher than those of Zr–O (802 vs. 776 $kJ.mol^{-1}$) [288–290].

UiO-66 family was employed in this work to retain $^{127}I_2$ (as a model molecule for radioactive I_2), as a recent study demonstrated the ^{131}I adsorption capacity of an amino-functionalized UiO-66 MOF [16]. This previous study also highlighted the MOF stability under conditions that simulates ^{131}I leaking during nuclear accidents (steam at 120 ºC and γ radiation from ^{60}Co source up to 2 MGy) [16]. Due to the facility of being chemically modified, the UiO-66 family is a great candidate for evaluating the effects of functionalizing organic linkers and/or replacing metallic sites on its capacity to retain iodine. For instance, aiming to understand the linker influence over the I_2 capture, some isoreticular structures of UiO-66, UiO-67, and UiO-68 were explored in another work [12], which mentioned an I_2 transformation into I_3^- that took place after the contact between the gaseous iodine and the UiO materials. The effect of functionalizing the aromatic ring of the linker with amino groups has been evaluated. In this case, an enhancement of the of $I_2 \rightarrow I_3^-$ conversion rate was observed in the presence of $–NH_2$ [12]. This reaction was monitored using UV-Vis and Raman spectroscopy. Furthermore, to this day, there is no mention in the literature of an in-depth spectroscopy study that relates the iodine adsorption to the metal content in the UiO-66 structure.

Thus, since the iodine uptake and the CTCs inside UiO-66 are both expected to be influenced by the metal cluster (as the band gap of UiO-66 depends on this parameter, as

observed in Chapter III) [249], this effect is to be evaluated. In this work, hafnium was chosen for replacing zirconium in UiO-66 due to its higher acidity and similar characteristics, as they are part of the same family in the periodic table. Additionally, the $I_2 \rightarrow I_3^-$ conversion mechanism involving a redox reaction inside this MOF is not yet elucidated. This emphasizes the importance of understanding the metal influence on the physical-chemical properties of the UiO-66 series. This study employs several characterization techniques such as SEM, EDS, FTIR, Raman spectroscopy, diffuse reflectance UV-Vis spectroscopy, PXRD, EPR, and N_2 sorption to characterize the UiO-66(Zr,Hf) obtained materials.

4.2. Structural characterization of the pristine UiO-66 samples

The weight percentage (wt.%) of hafnium and zirconium in the synthesized UiO-66 were assessed by ICP-OES and the results are displayed in Table 4.1, alongside to the atomic percentages of metal constituents (at.%) calculated through the elemental ratio Hf/Zr. The UiO-66(Zr) and UiO-66(Hf) exhibited 100 at.% Zr and 100 at.% Hf, respectively. The intermediate samples – UiO-66(Hf/Zr = 1:3), UiO-66(Hf/Zr = 1:1) and UiO-66(Hf/Zr = 3:1) – exhibited 25 at.% Hf, 51 at.% Hf and 75 at.% Hf, respectively. For such reason, in order to simplify the notation of the mixed UiO-66(Hf/Zr), they were named according to their various amounts of Hf – i.e., UiO-66(25% Hf), UiO-66(51% Hf) and UiO-66(75% Hf), hereafter. These values are identical, or very close, to the initial ratio of precursors during the synthesis, demonstrating that they were well accomplished.

Table 4.1: Total metal content (wt.%) and metal content ratio (at.%) of Hf and Zr calculated using ICP-OES and EDS spectroscopies for the different UiO-66 samples.

UiO-66	Total metal content		Metal content ratio			
(Hf:Zr)	ICP-OES ($\%_{wt}$)		ICP-OES ($\%_{at}$)		EDS ($\%_{at}$)	
	Hf	Zr	Hf	Zr	Hf	Zr
0:1	0	32.3	0	100	0	100
1:3	14.7	22.2	25.0	75.0	19.4	80.6
1:1	28.9	14.4	51.0	49.0	41.0	59.0
3:1	40.7	6.8	75.3	24.7	70.2	29.8
1:0	53.3	0	100	0	100	0

The main physical-chemical properties of the UiO-66 compounds obtained here are summarized in Table 4.2.

Table 4.2: Physical chemical properties of the UiO-66 compounds displaying the crystallite size (Φ), the lattice parameter (a), the band gap values, the CBM (E_{CB}) and VBM (E_{VB}) positions, the SSA_{BET} and the microporous volume (which should also be considered as the total pore volume of the samples).

UiO-66	Crystallite size Φ	Lattice parameter a	Band gap	E_{VB}	E_{CB}	$SSA_{(BET)}$	Microporous volume
(M)	nm	Å	eV	eV vs. SHE		$m^2.g^{-1}$	$cm^3.g^{-1}$
Zr	100 – 250	20.7696(8)	4.07	4.15	0.08	1262 ± 33	0.60
25% Hf	110 – 530	20.7670(6)	3.99	4.11	0.12	1016 ± 29	0.53
51% Hf	130 – 1,110	20.7435(6)	4.00	4.12	0.12	980 ± 25	0.46
75% Hf	150 – 2,210	20.7292(4)	4.01	4.12	0.11	898 ± 26	0.46
Hf	180 – 3,330	20.7232(7)	3.98	4.11	0.13	818 ± 24	0.41

4.2.1. Crystallography and textural properties

The SEM images of the UiO-66 products synthesized in this work are displayed in Figure 4.1. They show crystals morphology of typical aggregates of octahedral shapes in agreement with that expected for UiO-66 samples [264]. The EDS/elemental mapping image of UiO-66(51% Hf) reveals that Zr and Hf atoms are homogeneously dispersed throughout the crystallites. This observation is also verified by the EDS/elemental mapping of the other compounds with different Hf/Zr ratios (Figure 4.2). Moreover, the elemental ratios of hafnium and zirconium obtained by EDS are close to those obtained by ICP-OES (Table 4.1), showing that the crystals have a similar composition to that of the bulk powdered sample. In this work, the UiO-66 compounds exhibited crystallites ranging from 100 nm to 3.3 µm (Figure 4.1 and Figure 4.2). This difference is also dependent on the Hf/Zr atomic ratio, since the presence of hafnium seemed to induce the growth of bigger crystals. Aiming to emphasize this variation, the particle size distribution of the crystallites is presented in Figure 4.3. While UiO-66(Zr) presents crystallites ranging between 100 and 250 nm, UiO-66(Hf) can lead to crystallites up to 3.33 µm (Figure 4.2 and Table 4.2).

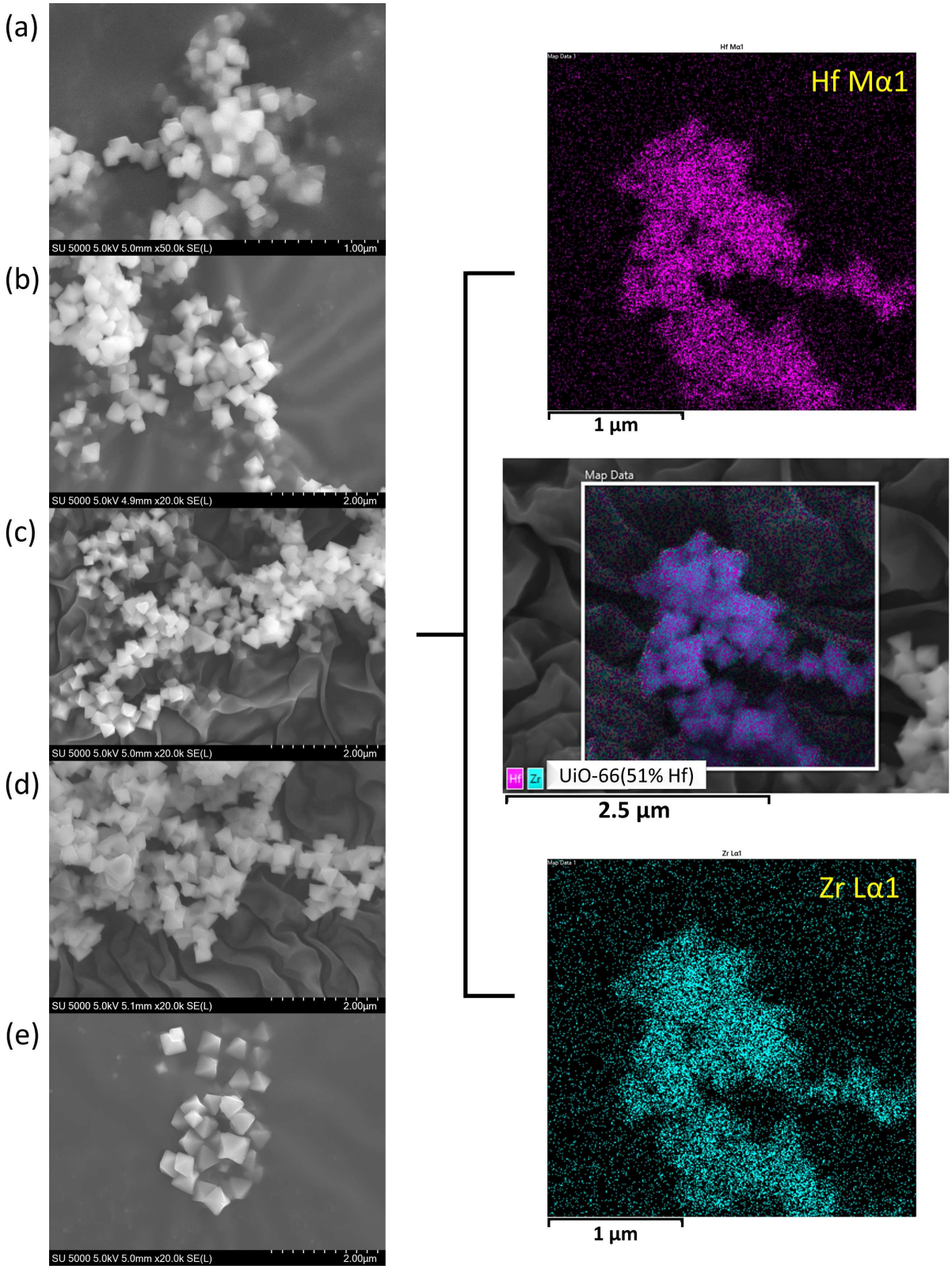

Figure 4.1: On the left side: SEM images obtained for (a) UiO-66(Zr), (b) UiO-66(25% Hf), (c) UiO-66(51% Hf), (d) UiO-66(75% Hf), and (e) UiO-66(Hf). On the right side: EDS/elemental mapping of UiO-66(51% Hf). Hf $M_{\alpha 1}$ signal is displayed in purple and Zr $L_{\alpha 1}$ in light blue.

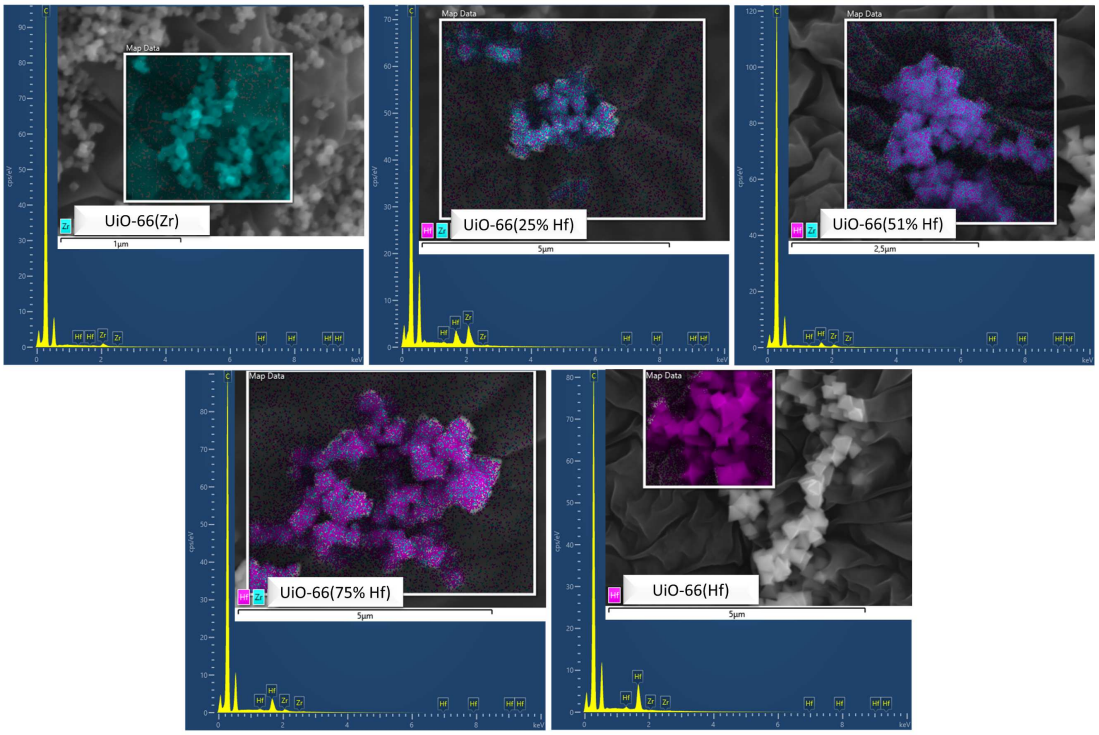

Figure 4.2: EDS spectra and elemental mapping of UiO-66(Zr), UiO-66(25% Hf), UiO-66(51% Hf), UiO-66(75% Hf), and UiO-66(Hf). Hf $M_{\alpha 1}$ signal is displayed in purple and Zr $L_{\alpha 1}$ in light blue.

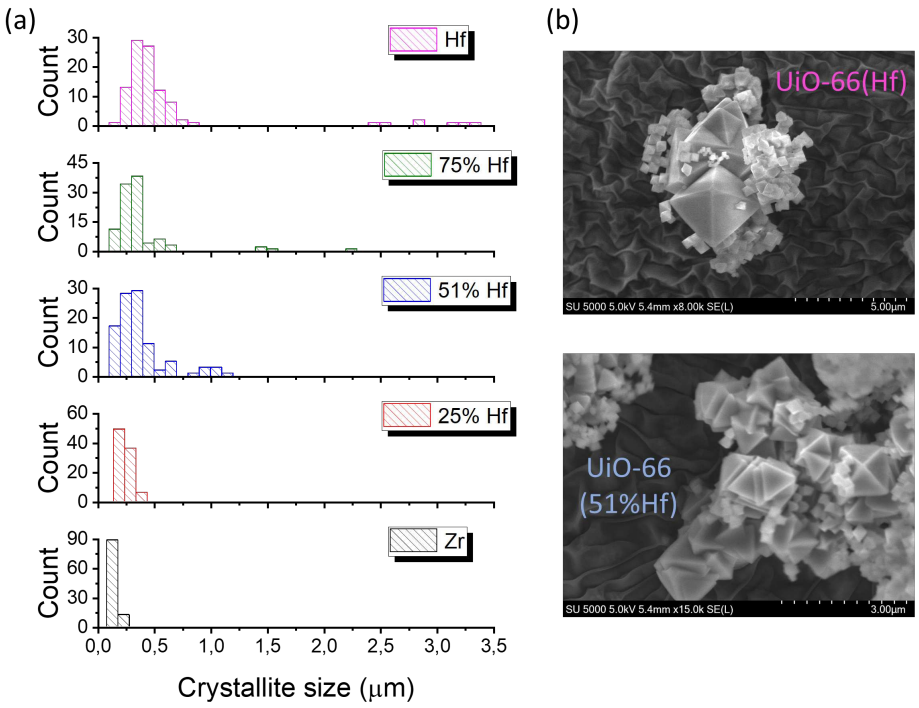

Figure 4.3: (a) Particle size distribution for the different UiO-66 samples obtained after the treatment of SEM images using the ImageJ software using 100 crystallites. (b) SEM images displaying the biggest crystallites found for UiO-66(Hf) – 3.33 µm – and UiO-66(41% Hf) – 1.11 µm.

Figure 4.4 shows PXRD patterns of UiO-66 compounds after activation and also the evolution of the lattice parameter *a* of the cubic cell. Typical diffraction Bragg peaks of the UiO-66 structure were observed at 2θ about 7.4º, 8.5º, 12.0º, 14.1º, 14.8º, 17.1º, 18.6º, 19.1º, 21.0º, 22.3º, 24.2º, and 25.8º, which have been attributed to its (111), (200), (022), (113), (222), (004), (133), (024), (115), (044), (135) and (006) crystal planes, respectively [291]. Lattice parameters were refined by Le Bail analysis method using the JANA software [292]. UiO-66 topology possesses an **fcc** cell, where the lattice parameter *a* was found to be a function of the Hf/Zr atomic ratio, going from *a* = 20.7696(8) Å in UiO-66(Zr) down to *a* = 20.7232(7) Å in UiO-66(Hf) (Table 4.2). It is worth mentioning that those values, as well as their variation, are in good agreement with those reported in other studies [264,286]. This is ascribed to the fact that Zr^{4+} and Hf^{4+} cations have a very similar ionic radius – 0.84 Å (Zr^{4+}) and 0.83 Å (Hf^{4+}) for environment coordination of VIII – [293] and, at the same time, the Hf^{4+} is known to present a higher electronegativity than the Zr^{4+} (0.96 against 0.90) [294]. Therefore, the higher acid character of Hf^{4+} contributes to decrease the size of the Hf–O bonds when comparing to the Zr–O bonds [294,295]. Moreover, the presence of a single (111) peak was observed at different Hf/Zr ratios, which reflects a solid solution of $Zr_{6-x}Hf_x$ type within UiO-66 crystals, as confirmed by the EDS cartography (Figure 4.1 and Figure 4.2). If one considers the segregation of two pure phases related to different amounts of UiO-66(Zr) and UiO-66(Hf) solids, a doublet of Bragg peaks should be visible instead.

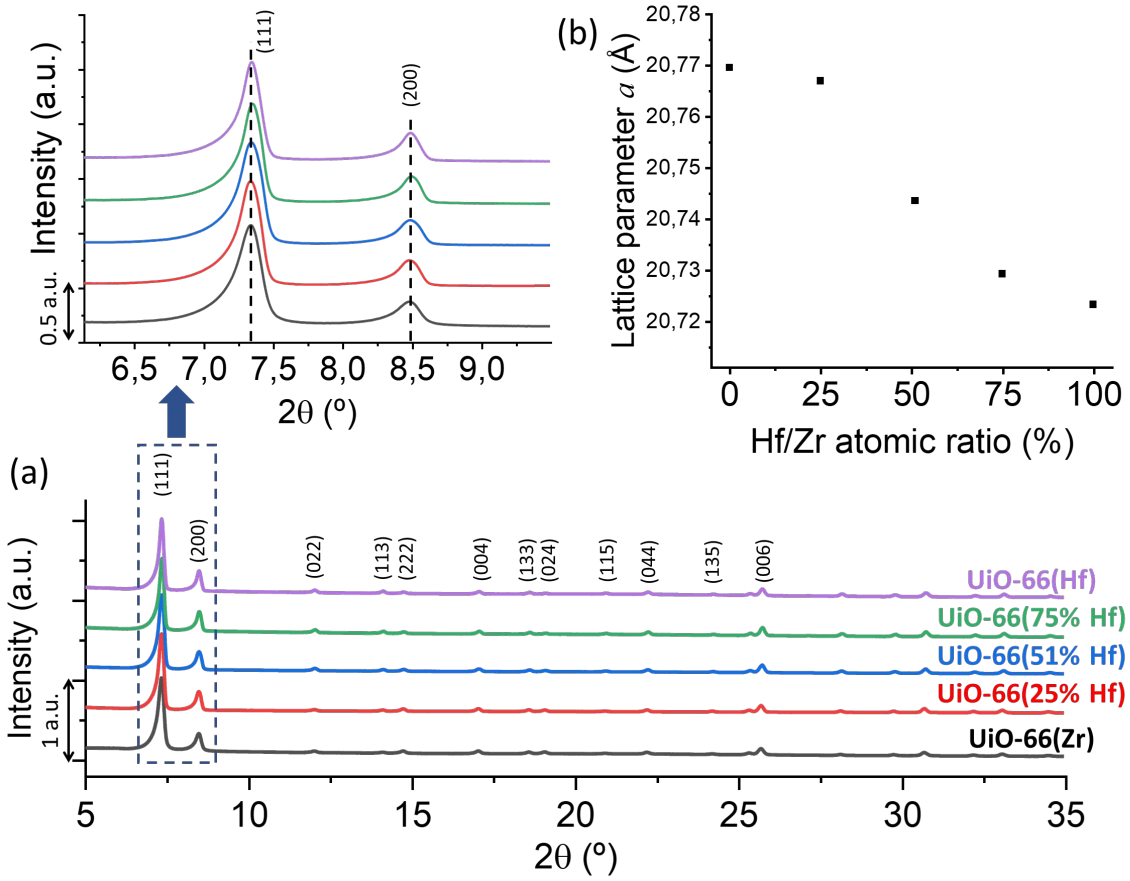

Figure 4.4: (a) powder XRD pattern of UiO-66(Zr) (black), UiO-66(25% Hf) (red), UiO-66(51% Hf) (blue), UiO-66(75% Hf) (green), and UiO-66(Hf) (purple) after activation using $\lambda_{CuK\alpha}$ = 1.5406 Å radiation. The zoom displays the first two diffraction peaks for each compound, with the (111) and (200) planes highlighted. (b) cubic lattice parameter *a* refined using the Le Bail method as a function of the Hf/Zr atomic ratio.

Figure 4.5 displays the nitrogen gas sorption isotherms collected for the series of UiO-66(Zr,Hf). All the compounds present a type-I isotherm according to IUPAC classification, which is characteristic of microporous materials (Table 4.2) [296]. One can see that the incorporation of hafnium in UiO-66(Zr) compound has a drastic effect over the samples' SSAs calculated by the BET method. When replacing zirconium cations by hafnium in the UiO-66 structure, the SSA decreases from 1262(33) $m^2.g^{-1}$ for UiO-66(Zr) to 818(24) $m^2.g^{-1}$ for UiO-66(Hf). It stays in between for the other Hf/Zr ratios: 1016(29) $m^2.g^{-1}$ for UiO-66(25% Hf), 980(25) $m^2.g^{-1}$ for UiO-66(51% Hf), and 898(26) $m^2.g^{-1}$ for UiO-66(75% Hf) (Table 4.2). The same behavior is observed for the microporous volume of the samples, which decreases from 0.598(8) $cm^3.g^{-1}$ in UiO-66(Zr) to 0.408(9) $cm^3.g^{-1}$ in UiO-66(Hf) (Table 4.2). The results are in agreement with others reported in the literature and they are coherent with the atomic mass of hafnium (178.49 u) and zirconium (91.224 u) [264,297]. Inarguably – since those values are

normalized to a mass unity (g^{-1}) – when considering an isostructural UiO-66 solid, the presence of a heavier metal that densifies the material will reduce its SSA and its specific microporous volume. However, this is not to be related to the actual surface or microporous volume per molar unit, as the materials synthesized here present the same pore structure. Indeed, when normalizing the SSAs to the molecular weight of UiO-66, the obtained values indicate that the surface area is independent of the Hf/Zr atomic ratio: 1.8 $km^2.mol^{-1}$ for all the samples containing hafnium, and 2.1 $km^2.mol^{-1}$ for the UiO-66(Zr) compound.

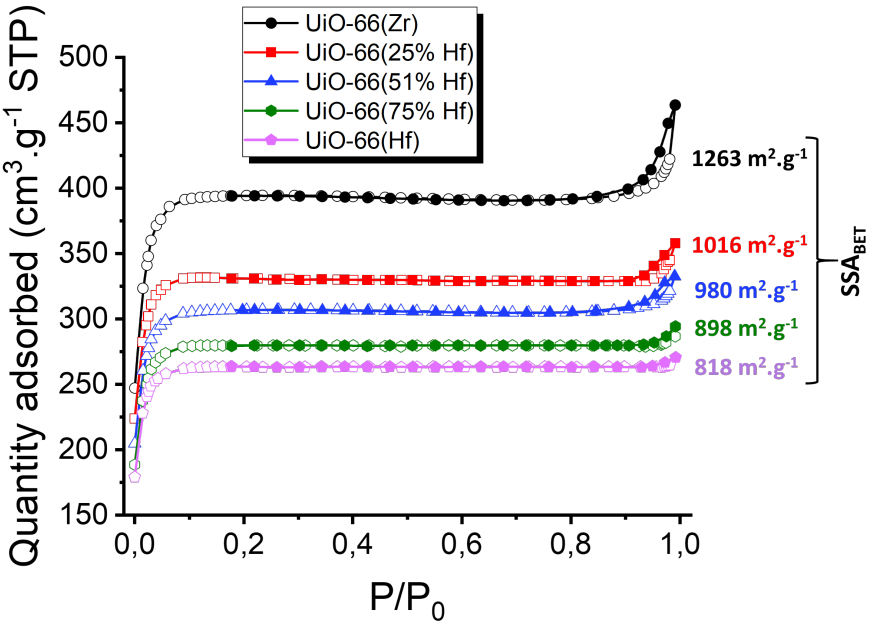

Figure 4.5: N_2 adsorption/desorption isotherms for UiO-66(Zr) (black), UiO-66(25% Hf) (red), UiO-66(51% Hf) (blue), UiO-66(75% Hf) (green), and UiO-66(Hf) (purple). The SSA_{BET} values are also highlighted for each compound.

4.2.2. Optical and electronic properties

Diffuse reflectance UV-vis spectroscopy was performed in order to evaluate the metal influence on the optic properties of the UiO-66(Zr,Hf) materials synthesized here (Figure 4.6). The spectrum of pristine UiO-66(Zr) shows only absorptions in the UV domain, at 242 nm with a shoulder at 292 nm (Figure 4.6a). This band is attributed to linker-based HOCO to LUCO transitions, as the binding energy of the zirconium d-orbitals is too low and prevents the overlap with the π* orbital of the BDC organic linker [27]. Then, it is observed that the relative intensity of the shoulder contribution at 292 nm increases progressively with the hafnium content to

finally give rise to a broad band shifting to around 240-300 nm (Figure 4.6a). Since the change in the intensity of this transition is not accompanied by a variation of its energy (there is no wavelength shift), this phenomenon is ascribed to the different molar extinction coefficients of zirconium and hafnium [248].

As discussed in Chapter III, the UiO-66(Zr,Hf) compounds exhibit direct band gaps and therefore, their energies were extracted from the direct Tauc plot [298] using the Kubelka-Munk function [177]. The obtained values are summarized in Table 4.2, alongside the respective E_{VB} and E_{CB} values. The incorporation of hafnium has a significant influence over the band gap of the samples (Figure 4.6b and Table 4.2). The E_g reduces from 4.07 eV in UiO-66(Zr) down to 3.98 eV in UiO-66(Hf). It is worth mentioning that the value obtained for UiO-66(Zr) is in agreement with the literature [285]; however, this happens to be the first time that experimental data is acquired for UiO-66(Hf) [250]. Although Yang *et al.* [250] demonstrated that there is an underestimation of the band gap energies for UiO compounds when E_g is calculated by DFT, an operation applied to their results allowed them to predict values that correspond exactly to the experimental data obtained elsewhere for UiO-66(Zr) (4.07 eV) [285] and UiO-67(Zr) (3.68 eV) [268]. Nevertheless, this method found the value of 3.74 eV for UiO-66(Hf), which is significantly different from the 3.98 eV obtained in this work.

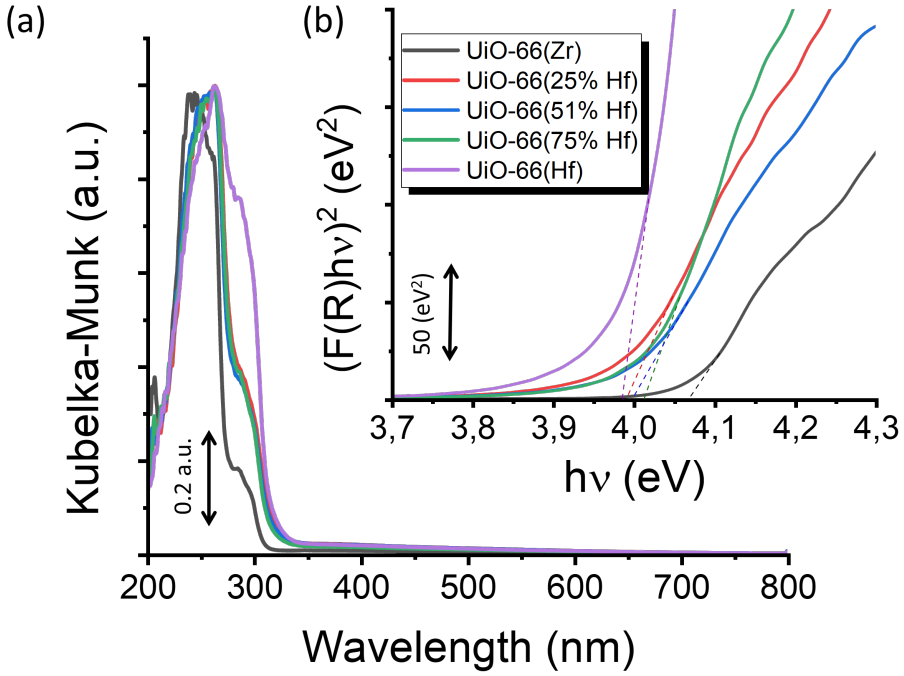

Figure 4.6: (a) Kubelka-Munk UV-vis spectra and (b) direct Tauc plot for UiO-66(Zr) (black), UiO-66(25% Hf) (red), UiO-66(51% Hf) (blue), UiO-66(75% Hf) (green), and UiO-66(Hf) (purple).

4.2.3. Vibrational spectroscopy

Aiming to investigate the influence of the metal Hf/Zr substitution on the chemical bonds of the UiO-66 compounds, FTIR and Raman spectroscopies were conducted. The Raman spectra were normalized to the band at 1618 cm^{-1} (C–O asymmetric stretching), while the FTIR spectra were normalized to the band at 1392 cm^{-1} (C=C–(COO) asymmetric stretching). These bands were chosen since they are not affected by the metal Hf/Zr substitution.

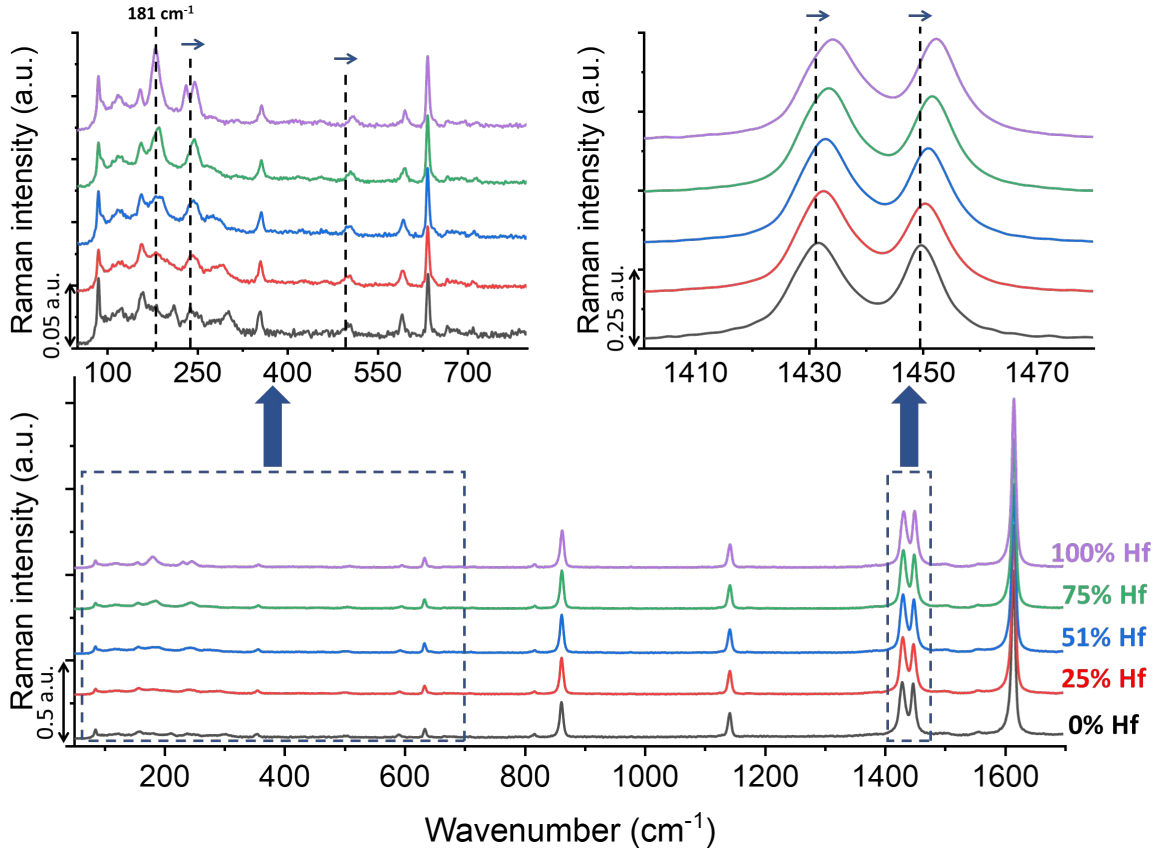

Figure 4.7: Raman spectra of UiO-66(Zr) (black), UiO-66(25% Hf) (red), UiO-66(51% Hf) (blue), UiO-66(75% Hf) (green), and UiO-66(Hf) (purple).

The evolution of the Raman spectra as a function of the Hf/Zr ratio is presented in Figure 4.7. The spectra clearly exhibit the development of a new band centered at 181 cm^{-1}, which is tentatively assigned to linker to metal-cluster in-plane bending + μ_3–O bending (μ_3– stands for an element which is connected to three metals) [285]. Moreover, blue-shift effects are observed at 238, 500, 1431, and 1449 cm^{-1} when hafnium content increases. The first blue-shifted band, at 238 cm^{-1}, relates to two vibrational modes: linker to metal-cluster out of plane bending and M–(OH)–M bending (M = Zr, Hf; Figure 4.8a); whereas the second one, at 500 cm^{-1}, is related

to the μ_3-O and μ_3-OH in-phase bending (cluster breathing) [285] (Figure 4.8b). In addition, the bands at 209 and 231 cm^{-1} are ascribed to the O–C–O translation mode and they are only present in UiO-66(Zr) and in UiO-66(Hf) Raman spectra, respectively (Figure 4.7) [285]. Another band, at 1431 cm^{-1}, is related to two vibrational modes: in-plane asymmetric (C=C)–H bending + asymmetric C=C stretching [285]. Finally, the last one, at 1449 cm^{-1}, is associated to the C–C symmetric stretching [285] (Figure 4.8c).

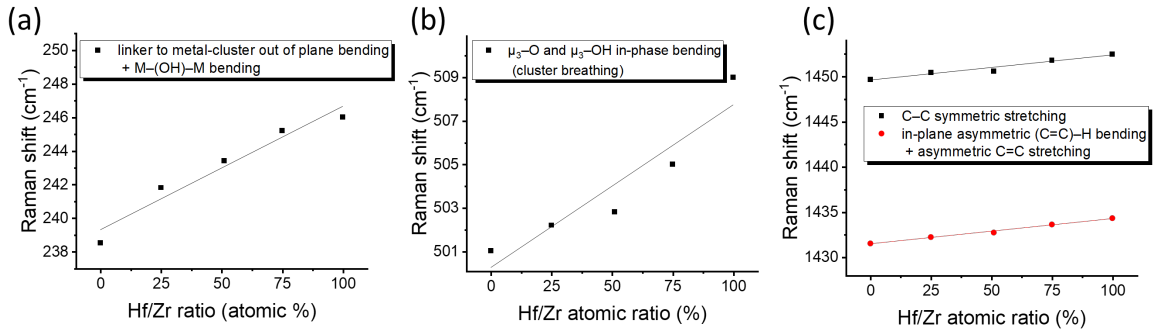

Figure 4.8: Raman bands evolution as a function of the Hf/Zr atomic ratio. (a) linker to metal-cluster out of plane bending + M–(OH)–M bending; (b) μ_3–O and μ_3–OH in-phase bending (cluster breathing); (c) C–C symmetric stretching (in black) and in-plane asymmetric (C=C)–H bending + asymmetric C=C stretching (in red).

In order to get complementary information about the metal influence on the vibrational behavior of the UiO-66 compounds, FTIR spectroscopy was also applied to these samples. As observed in the Raman spectra, the five FTIR bands at 554, 679, 702, 729, and 3675 cm^{-1} also shift toward higher wavenumbers with the increase of the hafnium content (Figure 4.9). The first two, at 554 and 679 cm^{-1} are related to the M–(OC) asymmetric stretching (Figure 4.10a) and to the μ_3–O stretching (Figure 4.10b), respectively [285]. The band at 702 cm^{-1} is influenced by three modes of vibration: μ_3–OH bending + O–C–O bending + C=C–(COO) bending, while the one at 729 cm^{-1} corresponds to the aromatic ring torsion mode (Figure 4.10b) [285]. The last band, at 3675 cm^{-1}, is related to the OH stretching mode (Figure 4.10c) [285]. Moreover, it is interesting to note that the relative intensity of the bands at 448 and 474 cm^{-1} dramatically depends on the Hf/Zr atomic ratio (Figure 4.9): a higher content of hafnium favors the band at 448 cm^{-1} (antiphase μ_3–OH stretching), whereas higher content of zirconium leads to an increase of the one at 474 cm^{-1} (in-phase μ_3–OH stretching) [285].

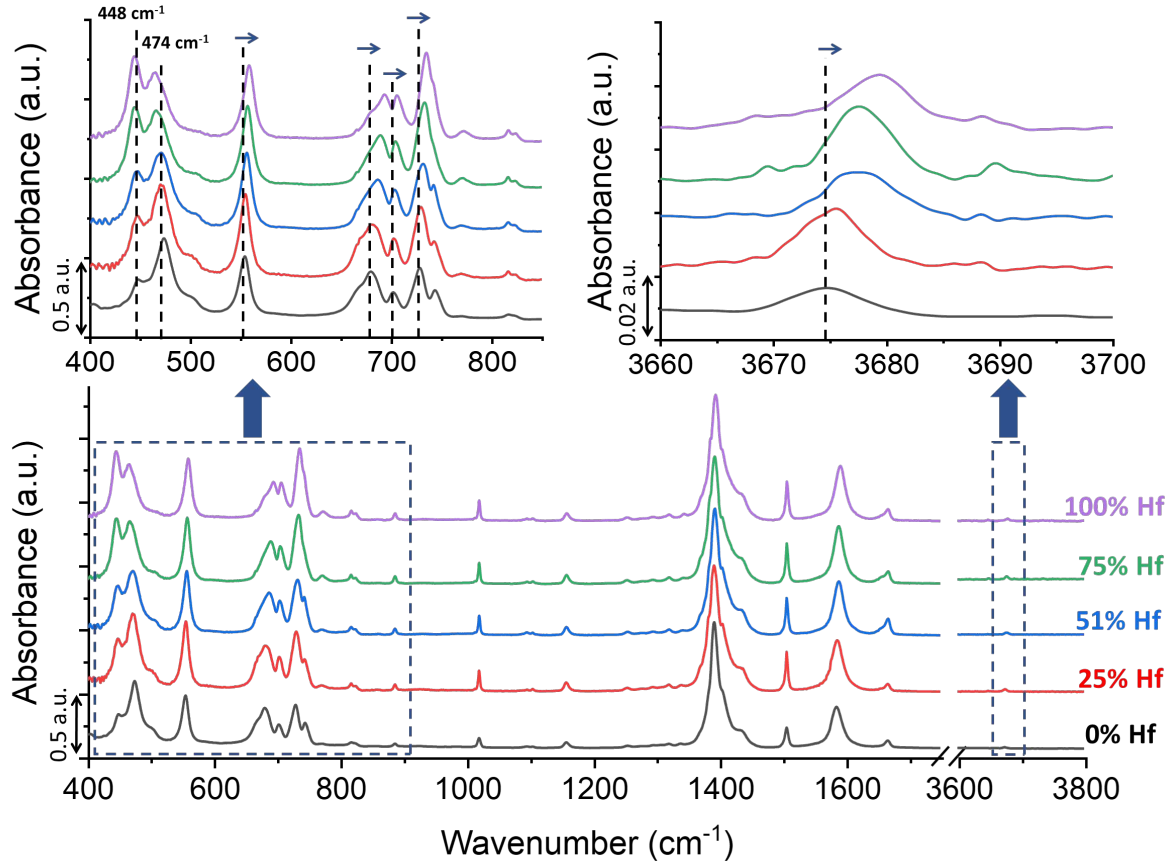

Figure 4.9: FTIR spectra of UiO-66(Zr) (black), UiO-66(25% Hf) (red), UiO-66(51% Hf) (blue), UiO-66(75% Hf) (green), and UiO-66(Hf) (purple).

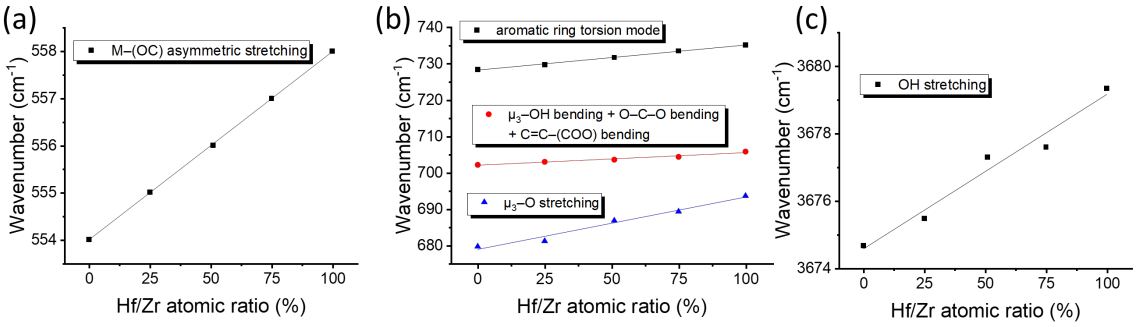

Figure 4.10: FTIR bands evolution as a function of the Hf/Zr atomic ratio. (a) M–(OC) asymmetric stretching; (b) aromatic ring torsion mode (in black), μ_3–OH bending + O–C–O bending + C=C–(COO) bending (in red), and μ_3–O stretching (in blue); (c) OH stretching.

The presence of blue-shifts in the FTIR and Raman bands implies that these vibrational modes require higher energy in UiO-66(Hf) than in UiO-66(Zr). Studies have shown that the average μ_3–(O,OH) bond is shorter in UiO-66(Hf) than in UiO-66(Zr) (2.102(17) against

2.233(1) Å) [264,286]. An identical trend is also observed for the M–(OC): Hf–(OC) = 2.086(8) Å and Zr–(OC) = 2.107(2) Å (OC = oxygen from carboxyl group) [264,286]. However, the opposite was found for the O–C bond (from bidentate carboxylate group): 1.304(21) Å in UiO-66(Hf) against 1.256(2) Å in UiO-66(Zr) [264,286]. These features are all consistent with the higher acidity of Hf^{4+} compared to that of Zr^{+4}, which increases the interaction between the metallic cation and the oxo, hydroxyl, and carboxyl groups within the hexanuclear $[M_6O_4(OH)_4]$ core, stiffening the interatomic bonding in UiO-66(Hf) [294,299]. Therefore, it explains the blue-shifts regarding the μ_3–O, the μ_3–OH, and the M–(OC) species. The other blue-shifts, related to the aromatic part of the material, are ascribed to the smaller cubic lattice parameter of UiO-66(Hf).

The vibrational frequency of the main FTIR and Raman bands are presented in Table 4.3 alongside their assignment. The attribution of the bands resulted from the animations of vibrational modes of a hydroxylated UiO-66(Zr) that were calculated by Valenzano *et. al.*, [285] and are available at the CRYSTAL Web site: https://www.crystal.unito.it/vibs/uio66_hydro/.

Table 4.3: Bands assignment for the UiO-66 vibrational modes active in Raman [(1)] and FTIR [(2)] spectroscopies.

Wavenumber (cm^{-1})					Bands assignment
Calculated (Ref. [285])	FTIR (this work)		Raman (this work)		
UiO-66 (Zr)	UiO-66 (Zr)	UiO-66 (Hf)	UiO-66 (Zr)	UiO-66 (Hf)	
73 [(1)]	–	–	85	85	Lattice torsion mode
127 [(1), (2)]	–	–	118	118	Linker rocking mode
163 [(1)]	–	–	156	156	Cluster torsion mode
196 [(1)]	–	–	181	181	Linker to metal-cluster in-plane bending + μ_3–O bending
206 [(1), (2)]	–	–	231	–	O–C–O translation mode
237 [(1)]	–	–	238	247	Linker to metal-cluster out of plane bending + M–(OH)–M bending
272 [(1)]	–	–	270	–	O–C–O torsion mode
358 [(1)]	–	–	355	355	Carboxylate to aromatic ring in-plane bending + carboxylate to metal-cluster rocking
447 [(1), (2)]	448	448	–	–	μ_3–OH antiphase stretching
470 [(1), (2)]	474	474	–	–	μ_3–OH in-phase stretching
501 [(1)]	–	–	500	509	μ_3–O and μ_3–OH in-phase bending (cluster breathing)
556 [(1), (2)]	554	558	–	–	M–(OC) asymmetric stretching
593 [(1)]	–	–	591	591	M–(OC) symmetric stretching
648 [(1)]	–	–	635	635	Aromatic ring in-plane bending
673 [(1), (2)]	679	693	667	667	μ_3–O stretching
711 [(1), (2)]	702	706	–	–	OH bending + O–C–O bending + C=C(COO) bending
718 [(1), (2)]	729	735	–	–	Aromatic ring torsion mode
771 [(1), (2)]	771	771	–	–	OH bending + out of plane CH bending (in-phase)
814 [(1), (2)]	816	816	816	816	OH bending + out of plane CH bending (antiphase)
875 [(1)]	–	–	862	862	C=C(COO) symmetric stretching (in-phase)
1023 [(1)]	1019	1019	–	–	Out of plane, antiphase CH bending
1164 [(1)]	–	–	1143	1143	Aromatic ring breathing + in-plane symmetric CH bending (scissoring)
1165 [(1), (2)]	1158	1158	–	–	In-plane symmetric CH bending (scissoring) + C–O symmetric stretching
1367 [(1), (2)]	1392	1392	–	–	C=C(COO) asymmetric stretching
1408 [(1), (2)]	1405	1405	–	–	C–O symmetric stretching + C–C asymmetric stretching
1439 [(1), (2)]	1435	1435	1431	1434	In-plane asymmetric CH bending (scissoring) + asymmetric C=C stretching
1474 [(1)]	–	–	1449	1452	C–C symmetric stretching
1539 [(1), (2)]	1507	1507	–	–	C=C symmetric stretching (antiphase) + in plane symmetric CH bending (rocking)
1607 [(1), (2)]	1591	1591	1618	1618	C–O asymmetric stretching
1665 [(1), (2)]	1666	1666	–	–	C=C symmetric stretching
3853 [(1), (2)]	3675	3680	–	–	OH stretching

4.3. Iodine adsorption and evolution within UiO-66 porous structure

In order to investigate the possible influence of the metal, the powdered samples UiO-66(Hf), UiO-66(75% Hf), UiO-66(51% Hf), UiO-66(25% Hf) and UiO-66(Zr) have been exposed to gaseous iodine flow for 1 hour or 16 hours. The glass cell used to capture iodine (Figure 2.4) was prepared and sealed inside a glovebox under argon atmosphere, which avoided the contact of the powder with atmospheric water. At first, the kinetic iodine sorption curves were obtained and are presented in Figure 4.11.

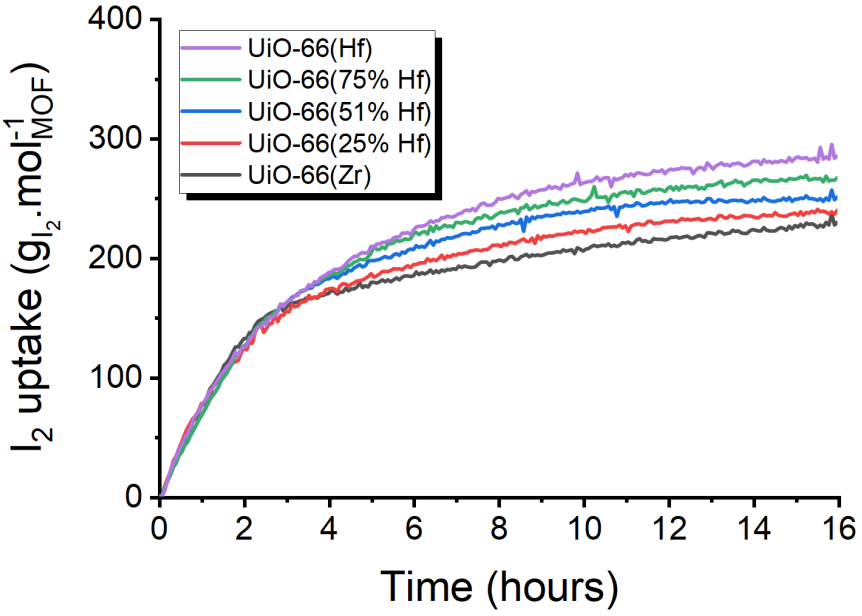

Figure 4.11: Adsorption kinetics of gaseous iodine during 16 hours in UiO-66(Zr) (black), UiO-66(25% Hf) (red), UiO-66(51% Hf) (blue), UiO-66(75% Hf) (green), and UiO-66(Hf) (purple). The I_2 adsorption and the UV-Vis spectra were conducted at room temperature.

Even though early stages (1-2 h) of the adsorption process on UiO-66(Hf) and UiO-66(Zr) seem to lead to an equivalent amount of iodine trapped by the UiO-66 pores (76 $g.mol^{-1}_{(UiO-66)}$ = 0.30 I_2 molecules per unit cell of UiO-66), the presence of hafnium significantly enhances the adsorbed iodine amounts from contact times longer than two hours. This feature put forward possibility that two different adsorption processes exist within the UiO-66 cavities. The first one could occur regardless the metal nature of the inorganic core, whereas in the second step, the presence of hafnium seems to favorize the increase of adsorbed iodine content. Different adsorption sites for I_2 within UiO-66(Hf) structure were already reported in the literature depending on the presence of defects on its structure [168]. Here, after 16h contact with

the gaseous iodine stream, the UiO-66(Hf) phase was able to adsorb 285 g of I_2 per mol of UiO-66 (approximately 1.12 I_2 molecules per unit cell of UiO-66), whereas UiO-66(Zr) only captured 230 $g.mol^{-1}_{(UiO-66)}$ (approximately 0.90 I_2 molecules per unit cell of UiO-66). The other three samples – UiO-66(25% Hf), UiO-66(51% Hf), and UiO-66(75% Hf) – stayed in between those values (Table 4.4), which confirms the premise that hafnium favors the I_2 capture.

Table 4.4: Iodine uptake and fitted kinetic constants data for the UiO-66 compounds using the LDF model [180].

UiO-66	I_2 uptake			k_{LDF}	R^2	time [$F(t)$ = 0.90][a]	time [$F(t)$ = 0.99] [a]
(M)	$mg.g^{-1}$	$g.mol^{-1}$	$mol.mol^{-1}$	(h^{-1})			
Zr	138	230	0.91	0.323(5)	0.943	7 h 8 min	14 h 15 min
25% Hf	132	240	0.95	0.308(3)	0.981	7 h 29 min	14 h 57 min
51% Hf	126	250	0.98	0.318(2)	0.995	7 h 14 min	14 h 59 min
75% Hf	128	267	1.05	0.292(1)	0.997	7 h 53 min	15 h 46 min
Hf	130	285	1.12	0.267(1)	0.996	8 h 37 min	17 h 15 min

[a] t = time necessary to reach $F(t)$ = 0.90 or $F(t)$ = 0.99 from LDF fit

For better understanding the hafnium influence on the I_2 adsorption kinetics, the experimental data of the iodine adsorption in UiO-66 compounds were fitted according to the LDF model (Figure 4.12). The effective mass transfer coefficient (k_{LDF}), the correlation coefficient (R^2), and the equilibration time to reach $F(t)$ = 0.90 and $F(t)$ = 0.99 are displayed in Table 4.4. There is a clear dependence between the k_{LDF} values and the hafnium amount in the UiO-66 structure, where the UiO-66(Hf) exhibits the smallest mass transfer coefficient (0.267(1) h^{-1}), and UiO-66(Zr) the highest (0.323(5) h^{-1}). The other three compounds (UiO-66(25% Hf), UiO-66(51% Hf) and UiO-66(75% Hf)) are in between those values. However, surprisingly, the UiO-66(51% Hf) exhibits a small shift from the expected behavior, since its k_{LDF} value is higher than both UiO-66(25% Hf) and UiO-66(75% Hf) (Table 4.4 and Figure 4.12). Still, this is coherent with the residence time of iodine in the UiO-66 compounds, which goes from 30 min in UiO-66(Hf) to 90 min in UiO-66(Zr), staying in between for UiO-66(25% Hf) (50 min), for UiO-66(51% Hf) (80 min), and for UiO-66(75% Hf) (60 min). Furthermore, although the maximum capacity of iodine adsorption by the materials here evaluated was not achieved in 16 hours, the LDF exponential curve fits quite well with the experimental data, as verified by the R^2 values between 0.981 and 0.997, except for UiO-66(Zr) which exhibited a slightly smaller R^2 of 0.943. The UiO-66 compounds can achieve $F(t)$ = 0.90 in approximately

seven to eight hours. For instance, the UiO-66(Zr) achieves 90% of its total adsorption capacity (considered from a total of 16 hours of contact) in 7 h 8 min whereas, in the same conditions, UiO-66(Hf) took 8 h 37 min. Finally, the UiO-66 compounds with 50% or less of hafnium can take up to 14 h 57 min to achieve 99% of their adsorption capacity. This value rises for hafnium-richer (>50%) UiO-66, with t = 15 h 46 min and t = 17 h 15 min for UiO-66(75% Hf) and UiO-66(Hf), respectively.

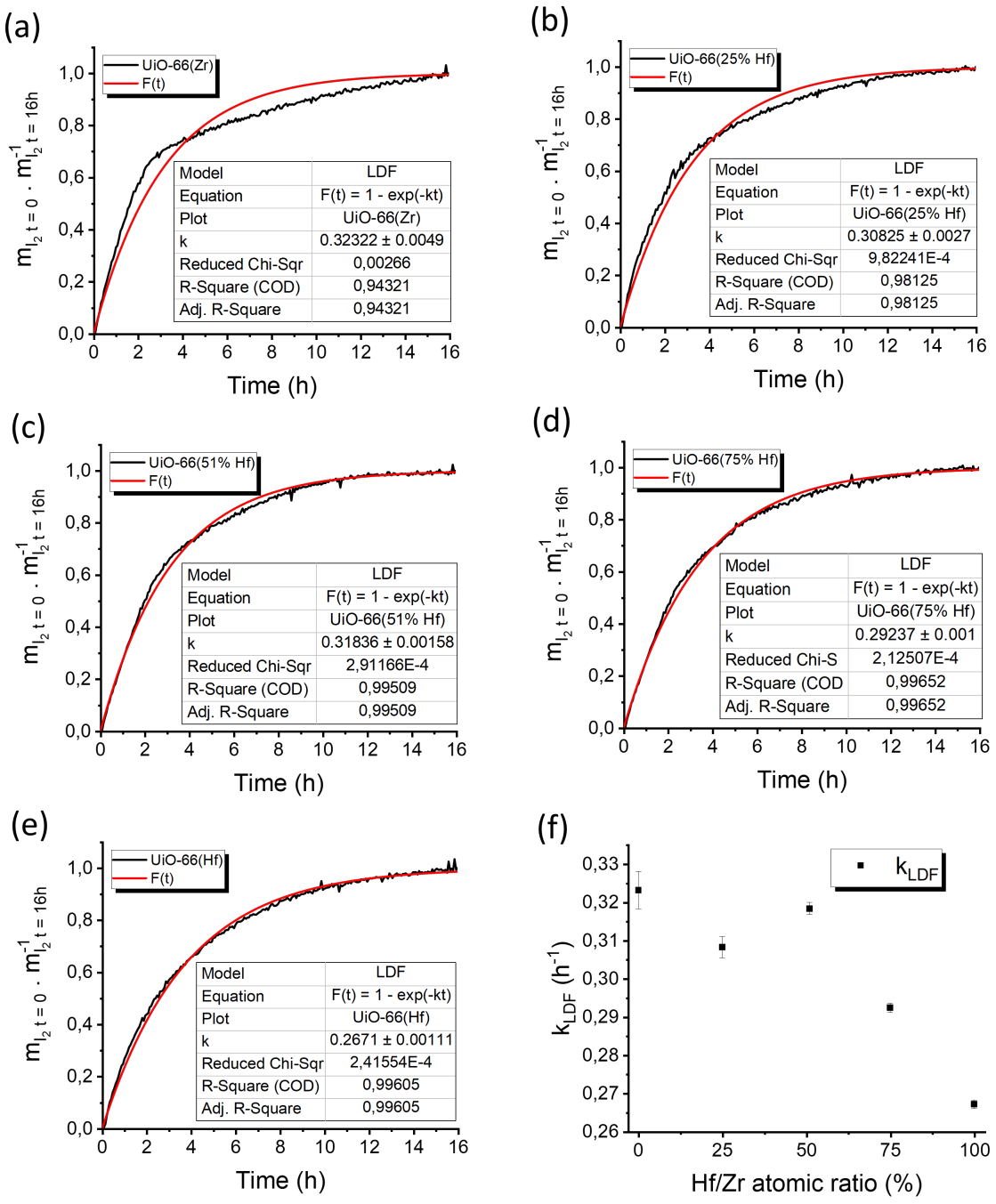

Figure 4.12: Adsorption kinetics plotted according to the Linear Driving Force (LDF) model for (a) UiO-66(Zr), (b) UiO-66(25% Hf), (c) UiO-66(51% Hf), (d) UiO-66(75% Hf), and (e) UiO-66(Hf). In (f), the plot of the effective mass transfer coefficient (k_{LDF}) against the Hf/Zr atomic ratio is also displayed.

4.3.1. Diffuse Reflectance UV-Vis spectroscopy of the I_2@UiO-66 samples

At this point, it is worth mentioning that the color of the samples drastically changes after 16 hours of contact with the iodine gaseous stream. Indeed, the white original UiO-66 powders became orange-brown immediately after contact with I_2 but turned yellow after being exposed to the ambient atmosphere for 72 hours (Figure 4.13). Due to their similar color change, the iodine chemical behavior encapsulated in the three UiO-66 samples was first studied by UV-vis spectroscopy. Figure 4.13 presents the spectra obtained after leaving the iodine bench and after 72 hours of exposition to the ambient air atmosphere. For comparison purposes the spectra of the pure UiO-66 are also displayed.

After the contact between UiO-66 and iodine, the three I_2@UiO-66 samples showed the same behavior with the presence of two new broad bands maximizing at 292 and 361 nm, in addition to the bands of the UiO-66. These new contributions at 292 and 361 nm reveal the formation of the anionic I_3^- species [300]. However, due to the successive forms of the iodine species after adsorption, this signature includes probably other contributions in the visible range between 400 and 550 nm. The first one, corresponding to the "isolated" iodine form in gas phase, is expected to be observed at 520 nm due to the allowed $\pi_g^* \rightarrow \sigma_u^*$ transition [73,74]. Additionally, the spectral signature at lower wavelengths (around 400-500 nm) was attributed to CTCs between the I_2 and the aromatic ring of the BDC linker, since I_2 is well known for forming this type of interaction with benzene, which presents a high electron donor character [77,78]. Thus, "free" or weakly perturbed iodine molecules are assumed to contribute to the observed absorption around 400-500 nm. Consequently, whatever the metal Hf/Zr nature, the iodine adsorption mechanism within the framework of the UiO-66 series is initiated by the adsorption of "free" I_2 molecules that progressively go through the "perturbed" I_2 moiety and then, are transformed into I_3^-, which is the most stable species. At this point, it is already possible to deduce that the adsorption that occurs during the first 1-2 h is mainly dominated by "free" I_2 molecules, reason why there is no influence of the Hf/Zr content over the amount of I_2 trapped within the pores of UiO-66 for $t < 2$ h.

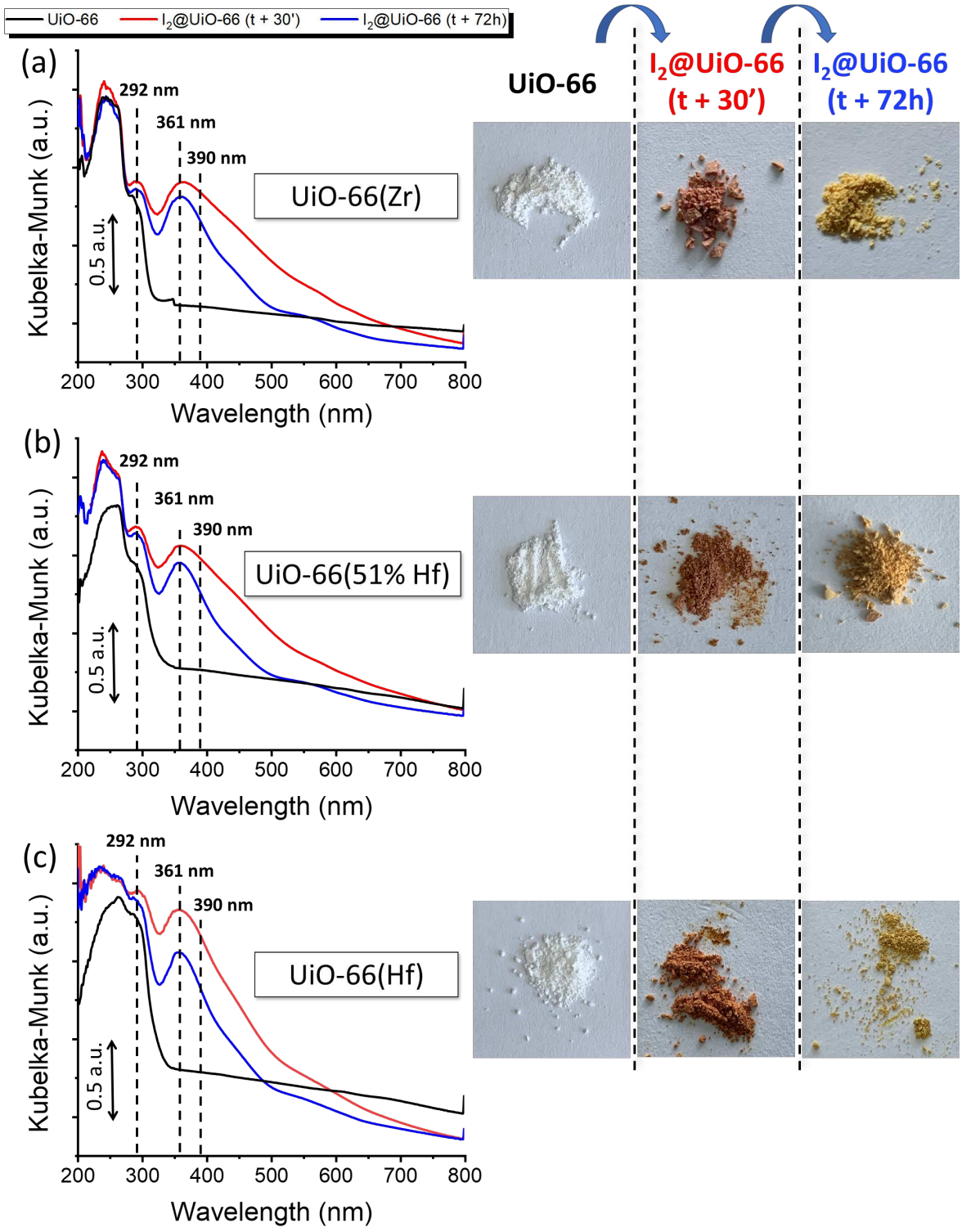

Figure 4.13: On the left side: UV-vis spectra from the pure UiO-66 (black), from the I_2@UiO-66 after 30 minutes of atmosphere exposure (red), and from the I_2@ UiO-66 after 72 hours of ambient air exposure (blue) for: (a) UiO-66(Zr), (b) UiO-66(51% Hf) and (c) UiO-66(Hf). On the right side: pictures of UiO-66 compounds before and after the iodine adsorption (30 minutes and 72 hours).

4.3.2. Characterizing the iodine adsorption and evolution using vibrational spectroscopy

Raman experiments were carried out in order to follow the sorption and evolution process of iodine within the three Hf/Zr compositions of the UiO-66 structures. It is worth mentioning that most of the UiO-66 bands keep the same positions after the iodine contact. However, changes can be observed in terms of relative intensity for some bands related to the BDC linker and, when hafnium is present, to the hydroxyl and oxo groups, which will be discussed below. Figure 4.14 shows the evolution of the Raman spectra of the I_2@UiO-66 compounds after 16 h of exposure in the 50–275 cm^{-1} region, which is characteristic of the iodine species inserted in UiO-66(Zr), UiO-66(51% Hf), and UiO-66(Hf). The spectra were normalized to the band at 1618 cm^{-1}, which is not affected by the iodine adsorption. They all showed the development of three bands centered at 115, 173, and 206 cm^{-1}, while a fourth component is observed at 156 cm^{-1} in I_2@UiO-66(Zr) (Figure 4.14a), and at 141 cm^{-1} in I_2@UiO-66(51% Hf) and I_2@UiO-66(Hf) (Figure 4.14b and c).

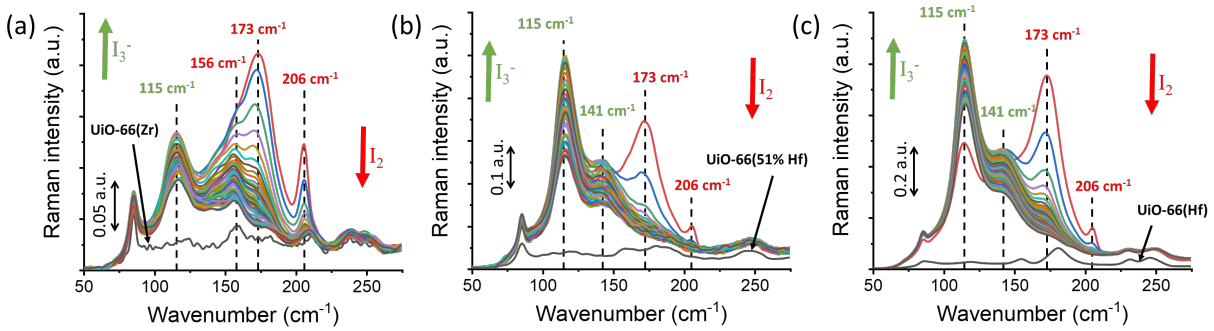

Figure 4.14: Raman spectra of (a) I_2@UiO-66(Zr), (b) I_2@UiO-66(51% Hf) and (c) I_2@UiO-66(Hf) recorded as a function of time from 30 minutes to 3 days after the UiO-66 exposure to the iodine stream. The first measurement was made after 30 minutes of leaving the iodine bench (red). The following were taken each hour on the first day, each two hours on the second day, and each four hours on the third day. The spectra of the pristine UiO-66 are displayed in black and highlighted by an arrow. The bands highlighted in red reduce in intensity over time, while green signals increase.

In order to identify the signature of the single iodine species that are present in the Raman spectra and to distinguish the Raman contribution from "free" I_2, "perturbed" I_2, and I_3^-, MCR-ALS algorithm was applied to the Raman experimental data. This method aims to extract relevant information of the single components present in a complex system. By using a bilinear model decomposition of the experimental data into the product of two matrices, MCR-ALS provides the spectra and the concentration peak profiles corresponding to the single components [179]. The MCR-ALS calculation allowed the extraction of three spectra assumed

to correspond to three species: "free I_2", "perturbed I_2", and "I_3^-" (Figure 4.15). The first one shows mainly a band at 206 cm^{-1}, while the second spectrum displays a broad band at 173 cm^{-1} with a shoulder around 156 cm^{-1}. The third spectrum is characterized by a main band centered typically at 115 cm^{-1} with a shoulder at 141 cm^{-1}. These bands were summarized in Table 4.5 and their values were compared to other reported in the literature, which allowed the identification of these three species.

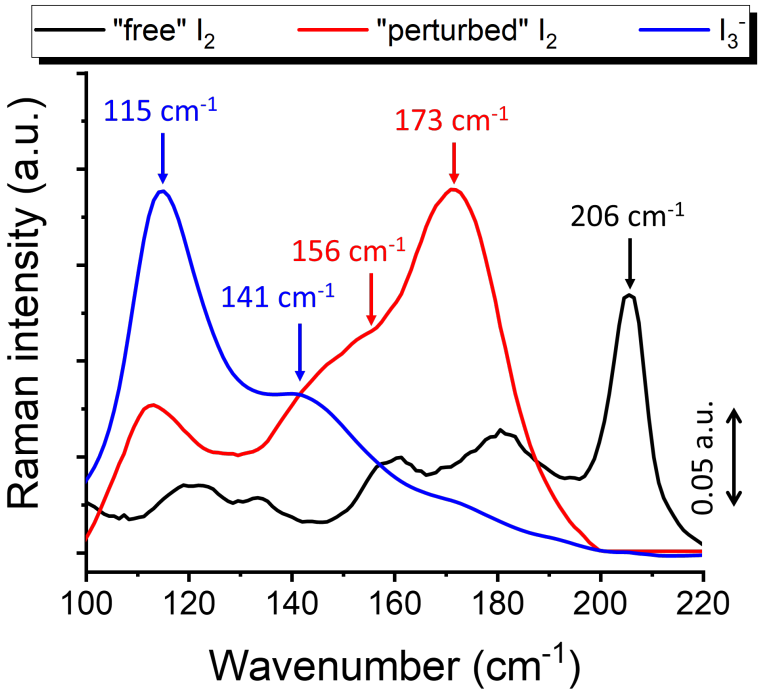

Figure 4.15: MCR-ALS spectra for the iodine species extracted from the successive collection of I_2@UiO-66 Raman spectra: "free" I_2 (black), "perturbed" I_2 (red), and I_3^- (blue), after being exposed under ambient air up to 72 hours.

Table 4.5: Wavenumbers and their corresponding band assignments for the three distinct iodine species observed for I_2@UiO-66 samples using Raman spectroscopy.

Wavenumber (cm^{-1})		Bands assignment	Reference
Literature	This work		
200-210	206	"free" I_2 inside the pores	[82]
150-180	156, 173	"perturbed" iodine	[84]
112, 143	115, 141	I_3^-	[83]

Due to the close proximity between the band observed at 206 cm^{-1} and that reported for isolated iodine in gas phase (210 cm^{-1}), the 206 cm^{-1} vibration was assigned to the symmetric

stretching of the I_2 molecule assumed to be trapped in the porous volume of the MOF, in the absence of strong interaction with its walls [82]. The progressive appearance of contributions at about 173 and 150 cm^{-1}, concomitantly to the reduction of the 206 cm^{-1} band, was attributed to the interaction between the I_2 and the UiO-66. This intermediary state, which is associated to the perturbed iodine, presents lower wavenumbers than the crystalline I_2 solid (180 – 188 cm^{-1}) [80]. This is ascribed to the presence of strong electron donor molecules – in this case, the aromatic ring from the BDC linker – that induces a decrease on the frequency of these vibrational modes [301]. This species is defined as "perturbed" iodine, due to a CTC that may generate different polynuclear iodine species of I_n^{-1} type (n = 3, 5, 7, …) [84]. Finally, the band centered at 115 cm^{-1}, which is observed in the third extracted spectrum, is attributed to I_3^- and corresponds to the final stable state. It is worth mentioning that this assignment is definitely confirmed by the MCR-ALS approach, with the extraction of two contributions relative to the symmetric stretching of the I_3^- molecule (115 cm^{-1}) and to its asymmetric stretching, which presents higher energy (141 cm^{-1}) [90]. Even though the asymmetric stretching (141 cm^{-1}) of the I_3^- is not supposed to be active in Raman spectroscopy, the specific environment of such molecule or its confinement inside the UiO-66 framework induces a small deformation on its structure. At that point, due to the lowering of its symmetry, this vibrational mode becomes optically active [85]. In addition, the spectrum assigned to perturbed I_2 also shows a band at around 156 cm^{-1} as a shoulder of the main band observed at 173 cm^{-1}; this feature is particularly observable in the case of I_2@UiO-66(Zr). This shoulder may be assigned to successive evolution stage of the perturbed iodine, probably superimposed with the residual contribution of the asymmetric stretching of I_3^-, which cannot be resolved by the MCR procedure [84,90]. Therefore, despite the complexity of the iodine species within the framework of UiO-66 materials, this works focuses on the contribution of the progressive evolution from the most currently reported ones: "free" I_2, "perturbed" I_2, and I_3^- [302].

The evolution and the relative intensity of these bands in Raman spectra (Figure 4.14) were found to be dependent on the Hf/Zr atomic ratio. The first spectra recorded after the 16h iodine exposure procedure show that the relative intensity of the 206 cm^{-1} band is much higher for I_2@UiO-66(Zr) (Figure 4.14a) than for I_2@UiO-66(Hf) (Figure 4.14c). The intensity of this band gradually decreases with time to the benefit of another at 173 cm^{-1} and also at 156 cm^{-1}, which becomes clearly observable. Then, the other band intensity at 115 cm^{-1} starts to increase. This finding reinforces the idea that the "free" I_2 trapped within the UiO-66 pores was slowly transformed into "perturbed" iodine and then, into I_3^-, in agreement with the UV-vis results

(Figure 4.13). However, this transformation did not follow the same kinetics in I_2@UiO-66(51% Hf) and in I_2@UiO-66(Hf). Indeed, contrary to what was observed in I_2@UiO-66(Zr), the band at 206 cm^{-1} is almost unperceptive in the Hf-containing UiO-66 compounds since the beginning of the analysis (t = 30 min). In these cases, the most intense band at t = 30 min is the one at 173 cm^{-1}, suggesting that the transformation from the "free" I_2 into "perturbed" I_2 had already occurred during the passage of the gaseous iodine stream. Moreover, it is interesting to note that the asymmetric I_3^- stretching at 141 cm^{-1} is clearly observed with I_2@UiO-66(51% Hf) and I_2@UiO-66(Hf) since the first hours of analysis, whereas this contribution is overlapped by the broad band at 156 cm^{-1} in I_2@UiO-66(Zr) and never observed, even after 72 hours. In addition, the higher intensities of the normalized bands at 206, 173, and 115 cm^{-1} highlight the dramatic influence of hafnium on the spectral concentrations of the iodine species. Indeed, high I_3^- contents are observed from shorter times (1-3 hours) and remain at a magnitude order of intensity of about five times for UiO-66(51% Hf) and nine times for UiO-66(Hf), compared to that of UiO-66(Zr) (Figure 4.16). Therefore, these results tend to demonstrate the more efficient and faster I_2 to I_3^- transformation in the presence of hafnium. In fact, the slow I_2 to I_3^- conversion in the case of UiO-66(Zr) creates a lot of I_n^- intermediate species (at about 150 cm^{-1}). However, when hafnium is present, the I_2 to I_3^- evolution occurs in such a time scale that these intermediates are not visible in the Raman spectra – this feature is highlighted by the absence of the band related to the I_n^- species at about 156 cm^{-1}.

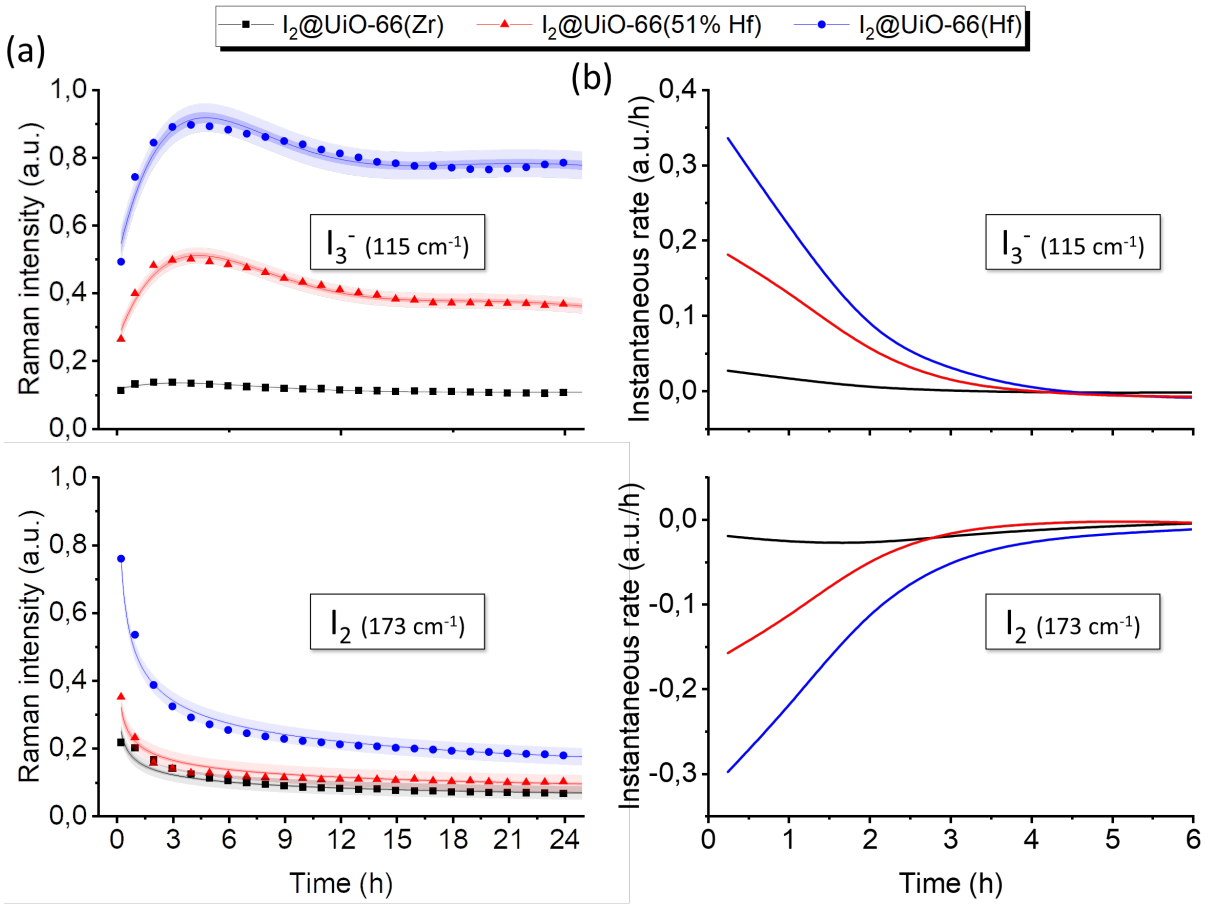

Figure 4.16: I_3^- (115 cm^{-1}) and "perturbed" I_2 (173 cm^{-1}) peak concentration profiles (a) and their first order derivative (b) for I_2@UiO-66(Zr) (black), I_2@UiO-66(51% Hf) (red), and I_2@UiO-66(Hf) (blue).

In order to emphasize this point, the higher normalized intensities achieved for the bands at 173 and 115 cm^{-1} were plotted as a function of the Hf/Zr atomic ratio and are presented in Figure 4.17. Aiming to confirm the results of the samples that have been in contact with the gaseous iodine for 16 hours, a comparison was also performed with the UiO-66 compounds in contact with the I_2 gas stream for only one hour. Although the signal/noise ratio of these spectra was relatively low due to weaker sorption rate (i.e., lower trapped iodine content within the UiO-66 pore) compared to the 16h iodine exposure, the trend reported in Figure 4.17 is similar for both bands and shows an increase of the spectral concentration of the iodine species with the hafnium content. This confirms that I_2@UiO-66(Hf) has the higher capacity to trap iodine within its pores and this uptake decreases together with the hafnium amount in the UiO-66 framework, which is in total agreement with the adsorption kinetic measurements (Figure 4.11).

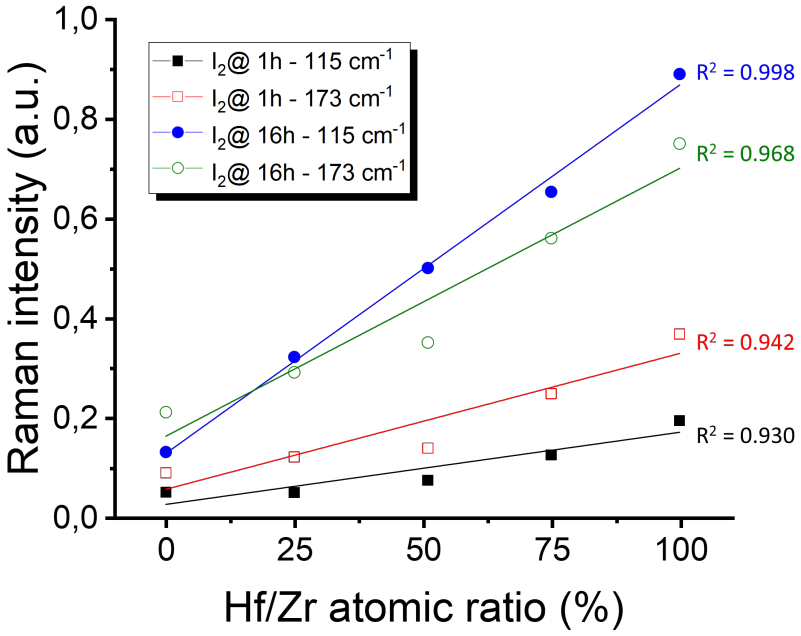

Figure 4.17: Higher achieved Raman intensities after 1h of I_2 contact for the bands at 115 cm^{-1} (black) and at 173 cm^{-1} (red); and after 16h of I_2 contact for the bands at 115 cm^{-1} (blue) and at 173 cm^{-1} (green).

Intending to obtain a systematic comparison for the iodine uptake and for the conversion kinetics as a function of hafnium content, the normalized intensities of the bands at 115 and 173 cm^{-1} (corresponding to adsorbed iodine and I_3^-, respectively) were plotted against time and are presented in Figure 4.16a. The corresponding instantaneous rate obtained from the first order derivative is reported in Figure 4.16b. The evolution of the bands at 115 and 173 cm^{-1} and their first order derivative confirms that the Hf/Zr atomic ratio influences the transformation of I_2 into I_3^- (Figure 4.16). The I_2@UiO-66(Hf) exhibits the fastest transformation as confirmed by its first order derivative (Figure 4.16b) and the highest Raman intensity plateau among all the materials, which suggests that it also captured more iodine than UiO-66(51% Hf) and UiO-66(Zr). In this case, the I_3^- highest signal was obtained after 4h, and the lowest I_2 signal after 24h. The I_2@UiO-66(51% Hf) presented an intermediate kinetic of iodine evolution. However, even though its uptake capacity is lower than I_2@UiO-66(Hf), the maximum I_3^- and minimum I_2 intensities were also reached after 4 and 24h, respectively. Finally, the I_2@UiO-66(Zr) had the lowest kinetic transformation and captured less iodine than the others. It reached the I_3^- and I_2 plateaus after 3 and 18h, respectively. These results agree with the adsorption kinetic measurements (Figure 4.11).

Aiming to obtain additional information on the interaction of iodine with the UiO-66 framework, the spectral study was continued by coupling the Raman study with FTIR analysis and focusing on the vibrational modes of the lattice perturbed by the iodine species above 400 cm^{-1}. The FTIR and the Raman spectra of the three pristine samples – UiO-66(Zr), UiO-66(51% Hf) and UiO-66(Hf) – and after the iodine contact under ambient air for 30 minutes and 72 hours are presented in Figure 4.18. Firstly, considering the FTIR spectra (Figure 4.18a), two different behaviors are observed in the 400-500 and 650-750 cm^{-1} regions depending on the nature of the metal Hf/Zr. In UiO-66(Zr), the relative intensity ratio ($I_{\lambda 1}/ I_{\lambda 2}$) of the bands at 729 and 743 cm^{-1} (I_{729}/I_{743}) decreases after 30 min and increases again after 72 h, reaching the initial intensity ratio of the pristine MOF. On the other hand, in pristine UiO-66(Hf), the band at 735 cm^{-1} progressively decreases in favor of a band at 745 cm^{-1}, which is the only one observed after 72 h of analysis. Since the bands at 729 – 735 cm^{-1} are related to the aromatic ring torsion mode, the spectral change indicates that the I_2 molecules interact with this part of the UiO-66 during its evolution, regardless of the nature of the metal that is present in the structure. This finding is in agreement with the CTCs between the I_2 and the aromatic ring of the BDC linker [77,78].

Moreover, the spectra recorded for I_2@UiO-66(Hf) show the development of a new band at 675 cm^{-1}, at the same time that the relative intensity of the band at 443 cm^{-1} decrease when comparing to the spectrum UiO-66(Hf). This evolution is not observed for UiO-66(Zr), while the UiO-66(51% Hf) presents an intermediate behavior between the UiO-66(Zr) and the UiO-66(Hf). These bands, at 675 and 443 – 446 cm^{-1}, are related to the μ_3–O stretching and μ_3–OH antiphase stretching, respectively. This finding suggests that the oxo and hydroxyl groups have an influence over the iodine transformation within the UiO-66 structure when hafnium is present. Considering the Raman spectra (Figure 4.18b), differences are also noticed right after the end of I_2 exposure (t + 30 min) and after 72 hours for the bands at about 1144, 1433, and 1452 cm^{-1} in UiO-66(Hf), whereas these modes are very weakly perturbed in UiO-66(Zr). It is worth mentioning that these bands are attributed to organic linker vibrations (Table 4.3). No changes related to the metal Hf/Zr inorganic polyoxo/hydroxo cluster vibrational modes were identified in the Raman spectra after the iodine contact. However, the linker-related aromatic C–H stretching modes in the 3050-3080 cm-1 spectral range are more perturbed in I2@UiO-66(Hf) than in I2@UiO-66(Zr) (Figure 4.19).

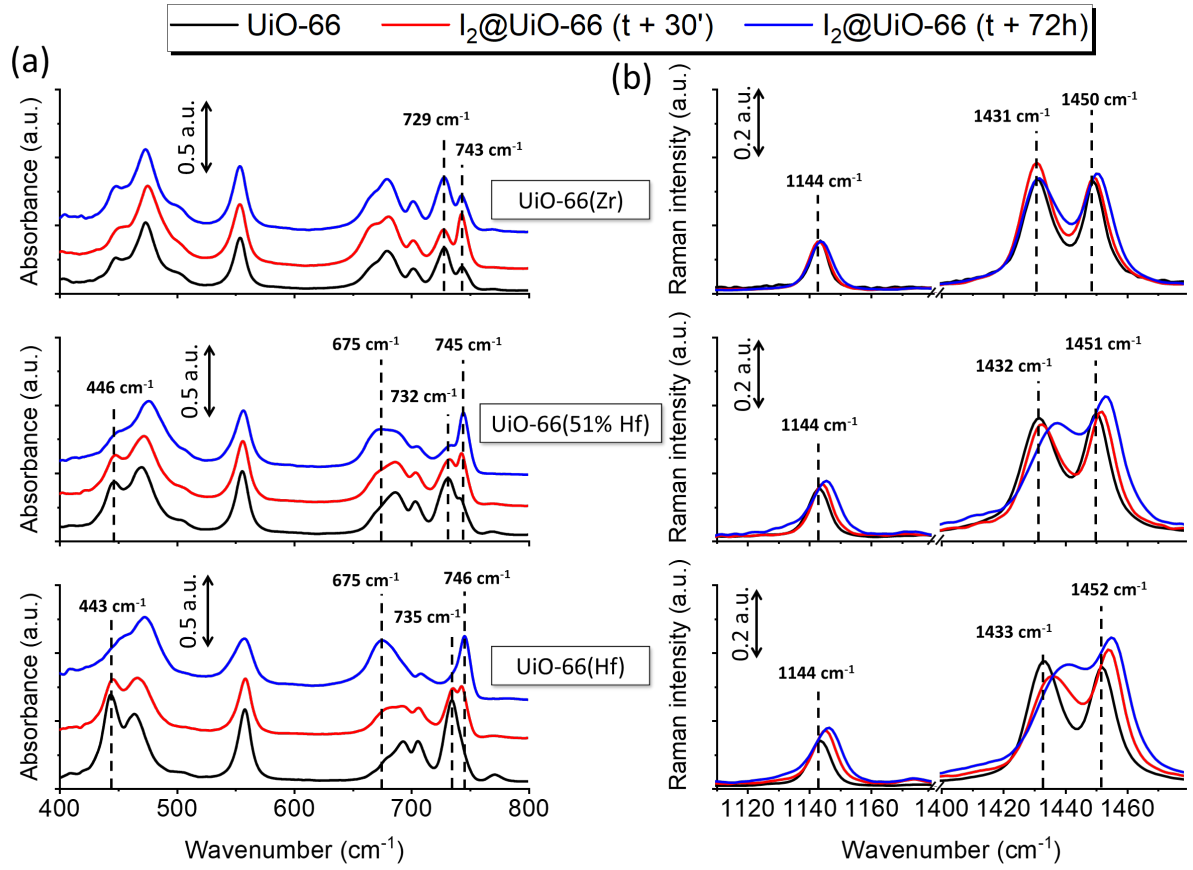

Figure 4.18: (a) from top to bottom: FTIR spectra of UiO-66(Zr), UiO-66(51% Hf), and UiO-66(Hf). (b) from top to bottom: Raman spectra of UiO-66(Zr), UiO-66(51% Hf), and UiO-66(Hf). In black: the spectra of the pristine MOF; in red: the spectra of the I_2@UiO-66 after 30 minutes of atmosphere exposure; in blue: the spectra of the I_2@UiO-66 after 72h of atmosphere exposure.

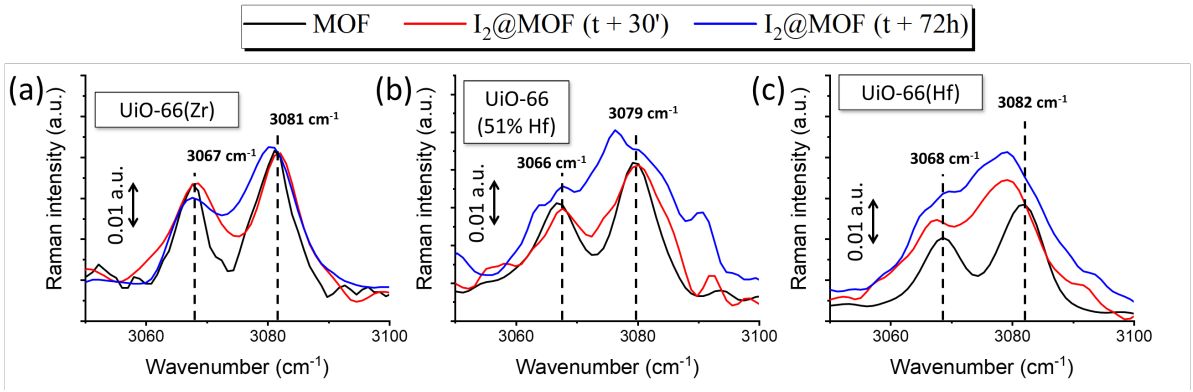

Figure 4.19: Raman spectra of (a) UiO-66(Zr), (b) UiO-66(51% Hf), and (c) UiO-66(Hf) displaying the C-H stretching range. In black: the spectra of the pristine MOFs; in red: the spectra of the I_2@MOFs after 30 minutes of atmosphere exposure; in blue: the spectra of the I_2@MOFs after 72h of atmosphere exposure.

4.3.3. EPR investigation of the possible metal center redox

Since the substitution of zirconium by hafnium induces clear spectral change in the Raman/FTIR spectra and leads to significant changes in the I_2 adsorption process (kinetic of reaction and nature of stable species), the role of these metallic centers was further investigated using EPR to determine whether a redox mechanism involving the cation (Zr^{4+} or Hf^{4+}) was associated with the I_2 capture by UiO-66. Aiming to detect and to enhance such redox process, the I_2@UiO-66(Zr) and I_2@UiO-66(Hf) were irradiated after the exposure to iodine, as presented in Figure 4.20. The spectra reveal that the metallic cations (Zr^{4+} and Hf^{4+}) are not reduced to its trivalent state during the I_2 adsorption and transformation to I_3^-, as shown by the absence of a signal at $g < 2$. In fact, as the g matrix is governed by the electronic structure of the transition metal, if reduction of Hf^{4+} and Zr^{4+} occurs, it must result in Hf^{3+} and Zr^{3+}, which exhibits a d^1 electronic configuration that corresponds to a g value below $g = 2$ [303,304].

The EPR spectra obtained after I_2@UiO-66(Hf) irradiation show a small peak centered at $g = 2.01217$ (Figure 4.20b) and a second peak at $g = 2.00230$ that develop through the irradiation time. The former signal could correspond to an unpaired electron located over an oxygen atom, while the latter signal is assigned to a free electron. When the irradiation of the I_2@UiO-66 sample is cut off, both signals remain with lower intensity. It is worth noting that, although the irradiation of I_2@UiO-66(Zr) induces the formation of both signals, the peak at $g = 2.00230$ is very weak compared to that of I_2@UiO-66(Hf). This result could be related to the larger amount of I_3^- stabilized in the pores of I_2@UiO-66(Hf), as revealed by Raman spectroscopy (Figure 4.14 and Figure 4.16). In fact, the presence of higher amount of I_3^- is associated with the formation of more unpaired electrons in the course of the $I_2 \rightarrow I_3^-$ transformation. Furthermore, Miyajima *et al.* evaluated the interaction between iodine and aromatic compounds present in coal tar pitches by EPR [72]. They verified that the CTCs between iodine and aromatic compounds having a π-conjugated system produce an EPR signal – very similar to that obtained in this work – that is related to the presence of organic cation radicals [72]. These statements reveal that the reaction mechanism between UiO-66 and I_2 only involves the organic part of the framework and is not influenced by a redox phenomenon of the metal sites.

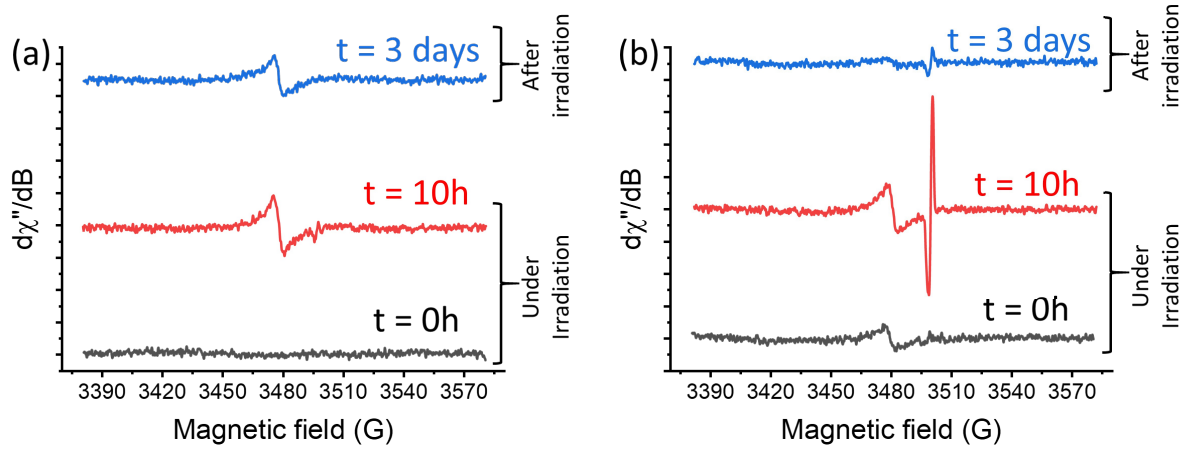

Figure 4.20: EPR spectra under irradiation at t = 0 h (black), at t = 10 h (red), and after the end of the irradiation at t = 72 hours for (a) I_2@UiO-66(Zr) and (b) I_2@UiO-66(Hf).

4.3.4. Proposed model for the I_2 reduction mechanism

To sum it up, the influence of the oxo and hydroxyl groups on the iodine evolution within UiO-66(Hf) structure (Figure 4.18a) agrees with the higher acid character of hafnium compared to zirconium [285,294,295]. Actually, in UiO-66(Hf), the shrinkage of the μ_3–O and M–(OC) bonds combined with the increase on the length of the O–C bond impoverishes the electronic cloud on the carboxylate group [294,299]. Then, aiming to neutralize this disparity, the electronic cloud from the aromatic ring is delocalized towards the carboxylate. This effect enriches the electron density on the oxo and hydroxyl groups, which affects their vibrational modes (Figure 4.18a). This phenomenon, coupled with the slightly lower band gap of Hf-based UiO-66 (Figure 4.6 and Table 4.2), may also explain the different I_2 loading (Figure 4.11 and Table 4.2) and kinetic behavior (Figure 4.16) in both samples. Indeed, when a semiconductor is irradiated, photons that have energy greater than or equal to the band gap of that material can excite electrons from the VB to the CB. In this process, when an electron (e^-) jumps into the CB, it leaves a hole (h^+) in the VB, which is considered as a positive charge [187]. Although these entities have relatively low lifetimes and can annihilate themselves by recombining due to electrostatic interactions, this effect is reduced for materials with low mobility of charge carriers (electrons and holes) [108]. In this scenario, some materials can trap the produced electrons, the holes, or both [182]. Since UiO-66 compounds present a pure linker-based transition [27], both the electrons and holes are created in the aromatic part of the UiO-66 network, which is confirmed by the absence of a redox phenomenon on the metal site – as demonstrated by EPR – and can be related to the low binding energy of the d^0 orbitals of Zr^{4+} and Hf^{4+} [27]. However, due to the

higher delocalization of the electronic cloud from the BDC linker towards the inorganic cluster in UiO-66(Hf), the electron-hole recombination is expected to be more difficult, which favors the formation of I_3^- and, consequently, its adsorption on the aromatic ring.

These features allowed the proposition of a model for the transformation mechanism of I_2 to I_3^- in the pores of UiO-66, which is presented in Figure 4.21. In this case, the entire mechanism is based on the formation of an electron-hole pair in the BDC linker, as represented by the electron donor-acceptor (EDA) complex between the BDC linker and the I_2 gaseous molecule, which should be favored by the smaller band gap of UiO-66(Hf) when comparing to that of UiO-66(Zr). Here, it is worth mentioning that the connection between organic and solid-state chemistry is still not highly developed in the case of MOFs. As reported by Mancuso *et al.*, [305] MOFs can present characteristics of both a solid with a well-defined boundary and also of an infinite quasi-molecule.

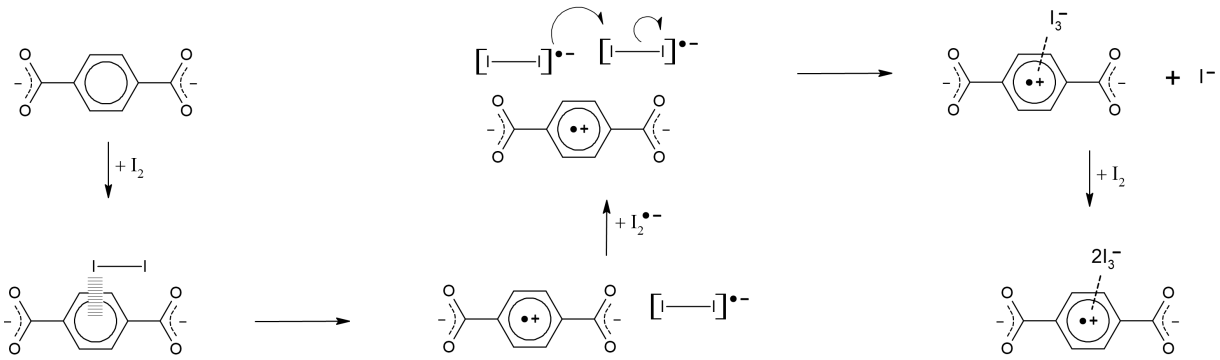

Figure 4.21: Proposed model for the mechanism of I_2 to I_3^- transformation within UiO-66 framework.

According to Kolobov *et al.*, [105] this creates some unusual mixed concepts between coordination chemistry (i.e., LMCT) and semiconductors physics (band gap structure) in the MOF literature. From this perspective, one must keep in mind that the proposed model for the mechanism in this work only represents a monomolecular interaction between the BDC linker and I_2 molecules. When the entire crystalline structure of UiO-66 is considered, the unpaired electron created in the aromatic ring should be able to move through the MOF network. In fact, the EPR signal at g = 2.01217 (related to an unpaired electron located over an oxygen atom), suggests that the electron can move over the UiO-66 lattice through the oxygens present in the inorganic $[M_6O_4(OH)_4]$ (M = Zr, Hf) cluster. Also, when considering the entire UiO-66 lattice, the formation of the electron-hole pair can occur in different linkers, which would help to avoid the recombination process. For instance, Santiago Portillo *et al.* evaluated the lifetimes of

photoinduced states in a NH_2-UiO-66(Zr/Ti) material by transient absorption spectroscopy (TAS) and concluded that the bleaching of the ground state are related to a combination of triplet excited states and trapped electrons, which can live up to 25 μs after the lase pulse, demonstrating the relative short life-times of these entities [306]. That being said, the next steps of the mechanism can be easily described by a monomolecular approach in which through the proximity and subsequent polarization of a gaseous iodine molecule by the aromatic ring of the BDC linker, the excited electron jumps from the BDC conduction band (HOCO, π*) to the conduction band of the I_2 molecule (LUMO, σ^*_{5p}), forming an intermediate radical species: $I_2^{\bullet-}$. Then, the radical iodine species can react with another $I_2^{\bullet-}$ to form I_3^- and I^- – which was already described elsewhere for a system composed by iodine in acetonitrile solution [300]. At this point, it is worth mentioning that the EPR spectrum of iodine ions and radicals are hardly observed at room temperature due to the enormous anisotropy of their *g*-factor and to the fast electron spin relaxation that is caused by the large spin-orbit interaction of the iodine atom [72]. For this reason, no signal was observed for the I^- and $I_2^{\bullet-}$ species in the EPR measurements (Figure 4.20).

Finally, the recently formed I_3^- is further stabilized in UiO-66(Hf) than in UiO-66(Zr) due to the higher acidity of Hf^{4+} compared to that of Zr^{4+}, which is also responsible for the smaller lattice parameter of UiO-66(Hf) (*a* = 20.7232(7) Å against *a* = 20.7696(8) Å in UiO-66(Zr)). The enhanced I_3^- stabilization in UiO-66(Hf) should be ascribed to the higher delocalization of the electronic cloud towards the carboxylate group in the presence of hafnium [294,299], which is caused by the shrinkage of the M–(OC) bond (Hf–(OC) = 2.086(8) Å and Zr–(OC) = 2.107(2) Å) [264,286] and by the increase on the length of the O–C bond (UiO-66(Hf): 1.304(21) Å; UiO-66(Zr): 1.256(2) Å) [264,286]. This feature impoverishes the electronic density in the aromatic cycle of the BDC linker, which further stabilizes the $BDC^{\bullet+}$ radical and improves its interaction with the I_3^- species.

4.4. Conclusions

In this work, a series of UiO-66 with different Hf/Zr metal ratios was successfully synthesized and thoroughly characterized before assessing their ability to capture iodine. Characterization shows that crystallites are slightly larger at higher hafnium contents and that the BET specific surface area, lattice parameters and band gap decrease from UiO-66(Zr) to

UiO-66(Hf). The substitution of zirconium by hafnium also induces significant shifts and relative intensity changes in the FTIR and Raman spectra for some bands, which was ascribed to a higher acidity of hafnium compared to zirconium. After exposure to iodine, UiO-66(Hf) showed the best loading capacity (285 $g.mol^{-1}$, followed by UiO-66(51% Hf) with 250 $g.mol^{-1}$, and by UiO-66(Zr) with 230 $g.mol^{-1}$). The Raman spectra recorded at the end of iodine exposure process show new bands in the 100-210 cm^{-1} region attributed to various iodine species. Chemometric analysis using MCR-ALS algorithm allowed the extraction of three spectra corresponding to I_3^-, "perturbed" I_2 and "free" I_2 and the evolution of these species as a function of time was correlated to the kinetic of I_2 to I_3^- transformation. The faster conversion is observed for UiO-66(Hf) followed by UiO-66(51% Hf), and by UiO-66(Zr). Furthermore, FTIR and Raman spectra of the samples obtained after iodine exposure showed that the oxo and hydroxyl groups of the inorganic clusters are perturbed in UiO-66(Hf) but not in UiO-66(Zr). These results reveal that the metal content of UiO-66 has an influence on the evolution of trapped iodine in UiO-66. In this context, since EPR spectra revealed that there is no redox phenomenon in the metal cations (Hf^{4+} and Zr^{4+}) during the I_2 to I_3^- transformation, the smaller band gap of UiO-66(Hf) could explain the lower electron-hole recombination rates. This feature may favor the I_3^- formation at the same time that the higher acidity of Hf^{4+} helps to stabilize the I_3^- species in the $BDC^{\bullet+}$ radical. This chapter is based on the article published in the ACS Applied Materials & Interfaces journal (ACS Appl. Mater. Interfaces 2022, 14, 29916−29933).

Chapter V: Insights on the Iodine Diffusion Process Within UiO-67_NH_2 Single Crystals Using Raman Spectroscopy

5.1. Introduction

Among the different isoreticular structures that can be obtained with the UiO family, the UiO-67_NH_2 member stands out due to its ability to form single crystals with up to 140 µm in size [12]. Although the zirconium based UiO-67_NH_2 was already reported in the literature for capturing I_2, to this day, there is no mention of a hafnium-based UiO-67_NH_2 being used for such purposes. Nevertheless, UiO-67(Zr)_NH_2 was found to be one of the best candidates among UiO compounds to adsorb gaseous iodine after 48 hours of exposure (with an I_2 uptake capacity of 1071 $mg.g^{-1}$ in dynamic conditions) [12]. Therefore, it is of great interest to evaluate the I_2 capture by UiO-67_NH_2 with different metal (Zr/Hf) compositions by coupling the best materials for iodine capture and I_3^- stabilization from the two previous studies regarding I_2@UiO compounds [12,13]. In fact, the comprehension of this I_2 into I_3^- transformation can improve the systems used to capture iodine species and guarantee a better stabilization of such pollutants in a long term.

Therefore, because of the relatively large size of crystals that can be obtained for the UiO-67_NH_2 compounds, this material makes it possible to carry out different studies that could only be conducted in single crystal samples (i.e., Raman mapping and SC-XRD). For this reason, the present chapter focuses on adsorbing gaseous iodine in UiO-67_NH_2 compounds with three metal compositions: zirconium, hafnium, and a mixture of zirconium and hafnium (1/1 molar ratio). Apart the classical structural and textural characterizations (XRD, BET, SEM), this study was mainly conducted by using different vibrational (IR, Raman) and electronic (UV-Vis) spectroscopies. In particular, Raman spectroscopy was able to produce 2D and 3D mapping by means of different wavelength excitation sources (515, 633, and 785 nm) in order to probe the encapsulated iodine molecules. In this way, resonance effects with both I_3^- and I_2 species are to be expected and the spatial distribution of such components in the different UiO-67(Zr,Hf)_NH_2 crystals were highlighted.

5.2. Structural characterization of the pristine UiO-67_NH_2 samples

Initially, the metal composition of the three samples was evaluated using ICP-OES, SC-XRD and EDS spectroscopy (Table 5.1). The results show that hafnium is found in higher concentrations compared to zirconium in the bimetallic UiO-67(Zr/Hf)_NH_2. Yet, these values are very close to the initial ratio of precursors during the synthesis (1:1).

Table 5.1: Metal content ratio (at.%) of Hf and Zr calculated using ICP-OES, SC-XRD, and EDS spectroscopy for the different UiO-67_NH_2 samples.

UiO-67_NH_2	Metal content ratio ($\%_{at}$)					
(M)	ICP-OES		SC-XRD		EDS	
	Hf	Zr	Hf	Zr	Hf	Zr
Zr	0	100	0	100	0	100
Zr/Hf	60.0	40.0	53.7	46.3	54.0	46.0
Hf	100	0	100	0	100	0

5.2.1. Crystallography and textural properties

To facilitate the comprehension and discussion of this section, a comparison between the structures of UiO-66_NH_2 and UiO-67_NH_2 is presented in Figure 5.1.

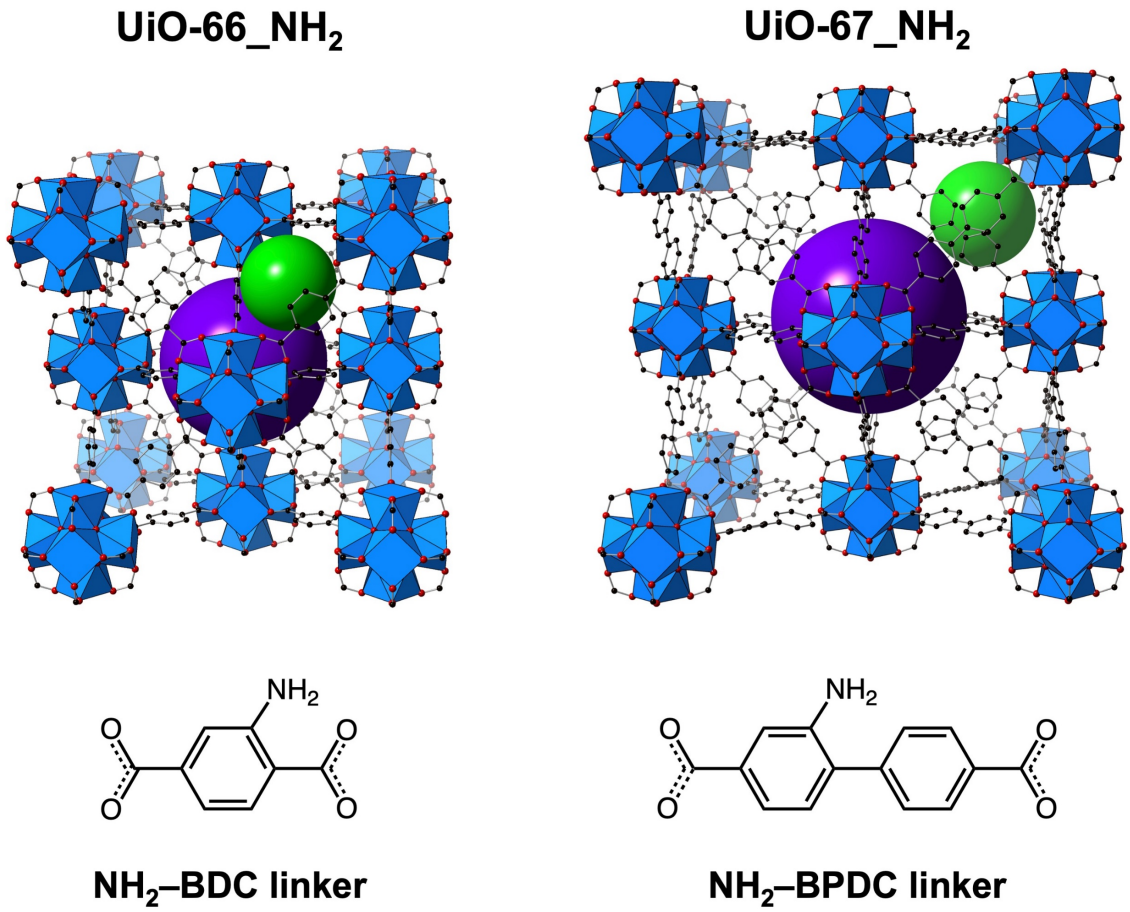

Figure 5.1: Structure of UiO-66_NH_2 and UiO-67_NH_2 showing their respective organic linkers: NH_2–BDC (2-aminobenzene-1,4-dicarboxylate) and NH_2–BPDC (2-amino-[1,1'-biphenyl]-4,4'-dicarboxylic acid). The octahedral and tetrahedral cages are represented in purple and green, respectively. The amino group and the hydrogen atoms were omitted from the structure for better clarity.

The crystal morphology of the UiO-67_NH_2 compounds was evaluated from SEM technique and is represented in Figure 5.2 alongside the EDS elemental mapping of the UiO-67_NH_2 samples. All the samples exhibit crystals with typical octahedral shape, which is expected for the UiO family [12,307]. It was observed that the crystal growth was favored in the bimetallic UiO-67(Zr/Hf)_NH_2 sample, which exhibits the biggest crystal sizes (∅ ≈ 140 μm) compared to both the UiO-67(Hf)_NH_2 and UiO-67(Zr)_NH_2 – ∅ ≈ 44 μm and ∅ ≈ 51 μm, respectively. Moreover, the triangular surfaces of the octahedra are smoother for the bimetallic UiO-67(Zr/Hf)_NH_2, when compared to the other two samples. These features suggest that the amino group and the metal sites have a co-influence on the growth of UiO-67_NH_2 crystal. According to the work of Firth *et al.* [308] over the crystal growth of hafnium-based UiO-66, the organic linkers do not play an important role in the initial cluster formation; instead, they are involved latter in the reaction through post-cluster formation linker exchange. The framework growth with double cluster and even inter-cluster formation was ascribed to a transition from the **fcu** to a **hcp** unit [308]. Nevertheless, this was not the case in this work, as proven by SC-XRD. That being said, the improved growth of the crystals in the bimetallic UiO-67(Zr/Hf)_NH_2 can be ascribed to a cooperative effect between the two metals and the rearrangement of the framework. In fact, Firth *et al.* [308] demonstrated that the crystalline framework grows alongside the linking of clusters together, suggesting that once they are linked, the dicarboxylate linkers are less labile and dissociation is kinetically and entropically less favorable. In other words, the co-presence of zirconium and hafnium must influence the dissociation of the NH_2–H_2BPDC linkers and their competition with the benzoic acid, slowing the reaction and consequentially, favoring the crystal growth.

The distribution of zirconium, hafnium, and nitrogen in the crystals of the prepared compounds was evaluated through SEM technique and EDS elemental mapping (Figure 5.2). It is worth mentioning that shadow spots present in the bottom part of the images are due to the size of the crystals and to their relative position to the EDS detector, which reduces the intensity of the signal captured from these areas. Also, zirconium and hafnium elements are well distributed in the bimetallic UiO-67_NH_2, revealing that the UiO-67(Zr/Hf)_NH_2 structure exhibits a homogeneous distribution of metals rather than two distinct families of crystal phases with an aggregation process (this would result in one phase with high hafnium content, and a second one with high zirconium content).

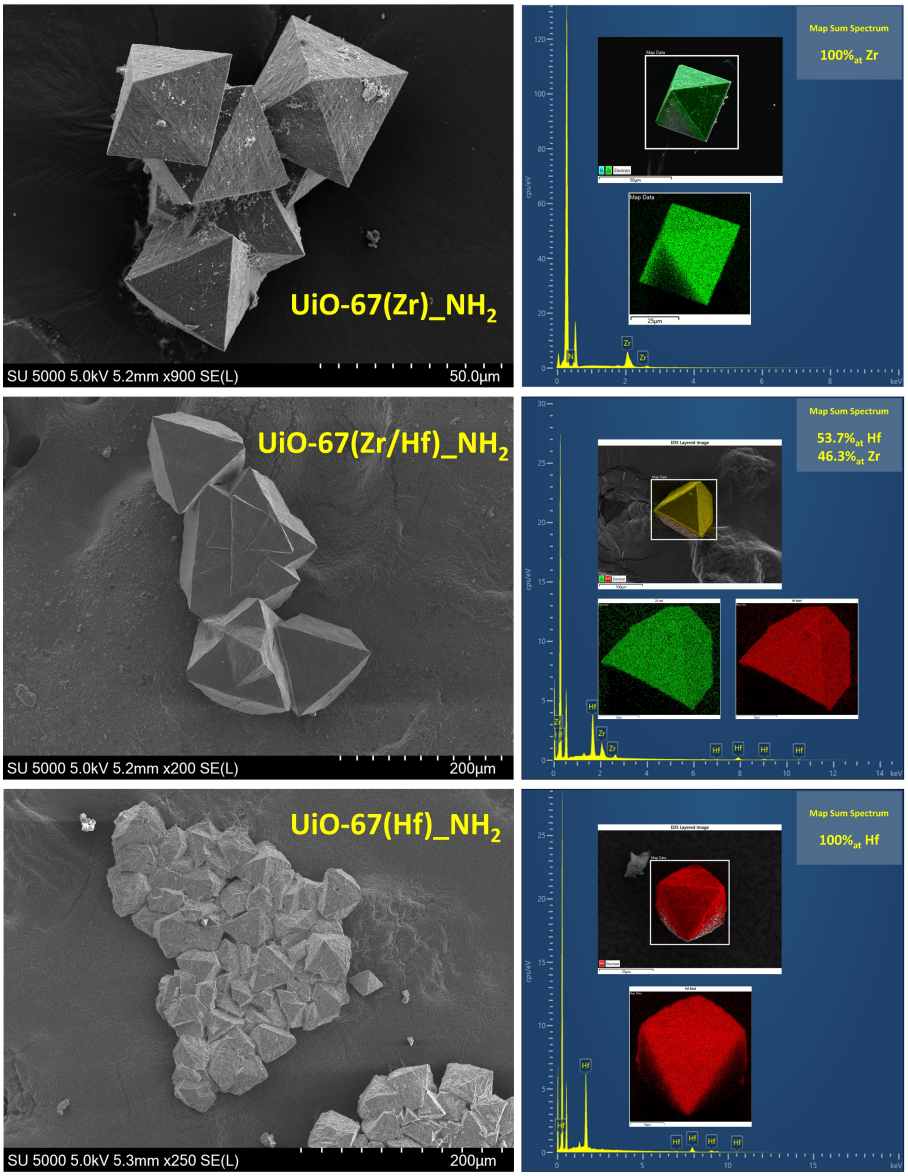

Figure 5.2: On the left: SEM images of UiO-67(Zr)_NH_2 (on top), UiO-67(Zr/Hf)_NH_2 (in the middle), and UiO-67(Hf)_NH_2 (on bottom). On the right: SEM-EDS layered images, elemental mapping, and EDS spectra. In green: $Zr_{L\alpha 1}$. In red: $Hf_{M\alpha 1}$.

Due to the relatively large and well-shaped octahedral crystal size (24 – 140 □m) obtained for the UiO-67(Zr,Hf)_NH_2 compounds, SC-XRD analysis was carried out for the three samples, for which diffraction intensities were collected after the activation procedure. The positions and relative intensities of the diffraction Bragg peaks obtained from the SC-XRD refinement for the UiO-67(Zr,Hf)_NH_2 compounds are in good agreement with data from literature, with the observation of a typical cubic cell (space group *Fm*-3*m*, n°225), and a cell parameter of about 26.7 Å [268,309,310]. All three samples exhibited an important disorder related to the organic linker rotational movement along its axis, as verified by the shape of the elongated

ellipsoids related to the aromatic carbons (Figure 5.3a). Moreover, the amino group also exhibited a great disorder associated due to the diffraction technique itself, which usually reveals the average positions of electronic densities in case of disordering configuration. In fact, the nitrogen atoms may have four equivalent positions because of the symmetry of the linker (2-amino, 3-amino, 2'-amino and 3'-amino) and therefore, they were refined considering an arbitrarily occupancy rate of 25% for each of these four possible sites (Figure 5.3b). On the other hand, it is not possible to distinguish the bridging □□–OH and □3–O positions (oxo and hydroxyl groups from the inorganic cluster that are connected to three M^{4+} cations, where M = Zr or Hf) within the metallic hexameric [$M_6O_4(OH)_4$] cluster because of their high cubic symmetry (*Fm*-3*m*), which creates an elongation on the ellipsoids (correlated to the hybrid OH and O group). Again, the refined sites for the □3–OH/O species are related to the average positions, considering that M–O bond distance will be shorter than the M–OH bond distances. Furthermore, the Zr/Hf ratio in the bimetallic UiO-67(Zr/Hf)_NH_2 crystal (46%$_{at}$ of Zr and 54%$_{at}$ of Hf) was obtained through the refinement of the occupancy rate considering that both cations were located at a unique spatial position in the hexanuclear core.

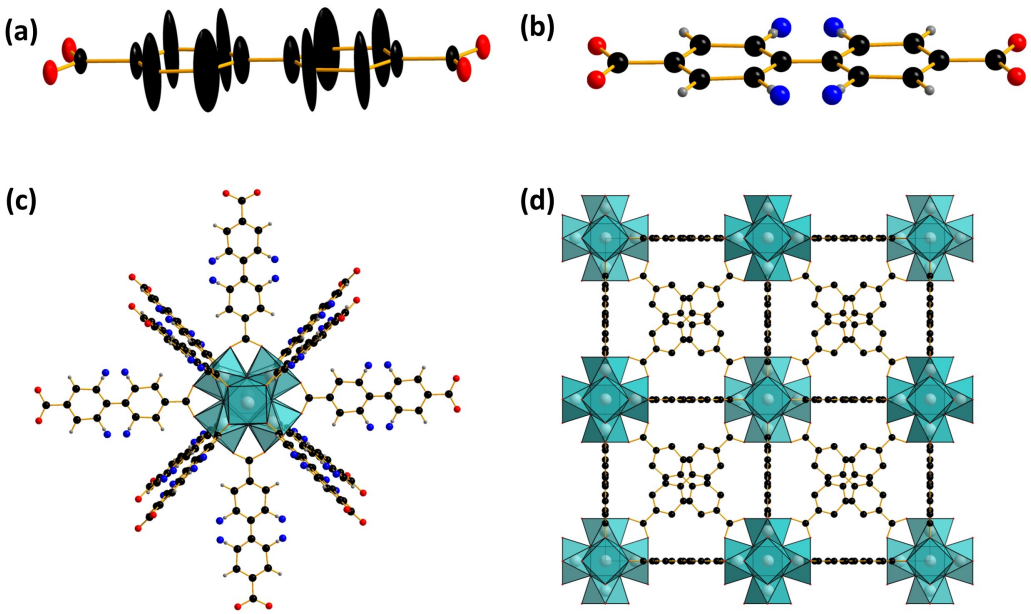

Figure 5.3: Structural disorder (a) of the carbon atoms of the aromatic rings of the linker and (b) of the NH_2 function. Structural representation (c) of an hexameric $M_6O_4(OH)_4(NH_2\text{-BPDC})_{12}$ node, and (d) of the UiO-67_NH_2 network (in this last case hydrogen and nitrogen atoms have been omitted for clarity).

The distances and the angles corresponding to the metal-oxygen bonds within the atomic arrangement of the structure are an important feature to be evaluated in these systems, as they were already ascribed to influence the iodine interaction with UiO-66(Zr,Hf) compounds [13]. The lattice parameter *a* was found to depend on the hafnium content, as the Zr^{4+} substitution by Hf^{4+} is sufficient to reduce it from 26.786(2) Å in UiO-67(Zr)_NH_2, to 26.7376(6) Å and 26.723(2) Å in UiO-67(Zr/Hf)_NH_2 and UiO-67(Hf)_NH_2, respectively (Table A3). This decrease is in agreement with the behavior observed for a series of Zr/Hf-based UiO-66 compounds [13] and was ascribed to the shrinkage of the M–(OC) bond when passing from the UiO-66(Zr) (Zr–(OC) = 2.107(2) Å) [264] to the UiO-66(Hf) (Hf–(OC) = 2.086(8) Å) [285]. In fact, since Zr^{4+} and Hf^{4+}exhibit quite similar ionic radius (0.84 Å and 0.83 Å for Hf^{4+} and Zr^{4+}, respectively) concomitantly to a higher electronegativity of hafnium compared to that of zirconium (0.96 against 0.90), the Hf^{4+} is considered to present a higher Lewis acidity than the Zr^{4+} [289,290,294,295,299,311]. For such reason, the Hf^{4+} presence in UiO-66 samples induces a stiffening of the interatomic bond between the hexanuclear [$M_6O_4(OH)_4$] core and the oxygen from carboxyl groups [285]. In the case of the UiO-67(Zr,Hf)_NH_2 compounds, the occurrence of hafnium also reduces the M–(OC) bond length from 2.221(5) Å in UiO-67(Zr)_NH_2, to 2.204(5) Å in UiO-67(Zr/Hf)_NH_2, and to 2.206(9) Å in UiO-67(Hf)_NH_2, as calculated from the single-crystal XRD refinement. This feature is coherent with the higher acid character of Hf^{4+}, as mentioned above.

In order to complement the textural properties of the UiO-67(Zr,Hf)_NH_2 compounds, N_2 sorption experiments were conducted after the activation procedure. All the three samples exhibited a type I isotherm (Figure 5.4) according to the IUPAC classification, which is indicative of microporous materials [296]. Also, the SSA values obtained for the compounds by applying the BET method are similar to other reports found in the literature [12], with 1329, 1234, and 914 $m^2.g^{-1}$ for UiO-67(Zr)_NH_2, UiO-67(Zr/Hf)_NH_2 and UiO-67(Hf)_NH_2, respectively. The related porous volumes are 0.68, 0.65, and 0.48 $cm^3.g^{-1}$, respectively. Moreover, the substitution of the zirconium by hafnium reduced the SSA values, which has already been reported in the case of the UiO-66(Zr,Hf) series, as detailed in Chapter IV [13]. This decreasing behavior is consistent with the atomic weight of both considered elements (Zr = 91.224 $g.mol^{-1}$; Hf = 178.49 $g.mol^{-1}$), as the SSA is normalized by the mass of the material.

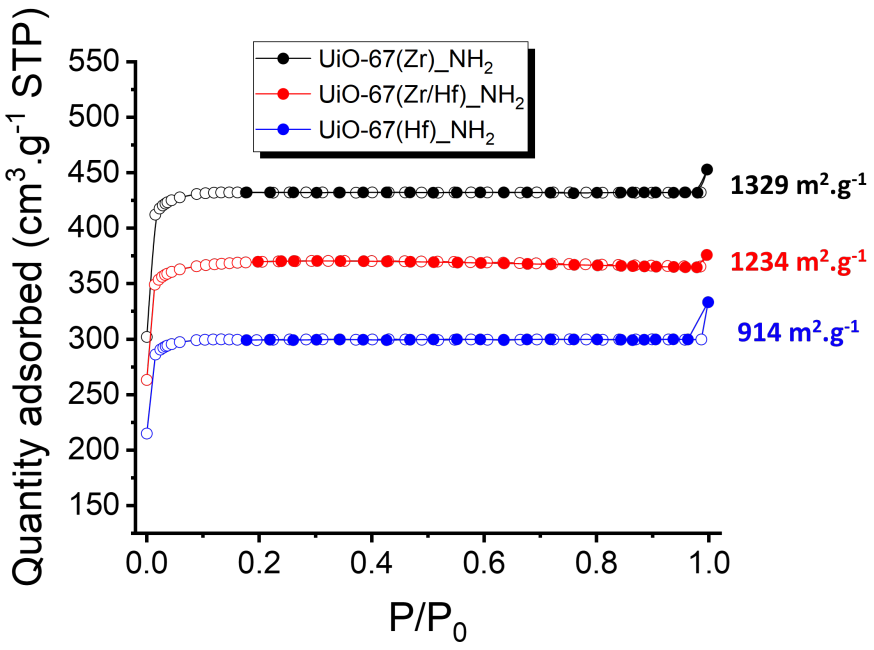

Figure 5.4: N_2 sorption isotherms at 77K, for UiO-67(Zr)_NH_2 (black), UiO-67(Zr/Hf)_NH_2 (red) and UiO-67(Hf)_NH_2 (blue) degassed at 60 ºC.

5.2.2. Evaluating defects using liquid NMR

Moreover, the presence of defects related to missing NH_2-BPDC linkers was evaluated using liquid ^1H NMR spectroscopy (Figure 5.5). For comparison purposes, the benzoate spectrum is represented in the Annex file (Figure A22). Indeed, the benzoate (coming from the deprotonation of benzoic acid used as modulator in the syntheses process) is able to partially substitute the NH_2–BPDC linker by generating defects of organic ditopic linkers. In fact, when an organic dicarboxylate linker is removed from the UiO-67_NH_2 structure, it leaves the coordinating site with metallic centers (Zr or Hf) available for two monotopic benzoate molecules instead. Considering these two types of coordination modes (monotopic versus ditopic), if the molecular formula for the pristine UiO-67_NH_2 compound is represented by $[M_6O_4(OH)_4L_6]$ (L = NH_2–BPDC), the absence of x ditopic linkers creates $2x$ carboxylate defects. Therefore, considering the presence of benzoate (B), the experimental molecular formula must be written as $[M_6O_4(OH)_4(L)_{6-x}(B)_{2x}]$. With that in mind, the integration of the NMR signal related to the benzoic acid was compared to that of the NH_2–BPDC linker for the three compounds, according to Equation (4.1).

$$\frac{2x}{6-x} = \frac{\int(B)}{\int(L)} \qquad (4.1)$$

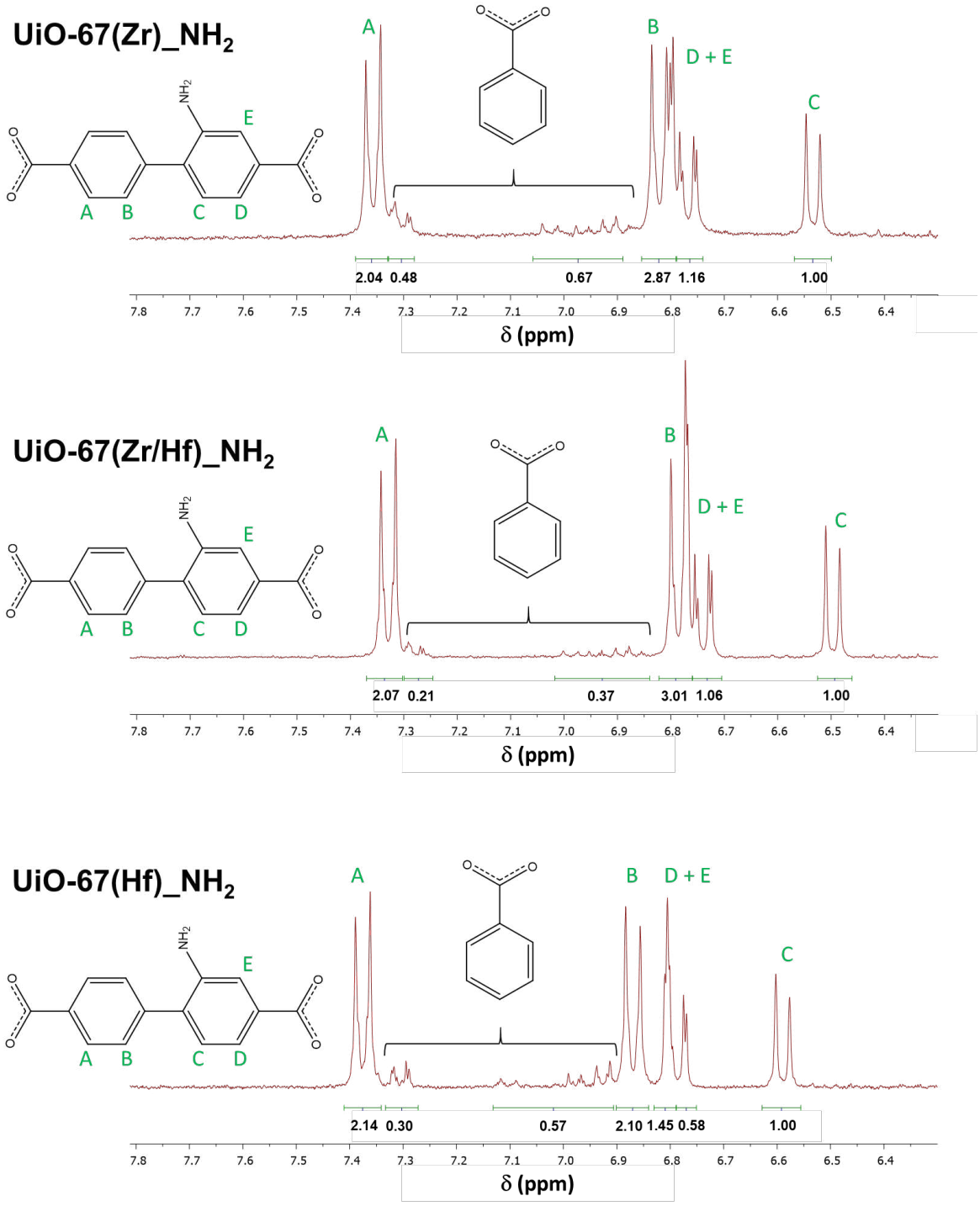

Figure 5.5: ^{1}H NMR spectra of UiO-67(Zr)_NH_2, UiO-67(Zr/Hf)_NH_2, and UiO-67(Hf)_NH_2 showing the contributions related to the NH_2-BPDC linker and to benzoate and formate molecules. The integrated values for each signal are displayed on the bottom part of the graphic.

In light of this, the following chemical formulas were obtained considering the defects for each sample: UiO-67(Zr)_NH_2 = $[Zr_6O_4(OH)_4](L)_{5.38}(B)_{1.24}$]; UiO-67(Zr/Hf)_$NH_2$ = $[Zr_{2.76}Hf_{3.24}O_4(OH)_4](L)_{5.67}(B)_{0.66}$]; UiO-67(Hf)_$NH_2$ = $[Hf_6O_4(OH)_4](L)_{5.52}(B)_{0.96}$]. Therefore, the UiO-67(Zr)_NH_2, UiO-67(Zr/Hf)_NH_2, and UiO-67(Zr)_NH_2 compounds were found to exhibit 10.3, 5.5, and 8.0% of missing NH_2–BPDC linkers, respectively. These results show that the number of defects in the samples are not directly connected to the hafnium content.

At this point, to facilitate the comprehension of this chapter, the textural and physical chemical properties of the UiO-67(Zr,Hf)_NH_2 compounds were summarized in Table 5.2.

Table 5.2: Resume of the physical chemical properties for the UiO-67_NH_2 compounds.

UiO-67_NH_2	Crystal size	$SSA_{(BET)}$	Microporous volume	Missing NH_2-BPDC linkers
(M)	µm	$m^2.g^{-1}$	$cm^3.g^{-1}$	%
Zr	32 – 51	1329 ± 36	0.68	10.3
Zr/Hf	105 – 140	1234 ± 34	0.65	5.5
Hf	24 – 44	914 ± 25	0.48	8.0

5.2.3. Vibrational spectroscopy

The vibrational modes of the synthesized UiO-67(Zr,Hf)_NH_2 series were investigated by using FTIR and Raman spectroscopies (Figure 5.6) and are in agreement with other reports found in the literature [312,313]. Although no hydroxyl groups were revealed from the single-crystal XRD refinement, the first FTIR absorption band, at 440 cm^{-1} (Figure 5.6), was ascribed to the asymmetric stretching of the μ_3–OH groups [268,312]. The absence of this contribution in the crystallographic structure is due to a limitation of the XRD technique, which is not able to thoroughly locate the position of hydrogen atoms from the hydroxyl groups, present in the hexameric $[(Zr,Hf)_6O_4(OH)_4]$ core, related to the UiO topology. Nevertheless, the occurrence of hydroxyl groups in the inorganic cluster was also confirmed by the occurrence of the FTIR absorption band around 710 cm^{-1} (Figure 5.6), which is ascribed to the μ_3–OH bending [268]. The other FTIR bands between 400 and 800 cm^{-1} were assigned to the inorganic vibrational modes [i.e., ν_{as}(M–(OC) at 635 cm^{-1}, and ν(M–O) at 665 cm^{-1}] within the inorganic cluster [268,312]. The bands related to the organic linker are visible starting from 700 cm^{-1}, worth mentioning the aromatic ring torsion mode at 770 cm^{-1}, the C–H bending at 1008 cm^{-1}, the C–O symmetric stretching at 1402 cm^{-1}, the C–O asymmetric stretching at 1595 cm^{-1}, and the C=C

symmetric stretching at 1664 cm^{-1} [268,312]. Finally, the amino group functionalization was confirmed by the presence of the C–N stretching mode at 1275 cm^{-1}.

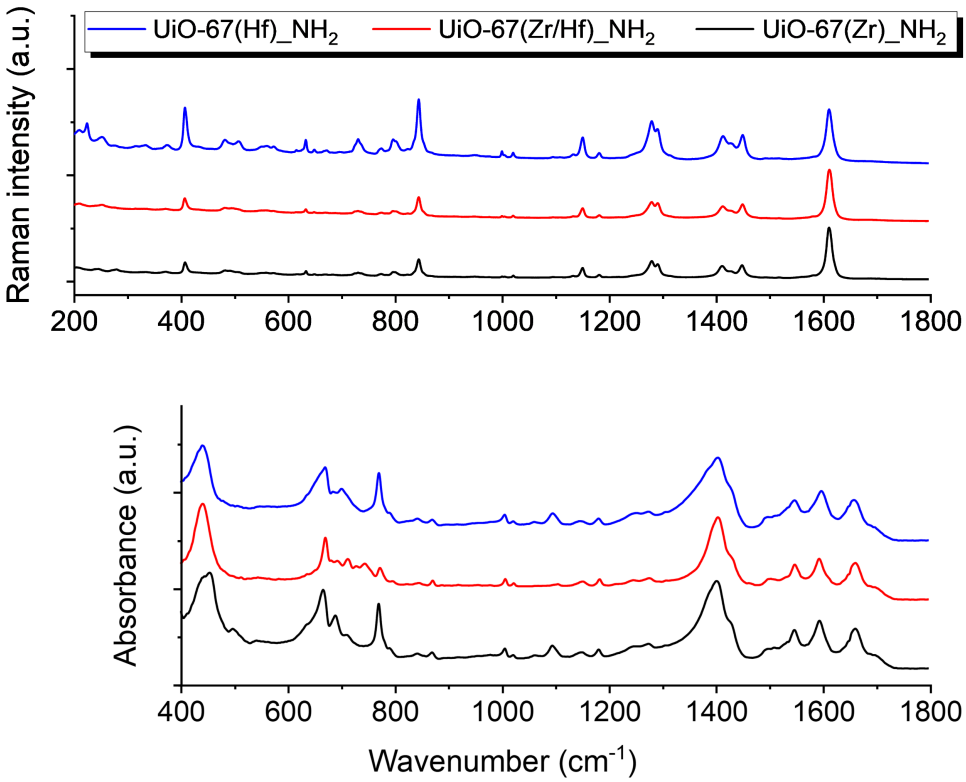

Figure 5.6: Raman spectra collected with a wavelength excitation of 785 nm (top) and FTIR spectra (bottom) for the pristine UiO-67(Zr)_NH$_2$ (black), UiO-67(Zr/Hf)_NH$_2$ (red), and UiO-67(Hf)_NH$_2$ (blue) compounds.

The Raman spectra were collected in order to obtain additional information about the vibrational modes of the UiO-67(Zr,Hf)_NH$_2$ compounds. Up to 400 cm^{-1}, the Raman bands were attributed to hexameric polyoxo-hydroxo core and/or lattice vibrations [268,285]. Then, between 400 and 700 cm^{-1}, the bands related to the mixture of cluster and linker vibrations are observed [268,285]. The purely organic linker vibrations were found from 700 cm^{-1}, worth mentioning the bands at 846 cm^{-1} (C–C breathing mode) [285,313,314], at 1152 cm^{-1} (aromatic ring breathing mode) [285,313,314], at 1452 cm^{-1} (O–C–O symmetric stretching) [268,313], and at 1613 cm^{-1} (O–C–O asymmetric stretching) [268,313].

5.2.4. Optical and electronic properties

The UV-vis spectra were collected to evaluate the metal (Zr, Hf) influence over the electronic transitions and over the band gap energies of UiO-67_NH_2 materials (Figure 5.7). All the compounds exhibit broad absorption bands between 200 and 450 nm, with a tail that continues up to 600 nm. Based on EPR data and computational studies, Nasalevich *et al.* [27] demonstrated that its UiO-66_NH_2(Zr,Hf) parent presents a LBT, which is independent on its metal content (zirconium or hafnium). This feature was ascribed to the low binding energy of the empty d^0 orbitals of Zr^{4+} and Hf^{4+}, which inhibits the overlap with the π^* orbital of the NH_2–BDC linker, despite their geometric suitability [27].

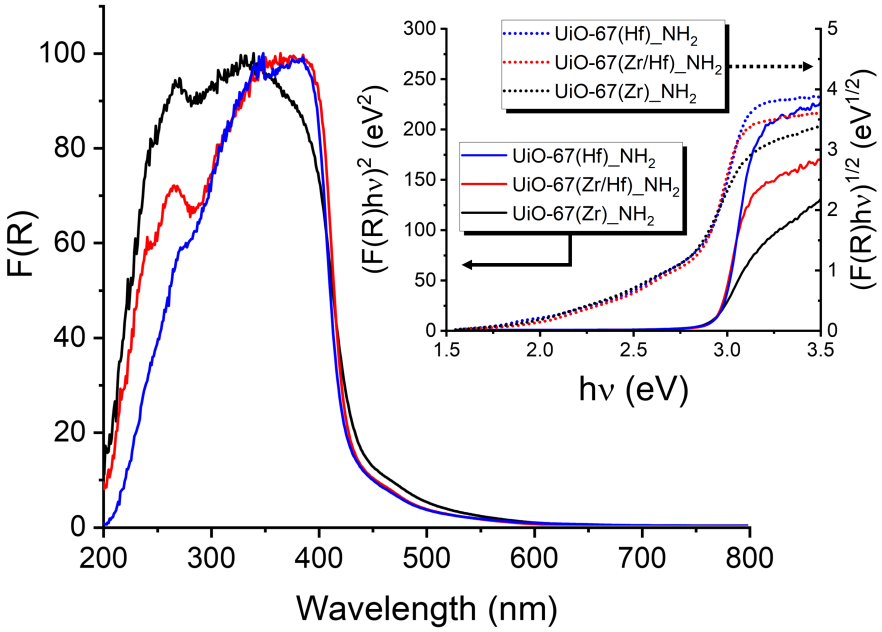

Figure 5.7: UV-vis spectra of UiO-67(Zr)_NH_2 (black), UiO-67(Zr/Hf)_NH_2 (red), and UiO-67(Hf)_NH_2 (blue) materials. Inset: Tauc plot considering both direct (straight lines) and indirect (dotted lines) transitions.

Note that the main difference between UiO-66_NH_2 and UiO-67_NH_2 is the size of the linker (Figure 5.1), as the former has only one aromatic ring (NH_2–BDC) against two from the latter (NH_2–BPDC). Therefore, it is possible to infer that UiO-67_NH_2 also exhibits a LBT process. Furthermore, according to a computational study conducted by Yang *et al.* [250] over the UiO family, the PDOS calculated for UiO-67(Zr) and UiO-67(Hf) reveals that both the VBM and the CBM of UiO-67 are located on the organic linker (mostly *p*-orbitals of carbon and oxygen atoms) [250]. Finally, as already discussed by Yasin *et al.* [249], the presence of –NH_2 functions does not shift the positions of the VBM and CBM to the inorganic cluster. Instead, it

adds mid-gap states that reduce the band gap energies without influencing their positions. Therefore, all these features converge to the same point, where it is assumed that both the VBM and the CBM of UiO-67_NH_2 are located on the NH_2–BPDC linker regardless the metallic content of the MOF (zirconium and/or hafnium), similarly to what was observed for its UiO-66_NH_2 parent [249].

As discussed in Chapter III, the UiO-67(Zr,Hf)_NH_2 compounds exhibit direct band gaps regardless their metal content (Zr, Hf). However, when measuring their energies through the Tauc plot [214,298] of the Kubelka-Munk function [177], both considerations (direct and indirect) resulted in linear behaviors around 3.0 eV, as shown in Figure 5.7. Moreover, for the entire UiO-67(Zr,Hf)_NH_2 series, the obtained $E_{g(dir)}$ and $E_{g(ind)}$ values are very similar. Therefore, considering the study of Coulter and Birnie [216] that demonstrated how some materials can present, simultaneously, direct and indirect band gaps, both E_g values were acquired here.

First, the $E_{g(dir)}$ was obtained by extrapolating the linear region of the $(F(R)h\nu)^2$ curve to the intercept with the abscissa axis, resulting in a $E_{g(dir)}$ value of 2.9 eV for UiO-67(Zr)_NH_2, UiO-67(Zr/Hf)_NH_2, and UiO-67_NH_2 (Hf). However, when evaluating the indirect Tauc plot, one can observe that the curve has an initial inclination between 1.50 and 2.75 eV (Figure 5.7). Therefore, a baseline correction must be done in the $(F(R)h\nu)^{1/2}$ curve, as proposed by Makuła, Pacia, and Macyk [222]. In this case, the $E_{g(ind)}$ was obtained by extrapolating the linear region of the $(F(R)h\nu)^{1/2}$ curve until it intercepts the baseline of the data, resulting in a $E_{g(ind)}$ value of 2.8 eV for UiO-67(Zr)_NH_2, UiO-67_NH_2 (Zr/Hf), and UiO-67_NH_2 (Hf). When considering the Kubelka-Munk UV-Vis spectra, all the samples exhibit a linear region around 425 nm. In fact, it is assumed that the first electronic transition starting from lower to higher energies (higher to lower wavelengths) in the UV-vis spectra corresponds to the HOCO – LUCO transition in crystalline materials [27]. For this reason, it is possible to extrapolate the tangent line to the absorption band edge until it intercepts the abscissa axis and by transforming the wavelength to eV energies, find the E_g values for the materials. This interception occurs at 436, 429, and 426 nm – which corresponds to 2.84, 2.89, and 2.91 eV – for UiO-67(Zr)_NH_2, UiO-67(Zr/Hf)_NH_2, and UiO-67(Hf)_NH_2, respectively. Here, it is worth noticing that these results are in between the indirect and the direct band gaps and, although $E_{g(ind)} < E_{g(dir)}$, both of them are quite similar when comparing the same UiO-67_NH_2 material (i.e., $E_{g(dir)}$_UiO-67(Zr)_NH_2

= 2.9 eV and $E_{g(ind)}$_UiO-67(Zr)_NH_2 = 2.8 eV), which supports the need for acquiring both values.

5.3. Iodine adsorption and diffusion within UiO-67_NH_2 framework

The iodine adsorption has been investigated in many MOF materials, for which the conversion of I_2 into I_3^- has been often reported. Indeed, such a transformation was evaluated in few studies so far for UiO materials [12,13,156]. Also, other zirconium-based MOFs were found to present the same behavior when reducing the gaseous iodine molecules (MOF-808, NU-1000, MOF-867, UiO-66, and UiO-67) [156]. In some cases considering other metal sites, such as the nickel-based BOF-1, the electron transfer towards the I_2 molecules was ascribed to an oxidation of the metal sites, from Ni^{2+} into Ni^{3+} [129]. A similar feature was found for vanadium-based MOFs, where the oxidation of the V^{3+} centers were responsible for the production of I_3^- [130]. However, this was proven not to be the case in zirconium-based UiO-66 [12]. In fact, the mechanism for the I_2 reduction in UiO materials was only later proposed [13]. As discussed in Chapter IV, the I_2 reduction into I_3^- was attributed to an EDA complex between the iodine molecule and the aromatic ring of the UiO linker [13]. This CTC between the organic linker and the iodine molecule was reported before in a MIL-53_NH_2 material, where the presence of high electron donor groups such as $–NH_2$ favored the I_2 adsorption by the MOF in a diluted cyclohexane solution [25].

The UiO-67(Zr,Hf)_NH_2 samples were loaded with gaseous iodine following the same conditions as in previous studies – in contact with I_2 gas stream in a concentration of 0.08 $mg.L^{-1}$ in argon, with a 10 $L.h^{-1}$ flow rate, at room temperature [12,13]. A summary of the features observed after the iodine loading is presented in Table 5.3.

Table 5.3: Iodine uptake and fitted kinetic constants data for the UiO-67_NH_2 compounds using the LDF model [180].

UiO-67 _NH_2	I_2 uptake after 16 h			I_2 uptake after 48 h			k_{LDF}	R^2
(M)	$mg.g^{-1}$	$g.mol^{-1}$	$mol.mol^{-1}$	$mg.g^{-1}$	$g.mol^{-1}$	$mol.mol^{-1}$	h^{-1}	
Zr	376[a]	832[a]	3.28[a]	749[a]	1658[a]	6.53[a]	0.0487 ± 2	0.977
Zr/Hf	533	1263	4.98	1196	2835	11.2	0.0427 ± 2	0.968
Hf	885[a]	2419[a]	9.53[a]	1254[a]	3428[a]	13.5[a]	0.0778 ± 3	0.988

[a] not saturated kinetic curve at t = 48h; k_{LDF} = mass transfer coefficient from the linear driving force (LDF) model [$F(t) = 1 – \exp[–k_{LDF}t]$]; R^2 = correlation coefficient.

The adsorption kinetics evaluated by UV-vis for the different compounds are presented in Figure 5.8. The hafnium content has a clear influence over the amount of iodine captured by the material, where UiO-67(Hf)_NH_2 exhibits the greatest capacity to retain I_2 (3428 $g.mol^{-1}$ after 48 h of I_2 loading), followed by the mixed UiO-67(Zr/Hf)_NH_2 (2835 $g.mol^{-1}$ after 48 h of I_2 loading), and lastly by the UiO-67(Zr)_NH_2 sample (1658 $g.mol^{-1}$ after 48 h of I_2 loading). This tendency is in agreement with results obtained previously for I_2@UiO-66 compounds, as mentioned before in Chapter IV [13].

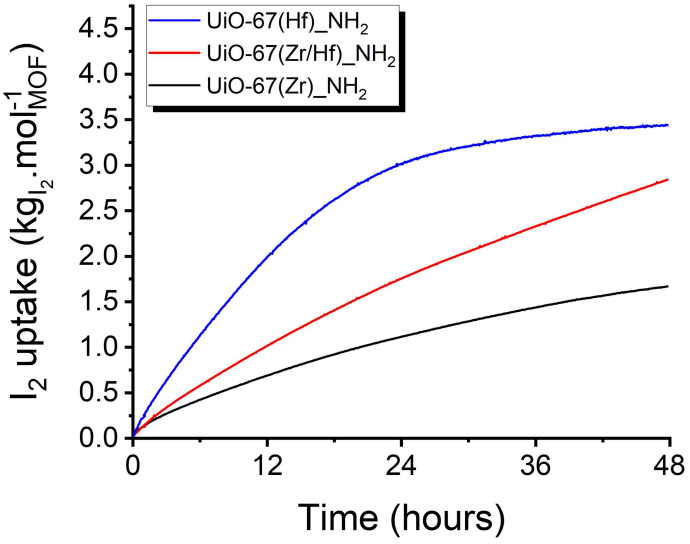

Figure 5.8: Adsorption kinetics of gaseous iodine during 48 hours in UiO-67(Zr)_NH_2 (black), UiO-67(Zr/Hf)_NH_2 (red), and UiO-67(Hf)_NH_2 (blue). The I_2 adsorption and the UV-Vis spectra were conducted at room temperature.

Indeed, the higher acidity of Hf^{4+} reduces the length of the M–(OC) bond from 2.221(5) Å in UiO-67(Zr)_NH_2, to 2.206(9) Å in UiO-67(Hf)_NH_2. As a result, the electron cloud of the NH_2–BPDC aromatic ring is delocalized towards the metal center, similar to what was observed in I_2@UiO-66(Zr,Hf) systems [13]. This effect enhances both I_2 uptake and I_3^- formation as it improves the charge separation and reduces the electron-hole recombination. The kinetic evaluation of the iodine adsorption using the LDF model is represented in Figure 5.9. It is worth mentioning that the k_{LDF} and R^2 values for the bimetallic UiO-67(Zr/Hf)_NH_2 are the smallest among all three samples, which should be related to the fact that this compound is the furthermost from reaching an adsorption plateau after 48 h of iodine adsorption (Figure 5.8 and Figure 5.9).

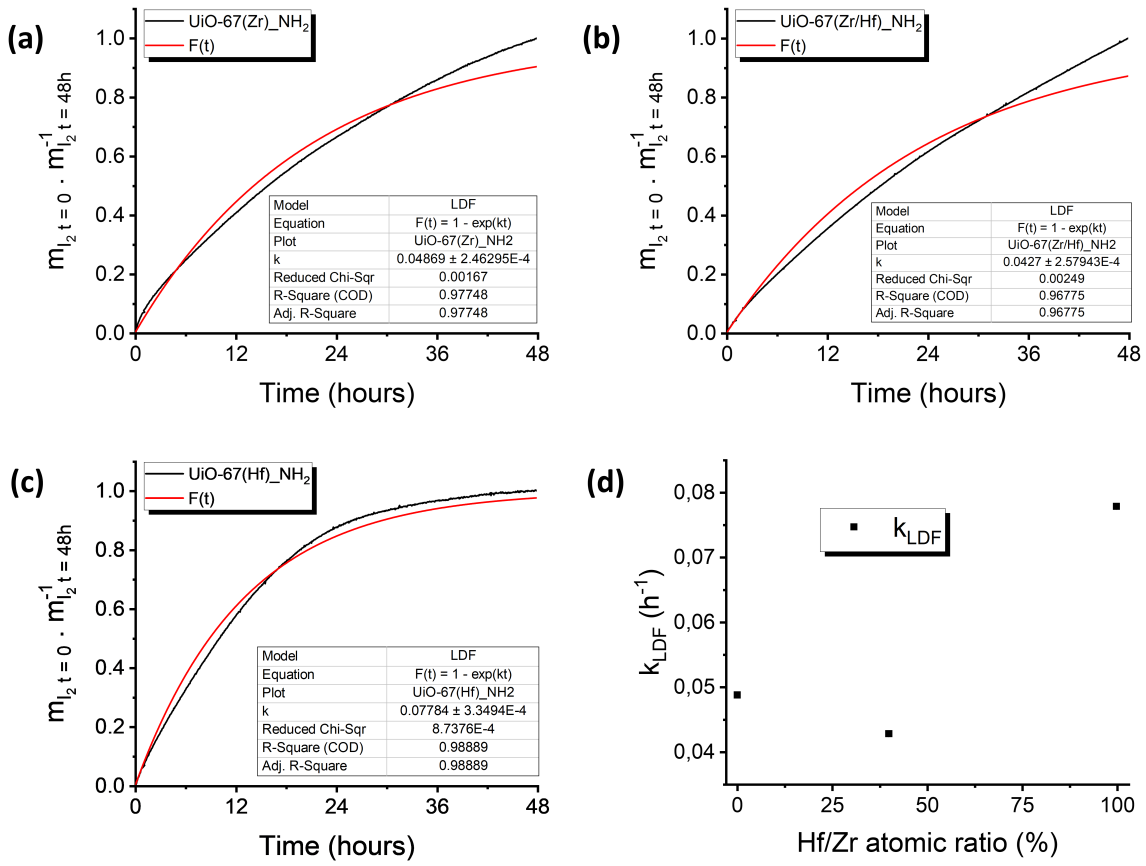

Figure 5.9: Adsorption kinetics plotted according to the Linear Driving Force (LDF) model (a) UiO-67(Zr)_NH$_2$, (b) UiO-67(Zr/Hf)_NH$_2$, and (c) UiO-67(Hf)_NH$_2$. In (d), the plot of the effective mass transfer coefficient (k_{LDF}) against the Hf/Zr atomic ratio is also displayed. Note that the curves in (a) and (b) are not saturated after 48 h, which is the reason why they exhibited the poorest R^2 coefficients.

Note that the defects do not follow the same trend as observed for the I_2 adsorption capacity (i.e.: the zirconium-based compound exhibits more defects but less iodine uptake), implying that they did not have a considerable influence over the I_2 capture. Nevertheless, it seems that both the zirconium and hafnium-based UiO-67_NH$_2$ seemed to start arriving at a plateau after 48 h of adsorption, inferring that, contrary to the bimetallic sample, these compounds start to reach their maximum adsorption capacity. This effect might be related to a diffusion process of iodine through the UiO-67_NH$_2$ crystallites, which could be faster in the monometallic UiO-67_NH$_2$ samples. In fact, since the UiO-67(Zr/Hf)_NH$_2$ crystals size are up to three times bigger than the monometallic samples, it is plausible that the diffusion process takes more time in this compound. Additionally, there is no direct correlation between the porous volumes of the UiO-67(Zr,Hf)_NH$_2$ and the amounts of iodine trapped within the pores of the UiO-67 frameworks.

Seeking to understand the spatial distribution of the different iodine species, Raman mappings were conducted for the three UiO-67(Zr,Hf)_NH_2 compounds using three distinct excitation wavelengths (λ_1 = 515 nm, λ_2 = 633 nm, and λ_3 = 785 nm) to take advantage of possible Raman resonance effect [315–317]. The laser wavelengths have been chosen to correspond or not to the UV-vis absorption bands of the iodine species (Figure 5.10), aiming to enhance specific vibrations of these compounds. The adsorption of I_2 by the UiO-67_NH_2 samples gave rise to two bands maximizing at 290, and 350 nm, that were attributed to the formation of the anionic I_3^- species [300]. Other iodine forms may also be present in the spectra between 400 and 550 nm, resulting in a long adsorption tail towards the near-infrared region [13]. In fact, since the $\pi_g^* \rightarrow \sigma_u^*$ transitions related to the "isolated" iodine form in the gas phase (gaseous iodine without any interaction with the material) is expected to be found at about 520 nm [73,74], a signature assigned to the formation of a CTC between the I_2 and the NH_2–BPDC linker – which is a strong electron donor – is expected to be present at lower wavelengths (400 – 500 nm) [77,318].

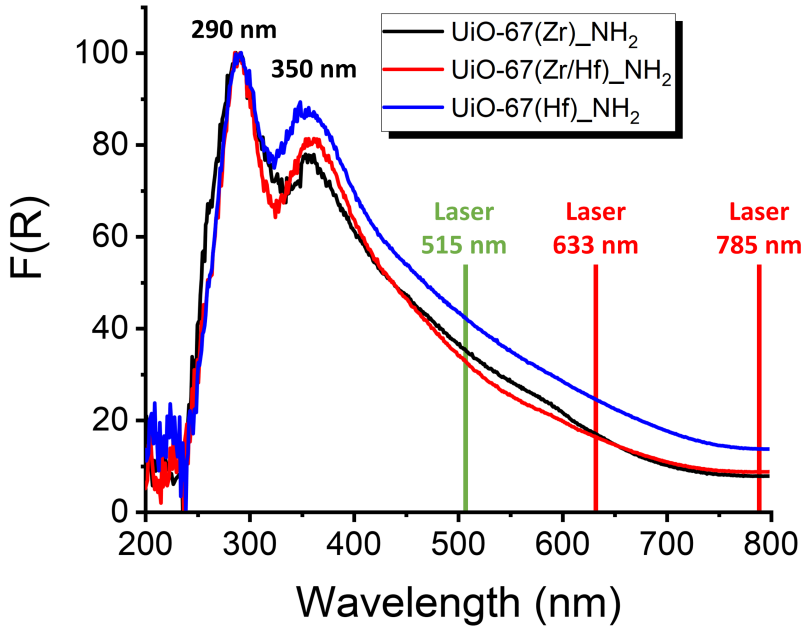

Figure 5.10: UV-vis spectra obtained for UiO-67(Zr,Hf)_NH_2 materials after 48 h of iodine exposure. In black: I_2@UiO-67(Zr)_NH_2, in red: I_2@UiO-67(Zr/Hf)_NH_2, and in blue: I_2@UiO-67(Hf)_NH_2. The samples were mixed with $BaSO_4$ in a concentration of 3% before the analysis. The position of the lasers' wavelength used for the Raman mapping are also highlighted.

It is worth remembering that the CTC between the I_2 and the aromatic ring of the BDC linker was found to be favored by the smaller band gap of the hafnium-based samples in UiO-

66 materials (Chapter IV) [13]. However, in the present work, the E_g values are not influenced by the metal site (E_g^{ind} = 2.8 eV, and E_g^{dir} = 2.9 eV), probably because of the presence of the amino group in the UiO-67_NH_2 linker. In fact, in the absence of the –NH_2 groups, the PDOS related to oxygen atoms in the valence band are influenced by the metal content of the sample and therefore, it can increase in energy in the presence of hafnium [249,250]. In contrast, when the –NH_2 group is considered, it creates a mid-gap state which virtually becomes the new valence band maximum, with no regard to the metal content [249]. For this reason, the E_g value is not a parameter to be considered here. Nevertheless, although UiO-67(Hf)_NH_2 presents the same band gap value as the other two samples, it demonstrated clearly higher iodine trapping capacity (3428 g.mol^{-1}) than UiO-67(Zr/Hf)_NH_2 (2835 g.mol^{-1}) and, especially, than UiO-67(Zr)_NH_2 (1658 g.mol^{-1}), as shown in Figure 5.8 and Table 5.3. This behavior suggests that other parameters than the band gap values influence the I_2 adsorption and evolution processes.

5.3.1. Non-resonance Raman mappings of I_2@UiO-67(Zr,Hf)_NH_2 compounds

At first, to obtain Raman spectra representative of the sample's composition, the excitation wavelength had to be chosen to avoid coupling with an electronic absorption of the iodine containing material. Therefore, considering the UV-vis spectra of the iodine loaded UiO-67(Zr,Hf)_NH_2 materials presented in Figure 5.10, the 785 nm laser line that falls out of the absorption band was used to avoid Raman resonance effects and specific band intensity enhancement. Moreover, it is worth noting that Juang, Finzi and Bustamante [319] demonstrated that the penetration depth of the Raman laser increases with the wavelength source, which is the reason why the 785 nm laser is expected to penetrate deeper in the samples. The Raman mappings obtained in this non-resonance condition, after 16 h of I_2 contact, are displayed in Figure 5.11. Here, the zirconium-based UiO-67_NH_2 compound exhibited more I_2 (at 170 cm^{-1}) and I_3^- (at 107 cm^{-1}) species in the edges of the crystal than in its center. A similar feature was observed for the bimetallic UiO-67(Zr/Hf)_NH_2, for which the iodine species are more concentrated in the edges of the crystal (red and brown regions). In contrast, after exposure of hafnium-based UiO-67_NH_2 to gaseous iodine, both I_2 and I_3^- species were homogeneously dispersed throughout the crystal. Here, it is worth mentioning that, after 16 h of exposure to iodine, the I_2 adsorption curves show that the maximum loading capacity is not reached whatever the metal content (Figure 5.8). However, the amount of iodine trapped by the hafnium sample is higher than that adsorbed by the bimetallic UiO-67(Zr/Hf)_NH_2 and by the

zirconium-based UiO-67_NH_2, regardless the duration of I_2 exposure. This validates the statement that replacing zirconium by hafnium in UiO compounds improves the kinetic of iodine adsorption [13,168].

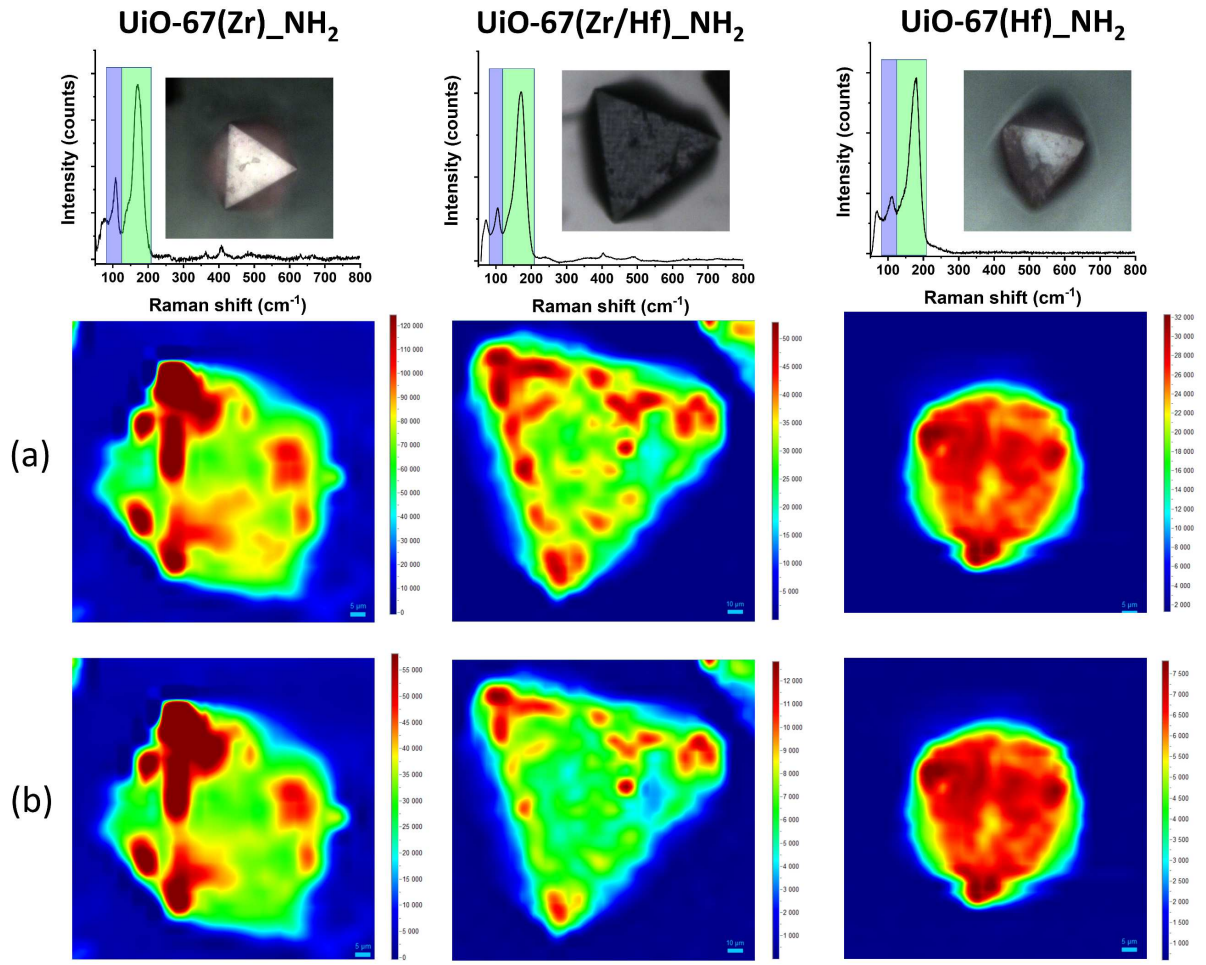

Figure 5.11: Non-resonance Raman mappings (λ_{ex} = 785 nm) over UiO-67(Zr)_NH_2, UiO-67(Zr/Hf)_NH_2, and UiO-67(Hf)_NH_2 crystals obtained after 16 h of iodine loading. The average spectra obtained by all the collected single spectrum at different XY points for the same crystal are displayed in the top of the figure. (a) spatial distribution of the "perturbed" I_2 – green region in the average spectra (centered at 170 cm^{-1}) –; (b) spatial distribution of the I_3^- – blue region in the average spectra (centered at 107 cm^{-1}). The colors in the maps are representative of the intensity of the signal, going from blue (less intense) up to red-brown (most intense)

It is important to mention that the differences in the Raman maps when comparing two different compounds (i.e.: the I_2 distribution in UiO-67(Zr)_NH_2 and in UiO-67(Hf)_NH_2 materials) are not related to the total amount of I_2 trapped by the MOF. In fact, the colors only evaluate the relative concentration of the species in the same crystal (i.e.: the colors cannot be compared between two different crystals). The presence of hafnium in UiO-67_NH_2 clearly improved the iodine access to the center of the crystal, as demonstrated by the higher

homogeneity of both I_2 and I_3^- signals. On the other hand, a higher zirconium content is detrimental to the adsorption process, as zones of I_2 and I_3^- species are observed inhomogeneously in the crystals (Figure 5.11).

In order to verify if the same features are mantained for higher iodine loadings, Raman mappings were also conducted after 48 h of I_2 contact (Figure 5.12). In this case, the monometallic samples exhibited a more homogeneous distribution of both iodine species, whereas the bimetallic UiO-67(Zr/Hf)_NH_2 still exhibits an heterogeneous distribution with the presence of multiple zones more or less concentrated in I_2 and I_3^-. When comparing the maps recorded at 16 and 48h, it is clear that the increase of the iodine loading is accompanied by the I_2 and I_3^- migration to the center of the crystals (Figure 5.11 and Figure 5.12). However, this effect is not as marked in the bimetallic compound. This last point is probably related to the fact that UiO-67(Zr/Hf)_NH_2 does not seem to reach its maximum adsorption capacity after 48 h, contrary to the monometallic compounds for which the maximum I_2 uptake seems close to being reached (Figure 5.8). This behavior highlights a combined effect between zirconium and hafnium in UiO-67_NH_2 when adsorbing iodine, as the bimetallic compound is the one that has the highest potential to improve its I_2 uptake in longer contact times.

Contrary to what has been found in previous studies for I_2@UiO-66 (Chapter IV) [13], the spectra obtained for all the I_2@UiO-67(Zr,Hf)_NH_2 samples show only two contributions related to iodine: the first at around 170 cm^{-1} – related to "perturbed" I_2 –; and the second at 107 cm^{-1} – related to the symmetric stretching of I_3^- (Figure 5.11) [83,84,87,90,320,321]. It is worth mentioning that studies have reported the formation of polynuclear iodine species of I_n^- type (n = 5, 7, 9, …) after the CTC with organic donor molecules [302,322]. In fact, vibrations of I_5^- and I_7^- species were already observed around 170 cm^{-1} and contribute to the signal here named "perturbed" I_2 [85,89,90]. Note that, contrary to what was observed for UiO-66 compounds, the UiO-67_NH_2 materials seem to stabilize both "perturbed" I_2 and I_3^- species after the I_2 into I_3^- transformation reaches an equilibrium state (which happens a few weeks after the contact with the I_2 gas) [13]. This effect infers that UiO materials have a limited capacity to transform I_2 into I_3^-. Therefore, after reaching the maximum capacity of I_3^- transformation for greater iodine uptakes (which is the case for UiO-67_NH_2 compared to UiO-66), the new adsorbed I_2 do not transform into I_3^-. Instead, the molecules interact with the already formed I_3^- to produce the polyiodide I_n^- (n = 5, 7, 9, …) anions, which are then stabilized within the pores of the MOF. In addition, the fact that the band related to "free" I_2 (expected at about 210 cm^{-1}) is not present

in UiO-67(Zr,Hf)_NH_2 systems implies that the I_2 sorption and subsequent evolution into "perturbed" I_2 is already in an equilibrium state, as demonstrated elsewhere for UiO-66 compounds (Chapter IV) [13]. In UiO-66(Hf), the Raman band related to "free" I_2 vanishes 2 hours after leaving the iodine adsorption bench, whereas in UiO-66(Zr) this band is no longer observed after approximately 12 hours [13]. Finally, another interesting feature is the redshift observed in the "perturbed" I_2 and I_3^- vibrational modes: from 173 cm^{-1} in UiO-66(Zr,Hf) to 170 cm^{-1} in UiO-67(Zr,Hf)_NH_2 for "perturbed" I_2; and from 115 to 107 cm^{-1} for I_3^-, respectively. This behavior highlights the influence of replacing the BDC by the NH_2–BPDC linker in the interaction between the iodine molecule and the UiO-6*x*_*y* (*x* = 6 or 7; *y* = H or NH_2) compounds.

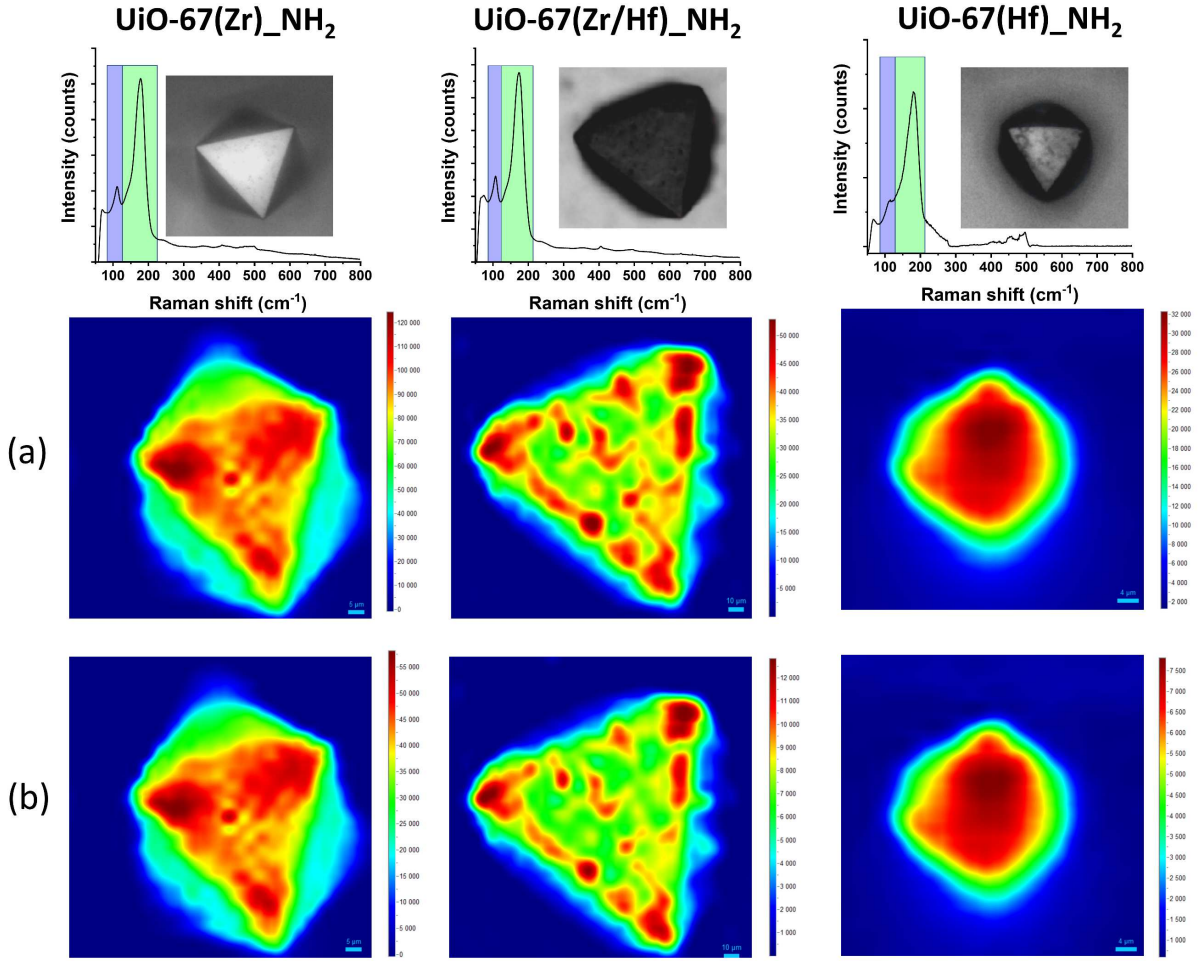

Figure 5.12: Non-resonance Raman mappings (λ_{ex} = 785 nm) over UiO-67(Zr)_NH_2, UiO-67(Zr/Hf)_NH_2, and UiO-67(Hf)_NH_2 crystals obtained after 48 h of iodine loading. The average spectra obtained by all the collected single spectrum at different XY points for the same crystal are displayed in the top of the figure. (a) spatial distribution of the "perturbed" I_2 – green region in the average spectra (centered at 170 cm^{-1}) –; (b) spatial distribution of the I_3^- – blue region in the average spectra (centered at 107 cm^{-1}). The colors in the maps are representative of the intensity of the signal, going from blue (less intense) up to red-brown (most intense)

5.3.2. Pre-resonance Raman mappings of I_2@UiO-67(Zr,Hf)_NH_2 compounds

The Raman mappings were also recorded using the λ_{ex} = 633 nm excitation laser line seeking to assess possible specific band intensity enhancement by exciting in the tail of the iodine species absorption bands (Figure 5.10). The mappings obtained after 16 h and 48 h of I_2 contact with the UiO67_NH_2 materials are presented in Figure 5.13 and Figure 5.14. The 2D spatial distributions are very similar to those obtained using the 785 nm excitation wavelength. After a 16-hour exposure to iodine, a homogeneous spatial distribution of the iodine species was observed for the hafnium-based UiO-67_NH_2, while the iodine species are concentrated in the edges of the crystal in the bimetallic UiO-67(Zr/Hf)_NH_2, and in the monometallic UiO-67(Zr)_NH_2 (Figure 5.13).

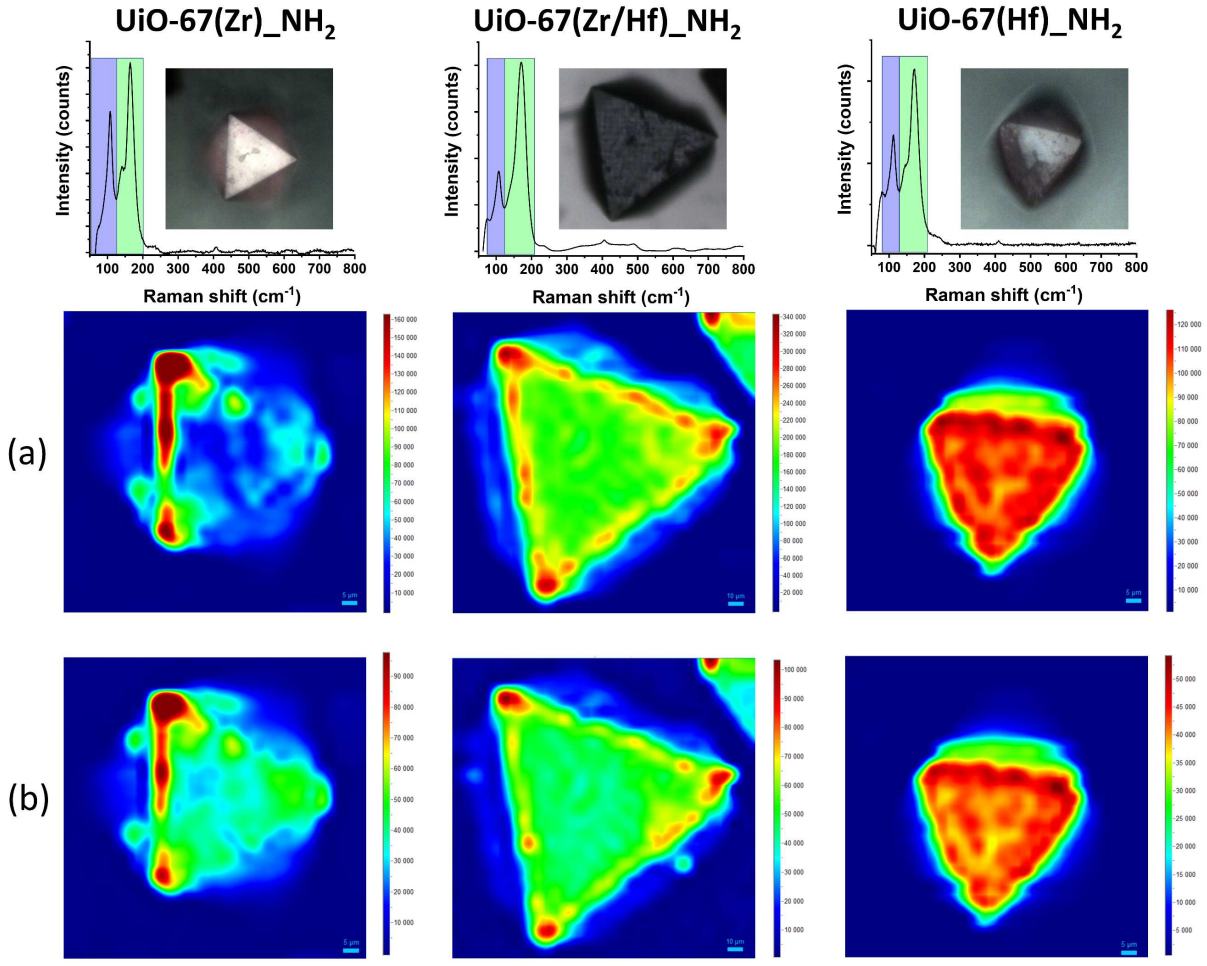

Figure 5.13: Raman mappings in pre-resonance conditions (λ_{ex} = 633 nm) over UiO-67(Zr)_NH_2, UiO-67(Zr/Hf)_NH_2, and UiO-67(Hf)_NH_2 crystals obtained after 16 h of iodine loading. The average spectra obtained by all the collected single spectrum at different XY points for the same crystal are displayed in the top of the figure. (a) spatial distribution of the "perturbed" I_2 – green region in the average spectra (centered at 170 cm^{-1}) –; (b) spatial distribution of the I_3^- – blue region in the average spectra (centered at 107 cm^{-1}). The colors in the maps are representative of the intensity of the signal, going from blue (less intense) up to red-brown (most intense).

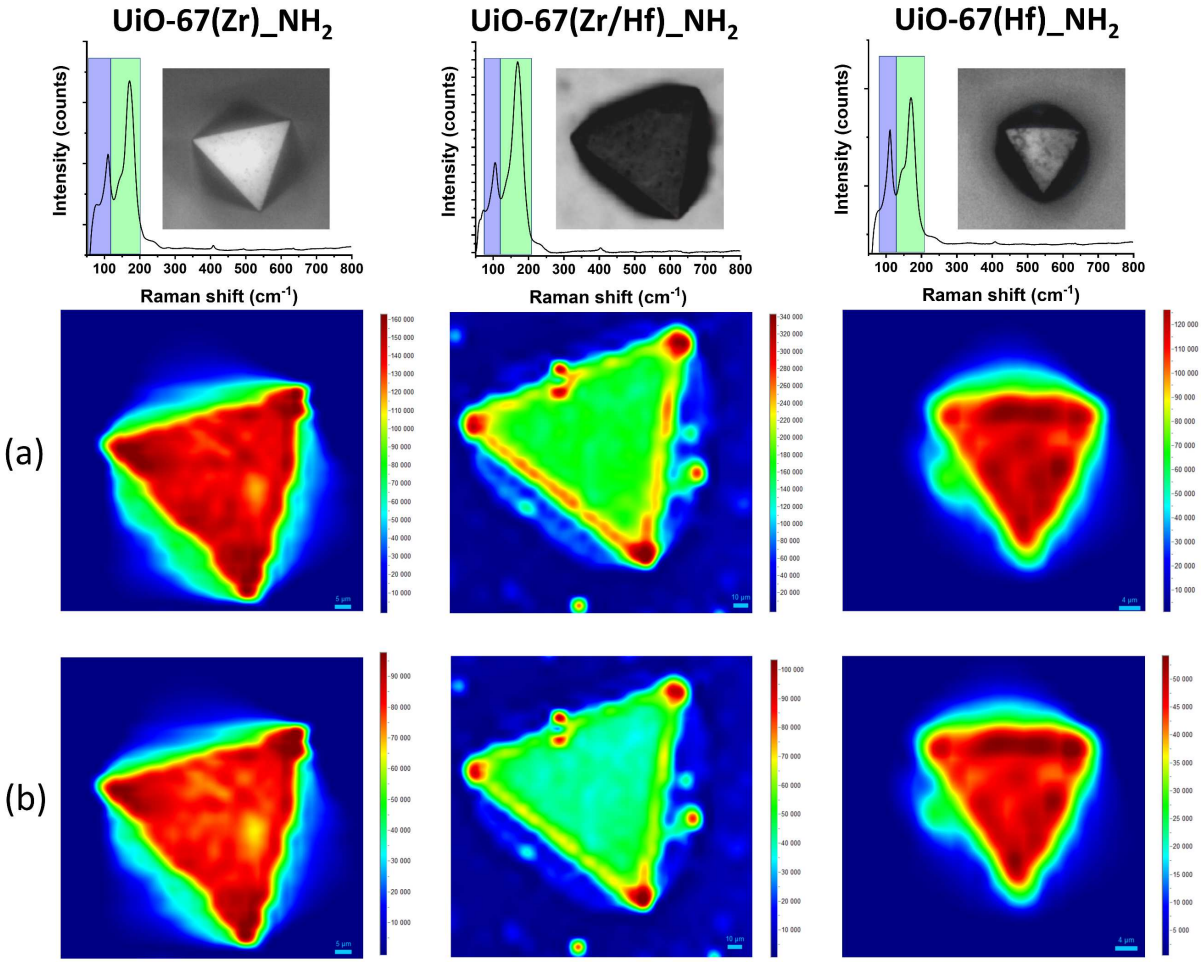

Figure 5.14: Raman mappings in pre-resonance conditions (λ_{ex} = 633 nm) over UiO-67(Zr)_NH_2, UiO-67(Zr/Hf)_NH_2, and UiO-67(Hf)_NH_2 crystals obtained after 48 h of iodine loading. The average spectra obtained by all the collected single spectrum at different XY points for the same crystal are displayed in the top of the figure. (a) spatial distribution of the "perturbed" I_2 – green region in the average spectra (centered at 170 cm^{-1}) –; (b) spatial distribution of the I_3^- – blue region in the average spectra (centered at 107 cm^{-1}). The colors in the maps are representative of the intensity of the signal, going from blue (less intense) up to red-brown (most intense).

On the other hand, for higher times of I_2 contact (48 h), both monometallic samples exhibited a homogeneous spatial distribution of I_2 and I_3^- species, contrary to UiO-67(Zr/Hf)_NH_2 which again presented a higher concentration of both signals in the edges of the crystal (Figure 5.14). This behavior agrees with that observed using the 785 nm excitation source, reinforcing the idea of a combined effect between Zr and Hf in UiO-67_NH_2, which shifts the adsorption maximum I_2 plateau to higher contact times (Figure 5.8, Figure 5.13, and Figure 5.14).

5.3.3. Resonance Raman mappings of I_2@UiO-67(Zr,Hf)_NH_2 compounds

The Raman mappings were finally carried out using an excitation wavelength of 515 nm (Figure 5.15). This excitation source corresponds to the spectral region in which electronic transitions related to both I_2 and I_3^- species are present, as observed in Figure 5.10 [73,74,77,300,318].

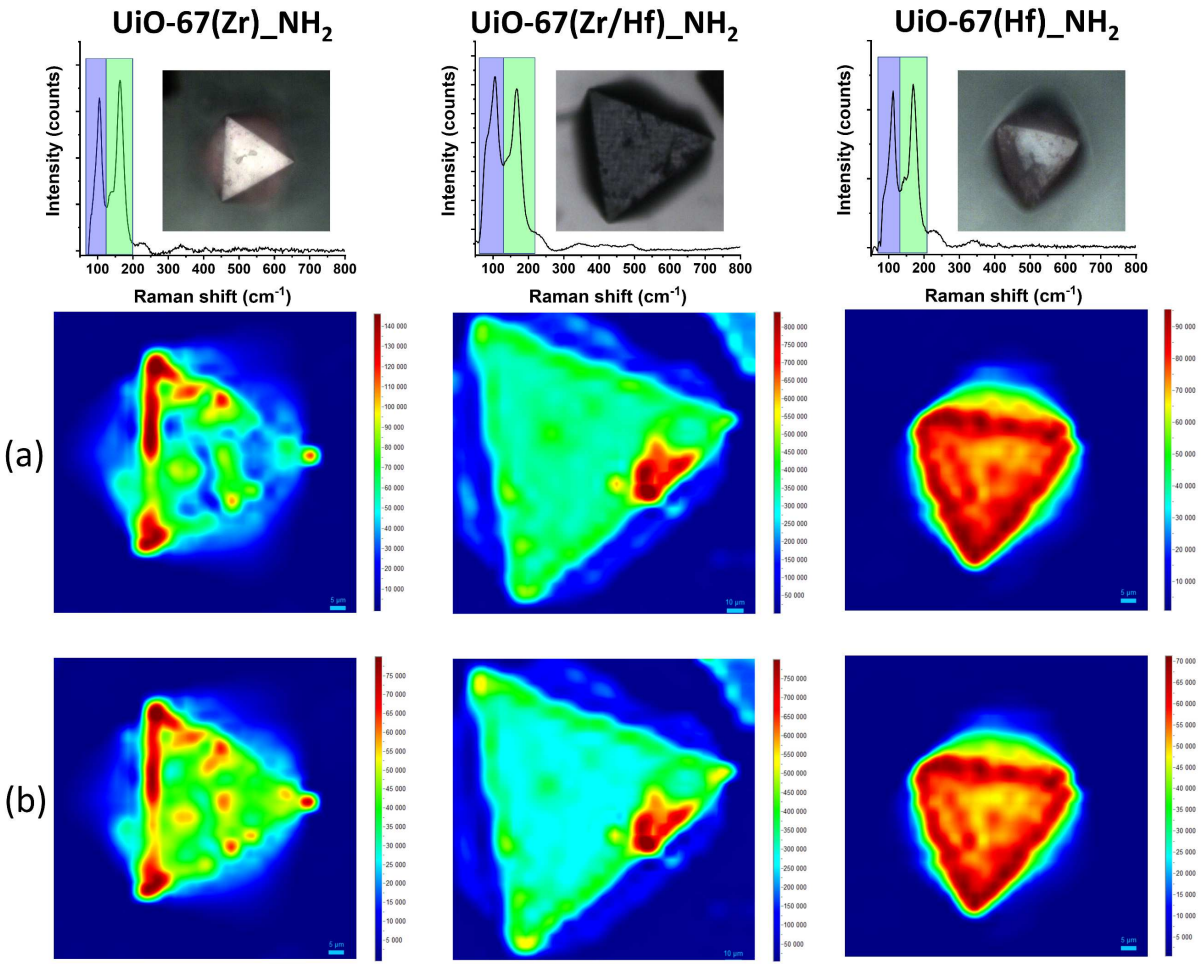

Figure 5.15: Resonance Raman mappings (λex = 515 nm) over UiO-67(Zr)_NH_2, UiO-67(Zr/Hf)_NH_2, and UiO-67(Hf)_NH_2 crystals obtained after 16 h of iodine loading. The average spectra obtained by all the collected single spectrum at different XY points for the same crystal are displayed in the top of the figure. (a) spatial distribution of the "perturbed" I_2 – green region in the average spectra (centered at 170 cm^{-1}) –; (b) spatial distribution of the I_3^- – blue region in the average spectra (centered at 107 cm^{-1}). The colors in the maps are representative of the intensity of the signal, going from blue (less intense) up to red-brown (most intense)

The coincidence between the excitation wavelength and that of the absorption bands is expected to selectively enhance the Raman bands intensities of the species involved in the electronic transition through Raman resonance effect. As observed using the 785 and 633 nm excitation laser lines, the difference in iodine concentration between the edges and the center of the crystal after 16h iodine loading was more marked when zirconium is present, but less

pronounced in the bimetallic UiO-67(Zr/Hf)_NH_2, and almost imperceptible in the UiO-67(Hf)_NH_2 (Figure 5.15). However, after 48 h of iodine loading, in addition to the inhomogeneity of the two UiO-67(Zr)_NH_2 and UiO-67(Zr/Hf)_NH_2 samples, the hafnium-based compound also exhibited zones with different I_2 and I_3^- concentrations, contrary to that observed for lower contact times (Figure 5.16).

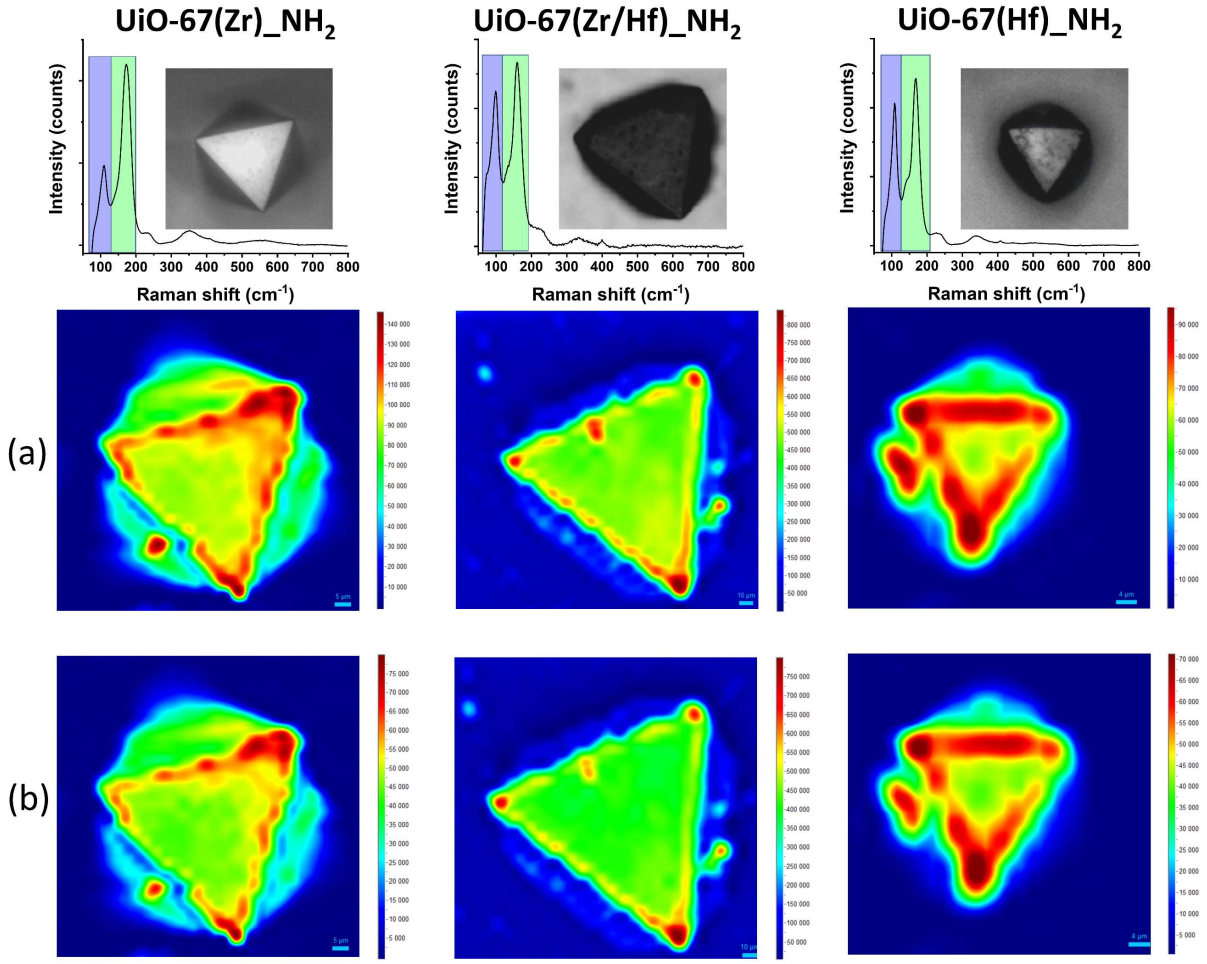

Figure 5.16: Resonance Raman mappings (λ_{ex} = 515 nm) over UiO-67(Zr)_NH_2, UiO-67(Zr/Hf)_NH_2, and UiO-67(Hf)_NH_2 crystals obtained after 48 h of iodine loading. The average spectra obtained by all the collected single spectrum at different XY points for the same crystal are displayed in the top of the figure. (a) spatial distribution of the "perturbed" I_2 – green region in the average spectra (centered at 170 cm^{-1}) –; (b) spatial distribution of the I_3^- – blue region in the average spectra (centered at 107 cm^{-1}). The colors in the maps are representative of the intensity of the signal, going from blue (less intense) up to red-brown (most intense).

It is worth mentioning that the change in the laser excitation source did not modify the positions of the I_2 and I_3^- bands, which were centered in the same wavenumbers for all three compounds: at 170 and 107 cm^{-1}, respectively. Nevertheless, the use of the 515 nm excitation wavelength was found to affect the relative intensities of the Raman bands characteristic of the

iodine species (Figure 5.11 to Figure 5.16). Indeed, while both the 785 and 633 nm spectra induce similar behavior with only weak differences when considering the relative areas of the bands at 107 cm^{-1} and 170 cm^{-1} ($[I_{170}/I_{107}]_{633,785nm} > 1$), this ratio is inversed for the Raman spectra collected at 515 nm ($[I_{170}/I_{107}]_{515nm} \approx 1$), for which the intensity of the 107 cm^{-1} line is significantly increased. This feature demonstrates the specific excitation of electronic transitions of the I_3^- species in resonance conditions (Figure 5.10) [316]. Indeed, the $\lambda_1 = 515$ nm excitation wavelength, which falls within the lower energy foot of the absorption band of the iodine species including I_3^- and adsorbed I_2 contributions (Figure 5.10), is assumed to induce more marked resonance effect for I_3^- [316]. This is equivalent to say that the I_3^- band will have a higher intensity in such conditions when compared to non-resonance circumstances [317]. This effect was less pronounced when using the $\lambda_2 = 633$ nm excitation wavelength, and negligible for the $\lambda_3 = 785$ nm laser (Figure 5.11 to Figure 5.16), as those excitation sources fall out of the main absorption bands related to the iodine species (Figure 5.10).

When the excitation is performed using the 515 nm laser, the higher intensity enhancement of the I_3^- band compared to non-resonance conditions suggest higher I_3^- concentration. However, it is worth noting that the Raman resonance effect does not allow determination of the relative spectral concentration of the species (Figure 5.10, Figure 5.15, and Figure 5.16) [317]. Moreover, all the cartographies showed that the I_2 and the I_3^- species are concentrated nearby, which indicates that there is no considerable iodine diffusion after its transformation into I_3^- (Figure 5.11 to Figure 5.16). The absence of I_3^- diffusion infers that the I_3^- has a stronger interaction with the UiO compounds than the I_2, which is in agreement with the results obtained for UiO-66 [13]. Indeed, in UiO-66(Zr,Hf) systems, it was proposed that the EDA complex between the BDC linker and the I_2 molecule generates a $BDC^{\bullet+}$ radical when reducing the I_2 into I_3^-, stabilizing this anionic species through an electrostatic interaction [13]. The formation of this radical was ascribed to the absence of a redox phenomenon associated to the inorganic sites of UiO materials, as demonstrated in other works [12,13,27].

As discussed in Chapter IV, the main reason for the absence of this metal reduction in zirconium and hafnium-based MOFs is the low binding energy (close to the vacuum level) of the *d*-orbitals from both Zr^{IV} and Hf^{IV} [27]. As a consequence, in I_2@UiO(Zr,Hf) systems, the I_2 reduction into I_3^- is purely related to the organic linker [13]. In fact, the EDA complex makes an electron to jump from the π^* orbital of the organic linker towards the σ^*_{5p} orbital of the I_2 molecule, leaving a hole (h^+) behind [13]. This entity was found to be stabilized through an

electrostatic interaction between the recently formed I_3^- and the electron donor benzenedicarboxylate cation radical ($BDC^{\bullet+}$) [13]. However, in amino-functionalized NH_2–BDC materials – such as MIL-125_NH_2(Ti) – the hole created upon excitation was found to be stabilized by the –NH_2 group and by the carboxylate function of the linker, creating the corresponding $NH_2^{\bullet+}$–BDC radical [257]. Moreover, since organic linkers found in MIL-125_NH_2 and UiO-67_NH_2, have a similar benzene-derived structure (apart from having an extra aromatic ring), the –NH_2 groups should act as a hole stabilized in both cases [256]. Therefore, it is assumed that the corresponding $NH_2^{\bullet+}$–BPDC can also be formed in UiO-67_NH_2 systems. This feature supports the hypothesis that I_3^- has specific sites for adsorption, which are the places that stabilized the h^+ entity (aromatic ring, –NH_2, or $-COO^-$) [13,256–258]. Therefore, in this case, the main reason why the I_3^- has a lower diffusion capacity than I_2 is the electrostatic interaction that it creates with the generated holes in the UiO-67_NH_2 structure.

5.3.4. 3D Raman mapping of I_2@UiO-67(Zr/Hf)_NH_2 in non-resonance conditions

Aiming to deeper evaluate the iodine distribution in the biggest crystal with a considerable resolution, a Raman cartography was also conducted in three dimensions for the UiO-67(Zr/Hf)_NH_2 compound after an adsorption time of 16h (Figure 5.17). In order to avoid the resonance effects with the iodine species and UiO-67(Zr/Hf)_NH_2, the 785 nm laser was used as the excitation source. Here, the spatial distribution of the species characterized by the two regions related to "perturbed" I_2 (green) and I_3^- (blue) were evaluated up to 105 µm depth. As already demonstrated in the 2D Raman mappings using the 785 nm excitation source, the iodine species were mainly found at the edges of the bimetallic UiO-67(Zr/Hf)_NH_2 compound. However, although the intensity of their contribution decreases with the depth (probably due to a loss of signal related to the laser probe in deeper distances and multi scattered phenomena) [323], the spatial distribution of "perturbed" I_2 and I_3^- is maintained, regardless the depth of the cartography. As already demonstrated in the 2D Raman mappings using the 785 nm excitation source, the iodine species were mainly found at the edges of the bimetallic UiO-67(Zr/Hf)_NH_2 compound.

With that in mind, one can conclude that several I_2 molecules did not reach the sites in the inner part of the crystals and therefore, they were not transformed into I_3^-, regardless its iodine exposure time (Figure 5.11 to Figure 5.17). This effect could be related to the faster

kinetic of the I_2 into I_3^- transformation when compared to the diffusion rate of the species, probably because of the crystal size (which is three times bigger for the bimetallic compound). Indeed, if the kinetic of I_2 adsorption and evolution into I_3^- is faster than the species diffusion throughout the crystal, it is expected that both iodine species are concentrated in the edges rather than in the center.

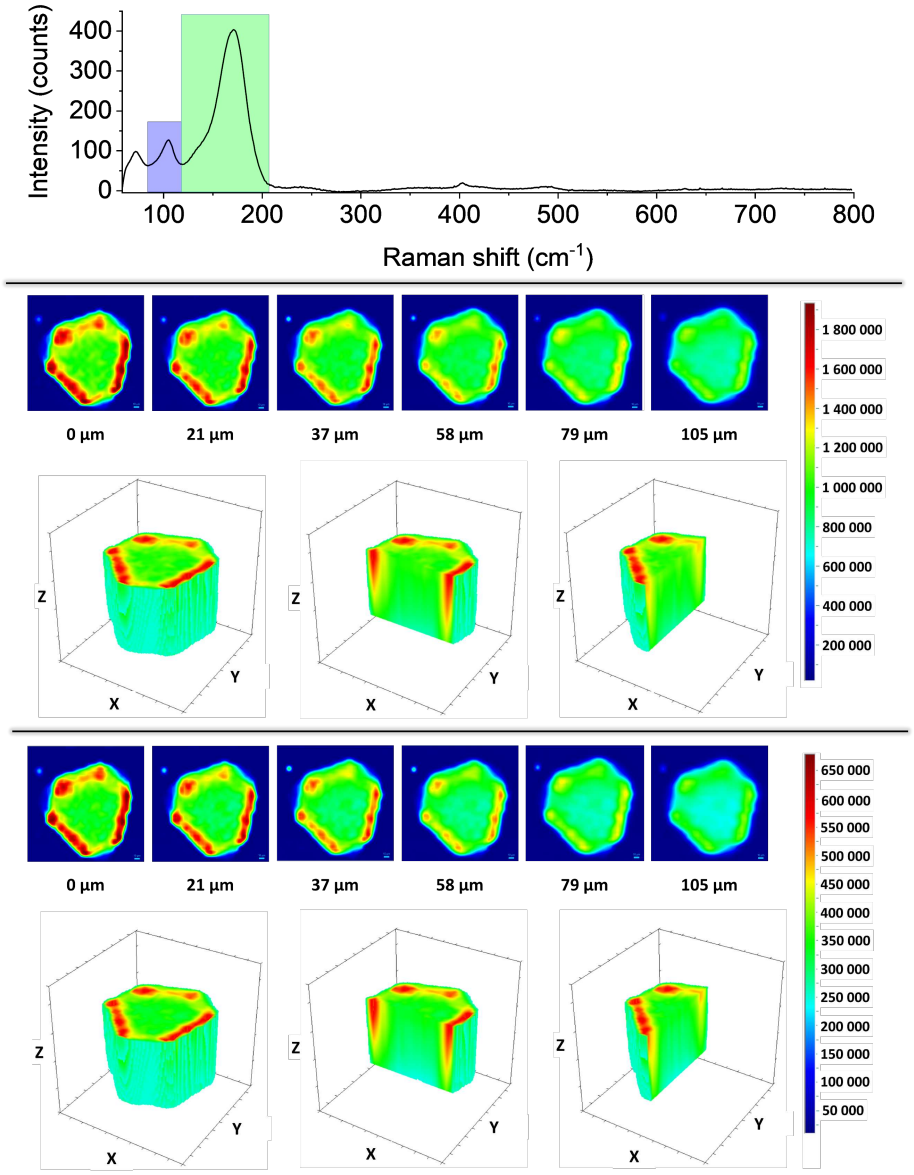

Figure 5.17: Non-resonance Raman mapping over a UiO-67(Zr/Hf)_NH_2 crystal performed in three dimensions ($0 \leq x \leq 205.5$ µm; $0 \leq y \leq 202.3$ µm; $0 \leq z \leq 105$ µm) at λ_{ex} = 785 nm. On top: The average spectra obtained by all the collected single spectrum at different XYZ points. In the middle: spatial distribution of the "perturbed" I_2 (green region in the average spectra). On bottom: spatial distribution of the I_3^- (blue region in the average spectra). The 2D cartographies display the XY plan in different depths. The 3D intensity map is highlighted in the left side alongside one slice of the XZ (middle) and YZ (right) plans.

Actually, it seems that the I_2 molecules are quickly attached to the NH_2–BPDC linkers located at the edges of the crystals, while the I_3^- anions are rapidly trapped by the respective $NH_2^{\bullet+}$–BPDC radicals right before their formation, which makes difficult their diffusion towards the center of the crystal. This behavior highlights the importance of tailoring not only the electronic structure and the functional groups of the MOFs when transforming iodine, but also their crystal size. In fact, in larger crystals, the diffusion process takes longer to reach the center of the structure, which can be detrimental if some of the transformed I_3^- molecules are trapped in their specific adsorption sites (aromatic ring, $–NH_2$, and $–COOH^-$) before reaching the center. This effect may not only reduce the mobility of this species, but also the number of available sites for new molecules to attach. Such behavior would also diminish the availability of locations for the EDA complex to take place. For instance, when considering the iodine trapped inside the UiO-67(Zr,Hf)_NH_2 compounds, the transformation into I_3^- and its sub-sequential adsorption in specific sites can, at some point, obstruct some of the entrances to deeper pores inside the crystal structure, disturbing the iodine diffusion.

In this work, the iodine-loaded samples were stored during one to two weeks to guarantee a complete transformation of I_2 into I_3^- before the acquisition of the Raman maps. For such reason, they provide only direct information on the equilibrium state (when considering the I_2 evolution into I_3^-). Moreover, as already discussed above, there is no redox phenomena related to the Zr^{4+} and Hf^{4+} centers in UiO materials. Therefore, it is assumed that, similarly to what was found for the UiO-66 system (Chapter IV) [13], the electron transferred to the I_2 species comes from the EDA complex with the NH_2–BPDC linker. Then, the hole formed during the charge transfer must remain in the corresponding $NH_2^{\bullet+}$–BPDC radical, as mentioned above. At this point, due to electrostatic interactions, the I_3^- species should be chemically adsorbed on the $NH_2^{\bullet+}$–BPDC radical in UiO-67(Zr,Hf)_NH_2, which would also stabilize the h^+ entities in the framework [13]. Considering these features, it can be proposed that, after the NH_2–BPDC linker reduces one I_2 molecule, it loses its ability to transform other I_2 molecules into I_3^- because of the electrostatic repulsion created by the presence of two holes in the same linker [324–326]. This behavior is coherent with the results obtained for the UiO-67_NH_2 compounds in this work as, even though there are still I_2 molecules available to be transformed in the pores, the transformation of I_2 into I_3^- in UiO-67_NH_2 systems reaches an equilibrium after a few days, regardless of the iodine loading. Indeed, since the UiO-67_NH_2 materials adsorbed up to 6 times more iodine than their UiO-66 parents after 16 h of I_2 contact (2419 against 285 $g.mol^{-1}$ for UiO-67(Hf)_NH_2 and UiO-66(Hf), respectively), lots of

untransformed I_2 molecules were trapped inside the pores – even after one week. This feature was ascribed to the bigger pores of UiO-67(Zr,Hf)_NH_2 materials (21.5 Å against 6.4 Å in UiO-66_NH_2) [327,328], which can accommodate more I_2 molecules (even though, at this point, the NH_2–BPDC linkers have reduced ability to transform them into I_3^-). Moreover, because –NH_2 is known to favor the I_3^- formation, the amino group effect must also be considered [12,24,25]. Actually, functions with high electron donor character can induce the polarization of the electronic cloud of the iodine molecule [25], improving the EDA complex between the linker and the I_2 molecule, which produces a faster I_2 into I_3^- transformation [12,13]. This feature results in a "perturbed" I_2 signal much more intense than that of I_3^- in non-resonance conditions for all the UiO-67(Zr,Hf)_NH_2 samples (Figure 5.11 to Figure 5.17).

Finally, in order to better understand the influence of the metal sites and of the resonance phenomenon on the stabilization and semi-quantification of the iodine species, the ratios between the areas of the I_2 and I_3^- signals were plotted according to the laser wavelength (Figure 5.18). This figure demonstrates that the [A_{170}/A_{107}] ratio increases gradually with the laser wavelength and that the resonance effect is more pronounced for the I_3^- vibrational mode, as the λ_{ex} = 515 nm laser generates the lower [A_{170}/A_{107}] signal (due to an increase in the A_{107} signal).

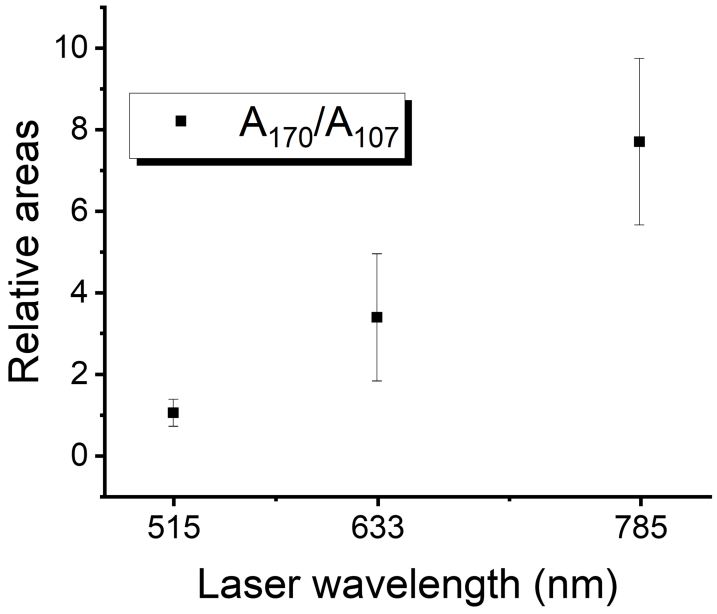

Figure 5.18: Ratio between the areas of the bands at 170 and 107 cm^{-1} for the different wavelength excitations (λ_1 = 515 nm, λ_2 = 633 nm, and λ_3 = 785 nm) considering the three compounds: UiO-67(Zr)_NH_2, UiO-67(Zr/Hf)_NH_2, and UiO-67(Hf)_NH_2.

5.4. Conclusions

Three UiO-67_NH_2 samples with different metal contents (Zr, Zr/Hf and Hf) were successfully synthesized and loaded with gaseous iodine. The hafnium-based UiO-67_NH_2 achieved the best retaining capacity after 48 h of I_2 contact, capturing 3428 g.mol^{-1} of iodine, followed by the mixed UiO-67(Zr/Hf)_NH_2 with 2835 g.mol^{-1}, and then by the zirconium-based UiO-67_NH_2, with 1658 g.mol^{-1}. Nevertheless, the bimetallic compound did not seem to reach a plateau regarding the I_2 adsorption, which infers that it may surpass the hafnium-based UiO-67(Hf)_NH_2 in contact times higher than 48 h. This feature was related to the size of its crystals, which are about three times bigger than the monometallic compounds and can attenuate the diffusion of the I_2 species. The I_3^- formation upon adsorption was again observed using Raman spectroscopy. Three laser excitation sources were used for evaluating the spatial distribution of the species: 515, 633, and 785 nm. A Raman resonance effect with the I_3^- species was observed with the 515 nm excitation wavelength, but it was less noticeable for the 633 nm laser, and absent with the 785 nm source. Also, the Raman mapping for low contact times (16 h) demonstrated that the UiO-67(Hf)_NH_2 displayed the most homogeneous distribution of both the I_2 and I_3^- species among the three compounds, whereas the zirconium-based and the bimetallic UiO-67(Zr,Hf)_NH_2 exhibited zones with different concentrations of such iodine species. However, for higher contact times (48 h), only the UiO-67(Zr/Hf)_NH_2 material exhibited an inhomogeneous spatial distribution of the iodine species, which was related to the fact that the I_2 capture did not reach its maximum adsorption plateau in this case. Additionally, the spatial distribution of the iodine species revealed that I_3^- does not diffuse after its formation, reason why the regions with more I_2 are also fulfilled with I_3^-. This effect was associated to the presence of specific adsorption sites for the I_3^- anions, as proposed before in other study using UiO-66(Zr,Hf) [13]. In fact, in UiO-67(Zr,Hf)_NH_2 systems, the cation radical $NH_2^{\bullet+}$–BPDC (analogous to the $BDC^{\bullet+}$ for UiO-66 materials) was ascribed to be the center for the specific adsorption of I_3^- anions. This feature indicates that there is a maximum amount of I_3^- that can be trapped in UiO materials before it gets saturated, which is intrinsically related to the hole-hole Coulomb repulsions in the organic linker radical [324–326]. This study increases the comprehension of the iodine evolution mechanism as it reinforces the stronger interaction between the anionic I_3^- species and the MOFs lattice when compared to that of the I_2 molecules. Further studies must be conducted in order to evaluate the stability of I_3^- species in different conditions such as temperature and humidity. This chapter is based on the article published in the Journal of Physical Chemistry C (J. Phys. Chem. C 2023, 127, 4618−4635).

Chapter VI: Charge Transfer Complexes in Terephthalate-Based MOFs: The Influence of Titanium

6.1. Introduction

The use of titanium-based MOFs can be particularly interesting for trapping iodine due to their improved photocatalytic properties, high acidity of the titanium, low toxicity, and possibility of creating LMCT complexes [26,27]. In 2009, Dan-Hardi *et al.* [26] reported for the first time a highly porous Ti-MOF that was synthesized under solvothermal conditions from a mixture of DMF, MeOH, terephthalic acid (H_2BDC) and TTIP. Named MIL-125(Ti) (MIL = Material from Institute Lavoisier) or $[Ti_8O_8(OH)_4(O_2C–C_6H_4–CO_2)_6]$, this crystalline MOF is composed by a quasi-cubic tetragonal structure formed by $TiO_5(OH)$ octahedra that are connected to each other through the BDC linkers alternating O species via edge sharing with OH, resulting in a octanuclear ring [26]. It presents two types of cages – octahedral and tetrahedral – with diameters of about 12 and 6 Å, respectively [26]. Free apertures between 5 - 7 Å provide access to its porous structure [26]. Studies have shown that microwave synthesis of MIL-125(Ti) is also achievable in times lower than one hour [329].

Band edge tuning through linker modification was also reported in the literature for MIL-125(Ti) compounds, whereas the electron rich amine linker NH_2-BDC served to increase the aromatic electron density of the linker, shifting up the VBM of MIL-125(Ti)_NH_2 compared to that of MIL-125(Ti) [105]. With these particular properties, hydrogen production using MIL-125(Ti)_NH_2 as a visible-light photocatalyst at irradiation wavelengths up to 500 nm was reported by Horiuchi *et al* [330]. Furthermore, MIL-125_NH_2 showed higher hydrophilicity than MIL-125 during water vapor adsorption but lower performance on the oxidative desulfurization of dibenzothiophene; the latter was ascribed to less steric hindrance to the active sites [253]. Yang *et al.* [331] developed a synthesis protocol that enhanced the photocatalytic performance for the oxidative desulfurization of 4,6-dimethyldibenzothiophene by using butyric acid as a modulator, which produced well-shaped truncated octahedron MIL-125(Ti) crystals. Furthermore, MIL-125(Ti)_NH_2 was already subject of study for capturing iodine from waste water, for which this porous solid was found to remove about 85% of I_2 within 90 minutes [332]. However, to this day, there is no mention in the literature of a MIL-125(Ti) compound being used for trapping gaseous iodine.

Clearly, MIL-125(Ti) and MIL-125(Ti)_NH_2 compounds exhibit a great photocatalytic performance, mostly related to the occurrence of titanium cations in its oxo-hydroxy inorganic cluster. Actually, the presence of Ti sites reduces the band gap of the material when compared to other terephthalic-based MOFs such as UiO-66(Zr) [13,105]. According to previous studies, in

particular that presented in Chapter IV, the smaller band gap of the MOF can improve the CTC between the compound and the I_2 molecule, which enhances the I_2 immobilization and boosts its transformation into I_3^- [13]. Also, the presence of titanium can alter the type of CTC from a LBT in UiO-6*x* (*x* = 6, 7, or 8) materials to a LMCT [27,249], which should modify the mechanism of the iodine evolution [13]. For this reason, this chapter is devoted to understanding the adsorption and evolution of iodine in the core of titanium-based MOFs MIL-125(Ti) and MIL-125(Ti)_NH_2. Moreover, CAU-1(Al)_NH_2 [333] (CAU stands for Christian Albrecht Universität) was also evaluated here for comparative purposes, as it presents an isostructural arrangement with MIL-125(Ti)_NH_2 materials, but with aluminum involved in a similar eight-ring based methoxy/hydroxy cluster linked through the amino-derivatives of BDC linker in the same way $[Al_8(OCH_3)_8(OH)_4(O_2C–C_6H_3(NH_2)–CO_2)_6]$. The nature of the metallic element (either Ti^{4+} or Al^{3+}) should influence both the band gap and the CTCs for this given MIL-125/CAU-1 topology. The synthesized materials were characterized by SEM, EDS, FTIR, Raman spectroscopy, diffuse reflectance UV-Vis spectroscopy, PXRD, EPR, and N_2 sorption.

6.2. Structural characterization of the pristine MIL-125 and CAU-1 samples

The summary of the physical chemical properties as well as iodine uptake values (after 72 h loading) of the three MOF samples – MIL-125(Ti), MIL-125(Ti)_NH_2 and CAU-1(Al)_NH_2 – that have been selected for the present study are presented in Table 6.1.

Table 6.1: Physical chemical properties for the MIL-125(Ti), MIL-125(Ti)_NH_2 and CAU-1(Al)_NH_2 materials highlighting the band gap energies, SSA_{BET}, microporous volume, and iodine uptake after 72 h of contact with I_2 flow.

MOF	Band gap		$SSA_{(BET)}$	Microporous volume	Iodine uptake*		
	Direct (eV)	Indirect (eV)	($m^2.g^{-1}$)	($cm^3.g^{-1}$)	(mol.mol^{-1})	(g.mol^{-1})	(g.g^{-1})
CAU-1(Al)_NH_2	2.8	2.6	1110 ± 22	0.52	4.2	1059	1.3
MIL-125(Ti)_NH_2	2.7	2.5	1099 ± 26	0.51	11.0	2782	1.7
MIL-125(Ti)	3.8	3.6	1207 ± 34	0.60	8.7	2213	1.4

*Experiments carried at room temperature after 72 h of iodine gas flow.

6.2.1. Crystallography and textural properties

Seeking to verify if the compounds produced in this work were well synthesized, their PXRD patterns were collected and are displayed in Figure 6.1. The examination of the XRD diffractograms shows a very good agreement with those reported in the literature [26,333].

Characteristic diffraction Bragg peaks of MIL-125(Ti), MIL-125(Ti)_NH_2, and CAU-1(Al)_NH_2 were verified at 2θ about 6.8º, 9.7º, 11.7º, 16.6º, 17.9º, and 19.5º, being attributed to the (101), (200), (211), (222), (312), and (400) crystal planes, respectively [334]. It is worth mentioning that no extra peak associated with titanium oxides or other related phases were observed in the PXRD patterns of MIL-125 compounds, which suggests that homogeneous crystallites were obtained rather than a mixture of other titanium-containing phases and individual MIL-125 crystals.

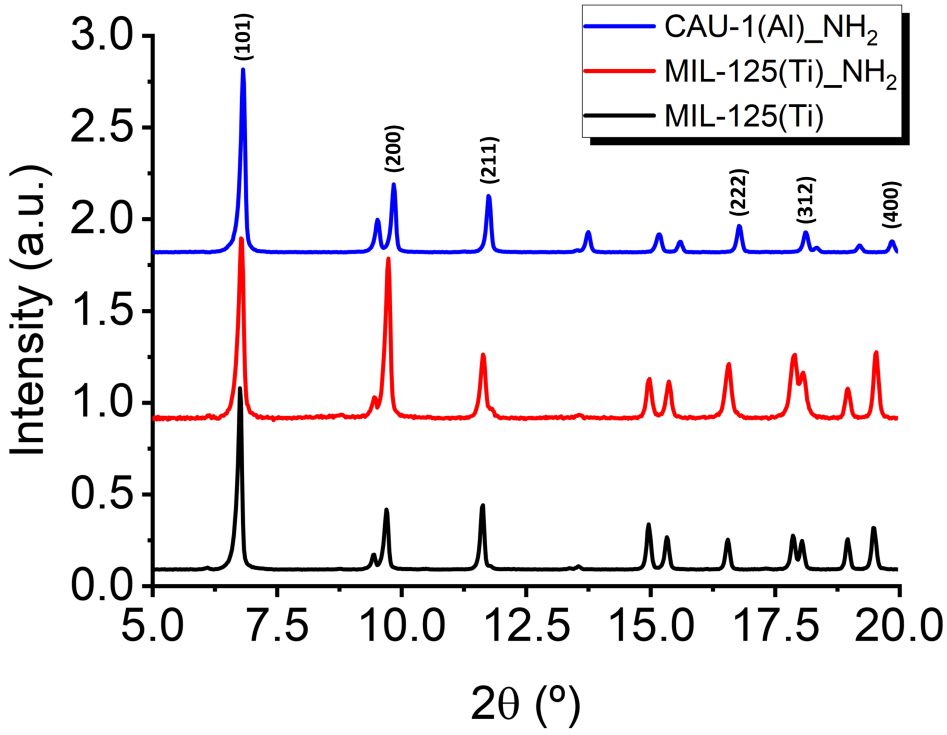

Figure 6.1: (a) powder XRD pattern of the activated MIL-125(Ti) (black), MIL-125(Ti)_NH_2 (red), and CAU-1(Al)_NH_2 (blue). $\lambda_{CuK\alpha}$ = 1.5406 Å.

Nitrogen sorption tests were conducted in order to obtain the SSA values from the BET method for the three samples (Figure 6.2), which exhibited a type I isotherm, characteristic of microporous materials according to the IUPAC classification [296]. All three values obtained for the SSAs (Table 6.1) agree well with other reports found in the literature (1181, 1109, and 1209 $m^2.g^{-1}$ for MIL-125(Ti), MIL-125(Ti)_NH_2, and CAU-1(Al)_NH_2, respectively) [331,335,336]. The presence of –NH_2 group slightly reduced the SSA of the MIL-125(Ti) due to the reduction of the pores' surface. On the other hand, the substitution of titanium from MIL-125(Ti)_NH_2 by aluminum did not have a considerable effect over the SSA in the CAU-15(Al)_NH_2 compound. In fact, since MIL-125(Ti)_NH_2 and CAU-1(Al)_NH_2 present an isostructural arrangement, the

effect of replacing the metallic content of the MOFs inorganic cluster should change the density of the sample and, consequently, their SSA values [13]. However, the presence of methoxy groups (–OCH_3) in CAU-1(Al)_NH_2 instead of the oxy groups in MIL-125(Ti)_NH_2 equipoise the variation observed between the atomic weight of both metals. Ultimately, the molecular weights of all three MOFs are quite similar – 1563.6 g.mol^{-1} for MIL-125(Ti), 1653.8 g.mol^{-1} for MIL-125(Ti)_NH_2, and 1606.5 g.mol^{-1} CAU-1(Al)_NH_2 – and therefore, also are their SSAs when normalized by mole units (SSAs = 1.8 km^2.mol^{-1} for all samples).

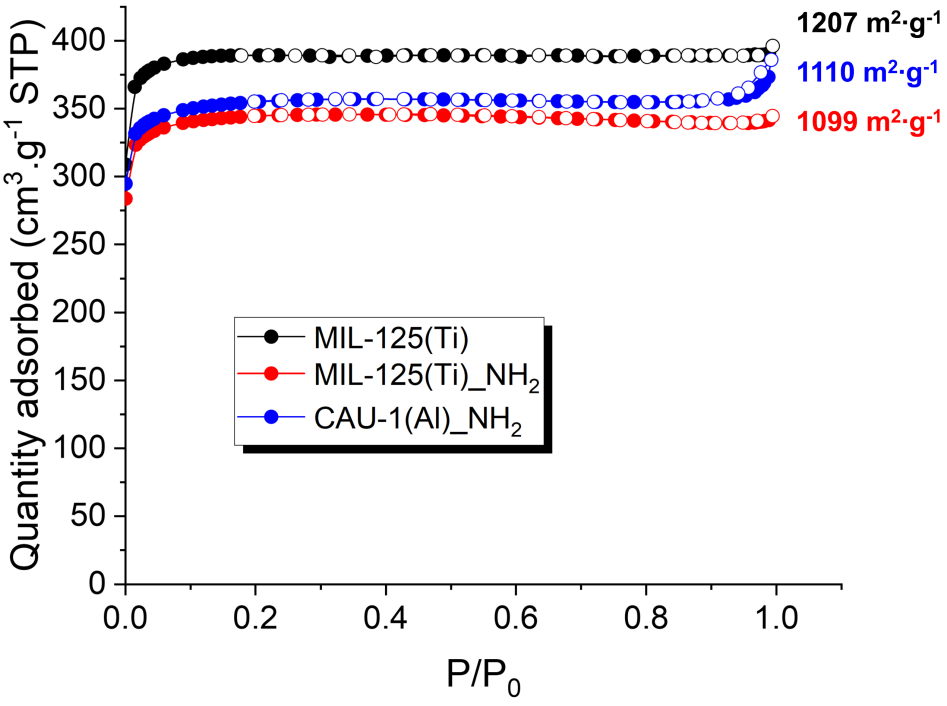

Figure 6.2: N_2 sorption tests and BET specific surface areas for MIL-125(Ti) (in black), MIL-125(Ti)_NH_2 (in red), and CAU-1(Al)_NH_2 (in blue).

The morphology of the MIL-125(Ti), MIL-125(Ti)_NH_2 and CAU-1(Al)_NH_2 crystallites was evaluated by SEM images, which are displayed in Figure 3. MIL-125(Ti) and MIL-125(Ti)_NH_2 exhibited crystallites that are analogous to truncated square pyramidal (≈ 1.0 µm) (Figure 6.3a) and tetragonal plate shapes (≈ 5.0 µm) (Figure 6.3b), respectively. These specific well-defined morphologies are in agreement with those expected for such materials [331,337]. On the other hand, CAU-1(Al)_NH_2 compound is characterized by cube-shaped crystals (≈ 400 nm), as reported in previous studies [338]. The absence of TiO_2 spheres indicates that no titanium impurities are present in both MIL-125 compounds. Moreover, a chemical map was also recorded for all the samples in order to assess their metal distribution. As expected, the

MIL-125(Ti) and MIL-125(Ti)_NH_2 crystallites exhibited a homogeneous Ti distribution and the absence of titanium oxide agglomerates. Note that nitrogen, like titanium, is also very well dispersed in MIL-125(Ti)_NH_2 crystallites (Figure 6.3b). A similar behavior is exhibited for nitrogen and aluminum in CAU-1(Al)_NH_2.

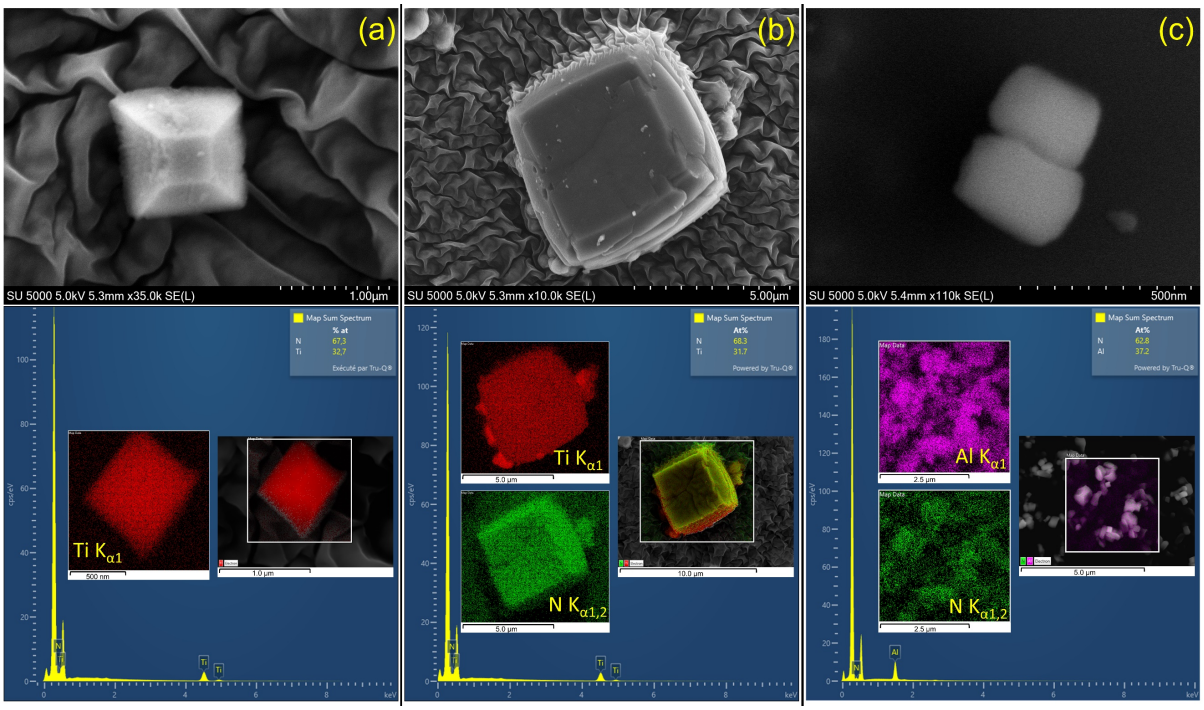

Figure 6.3: SEM images and EDS spectra displaying the elemental distribution of titanium (red), aluminum (pink), and nitrogen (green) throughout (a) MIL-125(Ti), (b) MIL-125(Ti)_NH_2, and (c) CAU-1(Al)_NH_2. Ti $K_{\alpha1}$, Al $K_{\alpha1}$, and N $K_{\alpha1,2}$ signals.

6.2.2. Vibrational spectroscopy

Aiming to identify the main vibrational modes of MIL-125(Ti), MIL-125(Ti)_NH_2, and CAU-1(Al)_NH_2, and also to confirm the absence of other impurities (such as amorphous TiO_2), the FTIR and Raman vibrational spectra of the activated materials were recorded and are displayed in Figure 6.4. The main band attributions are shown in Table 6.2.

Table 6.2: FTIR and Raman bands assignments for MIL-125(Ti), MIL-125(Ti)_NH_2, and CAU-1(Al)_NH_2

Wavenumber (cm^{-1})						Band assignments	Ref.
FTIR			Raman			M = (Al or Ti)	
MIL-125 (Ti)	MIL-125 (Ti)_NH_2	CAU-1 (Al)_NH_2	MIL-125 (Ti)	MIL-125 (Ti)_NH_2	CAU-1 (Al)_NH_2		
440	434	499	–	–	–	μ_2–OH stretching	[285,339]
541	558	550	–	–	–	M–(OC) asymmetric stretching	[13,285]
630	624	616	–	–	–	μ_2–O stretching	[285,340,341]
748	770	774	–	–	–	μ_2–OH bending	[285,340,341]
–	–	–	703	691	697	Octahedral μ_2–O	[337]
–	–	–	1144	1132	1137	Aromatic ring breathing	[285]
1158	1160	1167	–	–	–	(C=C)–H bending + O–C–O symmetric stretching	[285]
–	1335	1341	–	–	–	C–N stretching (aryl–NH_2)	[340]
1392	1382	1396	–	–	–	C=C–(COO) asymmetric stretching	[285,337]
1415	1424	1427	1433	1424	1428	O–C–O symmetric stretching	[285,340,342]
1441	1441	1441	1447	1447	1458	(C=C)–H bending + C=C stretching	[285,337,340]
–	1580	1580	–	1586	1594	N–H bending	[340]
–	–	–	1616	1627	1627	O–C–O asymmetric stretching	[285]
–	–	–	–	1627	1627	N–H bending	[340]
–	–	–	2934	2929	2945	C–H stretching	[343]
–	–	–	2970	2970	2988	C–H stretching	[343]
–	–	–	3078	3080	3086	C–H stretching	[343]
–	3380	3392	–	–	–	N–H stretching	[337]
3678	3656	3651	–	–	–	O–H stretching	[285]

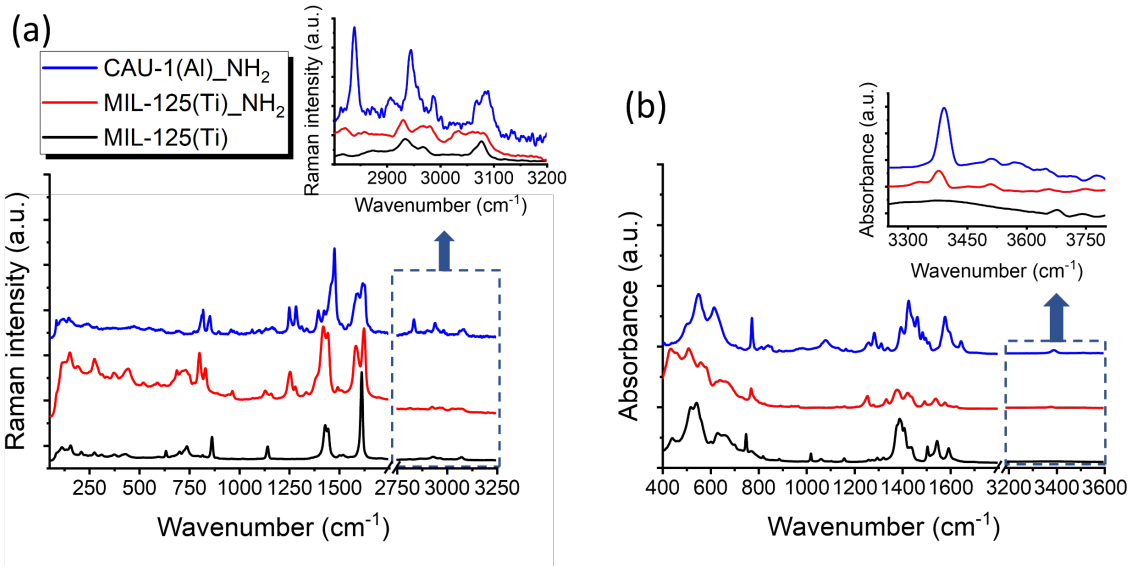

Figure 6.4: (a) FT-Raman and (b) FTIR spectra of MIL-125(Ti) (black), MIL-125(Ti)_NH_2 (red), and CAU-1(Al)_NH_2 (blue). The insight reveals a zoom in the region related to C-H and N-H stretching vibrations in Raman and FTIR spectra, respectively.

First, the presence of titanium oxide (as anatase or rutile) in the MIL-125(Ti) and MIL-125(Ti)_NH_2 samples was discarded after verifying that there is no sharp band at about 140–150 cm^{-1} related to TiO_2 species in the Raman spectra, which is in accord with the powder XRD results (Figure 6.1. and Figure 6.4a) [108]. When focusing on the inorganic cluster vibrational modes, the Raman spectra of MIL-125(Ti) and MIL-125(Ti)_NH_2 present a band related to the titanium cation with a typical octahedral coordination environment at 703 and 691 cm^{-1}, respectively [337]. Additionally, a similar signal was found for CAU-1(Al)_NH_2 at 697 cm^{-1}, which should be ascribed to the equivalent vibrational mode of the aluminum species in octahedral coordination. Inorganic cluster vibrational modes are also present in the FTIR spectra of all the three compounds, as demonstrated by the absorption bands related to Ti–O and Ti–OH vibrations at about 748 and 630 cm^{-1} for MIL-125(Ti) and at 770 and 640 cm^{-1} for MIL-125(Ti)_NH_2 [285,340]. The analogous vibrational mode for the aluminum compound was found at 774 and 616 cm^{-1} in the CAU-1(Al)_NH_2 spectra [341]. Furthermore, when considering the MIL-125 materials, both the position and the relative intensity of the bands comprised between 400 and 800 cm^{-1} (which are related to different O–Ti–O vibrations inside the inorganic octanuclear cluster) [337] are affected by the presence of the amino group in MIL-125(Ti)_NH_2. In fact, stretching vibrations of Ti–OH are present in MIL-125(Ti) and MIL-125(Ti)_NH_2 compounds at 440 and 434 cm^{-1}, respectively [285,339]. Moreover, the M–(OC) asymmetric stretching mode was found in the Raman spectra at 541, 558, and 550 for MIL-

125(Ti), MIL-125(Ti)_NH_2, and CAU-1(Al)_NH_2, respectively [13,285]. These features demonstrate that the occurrence of –NH_2 groups from the NH_2-BDC linker can also affect the vibrational modes of the inorganic oxo/hydroxy cluster. On the other hand, bands related to the vibrational modes of the linkers are present in all three spectra, for both infrared absorption and Raman scattering.

For instance, the aromatic ring breathing mode of the organic linker is observed in the Raman spectra between 1132 and 1144 cm^{-1} for all the three MOFs. Also, a band related to the asymmetric O–C–O stretching of the carboxylate group is observed at 1616 cm^{-1} in the Raman spectrum of MIL-125(Ti) and at 1627 cm^{-1} in MIL-125(Ti)_NH_2 and CAU-1(Al)_NH_2 compounds, respectively [285]. On the other hand, the symmetric O–C–O stretching is present at 1415, 1424, and 1427 cm^{-1} in FTIR spectroscopy for MIL-125(Ti), MIL-125(Ti)_NH_2 and CAU-1(Al)_NH_2, respectively [285,340,342]. This carboxylate vibration is also detected in the Raman spectra of the three compounds: at 1433, 1424, and 1428 cm^{-1}, respectively. Another component of the O–C–O symmetric stretching vibration was found in the FTIR spectra alongside the (C=C)–H bending mode at 1158, 1160, and 1167 cm^{-1} for MIL-125(Ti), MIL-125(Ti)_NH_2, and CAU-1(Al)_NH_2 [285]. Moreover, carbonyl vibrations C=C–(COO) are visible at 1392, 1382, and 1396 cm^{-1} for MIL-125(Ti), MIL-125(Ti)_NH_2, and CAU-1(Al)_NH_2, respectively [285,337]. Also, the C=C stretching is observed at 1441 cm^{-1} in the same region as the (C=C)–H bending mode in the FTIR spectra of all three compounds. In the Raman spectra this signal is present at 1447 cm^{-1} for the titanium-based materials, and at 1458 cm^{-1} for CAU-1(Al)_NH_2 [285,337,340]. The C–H stretching mode is also visible in the Raman spectra of all compounds between 2900 and 3200 cm^{-1} [343]. Lastly, a band related to the N–H bending mode was detected in Raman spectra at 1627 cm^{-1} due to the amino-functionalized terephthalate linkers for both MIL-125(Ti)_NH_2 and CAU-1(Al)_NH_2, respectively [340]. Furthermore, the C–N stretching mode related to aryl–NH_2 bond is observed in the FTIR spectra of MIL-125(Ti)_NH_2 at 1335 cm^{-1} and of CAU-1(Al)_NH_2 at 1341 cm^{-1} [340]. The N–H bending is observed in the Raman of MIL-125(Ti)_NH_2 and CAU-1(Al)_NH_2 at 1586 and 1594 cm^{-1}, respectively [340]. This vibrational mode is also active in FTIR, with a signal at 1580 cm^{-1} for both amino-functionalized materials, while the N–H stretching vibration is observed 3380 cm^{-1} for MIL-125(Ti)_NH_2 and 3392 cm^{-1} for CAU-1(Al)_NH_2 [337,340].

6.2.3. Optical and electronic properties

The analysis of the synthesized materials was also performed using diffuse reflectance UV-Vis spectroscopy as titanium-based MOF compounds are known to exhibit interesting optical properties that can improve the iodine adsorption and evolution [13,344]. The Kubelka-Munk plots of the diffuse reflectance UV-Vis spectra for the three pristine MOFs are displayed in Figure 6.5.

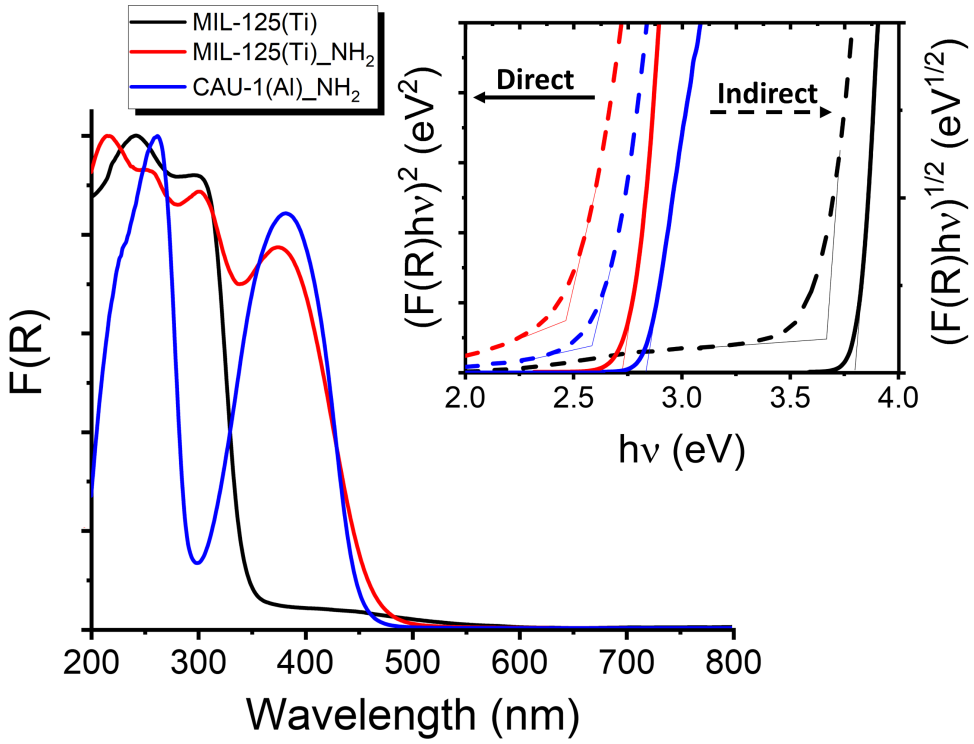

Figure 6.5: UV-vis spectra of MIL-125(Ti) (black), MIL-125(Ti)_NH_2 (red), and CAU-1(Al)_NH_2 (blue). Inset: the Tauc plot considering the compounds as presenting direct and indirect band gaps – $(F(R)h\nu)^2$ are exhibited in dotted lines, whereas $(F(R)h\nu)^{1/2}$ are shown in dotted lines.

It is worth mentioning that the spectra of all three pristine materials are in agreement with those reported in the literature [202,254,345]. MIL-125(Ti) spectrum exhibits two contributions at 242 and 300 nm, with an absorption edge at 350 nm [202]. Although the first contribution (at 242 nm) was assigned to HOCO – LUCO transitions in π–π* BDC linker orbitals in UiO-66 materials [13,27], other studies have shown that there is hardly any orbital overlap in MIL-125(Ti) and therefore, no π–π stacking is possible which keeps the electrons preferentially in a localized state (contrary to that observed for UiO-66) [246]. This behavior was ascribed to the long distance between the BDC linkers in MIL-125(Ti), which are about 7 Å apart [246,252]. Moreover, the inorganic clusters are also too far apart, which prevents the Mott transitions to occur [246].

Therefore, the absorption signal in the MIL-125(Ti) UV-Vis spectrum is attributed to the octahedrally coordinated titanium cations [253]. Indeed, linker-to-metal charge transfer is assumed to be present in MIL-125(Ti), as demonstrated by Hendon *et al.* [202]. Their study revealed that the valence band of MIL-125(Ti) is composed of BDC aromatic *2p* orbitals, while the CB is formed by titanium *d* orbitals and oxygen *p* orbitals [202]. This behavior is coherent with the work of Dan-Hardi *et al.* [26], who proposed that MIL-125(Ti) photogenerated electrons are trapped in the Ti^{4+} centers, inducing the Ti^{3+} formation. Similarly, the broad band in MIL-125(Ti)_NH_2 (with an absorption edge that extends up to 550 nm) was mainly assigned to the LMCT between the NH_2-BDC linker and the inorganic cluster [202,254]. It is interesting to note that De Miguel et al. [257] demonstrated that this charge separation in MIL-125(Ti)_NH_2 creates holes which are localized on the organic linkers either on the carboxylate or on the amino groups [257], while the electron stays in the titanium inorganic cluster [256].

Actually, the amino group acts as a hole stabilizer in MIL-125(Ti)_NH_2, prolonging the lifetime of the photoexcited state compared to that of MIL-125(Ti) [256]. This behavior demonstrates that the LMCT must take place from N or O atoms into Ti^{4+} cations [258]. In fact, studies have proven that the amino functionalization increases the VB energy in MIL-125(Ti)_NH_2 materials, a phenomenon which is basically caused by the introduction of mid-gap states related to the $–NH_2$ group [258,259]. This feature was already reported for other MOF materials such as the UiO-6*x* family (*x* = 6, 7, or 8) [249]. Actually, although the $–NH_2$ group has no influence over the CBM, the new VBM is above that of MIL-125(Ti) because of the strong electron donator character of aromatic amines [258]. This effect also reduces the band gap of the MIL-125(Ti)_NH_2 compound compared to that of MIL-125(Ti) [202]. Finally, the CAU-1(Al)_NH_2 compound exhibits two main absorption bands centered at 252 nm and 383 nm. Although no clear interpretation could be found for the photoexcitation of the CTCs formed within MIL-125(Ti)_NH_2, it seems that the spectrum of this material includes both the contributions of MIL-125(Ti) – at 300 nm, related to the LMCT – and of CAU-1(Al)_NH_2 – at about 380 nm. Thus, this indicates that the second absorption band, observed at 383 nm in the spectrum of CAU-1(Al)_NH_2, is probably due to its amino group, since this function is common to both Ti and Al-compounds. Nevertheless, the presence of LMCT complexes in aluminum-based MOFs is unlikely since Al^{3+} does not have *d*-orbitals (Al = [Ne] $3s^2$ $3p^1$; Al^{3+} = [He] $2s^2$ $3p^6$) that would be suitable to overlap with the NH_2-BDC π^* orbitals. Actually, the most common BDC-based MOFs do not exhibit LMCT complexes, as already discussed in other studies [13,27]. For instance, Nasalevich *et al.* [27] highlighted the differences in activity between

the MIL-125(Ti)_NH_2 and the hafnium and zirconium-based UiO-66_NH_2. The study showed that the LUCO of the MOF is located at the inorganic node in the case of MIL-125(Ti)_NH_2, whereas it is located in the linker in UiO-66(M)_NH_2 (M = Hf, Zr) compounds, as discussed in Chapter IV. This difference was ascribed to the fact that both hafnium and zirconium-based materials have *d*-orbitals with low binding energy, preventing the overlap with the π* orbitals from the BDC linker and, consequently, the electron-hole transitions between the linker and the inorganic oxo/hydroxy cluster. On the other hand, the *d*-orbitals of titanium meet both the spatial and energetic requirements, which allows an efficient interaction that leads to CTCs between the linker and the inorganic Ti–(O, OH) cluster, inducing the formation of delocalized Ti^{3+} species [27]. Therefore, for a LMCT to be observed in the case of CAU-1(Al)_NH_2, there must be an overlap between the NH_2-BDC π* and the unoccupied $3s^0$ orbital of the Al^{3+} cation, which is rather unlikely. For this reason, it is assumed that the CAU-1(Al)_NH_2 material exhibits a LBT mechanism, similar to that found for UiO-*n* (*n* = 6, 7, or 8) compounds [27,250].

Aiming to better understand the nature of these transitions, the band gaps of the samples were evaluated according to the Tauc method (see inset in Figure 6.5). Although MIL-125(Ti) compounds were already reported to present a direct band gap [346], articles considering an indirect band gap for such MOFs are also easily found in the literature [335]. Indeed, according to the methodology proposed in Chapter III, these materials exhibit indirect band gaps. However, because of the proximity of both $E_{g(dir)}$ and $E_{g(ind)}$ values in this case – especially in MIL-125(Ti)_NH_2 – calculations considering both scenarios were considered in this work. As expected, the presence of the amino group acts as an "antenna" that can push up the HOCO energy by adding new occupied bands, as mentioned before [105,249,258]. For such reason, the direct band gap of MIL-125(Ti) (3.8 eV) was reduced to 2.7 eV in MIL-125(Ti)_NH_2 and the indirect band gap decreased from 3.6 eV in MIL-125(Ti) to 2.5 eV in MIL-125(Ti)_NH_2. This feature is in accord with experimental and theoretical results reported in the literature [335,346]. Lastly, for CAU-1(Al)_NH_2, only values related to direct band gaps can be found in the literature. Zhang *et al.* [347] obtained a direct band gap of 3.0 eV for this material (which is close to that obtained here) when evaluating the E_g energies of a series of functionalized CAU-1(Al)_X (X = NH_2, OH, CH_3, $(CH_3)_2$, and $(OH)_2$). However, although the indirect band gap has not yet been considered in the literature for this material, as mentioned before, the proximity between the direct and indirect E_g makes it interesting to acquire both values [216]. Regardless of the nature of the band gap, direct or indirect, the same trend is observed when comparing CAU-1(Al)_NH_2 and MIL-125(Ti)_NH_2 which results in a very small increase in E_g values in

the presence of aluminum. The obtained value for the direct E_g went from 2.7 eV in MIL-125(Ti)_NH_2 to 2.8 eV in CAU-1(Al)_NH_2, whereas the indirect E_g passed from 2.5 to 2.6 eV, respectively. This difference should be related to the presence of titanium in MIL-125(Ti)_NH_2, as its empty *d*-orbitals exhibit a high electron acceptor character and therefore, push down the LUCO position by adding new unoccupied bands in the CBM [27,249].

6.2.4. Paramagnetic properties

The EPR spectra of all compounds were recorded to identify the paramagnetic species present in dark conditions and/or upon irradiation (Figure 6.6). The main signals observed in other works related to Ti^{3+}, to oxygen species, and to trapped holes (h^+) are summarized in Table 6.3. All the pristine MOF materials exhibit, in dark conditions, signals related to oxygen species at *g*-factor between 2.002 – 2.022 [348–350]. Actually, the initial signals at g = 2.006 in MIL-125(Ti) and at g = 2.004 in MIL-125(Ti)_NH_2 at 120 K were attributed to oxygen lacuna defects in the Ti–O inorganic cluster, possibly related to missing linkers in the MOF samples (Figure 6.6a and 6b) [351]. These defects compromise the charge stability of the pristine material, resulting in the Ti^{4+}–$O_2^{\bullet-}$ paramagnetic species [348]. On the other hand, CAU-1(Al)_NH_2 exhibited hyperfine signatures in dark conditions at both RT and 120 K (Figure 6.6c). These signals incorporate contributions of oxygen (resulting in the corresponding Al^{3+}–$O_2^{\bullet-}$ form) but also from nitrogen paramagnetic species ($^{\bullet}NH_2^+$) [350]. For illustrating this effect, the EPR powder spectrum of CAU-1(Al)_NH_2 at 120 K was simulated considering two paramagnetic species: the narrow line corresponding to the lacuna defects with a *g*-factor of 2.0042, and the nitrogen centered radical with *g*-matrix value of 2.008, 2.008, and 2.006 (Figure 6.7) [178].

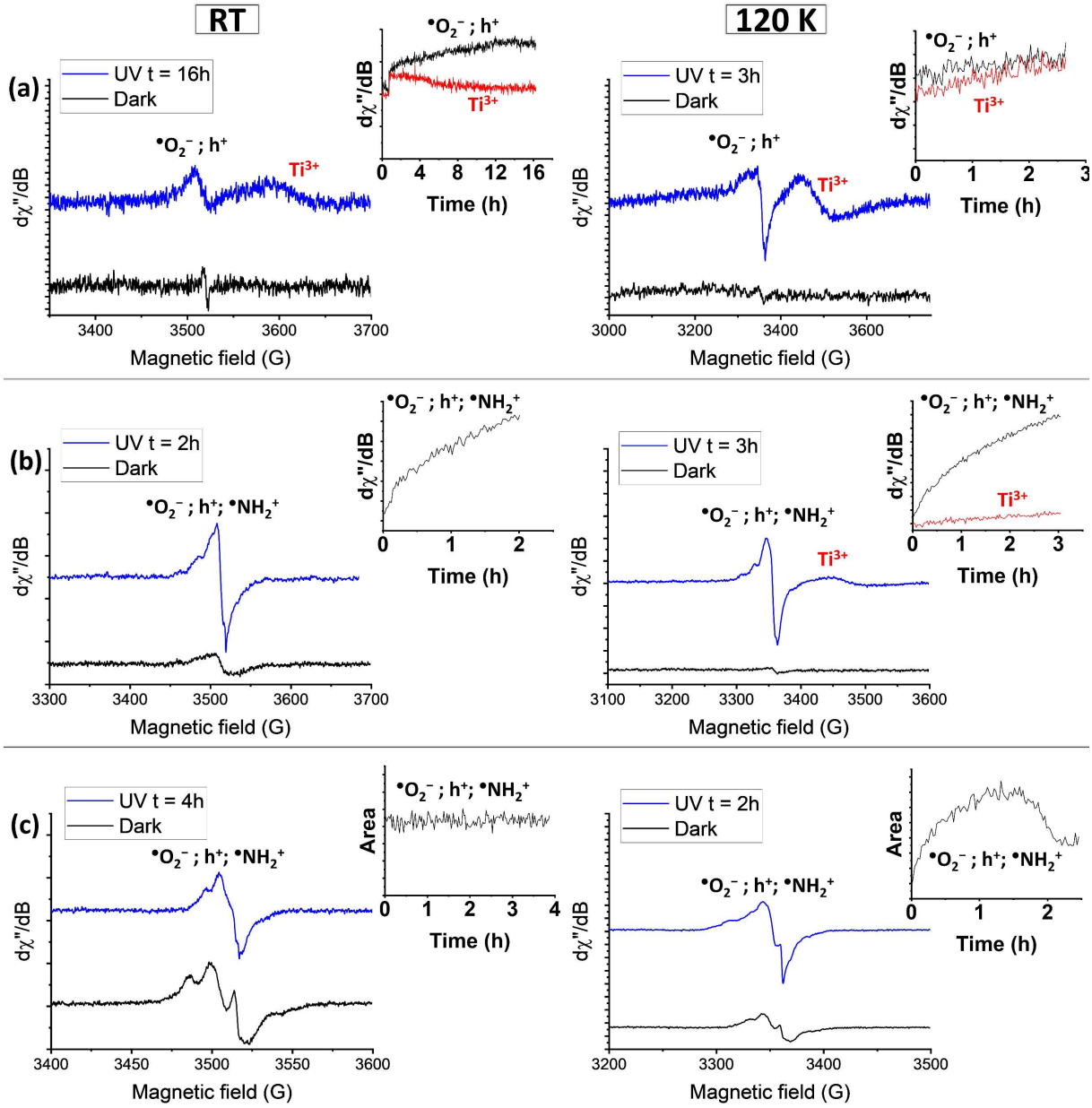

Figure 6.6: EPR spectra for (a) MIL-125(Ti), (b) MIL-125(Ti)_NH_2, and (c) CAU-1(Al)_NH_2 recorded at room temperature (RT) and at 120 K. Inset: time evolution of the signal's intensity (a, and b) and area (c) for each material.

Table 6.3: EPR parameters of paramagnetic species for TiO_2, MIL-125(Ti), MIL-125(Ti)_NH_2, and CAU-1(Al)_NH_2 compounds.

Reference	Material	Temperature	Attribution	*g*-factor		
				g_z	g_y	g_x
Howe *et al.* [348]	Anatase	4.2 K	Ti^{3+}	1.990	1.990	1.960
Micic *et al.* [352]	TiO_2 colloids	77 K	Ti^{3+}	–	–	1.928
Hurum *et al.* [353]	Anatase	10 K	Ti^{3+}	1.990	1.990	1.975
Hurum *et al.* [353]	Rutile	10 K	Ti^{3+}	1.975	1.975	1.940
Furukawa *et al.* [354]	Degussa P25	123 K	Ti^{3+}	1.982	1.977	1.971
Nasalevich *et al.* [349]	MIL-125(Ti)_NH_2	RT	Ti^{3+}	–	–	1.946
Carter *et al.* [350]	Degussa P25	130 K	Bulk Ti^{3+}	1.990	1.990	1.957
Carter *et al.* [350]	Degussa P25	130 K	Surface Ti^{3+}	–	–	1.930
This work	MIL-125(Ti)	RT	Ti^{3+}	–	–	1.934
This work	MIL-125(Ti)	120K	Ti^{3+}	–	–	1.932
This work	MIL-125(Ti)_NH_2	120K	Ti^{3+}	–	–	1.939
Carter *et al.* [350]	Degussa P25	130 K	$^{\bullet}O_2^-$	2.019	2.011	2.005
Komaguchi *et al.* [355]	Rutile	77 K	$^{\bullet}O_2^-$	2.020	2.010	2.003
Furukawa *et al.* [354]	Degussa P25	123 K	$^{\bullet}O_2^-$	2.024	2.009	2.003
Sun *et al.* [351]	MIL-125(Ti)_NH_2	RT	$^{\bullet}O_2^-$	2.023	2.015	2.003
Zeama *et al.* [356]	MIL-125(Ti)_NH_2	173 K	$^{\bullet}O_2^-$	2.023	2.015	2.003
Howe *et al.* [348]	Anatase	77 K	$^{\bullet}O_2^-$	2.025	2.009	2.003
Kumar *et al.* [357]	Anatase	4.2 K	$^{\bullet}O_2^-$	2.026	2.015	2.005
Kumar *et al.* [357]	Rutile	4.2 K	$^{\bullet}O_2^-$	2.026	2.017	2.008
This work	MIL-125(Ti)	RT	$^{\bullet}O_2^-$; h^+	–	–	2.007
This work	MIL-125(Ti)	120 K	$^{\bullet}O_2^-$; h^+	–	–	2.006
This work	MIL-125(Ti)_NH_2	RT	$^{\bullet}O_2^-$; h^+	–	–	2.004
This work	MIL-125(Ti)_NH_2	120 K	$^{\bullet}O_2^-$; h^+	–	–	2.004
This work	CAU-1(Al)_NH_2	RT	$^{\bullet}O_2^-$; h^+	–	–	2.004
This work	CAU-1(Al)_NH_2	120 K	$^{\bullet}O_2^-$; h^+	–	–	2.004
Kumar *et al.* [357]	Anatase	4.2 K	$Ti^{4+}O^{\bullet-}Ti^{4+}OH^-$	2.016	2.012	2.002
Kumar *et al.* [357]	Rutile	4.2 K	$Ti^{4+}O^{\bullet-}Ti^{4+}OH^-$	2.019	2.014	2.002
Howe *et al.* [348]	Anatase	4.2 K	Trapped holes	2.016	2.012	2.002
Hurum *et al.* [353]	Degussa P25	10 K	Trapped holes	2.024	2.014	2.007
This work	MIL-125(Ti)_NH_2	RT	$^{\bullet}NH_2^+$	2.008	2.008	2.006
This work	MIL-125(Ti)_NH_2	120 K	$^{\bullet}NH_2^+$	2.008	2.008	2.006
This work	CAU-1(Al)_NH_2	RT	$^{\bullet}NH_2^+$	2.008	2.008	2.006
This work	CAU-1(Al)_NH_2	120 K	$^{\bullet}NH_2^+$	2.008	2.008	2.006

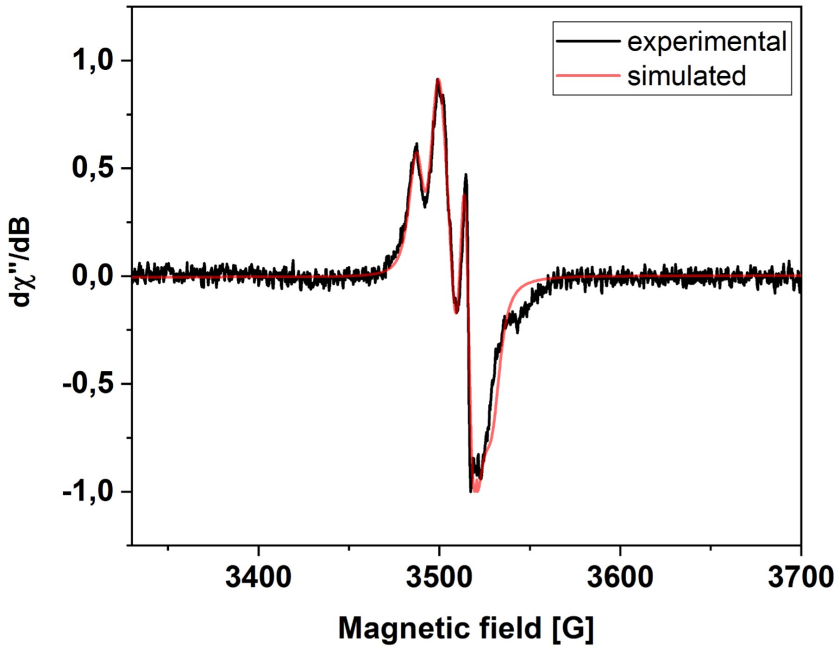

Figure 6.7: Experimental (black) and simulated (red) EPR spectra of CAU-1(Al)_NH_2 at 120 K using the EasySpin software. Two species have been introduced for the simulation: one corresponding to the narrow line with a g-factor of 2.0042 and the second due to nitrogen centered radical with g-matrix value of 2.008, 2.008, and 2.006. The hyperfine coupling with the nitrogen shows a weak anisotropy with $A_x = A_y = 25$ MHz and $A_z = 39$ MHz.

The hyperfine coupling with the nitrogen shows a weak anisotropy with $A_x = A_y = 25$ MHz and $A_z = 39$ MHz. This effect is related to the photogeneration of electron-hole pairs in the NH_2-BDC linker, which create holes that are further stabilized in nitrogen species as $^{\bullet}NH_2^+$ [256,257]. This effect was equally observed in the CAU-1(Al)_NH_2 spectrum at 120 K, and also in the MIL-125(Ti)_NH_2 spectra (with lower intensity) at both RT and 120 K. Additionally, the CAU-1(Al)_NH_2 material did not exhibit any signals related to Al^{3+} species, which is understandable since Al^{3+} is not a paramagnetic species (Al^{3+} = [He] $2s^2$ $2p^6$). Note also that the absence of a signature related to Al^{2+} is also obvious and highlights the impossibility of a LMCT to take place in the CAU-1(Al)_NH_2. This effect is in accord with the LBT mechanism in CAU-1(Al)_NH_2 as the material's valence and conduction band are purely related to its organic linker. On the other hand, the irradiation of the titanium-based MOFs induces a LMCT mechanism [26,27,202,254], which is responsible for reducing the Ti^{4+} cations into the Ti^{3+} paramagnetic species, as confirmed by the presence of a signal at $g = 1.934$ (RT), and at g = 1.932 (120 K) for MIL-125(Ti) [358]. However, because Ti^{3+} is hardly observed at RT due to high recombination rate, this signature was only observed at 120 K for MIL-125(Ti)_NH_2, at $g = 1.939$ [357,358]. This is the reason why the Ti^{3+} band reduces its intensity in MIL-125(Ti) (RT)

after reaching a maximum value after about 2h of irradiation, but it continues to rise at 120 K – for both MIL-125(Ti) and MIL-125(Ti)_NH_2 (Figure 6.6). Unarguably, the formation of Ti^{3+} through a LMCT mechanism is essentially associated to the stabilization of holes in the BDC or NH_2-BDC linker [13,256,257]. However, because the h^+ entity displays a signal at about g = 2.007 [348] (same position as the oxygen lacuna species), the signature which was initially related to $^{\bullet}O_2^-$ now increases with irradiation time due to the h^+ formation in both MIL-125(Ti) and MIL-125(Ti)_NH_2 compounds. In addition, a small contribution of $^{\bullet}NH_2^+$ is also observed in MIL-125(Ti)_NH_2 upon irradiation, as the amino group acts as a hole stabilizer. These features are coherent with the CTCs observed in terephthalate-based MOFs, as discussed by several authors [27,349].

6.3. Iodine adsorption and evolution

The three MOF powdered materials were put in contact with the iodine gas flow for five days in order to obtain information about their adsorption kinetics and maximum I_2 uptake capacity. Intending to reduce the influence of the different molecular weight of the samples, the kinetic was evaluated considering the mass of trapped iodine per mol of MOF (instead of mass of iodine per mass of MOF), as represented in Figure 6.8.

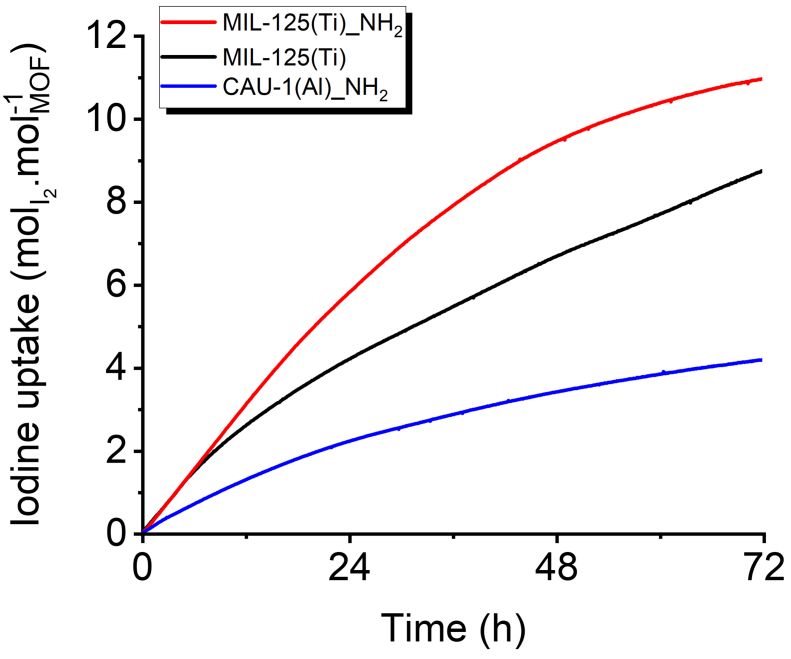

Figure 6.8: Iodine adsorption kinetics evaluated by UV-vis spectroscopy for 72 h of contact between the I_2 gas and the MOF powdered samples for: MIL-125(Ti) (black), MIL-125(Ti)_NH_2 (red), and CAU-1(Al)_NH_2 (blue).

To characterize and analyze the I_2 adsorption capacity of MOF materials, the SSA, which represents one of the most telling properties of these materials, was first considered. Indeed, a better iodine trapping ability is expected for materials with higher SSAs. Nevertheless, even though MIL-125(Ti)_NH_2 seems to exhibit the smaller SSA (1099 $m^2.g^{-1}$), it presents the best trapping capacity for I_2, reaching 11 $mol.mol^{-1}$ after three days. In the same conditions, MIL-125(Ti) (SSA = 1207 $m^2.g^{-1}$) and CAU-1(Al)_NH_2 (SSA = 1110 $m^2.g^{-1}$) adsorb 8.7 and 4.2 $mol.mol^{-1}$, respectively. However, as already mentioned before, all the three materials synthesized here showed similar SSAs values when normalized by mole unities (SSAs = 1.8 $km^2.mol^{-1}$), which should exclude the influence of this variable over the MOFs iodine uptake. Even so, although the SSA has an enormous influence on the adsorption process, studies have shown that if the pores are too large, the I_2 molecules have a tendency to pass through the framework without being adsorbed – which is the case for UiO-68 [12]. Other characteristics also have an impact over the iodine adsorption kinetics, such as the linker functionalization and the electronic structure of the materials [13,25]. With that in mind, several characteristics were compared in this work, such as amino group functionalization, band gap energies, metal sites, and CTCs (Table 6.4).

Note that it is very difficult to separate the influences of the different variables that may have an impact on the iodine adsorption capacity in MOF materials, especially when considering the amino group effect. This is mainly related to the fact that the $–NH_2$ functionalization reduces the band gap of the samples, at the same time that it improves the electron donor character of the linker [12,25]. For instance, when comparing the MIL-125(Ti) and MIL-125(Ti)_NH_2 compounds, the I_2 uptake increases 1.26 times after 72 h of I_2 flow in the presence of $–NH_2$, even though they have similar SSAs but different E_g energies (3.6 against 2.5 eV, respectively). The $–NH_2$ influence was also demonstrated in other works, where amino-functionalized UiO-66(Zr)_NH_2 and UiO-67(Zr)_NH_2 captured 2.78 and 4.89 times more iodine after 48 hours contact with I_2 than their parents UiO-66(Zr) and UiO-67(Zr), respectively (Table 6.4) [12]. In this previous work, even though the band gap energies of the samples were not evaluated, it is clear that the presence of the amino group and the introduction of another aromatic cycle on the organic linker of UiO-67(Zr)_NH_2 contributed to reduce the E_g values, as already reported in other studies [247,249,250]. Therefore, as discussed in Chapters IV and V, it seems that both the amino functionalization and the smaller band gap energies have a considerable effect on the I_2 uptake in MOF compounds.

Table 6.4: Comparison between different effects over the iodine uptake capacity: amino functionalization, charge transfer complexes (CTCs), band gap energies, and specific surface areas (SSAs) in UiO-66(Zr,Hf), UiO-67(Zr,Hf), MIL-125(Ti) and amino-derivates, as well as CAU-1(Al)_NH_2.

MOF	CTC	SSA ($m^2.g^{-1}$)	E_g (eV)	I_2 uptake * ($mol.mol^{-1}$)	Ref.
Amino functionalization					
MIL-125(Ti) → MIL-125_NH_2	LMCT	1207 → 1099	3.6 → 2.5	8.7[a] → 11.0[a]	PW
UiO-66(Zr) → UiO-66_NH_2	LBT	1387 → 825	N.A.	1.4[b] → 3.9[b]	[12]
UiO-67(Zr) → UiO-67_NH_2	LBT	1599 → 1565	N.A.	1.9[b] → 9.3[b]	[12]
Charge Transfer Complex					
CAU-1(Al)_NH_2 → MIL-125_NH_2	LBT → LMCT	1110 → 1099	2.6 → 2.5	4.2[a] → 11.0[a]	PW
UiO-66(Zr) → MIL-125(Ti)	LBT → LMCT	1387 → 1110	N.A. → 3.6	1.4[b] → 6.7[b]	[12][d]
UiO-66(Zr) → MIL-125(Ti)	LBT → LMCT	1263 → 95	4.1 → 3.6	0.9[c] → 3.1[c]	[13][d]
UiO-66(Zr)_NH_2 → MIL-125(Ti)_NH_2	LBT → LMCT	825 → 1110	N.A. → 2.5	3.9[b] → 9.4[b]	[12][d]
Band gap					
CAU-1(Al)_NH_2 → MIL-125_NH_2	LBT → LMCT	1110 → 1099	2.6 → 2.5	4.2[a] → 11.0[a]	PW
CAU-1(Al)_NH_2 → UiO-66(Zr)_NH_2	LBT	1110 → 825	2.6 → N.A.	4.2[a] → 3.9[b]	[12][d]
UiO-66(Zr) → UiO-66(Hf)	LBT	1263 → 818	4.1 → 4.0	0.9[c] → 1.1[c]	[13]
Specific Surface Area					
UiO-66(Zr) → UiO-67(Zr)	LBT	1387 → 1599	N.A.	1.4[b] → 1.9[b]	[12]
UiO-66(Hf) → UiO-66(Hf)_HCl	LBT	1119 → 1915	N.A.	0.6[e] → 0.9[e]	[168]
Lewis acidity					
UiO-66(Zr) → UiO-66(Hf)	LBT	1263 → 818	4.1 → 4.0	0.9[c] → 1.1[c]	[13]
UiO-67(Zr)_NH_2 → UiO-67(Hf)_NH_2	LBT	1329 → 914	2.9 → 2.9	6.5[b] → 13.5[b]	[359]

N.A. = not available. PW = present work. LMCT = linker-to-metal charge transfer. LBT = linker-based transfer. * Values were obtained as presented and converted into $mol.mol^{-1}$ considering one decimal place. [a] after 72 h of iodine contact. [b] after 48 h of iodine contact. [c] after 16 h of iodine contact. [d] data from MIL-125(Ti), MIL-125(Ti)_NH_2, and CAU-1(Al)_NH_2 were collected from this work. [e] adsorption values obtained after 72 h of contact with a 0.001 $mol.L^{-1}$ I_2/cyclohexane solution.

Moreover, the influence of the different CTCs can be evaluated by comparing CAU-1(Al)_NH_2 and MIL-125(Ti)_NH_2, as these materials exhibit similar SSA and E_g energies. In fact, the replacement of aluminum by titanium cations increases the I_2 uptake up to 2.62 times after 72 hours of contact with I_2, which was ascribed to the LMCT mechanism in the titanium-based MOF that improves charge separation (Table 6.4). Similarly, comparisons can be made with other works considering materials with similar BDC-based structures: UiO-66(Zr) vs.

MIL-125(Ti) and UiO-66(Zr)_NH_2 vs. MIL-125(Ti)_NH_2. In the first case, the E_g and SSA of MIL-125(Ti) are smaller than those of UiO-66(Zr); however, the presence of titanium creates an LMCT in MIL-125(Ti), which is able to improve the iodine capture by 3.44 times after 16 hours of I_2 contact [13] and even by 4.57 times after 48 hours of iodine contact [12]. This effect is again related to the better charge separation characteristic of LMCT processes [257], which enhances the interaction between the organic linker and the iodine species [13]. Inarguably, the excitation of an electron from the organic linker to the inorganic cluster reduces the probability of an electron-hole recombination. On the other hand, when comparing UiO-66(Zr)_NH_2 and MIL-125(Ti)_NH_2, the SSA value is actually greater in the titanium MOF. However, the presence of an LMCT instead of an LBT was still able to increase the iodine adsorption capacity in MIL-125(Ti)_NH_2 by 2.41 times after 48 h of gas flow [12]. These features demonstrate the great influence of an efficient charge separation on the I_2 capture caused by the presence of LMCT mechanisms.

The band gap effect was evaluated by comparing CAU-1(Al)_NH_2 to MIL-125(Ti)_NH_2. In this case, the titanium-based compound captures 2.62 times more iodine than the CAU-1(Al)_NH_2 for a band gap difference of 0.1 eV. However, the difference between the CTC of these materials (LMCT vs LBT) is also a source of influence. Therefore, considering the results and discussions reported in the previous chapters and in other works, the best adsorption capacity exhibited by MIL-125(Ti)_NH_2 is mainly ascribed to three factors: the amino group functionalization (strong electron donor character), the smaller band gap (improves the EDA complex), and the presence of a LMCT mechanism (enhances the charge separation within the compound).

6.3.1. Diffuse Reflectance UV-Vis spectroscopy of the iodine loaded samples

An interesting feature was observed after the I_2 contact with the powdered MOFs. Actually, the color of the samples drastically changed after three days of contact with the iodine gaseous stream. The white original MIL-125(Ti) powder became orange-brown immediately after contact with I_2, whereas the yellow pristine MIL-125(Ti)_NH_2 became purple-brown in the same conditions. On the other hand, despite their similar initial colors, I_2@CAU-1(Al)_NH_2 showed a different behavior from I_2@MIL-125(Ti)_NH_2, passing from yellow to orange-brown. Due to their color changes, the iodine loaded MOFs were first evaluated by UV-vis

spectroscopy (Figure 6.9). After the contact between the compounds and the I_2 gas, the three I_2-loaded samples showed the same behavior with the presence of one new broad band maximizing at about 360 nm. Moreover, the I_2@CAU-1(Al)_NH_2 compound exhibited a new absorption band at 291 nm, which was not seen in the I_2@MIL-125(Ti) nor in I_2@MIL-125(Ti)_NH_2 compounds, probably because of the superposition with the MOFs structural bands in the same region.

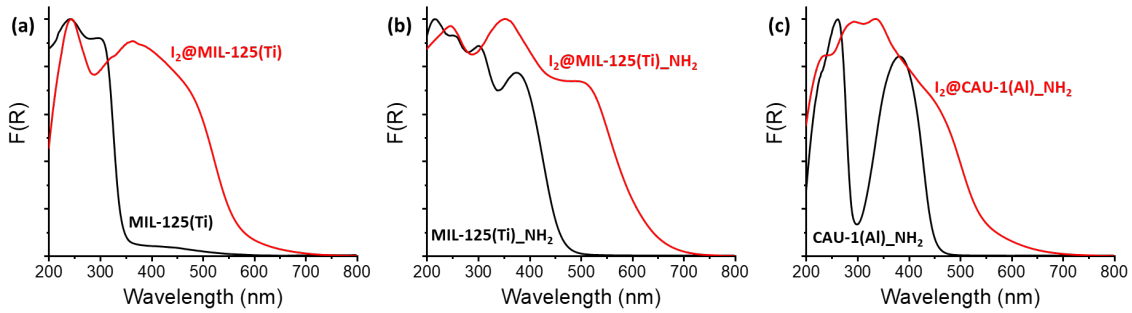

Figure 6.9: UV-vis spectra of the MOF compounds before (black) and after (red) three days of contact with I_2 for (a) MIL-125(Ti), (b) MIL-125(Ti)_NH_2, and (c) CAU-1(Al)_NH_2.

These new contributions reveal the formation of the anionic I_3^- species [300]. However, another band was clearly visible in the I_2@MIL-125(Ti)_NH_2 spectrum at 507 nm, whereas it is less visible in the other two I_2@MOFs. This signal was ascribed to the successive forms of the iodine species after adsorption, which includes other contributions in the visible range between 400 and 550 nm. The first one, is expected to be observed at 520 nm and corresponds to the iodine species in gas phase due to the allowed $\pi_g^* \rightarrow \sigma_u^*$ transition [74]. Furthermore, spectral signatures at lower wavelengths (around 400-500 nm) were related to the CTC between the I_2 molecules and the aromatic ring of the BDC linker, as I_2 is known to form strong interaction with species showing high electron donor character such as aromatic compounds [78]. These features show again that different iodine species are present in the MOF material after the contact with I_2 gas: "free" I_2, "perturbed" I_2, and I_3^-.

6.3.2. Characterizing the iodine adsorption and evolution using vibrational spectroscopy

In order to follow the evolution of these iodine species within the MOFs porous structure, the Raman spectra of the iodine loaded samples were collected after four hours of I_2 loading for three days, as shown in Figure 6.10. The first spectrum was recorded 30 minutes after leaving the iodine bench, whereas the other ones were obtained every hour for three days. This time scale was chosen aiming to assess the early development of the I_2 species. In fact, after 4 hours of contact, there is approximately one I_2 molecule per unit cell of material (which corresponds to 254 $g_{I2}.mol^{-1}{}_{MOF}$). At this point, the band related to the carboxylate stretching vibration – at about 1600 cm^{-1} – (Table 6.2) was not influenced by the iodine adsorption, which is the reason why it was chosen for the normalization of all Raman spectra. Here, the main iodine vibrational modes were observed between 90 and 210 cm^{-1}. The first contribution, related to the I–I stretching of a "free" iodine moiety, was found at 200 cm^{-1} for I_2@MIL-125(Ti), at 198 cm^{-1} for I_2@CAU-1(Al)_NH_2, and as a weak contribution at 198 cm^{-1} for I_2@MIL-125(Ti)_NH_2. This signal is related to benzene-I_2 complexes [322], and is ascribed to iodine molecules weakly perturbed by the materials' organic linkers [12,13]. For longer times, its intensity decreases, while a second contribution is formed with a maximum at 175 cm^{-1} in I_2@MIL-125(Ti), but at 180 cm^{-1} in I_2@CAU-1(Al)_NH_2 and I_2@MIL-125(Ti)_NH_2. The blue shift indicates that this iodine species has a higher interaction with the NH_2-BDC compared to the BDC linkers, probably due to the presence of amino groups. Moreover, this signal presents a red shift in all three compounds, going from 180 to 169 cm^{-1} in CAU-1(Al)_NH_2, from 175 to 167 cm^{-1} in MIL-125(Ti), and from 180 to 167 cm^{-1} in MIL-125(Ti)_NH_2.

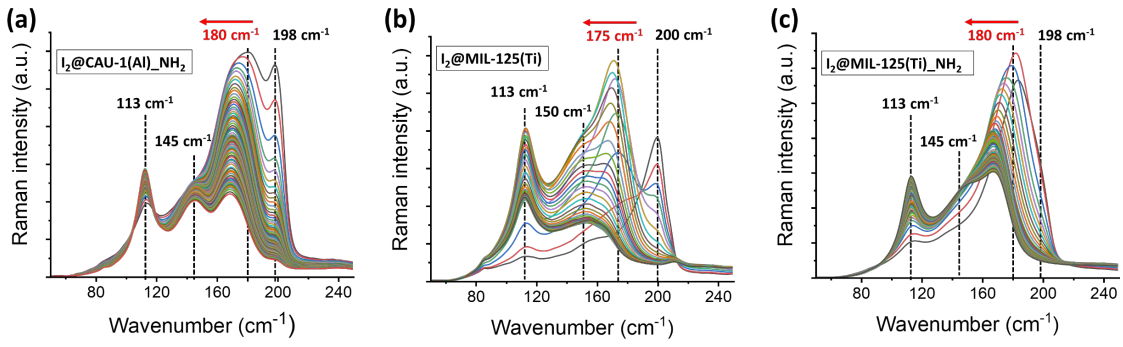

Figure 6.10: FT-Raman spectra (λ_{ex} = 1064 nm) recorded after 4 h of iodine exposure for the different compounds: (a) I_2@CAU-1(Al)_NH_2, (b) I_2@MIL-125(Ti), and (c) I_2@MIL-125(Ti)_NH_2. The first spectrum was collected 30 minutes after leaving the iodine bench (black line), where the others were obtained every hour for a three-day period.

The transformation of I_2 into I_3^- and I_n^- favors the iodine uptake by creating specific adsorption sites and stabilizing these anionic species through electrostatic interactions with the organic linker radical ($BDC^{\bullet+}$ or $NH_2^{\bullet+}$–BDC) [13,359]. For this reason, the effective charge separation in the Ti-based compounds (due to the LMCT mechanism) alongside the hole stabilizer –NH_2 group in MIL-125(Ti)_NH_2 guarantees a stronger adsorption of both I_3^- and I_n^- anions, as it attenuates the recombination process that would annihilate the positive charges located over the linker. This process is advantageous for the adsorption kinetics and also for the maximum iodine uptake capacity [13,359].

The observation of the Raman spectra shows that the iodine bands evolve differently for each compound. For instance, the spectrum collected after 30 minutes for MIL-125(Ti) only shows the contribution related to "free" I_2, while MIL-125(Ti)_NH_2 exhibits only "perturbed" iodine signatures, and CAU-1(Al)_NH_2 presents both of them concomitantly (Figure 6.10). This behavior infers that all the "free" I_2 available inside the pores of MIL-125(Ti)_NH_2 has been transformed during the iodine loading (before the Raman analysis). On the other hand, in MIL-125(Ti), the iodine species are mainly in the form of "free I_2", inferring that it exhibits a slow kinetic transformation. CAU-1(Al)_NH_2 stood in between the two samples and had contributions from both species. Moreover, the I_3^- is the final and most stable species in all three materials. However, the amino-based compounds (MIL-125(Ti)_NH_2 and CAU-1(Al)_NH_2) still show strong contributions of "perturbed" iodine molecules even after three days. This indicates that the –NH_2 groups can stabilize the I_n^- species in parallel to the I_3^- molecules. In order to deeply evaluate these features, the intensities of the Raman bands related to "free" I_2 and I_3^- were evaluated alongside their first derivatives (Figure 6.11). This gives an idea about the spectral concentration of these species and also about their rate of consumption/formation. Thus, the MIL-125(Ti)_NH_2 shows both the fastest I_2 consumption and I_3^- formation rates, followed by CAU-1(Al)_NH_2 and by MIL-125(Ti).

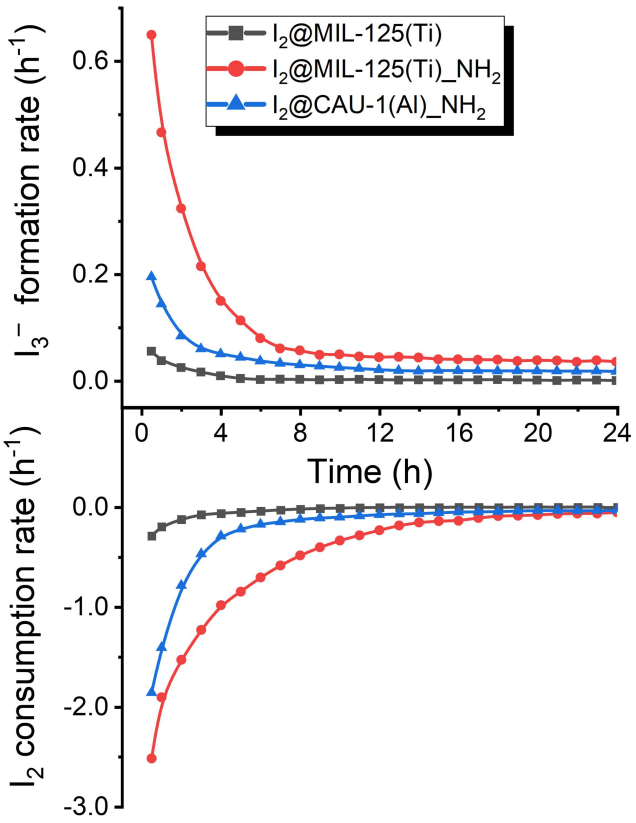

Figure 6.11: I_2 consumption and I_3^- formation rates obtained from the first derivative of the FT-Raman intensity signals related to "free" I_2 and I_3^- species after 4 h of iodine exposure for I_2@MIL-125(Ti) (in black), I_2@MIL-125(Ti)_NH_2 (in red), and CAU-1(Al)_NH_2 (in blue).

This behavior highlights the faster kinetic of iodine evolution within MIL-125(Ti)_NH_2, which agrees with the band gap energies of the samples, as $E_{g\_MIL\text{-}125\_NH2} > E_{g\_CAU\text{-}1\_NH2} > E_{g\_MIL\text{-}125}$. Indeed, as shown in Chapter IV, smaller band gaps facilitate the formation of the EDA complex and therefore, favor the I_2 reduction [13]. It is worth mentioning that the MIL-125(Ti)_NH_2 compound did not reach a plateau for the I_3^- formation, inferring that the I_2 reduction takes longer than three days to reach an equilibrium in this case. Moreover, since the "free" I_2 species seems to be stable after approximately 24 hours, it is assumed that this transformation continues to occur with the I_n^- species related to the "perturbed" I_2 signal. This effect is less significant for CAU-1(Al)_NH_2 and negligible for MIL-125(Ti).

6.3.3. Influence of iodine adsorption over the compounds' paramagnetic behavior

In order to confirm the band gap influence on the I_2 reduction, EPR measurements were conducted under UV irradiation for all the iodine-loaded samples after 4 h of iodine exposure (Figure 6.12). The signal related to oxygen $^{\bullet}O_2^-$ and h^+ species is still present in all compounds at *g*-factor between 2.003 and 2.007 [348–350]. Nevertheless, it is less intense when compared to that of pristine materials (Figure 6.6). A similar effect was observed for the signature of Ti^{3+} species, which was only verified in MIL-125(Ti) at 120 K after irradiation (g = 1.934) in the iodine-loaded samples [358]. These features are ascribed to the electron transfer between the MOF material and the iodine molecule. In fact, when I_2 is present, a great part of the excited electrons hops to the iodine molecular orbitals, either coming from the linker or from the inorganic cluster. This effect is more remarkable for the I_2@MIL-125(Ti)_NH_2 as the Ti^{3+} species was not observed for this material, probably because of the strong electron donor character of $–NH_2$, which facilitates the iodine reduction to the detriment of the LMCT mechanism. As a consequence, this would reduce the concentration of Ti^{3+} species, attenuating its signature. Note also that the hyperfine signature in CAU-1(Al)_NH_2 loses resolution after the iodine loading, which reinforces the influence of the $–NH_2$ group over the iodine reduction.

With that in mind, two routes were proposed for the electron transfer between the MOFs and the iodine molecules: the first considers that the electron is transferred from the BDC/NH_2-BDC organic linker directly to the I_2 molecule in a sort of HGCT; whereas in the second, the I_2 is reduced by the Ti^{3+} cations that were previously formed during the LMCT mechanism (Figure 6.13). Note that these two situations can coexist in this case because the titanium-based compounds may exhibit a CTC related to both the organic and inorganic parts of the MOFs (due to the presence of the LMCT mechanism). However, this feature is not possible in CAU-1(Al)_NH_2 as there is no electron transfer from the NH_2-BDC to the Al^{3+} methoxy/hydroxy cluster (as this material exhibits only an LBT system).

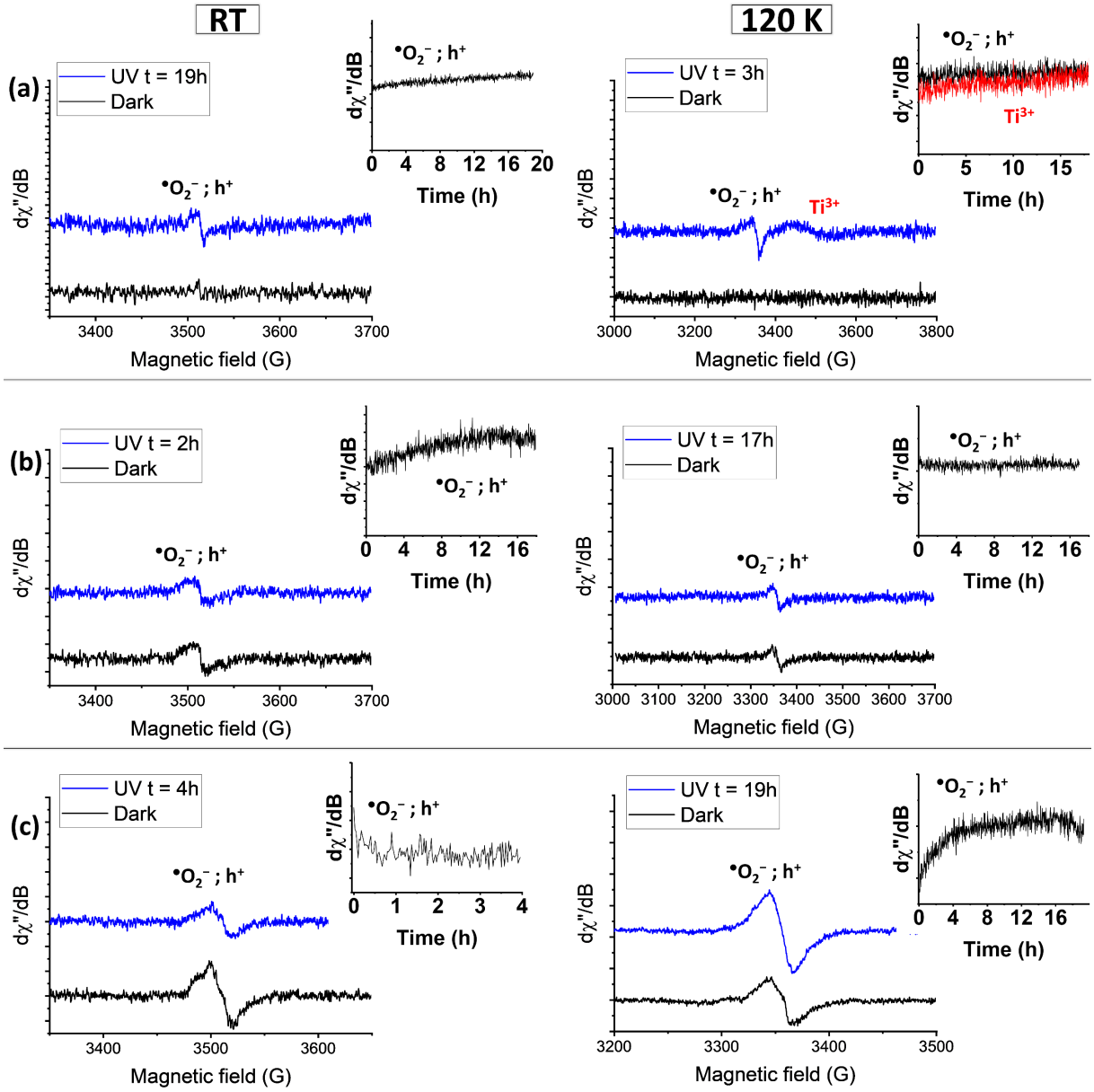

Figure 6.12: EPR spectra after 4h of iodine exposure for (a) I_2@MIL-125(Ti), (b) I_2@MIL-125(Ti)_NH_2, and (c) I_2@CAU-1(Al)_NH_2 at 120 K. Inset: time evolution of the signal's intensity for each material.

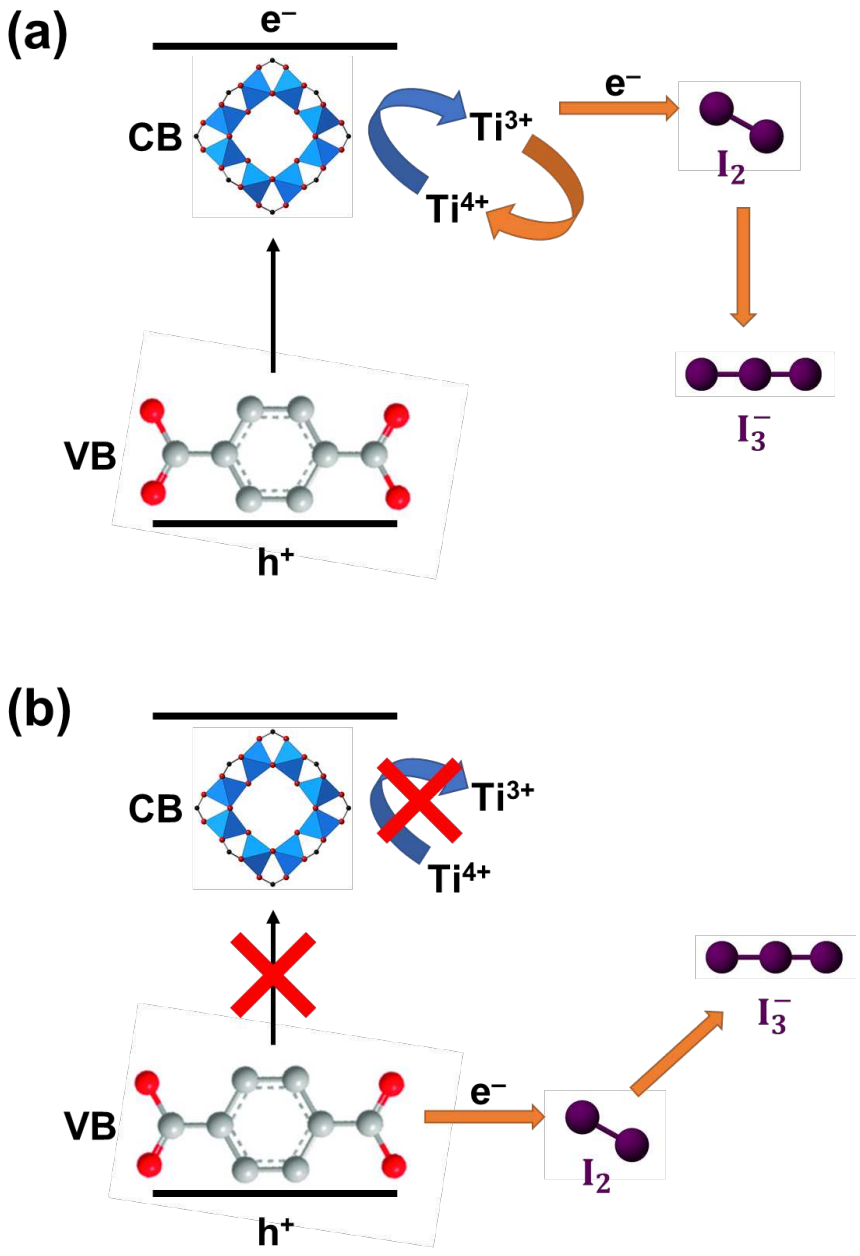

Figure 6.13: Scheme showing the proposed mechanism for the electron transfer towards the I_2 molecule in MIL-125(Ti) considering the possibility of a linker-to-metal charge transfer (a), and of a purely host-to-guest charge transfer (b). Note that the CTC between I_2 and MIL-125(Ti)_NH_2 can also be assumed to behave in the same manner. However, for CAU-1(Al)_NH_2, the only possible route is the one represented in (b).

6.4. Adsorption behavior for longer adsorption times

Because MIL-125(Ti)_NH_2 showed a considerable iodine uptake within three days and MIL-125(Ti) did not seem to reach its maximum adsorption capacity in these conditions (Figure 6.8 and Table 6.1), these two materials were also exposed to five days (120 h) of contact with the I_2 gas flow to obtain more information about their adsorption kinetics. To limit the impact of the samples' molecular weights, the kinetic was evaluated using the mass of trapped iodine per mol of MOF (rather than mass of iodine per mass of MOF), as shown in Figure 6.14. However, the values are also shown in $g.g^{-1}$ and $mol.mol^{-1}$ to facilitate the discussion (Table 6.5). The adsorption kinetic was evaluated using the LDF model [180].

Table 6.5: Iodine uptake capacities and kinetic data obtained for MIL-125 and MIL-125_NH_2 materials.

MOF	Iodine uptake[a]			k_{LDF}	R^2	t (F = 0.90)[b]	t (F = 0.99)[c]
	($g.mol^{-1}$)	($g.g^{-1}$)	($mol.mol^{-1}$)	(h^{-1})		(h)	(h)
MIL-125	2947	1.9	11.6	0.01991(7)	0.973	51 h, 36 min	94 h, 52 min
MIL-125_NH_2	2699	1.6	10.6	0.0382(2)	0.979	74 h, 4 min	114 h, 36 min

k_{LDF}: mass transfer coefficient from the LDF model. [a] Experiments carried out for 120 h of iodine gas flow at room temperature. [b] Equilibrium time to reach F = 0.90 from LDF fit. [c] Equilibrium time to reach F = 0.99 from LDF fit.

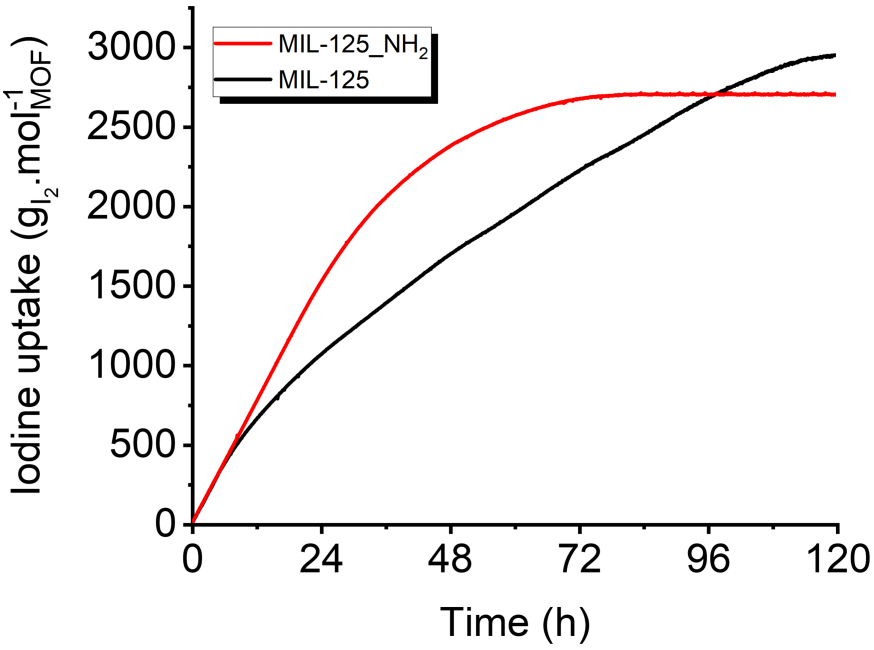

Figure 6.14: Iodine adsorption kinetics evaluated by UV-vis spectroscopy after 120 h of contact between the I_2 gas and the MOF powdered sample for: MIL-125 (black) and MIL-125_NH_2 (red).

After 120 h of iodine contact, the MIL-125 material exhibited a higher I_2 uptake of 2947 $g.mol^{-1}$, against 2699 $g.mol^{-1}$ for MIL-125_NH_2 in the same conditions. This behavior is related to its higher SSA (1207 against 1099 $m^2.g^{-1}$) coupled with the presence of a LMCT mechanism. In effect, improving the SSA creates more sites for iodine to adsorb, whereas the LMCT complex increases charge separation and facilitate the iodine adsorption [360]. However, it is clear that the adsorption kinetics of the amino-functionalized MOF is faster than that of MIL-125. In fact, MIL-125_NH_2 exhibited a mass transfer coefficient about twice the one of MIL-125: 0.0382 against 0.01991 h^{-1}. This feature is also visible in Figure 6.14, as the MIL-125_NH_2 clearly reached a plateau of maximum adsorption after about 72 hours, whereas MIL-125 appears to attain this plateau only after 120 h. Previous studies conducted in I_2@UiO systems showed the opposite behavior, with the amino-functionalized UiO-66_NH_2 exhibiting lower iodine adsorption kinetics but with a higher adsorption capacity at the end of the process [12]. In fact, Leloire *et al.* [12] observed an I_2 uptake capacity of 210 $mg.g^{-1}$ in a UiO-66 material after 48 h of iodine exposure (SSA = 1387 $m^2.g^{-1}$; k_{LDF} = 0.229 h^{-1}), whereas UiO-66_NH_2 was able to adsorb 565 $mg.g^{-1}$ in the same conditions (SSA = 825 $m^2.g^{-1}$; k_{LDF} = 0.0909). A similar effect was observed for UiO-67 and UiO-67_NH_2, as the former captured 222 $mg.g^{-1}$ (SSA = 1599 $m^2.g^{-1}$; k_{LDF} = 0.228 h^{-1}) against 1071 $mg.g^{-1}$ for the latter (SSA = 1565 $m^2.g^{-1}$; k_{LDF} = 0.0320 h^{-1}) [12]. In this case, the k_{LDF} reduction in the presence of $–NH_2$ groups should be related to the fact that UiO-6*x* (*x* = 6 or 7) does not have a great capacity of retaining I_2 when compared to MIL-125 compounds. In fact, because the Zr^{4+} cations cannot reduce into Zr^{3+}, the CTC in UiO-6*n* materials is mainly related to its organic linker, in a LBT complex [13]. This effect attenuates the charge separation and increases recombination phenomena, which was proven to reduce the iodine uptake capacity of MOF materials [360]. On the other hand, it is important to note that MIL-125 exhibits significant iodine uptake even without the presence of $–NH_2$ groups, primarily attributed to its LMCT complex, as discussed previously [360]. Consequently, the $–NH_2$ groups primarily functions to accelerate the adsorption process, which enhances the k_{LDF} value. However, it also introduces a steric effect that reduces the maximum uptake capacity. This particular characteristic is only noticeable in compounds exhibiting higher iodine uptakes and, therefore, was not observed in UiO-6*n* systems [12]. As a result, MIL-125_NH_2 exhibits a maximum adsorption plateau at shorter contact times [t(F = 0.90) ≈ 60 h], leading to an increased mass transfer coefficient according to the LDF model. In contrast, MIL-125 requires more time to reach its maximum adsorption capacity [t(F = 0.90) ≈ 115 h], even though it has the ability to adsorb a greater amount of iodine.

6.4.1. *In-situ* Raman spectroscopy: highlighting the early stages of iodine adsorption

For evaluating the behavior of the iodine molecules during the first moments of its adsorption within the MOF materials, the I_2 adsorption and evolution into I_3^- were evaluated using *in-situ* Raman spectroscopy from t = 0 min. For that, Raman spectra were collected each hour for five days under a continuous iodine gas flow. Then, the iodine supply was cut, and spectra were acquired each hour for three days with the sample open to the atmosphere (Figure 6.15). The main iodine vibrational modes were observed between 90 and 210 cm^{-1} and because the band related to the carboxylate stretching vibration (around 1600 cm^{-1}) was not influenced by the adsorption process, it was chosen for the normalization of the spectra.

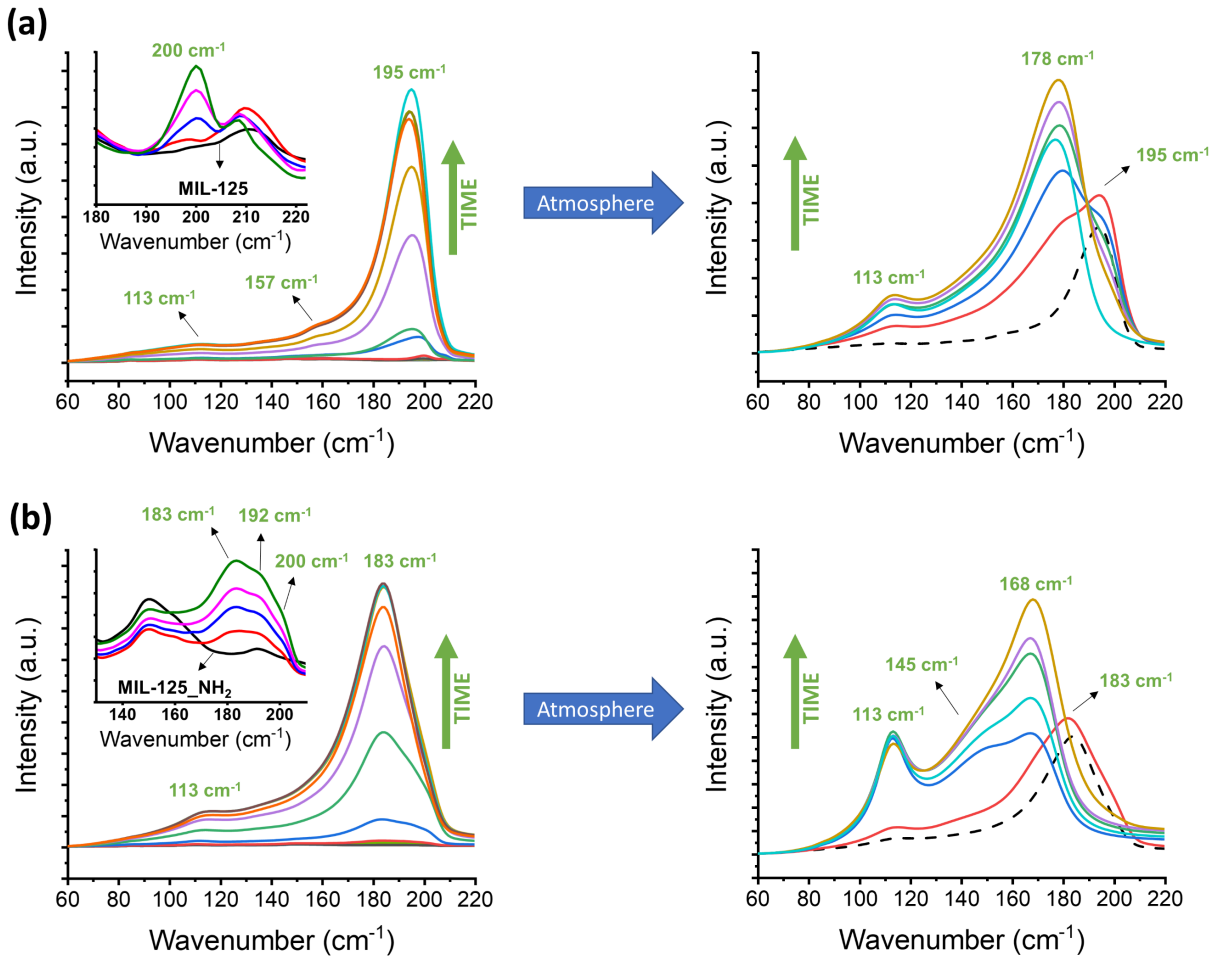

Figure 6.15: Raman spectra obtained from t = 0 for (a) I_2@MIL-125 and (b) I_2@MIL-125_NH_2, each spectrum was recorded in an interval of 12 hours. On the left side: *in-situ* Raman spectra showing the iodine adsorption process (inset: zoom on the spectra showing the first four hours of adsorption and spectrum of the respective pristine MOF). On the right side: spectra collected after opening the sample to the atmosphere showing the evolution from I_2 into I_3^- (the dotted spectrum represents the last data obtained before opening the quartz cell).

The first visible contributions were observed within the first hours of adsorption for both samples. I_2@MIL-125 showed a band at 200 cm^{-1} after one hour of adsorption. In the same conditions, I_2@MIL-125_NH_2 exhibited a broader band incorporating contributions of I–I stretching of "free" iodine molecules at 200, 192, and 183 cm^{-1}. These bands shifted towards lower wavenumber values within a few hours of analysis, down to 195 cm^{-1} and 183 cm^{-1} for I_2@MIL-125 and I_2@MIL-125_NH_2, respectively. This shift is again related to an increase on the interaction between the iodine molecules and the MOFs frameworks, and it is stronger in I_2@MIL-125_NH_2 due to the presence of the –NH_2 group that has a strong affinity for iodine [12]. These two initial signals reach their maximum intensity after 5 and 3 days for I_2@MIL-125 and I_2@MIL-125_NH_2, which is in accord with the I_2 adsorption kinetics experiments (Figure 6.14 and Table 6.5). It is worth mentioning that two other contributions were observed in I_2@MIL-125, at 157 and 113 cm^{-1}. On the other hand, although I_2@MIL-125_NH_2 exhibited only the 113 cm^{-1} signal, the 157 cm^{-1} band is probably hidden as a contribution of its main band at 183 cm^{-1}. These signals intensify after the fifth day, when the iodine flow was interrupted, and the quartz cell was open to the atmosphere. At this point, the intensity of the "free" I_2 signal decreased, while other contributions developed at 178 cm^{-1} for I_2@MIL-125 and 168 cm^{-1} for I_2@MIL-125_NH_2. As mentioned before, these signals (together with the band observed before opening the cell at 157 cm^{-1}) were related to molecular iodine in strong interaction with organic donor molecules [322], which can increase the length of the I–I bond [84] and form I_n^- anions (n = 5, 7, 9, …) [302]. Finally, the I_3^- signal was observed at 113 cm^{-1} for both compounds after a few hours of contact, but it was intensified after opening the quartz cell to the atmosphere. Note that the I_3^- signal is stronger in I_2@MIL-125_NH_2, which is related to the faster transformation of I_2 into I_3^- in the presence of the amino group. This feature was observed in previous studies and is related to the electron donor character of the –NH_2 group and to the smaller band gap of the MIL-125_NH_2 compound [12,13]. Additionally, the contributions related to $^{\bullet}I_2^-$ species may also be present because its vibrational mode (at 114 cm^{-1}) [85] overlaps with that of symmetric I_3^- stretching, suggesting a radical mechanism for the iodine reduction which would be favored by a better harvesting of the visible light [13]. To sum it up, the I_2 reduction can be thought as a CTC between the organic linker and the I_2 molecule according to Equations (6.1) and (6.2) for I_2@MIL-125 and I_2@MIL-125_NH_2, respectively.

$$nI_2 + 2BDC \rightarrow 2I_n^- + 2BDC^{\bullet+} \qquad (n = 3, 5, 7, 9 \ldots) \tag{6.1}$$

$$nI_2 + 2NH_2BDC \rightarrow 2I_n^- + 2NH_2^{\bullet+}BDC \qquad (n = 3, 5, 7, 9 \ldots) \tag{6.2}$$

It is worth mentioning that the I_2 evolution into I_3^- was already monitored within the first hours of analyses using *ex-situ* Raman spectroscopy – and presented in the previous chapters [12,13]. In these cases, the compounds were already impregnated with iodine before the acquisition of the Raman spectra, so the initial adsorption phase was neglected. However, this work shows that the iodine evolution was clearly boosted after opening the quartz cell to the atmosphere during the *in-situ* measurements, indicating that atmospheric water and/or oxygen may also have an influence over the I_2 evolution.

6.5. Thermal stability of trapped iodine species

TGA experiments were conducted in order to evaluate the thermal stability of the samples in the presence of iodine (Figure 6.16).

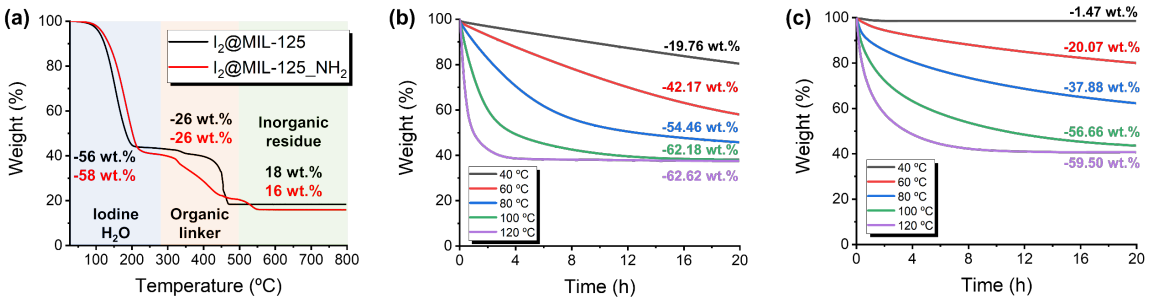

Figure 6.16: TGA experiments showing (a) the thermal decomposition of the I_2@MIL-125 and I_2@MIL-125_NH_2 compounds up to 800 ºC; and the weight loss observed during 20 hours at different temperatures for (b) I_2@MIL-125 and (c) I_2@MIL-125_NH_2.

First, the two iodine loaded materials were left open into the atmosphere for one week to establish an equilibrium between the iodine desorption and its evolution. Then, they were heated up to 800 ºC to evaluate the different regions in which there is a weight loss (Figure 6.16a). The first contribution appears between 25 and 280 ºC and is related to the loss of the adsorbed iodine and water molecules. Works conducted with UiO-6n systems also observed iodine releases in temperatures between 200 and 300 ºC depending on the organic linker [39]. I_2@MIL-125 showed a weight reduction of 56 wt.%, against 58 wt.% for I_2@MIL-125_NH_2. Note that, although the I_2@MOF samples were previously dried and prepared inside a glovebox, they were exposed to the atmosphere after the fifth day of I_2 adsorption and may adsorb water during the process. The second region, comprised between 280 and 500 ºC, is related to the

decomposition of the organic linkers (26 wt.% loss for both compounds). Finally, the last region is characterized by the presence of inorganic species (such as TiO_2) that are stable in the temperature range (800 ºC). In order to compare the stability of the iodine species in the different samples, TGA experiments were conducted using temperature plateaus of 40, 60, 80, 100, and 120 ºC for 20 h (Figure 6.16b and Figure 6.16c). In these conditions, I_2@MIL-125 showed a considerable weight loss which increased from 40 ºC (19.76 wt.% after 20 hours of heating) to 120 ºC with 62.62 wt.% loss (Figure 6.16b). However, at 100 ºC the compound already lost 62.18 wt.%, which is virtually the same amount than at 120 ºC, demonstrating that the MIL-125 compound is incapable to stabilize the adsorbed iodine at 100 ºC. On the other hand, the iodine species were found to be more stable in I_2@MIL-125_NH_2 (Figure 6.16c). The weight loss of this compound was negligible at 40 ºC (1.47 wt.% after 20 hours of heating) but increased gradually with the temperature, reaching a maximum of 59.50 wt.% at 120 ºC. This value is comparable to that of the experiment conducted up to 800 ºC (Figure 6.16a) and demonstrates that the MIL-125_NH_2 compound is unable to retain I_2 in temperatures higher than 120 ºC for higher exposure times. This temperature can be increased by enhancing the heating rate, which opens a path to propose thermal treatments that can stabilize iodine in the final inorganic structure at higher temperatures (> 500 ºC).

Considering the interaction between MOFs and iodine, Hughes et al. [361] observed a chemisorption phenomenon for I_2 adsorbed in ZIF-8 (ΔH_{ads} = −41.47 kJ.mol^{-1}), even though the interaction between MOF materials and gaseous I_2 is often related to weak and reversible Van der Waals type interactions [153,362–364]. Moreover, Tang et al. [136] also observed I_2 chemisorbed into Cd-based MOFs (HSB-W8 and HSB-W9) constructed using hydrogenated Schiff linkers: HSB-2 and TSBDC. It is worth mentioning that, in this case, no experiments nor simulations were applied to confirm the chemisorption phenomenon. Nevertheless, they attributed the I_2 chemisorption to the π-electron-rich stilbene moieties found in the HSB-W8 and HSB-W9 MOFs that form CTC with I_2 molecules, reducing them into I_3^- and other polyiodide anions [136]. To this day, there is no mention in literature of a study considering the stability of different iodine species trapped within titanium-based MOF frameworks.

6.5.1. *In-situ* Raman spectroscopy: iodine desorption experiments

For evaluating the influence of the amino group functionalization over the stability of the iodine species in the I_2-loaded MIL-125 compounds, *in-situ* Raman desorption experiments were conducted using a 785 nm excitation source (Figure 6.17).

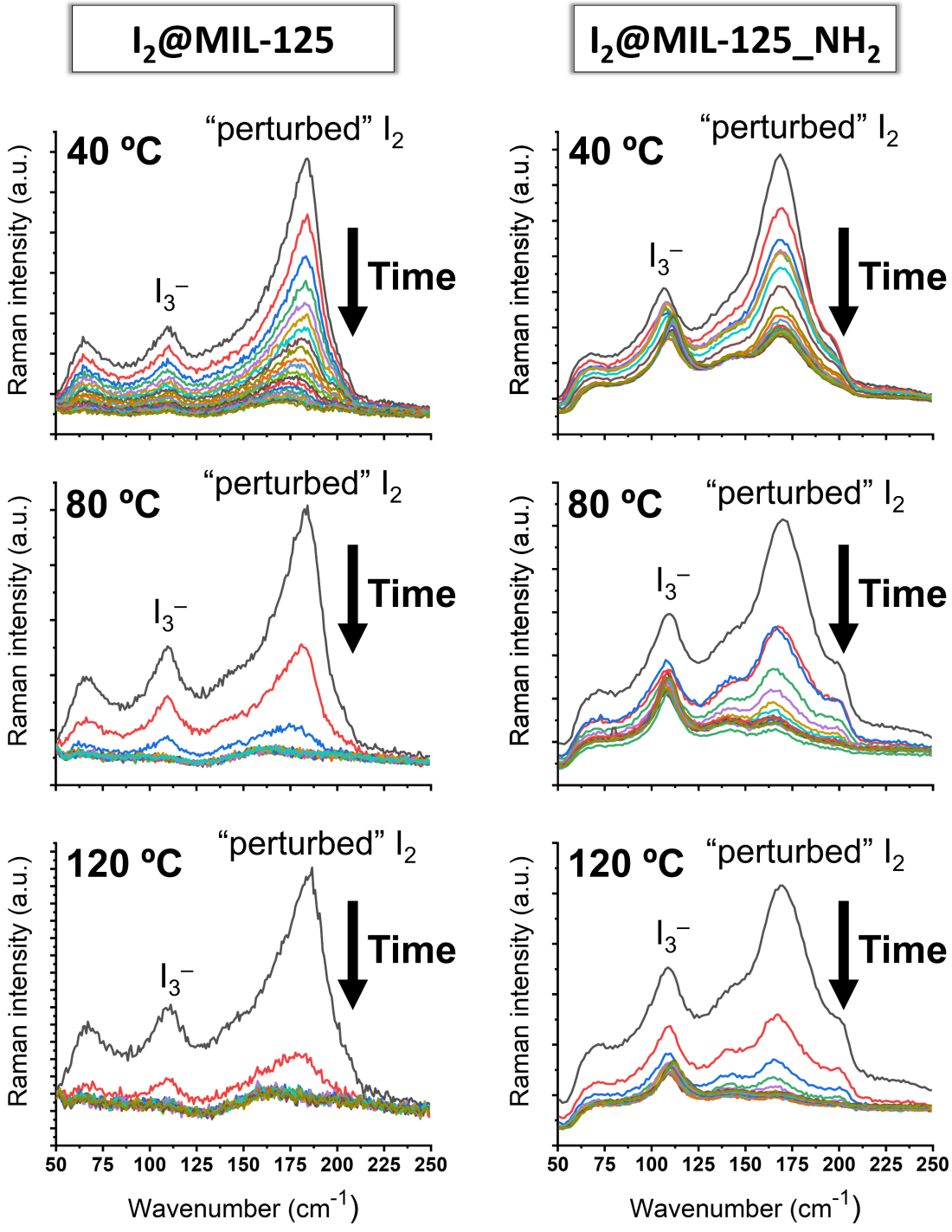

Figure 6.17: *In-situ* Raman desorption experiments collected during 19 hours for I_2@MIL-125 (on the left) and I_2@MIL-125_NH_2 (on the right) at 40, 80, and 120 ºC.

Again, to reach an equilibrium between I_2 and I_3^-, the samples were kept under air atmosphere during one week before the desorption experiment. After this period, no further fluctuations (related either to I_2 into I_3^- transformation or to partial iodine desorption at room temperature) were observed in their Raman spectra, and I_2@MIL-125 shows two stable bands at 113 and 178 cm^{-1} (I_3^- and "perturbed" I_2, respectively), whereas I_2@MIL-125_NH_2 main signals appear at 113 and 168 cm^{-1} (I_3^- and "perturbed" I_2, respectively). The amino functionalization had a clear influence over the stability of the remaining species within the pores of MIL-125 compounds. Indeed, in I_2@MIL-125, both I_2 and I_3^- signals progressively disappear after a few hours at 40 °C, and after a few minutes at 80 and 120 °C. On the other hand, after 19 hours the I_3^- signal is still present at 120 °C in I_2@MIL-125_NH_2, while traces of I_2 remain at 80 °C for this material. To characterize thoroughly the difference between these two behaviors observed for I_2@MIL-125 and I_2@MIL-125_NH_2 upon heating, the iodine desorption kinetics were studied using the Albery model [365], which is one of the most appropriate approaches.

Briefly, Albery *et al.* [365] observed that the kinetics of several heterogeneous materials (semiconductor electrodes, colloidal particles, oxide surfaces) are frequently treated as semilogarithmic plots, normalized by the initial concentration, and then tested for first-order kinetics, in which the decay signal often lies on a common curve. However, they perceived that the data is better fitted when the heterogeneity of the system is also pondered. With that in mind and considering that the rate constant comes from the Gibbs free energy of the system, a Gaussian distribution of the system's free enthalpy of activation ($\Delta G^{\ddagger}$) around its mean value ($\overline{\Delta G^{\ddagger}}$) was proposed, according to Equation (6.3). Here, γ is the distribution width, R is the gas constant (8.3144621 $J.K^{-1}.mol^{-1}$), T is the temperature (K), and x is the gaussian distribution x-axis [365].

$$\Delta G^{\ddagger} = \overline{\Delta G^{\ddagger}} - \gamma x R T \tag{6.3}$$

Then, the authors considered that a gaussian distribution around the rate constant logarithm average $[ln(\bar{k})]$ is more likely to be found than around its corresponding $\bar{k}$ data. Therefore, the former case was proposed, according to Equation (6.4) [365].

$$\ln (k) = \ln (\bar{k}) + \gamma^{x} \tag{6.4}$$

Finally, because the kinetics decay results from the sum of all the contributions of each microscopic state, the authors applied an integration on the Gaussian distribution in $\exp(-x^2)$.

The result leads to the Equation (6.5), which describes the initial concentration (C_0) with time (t) [365]. It is worth mentioning that when $\gamma = 0$, the system is considered homogeneous and therefore, the Equation (6.5) is reduced to the first-order exponential decay expression: $C/C_0 = e^{-kt}$.

$$\frac{C(t)}{C_0} = \frac{\int_{-\infty}^{+\infty} e^{-x^2 - \bar{k}t\cdot(e^{\gamma x})} dx}{\sqrt{\pi}} \quad (6.5)$$

In effect, the Albery model was often applied for evaluating the dynamic of microporous systems such as zeolites with considerable correlation coefficients (R^2) [366]. Therefore, to access the $\bar{k}$ values according to the Albery model for the "perturbed" I_2 and I_3^- species, the intensity of the signals related to the I_3^- (at 113 cm^{-1}) and I_n^- (at 178 and 168 cm^{-1} for I_2@MIL-125 and I_2@MIL-125_NH_2, respectively) species were considered. For that, the ratio between the Raman band's intensity at a given time and the initial intensity (I/I_0) was plotted against the time in hours. The model showed a good correspondence to the experimental data points (Figure 6.18).

Moreover, the amino-group influence over the I_3^- stabilization is now undeniable. In fact, after 19 hours, I_2@MIL-125_NH_2 was able to retain 73%, 30%, and 5% of its initial I_3^- signal at 40, 80, and 120 °C, respectively, whereas I_2@MIL-125 only retained 7%, 2%, and < 1% under the same conditions. Furthermore, the difference of the desorption kinetics for both species in the two materials is highlighted by their respective $\bar{k}$ values and lifetimes (Table 6.6 and Figure 6.19). Actually, the I_2@MIL-125 has systematically higher $\bar{k}$ values and smaller lifetimes than the I_2@MIL-125_NH_2 for both I_3^- and "perturbed" I_2 species. This feature indicates that anionic iodine species are stabilized at higher temperatures by the presence of the amino group, which is consistent with their interaction with the trapped $–NH_2^{\bullet+}$ holes, as discussed before. It is worth mentioning that, when considering I_2@MIL-125, both iodine species have very similar lifetimes for temperatures higher than 40 ºC, inferring that their desorption mechanism follows the same trend. On the other hand, a clear difference is observed when comparing the behavior of these species upon I_2@MIL-125_NH_2 heating. In this case, the lifetime of the I_3^- species is about two-times longer than that of the "perturbed" I_2 in the entire temperature range (Table 6.6 and Figure 6.19), reinforcing the influence of the amino group over the desorption mechanism.

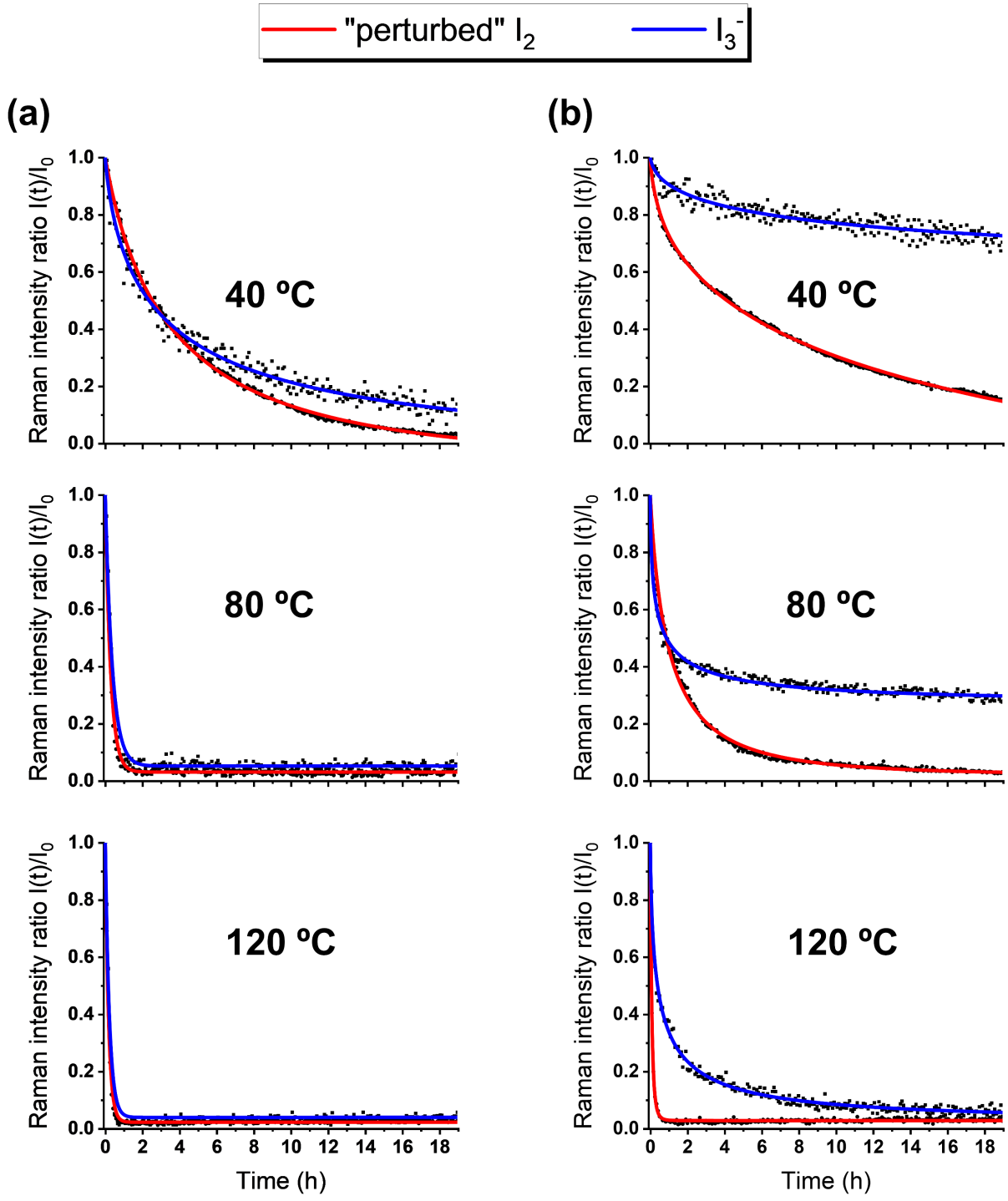

Figure 6.18: Raman intensities ratio $I(t)/I_0$ fitted according to the Albery method for the I_2 and I_3^- desorption in (a) I_2@MIL-125 and (b) I_2@MIL-125_NH_2.

Table 6.6: Rate constant average (k) obtained by the Albery method and coefficient of correlation (R^2) for the desorption of I_2 and I_3^- species in I_2@MIL-125, and I_2@MIL-125_NH_2 at different temperatures.

Temperature (ºC)	MOF	I_2			I_3^-		
		$\bar{k}$ (h^{-1})	Lifetime	R^2	$\bar{k}$ (h^{-1})	Lifetime	R^2
40	I_2@MIL-125	0.219(3)	4h 33min	0.998	0.11(2)	9h 5min	0.975
	I_2@MIL-125_NH_2	0.15(2)	6h 40min	0.998	0.04(2)	25h	0.984
50	I_2@MIL-125	0.435(6)	2h 17min	0.983	0.350(6)	2h 51min	0.979
	I_2@MIL-125_NH_2	0.28(3)	3h 34min	0.997	0.071(7)	14h 5min	0.963
60	I_2@MIL-125	0.76(2)	1h 18min	0.931	0.77(2)	1h 17min	0.932
	I_2@MIL-125_NH_2	0.38(1)	2h 37min	0.991	0.13(6)	7h 41min	0.983
70	I_2@MIL-125	2.80(2)	21 min	0.998	1.71(3)	35min	0.970
	I_2@MIL-125_NH_2	0.658(1)	1h 31min	0.993	0.29(5)	3h 26min	0.963
80	I_2@MIL-125	5.87(8)	10min	0.989	4.6(1)	13min	0.970
	I_2@MIL-125_NH_2	0.895(7)	1h 7min	0.999	0.52(1)	1h 55min	0.945
90	I_2@MIL-125	8.2(1)	7min	0.989	6.3(1)	9min	0.983
	I_2@MIL-125_NH_2	1.65(3)	36min	0.997	0.87(1)	1h 8min	0.956
100	I_2@MIL-125	18.1(6)	3min	0.981	15.4(6)	3min	0.961
	I_2@MIL-125_NH_2	2.47(1)	24min	0.998	1.38(8)	43min	0.938
110	I_2@MIL-125	33.8(4)	2min	0.984	29.7(3)	2min	0.978
	I_2@MIL-125_NH_2	4.02(5)	14min	0.997	1.85(4)	32min	0.983
120	I_2@MIL-125	62.7(6)	1min	0.988	57.4(6)	1min	0.998
	I_2@MIL-125_NH_2	6.51(2)	9min	0.994	2.87(4)	20min	0.982

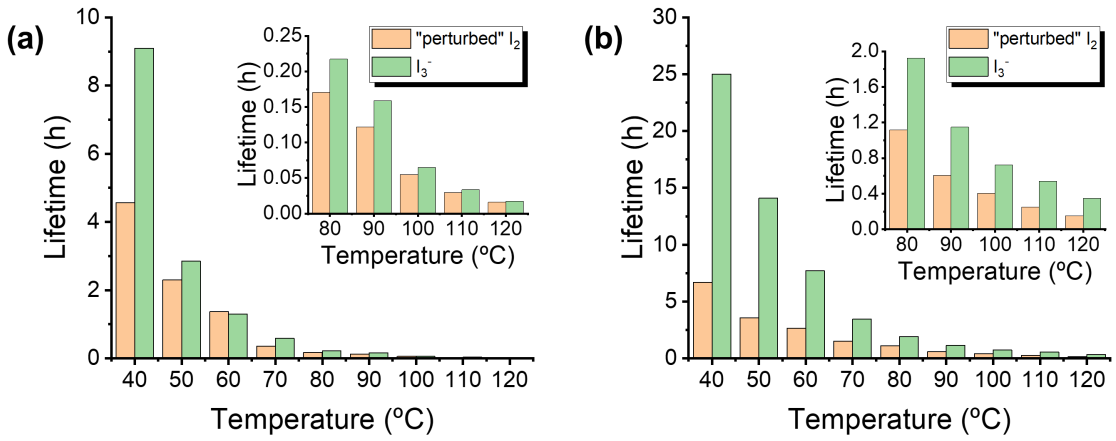

Figure 6.19: Lifetime of "perturbed" I_2 and I_3^- species obtained using the Albery method for (a) I_2@MIL-125 and (b) I_2@MIL-125_NH_2. Inset: zoom showing the behavior at temperatures above 80 ºC.

6.5.2. Evaluating the apparent activation energies of iodine desorption

For evaluating the differences between the behavior of both iodine species, the apparent activation energies of desorption were estimated using the relation between $\bar{k}$ values and the desorption temperature, according to the Arrhenius relation represented in Equation (6.6). Here, A is the pre-exponential factor, E_A is the activation energy (J.mol^{-1}), and T is the temperature (K).

$$k = Ae^{\left(-\frac{E_A}{RT}\right)} \quad (6.6)$$

The fitting of the $\bar{k}$ values using the Arrhenius equation for the desorption of I_2 and I_3^- in I_2@MIL-125 and I_2@MIL-125_NH_2 are shown in Figure 6.20, and the parameters of the linear regression are reported in Table 6.7. First, it is worth mentioning that the values obtained for the E_A of both iodine species are higher than 40 kJ.mol^{-1} in all compounds, which is ascribed to a physisorption phenomenon [156,367].

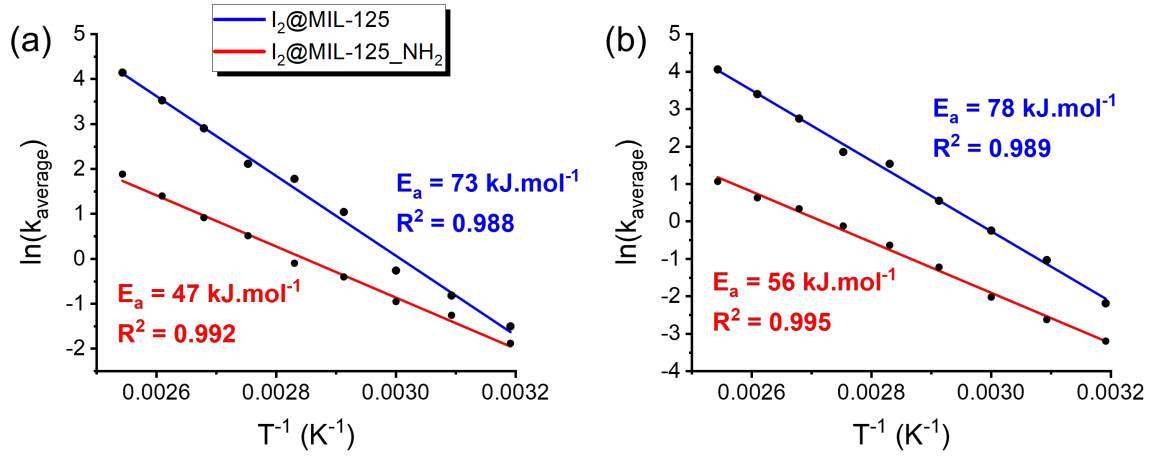

Figure 6.20: Arrhenius plots corresponding to the desorption of (a) I_2 and (b) I_3^- in I_2@MIL-125 (blue) and I_2@MIL-125_NH_2 (red) compounds. The apparent activation energy (E_a) and the coefficient of correlation (R^2) are also highlighted.

Table 6.7: Apparent activation energies (E_A) and pre-exponential factor for the I_2 and I_3^- desorption in I_2@MIL-125, and I_2@ MIL-125_NH_2.

MOF	A (h^{-1})		E_A (kJ.mol^{-1})	
	"perturbed" I_2	I_3^-	"perturbed" I_2	I_3^-
I_2@MIL-125	2.0×10^{11}	1.4×10^{12}	73 ± 5	78 ± 4
I_2@MIL-125_NH_2	1.6×10^{5}	1.3×10^{9}	47 ± 3	56 ± 2

Note that the E_A values obtained for I_2@MIL-125 are higher than those obtained for I_2@MIL-125_NH_2 and, in a first moment, one may be misled to conclude that higher E_A values are related to a more difficult desorption. However, the Raman spectra (Figure 6.17 and Figure 6.18), the lifetimes obtained by the Albery method (Table 6.6 and Figure 6.19), and TGA experiments (Figure 6.16) clearly show that iodine is further stabilized in the presence of $–NH_2$. To explain this, it is worth mentioning that the apparent activation energy (E_A) obtained through the Arrhenius equation is not a direct measure of the energy necessary for breaking the interaction between the iodine and the MOF lattice, leading to desorption. Instead, it also considers the number of molecules that are available for desorption, the disorder, and the kinetic energy of system.

In addition, it is noteworthy that, when particles desorb independently of each other, the desorption is considered first order and the pre-exponential factor A is interpreted as the vibration frequency of the adsorbed atoms – with order of magnitude higher than 10^5 s^{-1} [368], which is in agreement to the values obtained here. Moreover, when considering the I_2@MIL-125 compound, the pre-exponential term A and the apparent desorption energies are about the same for both iodine species (Figure 6.20 and Table 6.7), suggesting that a single mechanism is involved in the desorption of "perturbed" I_2 and I_3^- in this $–NH_2$ free material. On the other hand, for I_2@MIL-125_NH_2, the pre-exponential term A differs about 10^4 orders of magnitude between both iodine species ($\approx 10^5$ for "perturbed" iodine, and $\approx 10^9$ for I_3^-). This feature indicates that a rate-limiting stage is present during the iodine desorption in this compound. In fact, as mentioned above, the desorption kinetics are undoubtedly influenced by the amount of I_2 that is available for being desorbed in each compound, and this quantity is not the same in both samples. At this stage, it is worth noting that anionic species cannot transform into gas without losing their charges first. Therefore, both "perturbed" I_2 (or I_n^-) and I_3^- must oxidize back into I_2 before being desorbed (hence, the rate-limiting stage), as represented in Equations (6.7) and (6.8).

$$2\mathrm{I_n^-} + 2\mathrm{BDC^{\bullet+}} \rightarrow \mathrm{nI_2} + 2\mathrm{BDC} \qquad (\mathrm{n} = 3, 5, 7, 9 \ldots) \qquad (6.7)$$

$$2\mathrm{I_n^-} + 2NH_2^{\bullet+}BDC \rightarrow \mathrm{nI_2} + 2NH_2\mathrm{BDC} \qquad (\mathrm{n} = 3, 5, 7, 9 \ldots) \qquad (6.8)$$

In this scenario, the total amount of I_2 molecules that are available for the desorption depends on the initial amount of trapped iodine (which is higher in I_2@MIL-125), but also on the quantity of I_n^- (n = 3, 5, 7, 9 …) entities that recombined according to Equations (6.7) and (6.8). In I_2@MIL-125_NH_2, the strong interaction between the anionic iodine species and the

MOFs lattice attenuates their oxidation. Indeed, the presence of $–NH_2$ groups induces a more efficient charge separation through the formation of the $NH_2^{\bullet+}$–BDC cation radical [360]. This effect is related to the hole-stabilizer character of the amino-group, which allows a stronger interaction between the iodine anionic species and the $NH_2^{\bullet+}$–BDC linker when compared to the $BDC^{\bullet+}$, as discussed before [13,153,362–364]. Therefore, less I_2 molecules are available for the desorption in I_2@MIL-125_NH_2, as many of them are still stabilized in the form of anionic I_n^- species. For this reason, there is a significant gap between the pre-exponential values A in I_2@MIL-125_NH_2 (10^4 factor) and, at the same time, the lifetimes observed for the I_3^- are higher than those of "perturbed" I_2 (Table 6.6 and Figure 6.19). This feature indicates that the oxidation of the iodine anions, represented in Equation (6.8), is a rate-limiting step for the iodine desorption kinetics, which reduces the apparent activation energy (E_A).

On the other hand, I_2@MIL-125 exhibits similar lifetimes for both iodine species at temperatures higher than 40 ºC (Table 6.6 and Figure 6.19). Hence, Equation (6.7) is not a rate-limiting step in I_2@MIL-125. Consequently, most iodine anions are quickly transformed into I_2 in this case. This effect increases the number of molecules available for desorption and also the apparent activation energy related to the phenomenon. For this reason, there is no considerable difference over the kinetics of "perturbed" I_2 and I_3^- desorption in I_2@MIL-125. Indeed, for this compound, the E_A is essentially related to the release of the I_2 molecules from their adsorption sites and also to their diffusion from inside the MOFs pores to the atmosphere.

6.5.3. Evaluating iodine desorption and stability through computational modeling

DFT calculations were conducted for evaluating the theoretical desorption energies of both I_2 and I_3^- species. Due to the complexity of the system, only the organic linkers were considered during the simulation and therefore, the effect of the metal was neglected. In this case, the protonated (H_2BDC) and deprotonated (BDC) versions of the organic linker were considered, as well as their respective radical ($H_2BDC^{\bullet+}$, $BDC^{\bullet+}$) and amino-functionalized versions (NH_2–BDC, $NH_2^{\bullet+}$–BDC, NH_2–H_2BDC, $NH_2^{\bullet+}$–H_2BDC). The adsorption energies were computed by subtracting the energies of the separated components to the energies of the associated molecules. Thus, a more negative value is associated to a larger stabilizing interaction between both species. To ensure a good comparison, the unrestricted formalism for DFT computations was used whatever the spin states. Due to the size of the basis set, and

especially the presence of diffuse functions, no basis set superposition error (BSSE) correction was applied. The obtained results are summarized in Table 6.8.

Table 6.8: Adsorption energies (*E*), Helmholtz free energies (*H*), and Gibbs free energies (*G*) for the possible associations of organic linkers and iodine species.

I_2@	Energy (*E*) ($kJ.mol^{-1}$)	Helmholtz free energy (*H*) ($kJ.mol^{-1}$)	Gibbs free energy (*G*) ($kJ.mol^{-1}$)
Deprotonated linkers			
I_2@BDC	-126.7	-123.3	-87.3
I_2@BDC$^{\bullet+}$	-117.6	-108.2	-67.6
I_2@NH_2–BDC	-179.5	-178.1	-142.1
I_2@$NH_2^{\bullet+}$–BDC	-120.2	-115.0	-76.7
Protonated linkers			
I_2@H_2BDC	-25.8	-22.4	7.1
I_2@H_2BDC$^{\bullet+}$	-99.2	-90.8	-50.4
I_2@NH_2–H_2BDC	-37.7	-33.7	1.4
I_2@$NH_2^{\bullet+}$–H_2BDC	-33.5	-28.7	5.2

I_3^-@	Energy (*E*) ($kJ.mol^{-1}$)	Helmholtz free energy (*H*) ($kJ.mol^{-1}$)	Gibbs free energy (*G*) ($kJ.mol^{-1}$)
Deprotonated linkers			
I_3^-@BDC	–	–	–
I_3^-@BDC$^{\bullet+}$	240.5	251.3	278.2
I_3^-@NH_2–BDC	–	–	–
I_3^-@$NH_2^{\bullet+}$–BDC	246.1	249.7	273.3
Protonated linkers			
I_3^-@H_2BDC	–	–	–
I_3^-@H_2BDC$^{\bullet+}$	-486.2	-475.5	-346.5
I_3^-@NH_2–H_2BDC	–	–	–
I_3^-@$NH_2^{\bullet+}$–H_2BDC	-456.7	-340.4	-319.6

In the absence of the inorganic cluster moiety in the simulation, the use of both protonated and deprotonated versions of the organic linker is easily justified. Indeed, when considering the protonated organic linker, the hydrogen-oxygen interaction acts as a covalent bond. On the other hand, in the deprotonated case, there is no interaction between a positively charged element (either H^+ or Ti^{4+}) and the $–COO^-$ entity. For this reason, metallic cations exhibiting intermediate covalent/ionic bonds with the $–COO^-$ entity should stand in between

these two cases. For this reason, any comparison between the experimental and theoretical values obtained here must be conducted carefully.

Considering first the deprotonated linkers, the I_2 species tend to be further stabilized in the presence of $–NH_2$, as verified by the more negative energies in this case (*E*, *H*, and *G*). This finding is related to the higher electron donor character of amines, which enhances the stabilization of iodine species, as discussed before. It also corroborates the evidence that I_2 is harder to desorb in I_2@MIL-125(Ti)_NH_2 due to its strong interaction with $–NH_2$ groups, which leads to higher desorption lifetimes in all observed temperatures (Table 6.6 and Figure 6.19). In addition, I_2 has more negative Gibbs free energy in neutral organic linkers, which agrees with the mechanism proposed in Chapter IV. Indeed, the first step of the iodine adsorption is the interaction between the I_2 molecules and the organic linker, creating an EDA complex. Only then, the radical version of the organic linker is formed and, at this point, I_2 is transformed into I_3^-. Note that, for the protonated organic linkers, these tendencies are also verified, with exception of the I_2@$H_2BDC^{\bullet+}$ system that has much smaller energies (*E*, *H*, and *G*). In this case (as in I_2@$NH_2^{\bullet+}$–H_2BDC), an interaction between iodine and the oxygen of the linkers seems to appear. This interaction could be an artifact of the model due to the fact that these oxygen atoms are not available for bonding when they interact with a metallic framework. Thus, the stability of these two complexes is probably overestimated.

Contrary to what is observed for I_2, the I_3^- species is clearly stabilized only in the presence of cation radicals, as evidenced by the impossibility to obtain energy values for its interaction with neutral organic linkers. This evidence also agrees with the mechanism proposed for the iodine evolution, as it states that I_3^- is likely observed alongside cation radical organic entities (Chapter IV). Note also that the energy values are negative for the entire protonated series, while they are positive for the deprotonated organic linkers. This indicates that introducing positively charged elements (such as H^+ or Ti^{4+}) bounded to the carboxylate group helps to stabilize iodine species, which is coherent to the fact that the MOF lattice exhibits mostly "intermediate states" between these two forms of organic linkers. Finally, it is clear that, in the case of protonated linkers, the order of magnitude from the I_3^- interactions with the linkers is higher than those of I_2 species. This finding suggests a stronger interaction between I_3^- and the MOF lattice, which is in accord with the experimental results obtained here. Indeed, the desorption lifetimes of I_3^- species are considerably higher than those of I_2 (Table 6.6 and Figure 6.19). Finally, contrary to what was experimentally observed, no great variation was detected

when comparing the influence of $–NH_2$ over the I_3^- stabilization (i.e., $I_3^-@H_2BDC^{\bullet+}$ against $I_3^-@NH_2^{\bullet+}–H_2BDC$). This may be ascribed to the simplicity of the model. Indeed, the interaction of a neutral molecule (I_2) with the linker can be consistently described by a sorption model using only one molecule to simulate the framework. On the other hand, charged molecules introduce more complexity to the system. In this case, the attraction between a negatively (I_3^-) and a positively charged (the linker) molecule leads to the formation of a strong bond: the values around 400-500 kJ.mol^{-1} are closer to those associated to covalent bonds than to those of intermolecular interactions. Remarkably, this same reason explains why no value is obtained for the interaction of I_3^- with the deprotonated linker: the model implies the interaction of two negatively charged molecules, that prevents the stabilization of an aggregate.

6.6. Conclusions

Three different terephthalate-based MOFs (MIL-125(Ti), MIL-125(Ti)_NH_2, and CAU-1(Al)_NH_2) were successfully synthesized, structurally characterized, and evaluated according to their capacity to adsorb gaseous iodine in a continuous flow at room temperature. The iodine uptake of the compounds was evaluated using UV-Vis spectroscopy in which MIL-125(Ti)_NH_2 exhibited the best I_2 adsorption capacity (11.0 mol.mol^{-1}) after 72 h of contact with the gas flow, followed by MIL-125(Ti) (8.7 mol.mol^{-1}), and CAU-1(Al)_NH_2 (4.2 mol.mol^{-1}). Moreover, three iodine species were identified in the I_2-loaded MOFs (I_2@MOF) using Raman spectroscopy: “free” I_2 (≈ 198 cm^{-1}), “perturbed” I_2 (≈ 180 cm^{-1}), and I_3^- (at 113 cm^{-1}). I_2 into I_3^- transformation was found to be faster with MIL-125(Ti)_NH_2. The higher efficiency observed for MIL-125(Ti)_NH_2 is attributed to the presence of an amino group (which has a strong electron donor character), its smaller band gap (which favors the kinetic of the I_2 reduction), and to the presence of a LMCT mechanism (which enhances the charge separation in the MOF). Interestingly, the Ti^{3+} signal observed in the EPR spectra of the I_2@MIL-125(Ti) compound was negligible after the iodine contact, whereas in I_2@MIL-125(Ti)_NH_2 it was not even present. With that in mind, a mechanism is proposed for the charge transfer between the MOFs and the iodine. Briefly, because the titanium-based materials exhibit a LMCT mechanism, they can reduce the I_2 molecules by providing electrons either from their organic linkers or from their inorganic oxy/hydroxyl clusters. On the other hand, in CAU-1(Al)_NH_2 only electrons from its NH_2-BDC linker can be excited since this material shows a purely LBT process. This work improves the knowledge about the I_2 adsorption and reduction

mechanism in different MOF materials, especially for which a metal oxidation state change can occur (here Ti^{4+}/Ti^{3+}). It also demonstrates that several variables other than the SSA values and pore-size distribution have great influence over the I_2 uptake capacity, worth mentioning the presence of functional groups, the band gap energies, and the charge transfer mechanisms.

The influence of the amino group in MIL-125(Ti) over the iodine stabilization was then revealed using UV-Vis, TGA, and *in-situ* Raman spectroscopy. The I_2 uptake after five days of contact between the MOFs and the I_2 gas was slightly higher in MIL-125(Ti) (1.9 $g.g^{-1}$) than in MIL-125(Ti)_NH_2 (1.6 $g.g^{-1}$), whereas the I_2 conversion into I_3^- was favored by the presence of the $–NH_2$ group. The interactions between the MOFs and the "perturbed" I_2 and I_3^- species were evaluated using TGA and in-situ Raman desorption experiments in the 40 - 120 ºC temperature range. These techniques revealed that iodine species have comparable desorption kinetics in MIL-125(Ti), whereas MIL-125(Ti)_NH_2 material favored the stabilization of I_3^- thanks to a dipole-dipole interaction with the $NH_2^{\bullet+}$BDC organic linker. The desorption kinetics of both iodine species adsorbed on the MOFs were assessed using the Albery model, and their apparent desorption energies were calculated using the Arrhenius equation. While the E_A values were lower in the presence of $–NH_2$ (47 and 56 $kJ.mol^{-1}$ for "perturbed" I_2 and I_3^-, respectively, against 73 and 78 $kJ.mol^{-1}$), I_2@MIL-125(Ti)_NH_2 consistently demonstrated longer lifetimes for both iodine species over the entire temperature range studied. This effect is tentatively assigned to a rate-limiting step for the iodine species desorption kinetics in MIL-125(Ti)_NH_2. In essence, the stronger interaction between the anionic iodine species and $–NH_2^{\bullet+}$ radicals attenuate their oxidation into gaseous iodine, lowering the amount of I_2 available for desorption and, consequently, the energy required for the reaction. This study demonstrates that materials with improved charge separation – as in the case of MOFs showing LMCT complexes coupled with hole-stabilized groups such as $–NH_2$ – can stabilize iodine up to high temperatures by forming dipole-dipole interactions between the holes and the anionic iodine species, which is of great interest for applications in the nuclear industry field. Computational modeling using DFT-based methods confirmed the higher stability of the iodine species in the presence of amino groups. It also supported the presence of $NH_2^{\bullet+}$–BDC and $BDC^{\bullet+}$ radicals during the $I_2 \rightarrow I_3^-$ conversion, highlighting the stronger interaction between I_3^- and cationic radical organic linker species. Further studies must be conducted to evaluate the influence of water and/or oxygen over the iodine evolution in these materials. This chapter is partially based on the article published in the ACS Applied Materials and Interfaces journal (ACS Appl. Mater. Interfaces 2023, 15, 31032−31048).

General Conclusions and Perspectives

The immobilization of radioactive iodine has become an issue of great concern in the last few centuries due to the increase of nuclear energy production. Since then, because of their unique characteristics, several MOF materials have been investigated to trap gaseous I_2. With that in mind, three families of MOF materials were successfully synthesized in this work and used to adsorb iodine in a continuous gas flow: UiO-6*x* (*x* = 6 or 7), MIL-125, and CAU-1. An initial empirical study was conducted as a pre-base for discussing the influence of the electronic properties of such compounds over their CTCs with guest molecules. Indeed, previous studies indicated that band gap energies have an influence over the iodine uptake capacity and over its adsorption kinetics. Therefore, the Kubelka-Munk method was applied to diffuse reflectance UV-Vis spectroscopy data before evaluating the best data treatment for accessing the band gap of these hybrid materials. In this context, the Tauc model, the Cody band gap, the Boltzmann regression, and the Kramers-Kronig transformation were tested to determine the band gap energies and transition types of the different samples. At the end, an empirical method was proposed to distinguish between direct and indirect electronic transitions before acquiring the band gap energies using to the corresponding Tauc method (indirect or direct Tauc plots).

The effect of linker functionalization over the iodine uptake capacity have been already subject of several works using I_2@MOF systems, especially in UiO and MIL materials. Nevertheless, the metal content effect over these properties was not yet deeply explored. Therefore, the CTC between confined iodine molecules and MOF frameworks were studied using UiO-66(Zr,Hf), UiO-67(Zr,Hf)_NH_2, MIL-125, MIL-125_NH_2, and CAU-1 materials. Initially, the influence of the metal center over the iodine adsorption and evolution was discussed in UiO-66 systems. The presence of hafnium was found to reduce the lattice parameters, and the length of the M–O bonds of UiO-66 compounds. These effects were related to the smaller ionic radius of Hf^{4+} compared to Zr^{4+} as well as its more acidic character. Upon contact with gaseous iodine, hafnium was found to increase the gaseous iodine uptake capacity in these materials, while enhancing the kinetic transformation of I_2 into I_3^-, as observed by Raman spectroscopy. This effect was ascribed to the smaller band gap of hafnium-based UiO-66 compounds, which facilitated the electron-donor acceptor complex between the MOF and the I_2 molecules. A model mechanism for the I_2 into I_3^- transformation was proposed considering that no redox phenomena was observed in the inorganic moieties of the MOFs, inferring that the reduction of the iodine should be purely related to the UiO-66 organic linker.

In this case, the electron is transferred from the aromatic cycle of the BDC linker to the I_2 species, forming I_3^-. This latter species is then stabilized into the framework through an electrostatic interaction with the formed $BDC^{\bullet+}$ cation radical.

Seeking to probe the iodine diffusion and the mobility of the I_3^- species, and also for better understanding the interaction between the I_3^- species and the organic linker cation radical, Raman mapping spectroscopy was conducted on a series of UiO-67(Zr,Hf)_NH_2 materials. Indeed, as these compounds are known to form single crystals of a considerable size (up to 100 □m), they can be analyzed with an optimum spatial resolution at the micron scale. The results demonstrate the absence of I_3^- diffusion after its formation and indicate that this species is further stabilized when compared to I_2. This effect shows that specific adsorption sites are related to the stabilization of I_3^-, which is coherent with the proposition that a cation radical is formed and stabilized upon oxidation of the organic linker. Indeed, the CTC between I_2 and the NH_2-BPDC organic linker in UiO-67(Zr,Hf)_NH_2 produces I_3^- species and $NH_2^{\bullet+}$-BPDC cation radicals. Then, the generated holes are stabilized due to an "antenna" effect induced by the amino-group, and the I_3^- molecules are trapped nearby these sites by electrostatic interactions. This study also highlighted the influence of the crystal size over the iodine adsorption. In this case, bigger crystals tend to exhibit slower kinetic iodine adsorption due to partial blockage of pores and slow diffusion into the center of the crystals.

Later, a series of distinct and yet structurally similar MOFs (MIL-125(Ti), MIL-125(Ti)_NH_2, and CAU-1(Al)_NH_2) was used for evaluating the effect of the CTC types over the I_2 adsorption and evolution. To this end, a quartz cell was specifically designed and manufactured. It was then used for performing *in-situ* Raman spectroscopy during the contact between the MOFs and the iodine gas flow. Because these three materials exhibited very similar SSAs, the effect of other variables could be evaluated independently. The study revealed that, in MOFs that exhibit a LMCT (i.e., MIL-125(Ti) and MIL-125(Ti)_NH_2), the iodine adsorption capacity and transformation kinetics are much faster. This effect was related to a more efficient charge separation caused by the electron transfer over the inorganic cluster while stabilizing the hole on the inorganic linker. This feature reduces recombination phenomena and favors the production of I_3^- species, which are then stabilized through electrostatic interactions with the hole located on the MOF structure. Finally, thermal desorption experiments were conducted for I_2@MIL-125(Ti) and I_2@MIL-125(Ti)_NH_2 systems using *in-situ* Raman spectroscopy. The

iodine desorption kinetics were assessed using the Albery model and their apparent desorption energies were calculated through the Arrhenius equation. The results demonstrated that anionic I_3^- species are further stabilized on the MOFs structure when compared to molecular I_2. Moreover, $–NH_2$ groups were found to increase the stability of both species, as they consistently demonstrated longer lifetimes in this case. Indeed, MIL-125(Ti)_NH_2 shows all the characteristics (small band gap, improved charge separation, and strong electron donor functional groups) required to improve the gaseous iodine uptake. It also can retain the stabilized I_3^- species at higher temperatures. This effect was related to the great electron-donor character of amines and their "antenna" effect that stabilizes the holes, allowing a stronger interaction with the recently formed I_3^- species. These findings agree to the mechanism proposed for the iodine evolution and stabilization in other systems (UiO-66 and UiO-67_NH_2).

Computational modeling using DFT supported several experimental observations conducted across this work. For instance, the higher stability of the iodine species in the presence of amino groups was demonstrated by comparing their Helmholtz free energy of desorption to that of the organic linkers without $–NH_2$. The possible presence of $NH_2^{\bullet+}$–BDC and $BDC^{\bullet+}$ radicals during the $I_2 \rightarrow I_3^-$ conversion was also highlighted by the negative values of the Gibbs free energy for the interaction between these cation radicals and I_3^-. Finally, the absence of I_3^- diffusion observed using Raman mapping in single crystals of I_2@UiO-67(Zr,Hf)_NH_2 can be also ascribed to this strong interaction that I_3^- can form with positively charged organic linkers.

This work demonstrates how confinement effects in porous materials can modify the physical-chemical properties of both guest and host species and favor mechanisms of adsorption and stabilization that would not be possible otherwise. It also demonstrates that several variables can influence the adsorption capacity and the reactivity of such molecules, worth mentioning the specific surface areas, the band gap tailoring, the CTCs, the Lewis acidity, the crystal size, the functional group, and the efficient charge separation. For the short-term perspectives, computational simulations could be of great interest for comparing the experimental results obtained here. In this way, the interactions between other porous materials and molecules can be better understood, leading to advances in several areas such as gas sorption and photocatalysis.

These findings should be extrapolated to other systems to evaluate if these characteristics also play key roles over the adsorption of other guest molecules, such as CO_2,

H_2, and organic pollutants. For instance, photocatalysis has been proven to be an area of keen interest for CO_2 reduction and H_2 evolution, and MOF materials with high SSAs and effective charge separation are in the frontier of the field. Moreover, some of the major molecular pollutants present in the atmosphere nowadays are the Polycyclic Aromatic Compounds (PACs) and the Volatile Organic Compounds (VOCs). This covers most of halogenated hydrocarbons, alcohols, aldehydes, aromatics, alkanes, ketones, olefins, ethers, esters, paraffins, and other multi-ring benzenoid compounds. These substances can be harmful to humans and also to entire ecosystems since most of them are toxic, mutagenic, and carcinogenic, which increases the interest on methods to degrade them. The emissions of these pollutants can be controlled by using methods based on recovery (i.e., adsorption, membrane separation, and condensation), on destructive processes (i.e., photocatalysis, incineration, and biological degradation), or on a combination of both.

As in the case of iodine, the confinement effect of other molecules upon adsorption in MOF materials can modify their environment and therefore, alter their reactivity. For instance, these effects can improve the availability of target pollutants for the photocatalyst to act, increasing its performance. In addition, the enormous possibilities of CTC observed in MOF materials can be also an advantage when using them in different host-guest systems, as other molecules can interact in different ways with the MOF framework – acting sometimes as electron-donors or electron-acceptors. Finally, the possibility of chemically modifying these materials and tailoring their properties using different approaches means that they can be selectively improved to target specific pollutants. This feature can be of great interest in adsorption and photocatalysis. For these reasons, MOFs tend to be a great class of materials for the environmental remediation of gaseous pollutants, either by adsorption or photocatalysis mechanisms.

Bibliographic References

[1] L. B. Zablotska, *J. Urban Heal.* **2016**, *93*, 407.

[2] W. Lin, L. Chen, W. Yu, H. Ma, Z. Zeng, J. Lin, S. Zeng, *Atmos. Environ.* **2015**, *102*, 311.

[3] A. P. Møller, T. A. Mousseau, *Biol. Conserv.* **2011**, *144*, 2787.

[4] B. J. Riley, J. D. Vienna, D. M. Strachan, J. S. McCloy, J. L. Jerden, *J. Nucl. Mater.* **2016**, *470*, 307.

[5] T. Takemura, H. Nakamura, M. Takigawa, H. Kondo, T. Satomura, T. Miyasaka, T. Nakajima, *Sci. Online Lett. Atmos.* **2011**, *7*, 101.

[6] L. Pesce, P. Kopp, *Int. J. Pediatr. Endocrinol.* **2014**, *2014*, 1.

[7] W. Xie, D. Cui, S. R. Zhang, Y. H. Xu, D. L. Jiang, *Mater. Horizons* **2019**, *6*, 1571.

[8] S. U. Nandanwar, K. Coldsnow, V. Utgikar, P. Sabharwall, D. Eric Aston, *Chem. Eng. J.* **2016**, *306*, 369.

[9] B. J. Riley, J. Chun, J. V Ryan, J. Matyáš, X. S. Li, D. W. Matson, S. K. Sundaram, D. M. Strachan, J. D. Vienna, *RSC Adv.* **2011**, *1*, 1704.

[10] P. Wang, Q. Xu, Z. Li, W. Jiang, Q. Jiang, D. Jiang, *Adv. Mater.* **2018**, *30*, 1801991.

[11] T. Geng, S. Ye, Z. Zhu, W. Zhang, *J. Mater. Chem. A* **2018**, *6*, 2808.

[12] M. Leloire, C. Walshe, P. Devaux, R. Giovine, S. Duval, T. Bousquet, S. Chibani, J. Paul, A. Moissette, H. Vezin, P. Nerisson, L. Cantrel, C. Volkringer, T. Loiseau, *Chem. – A Eur. J.* **2022**, *28*, e202104437.

[13] P. H. M. Andrade, N. Henry, C. Volkringer, T. Loiseau, H. Vezin, M. Hureau, A. Moissette, *ACS Appl. Mater. Interfaces* **2022**, DOI 10.1021/acsami.2c07288.

[14] Y. Lei, G. Zhang, Q. Zhang, L. Yu, H. Li, H. Yu, Y. He, *Nat. Commun.* **2021**, *12*, DOI 10.1038/s41467-021-24830-1.

[15] X. Zhang, J. Maddock, T. M. Nenoff, M. A. Denecke, S. Yang, M. Schröder, *Chem. Soc.*

Rev. **2022**, 3243.

[16] M. Leloire, J. Dhainaut, P. Devaux, O. Leroy, H. Desjonqueres, S. Poirier, P. Nerisson, L. Cantrel, S. Royer, T. Loiseau, C. Volkringer, *J. Hazard. Mater.* **2021**, *416*, 125890.

[17] Z. J. Li, Y. Ju, H. Lu, X. Wu, X. Yu, Y. Li, X. Wu, Z. H. Zhang, J. Lin, Y. Qian, M. Y. He, J. Q. Wang, *Chem. - A Eur. J.* **2021**, *27*, 1286.

[18] G. Férey, *Chem. Soc. Rev.* **2008**, *37*, 191.

[19] C. Janiak, J. K. Vieth, *New J. Chem.* **2010**, *34*, 2366.

[20] N. A. Khan, Z. Hasan, S. H. Jhung, *J. Hazard. Mater.* **2013**, *244–245*, 444.

[21] T. Assaad, B. Assfour, *J. Nucl. Mater.* **2017**, *493*, 6.

[22] Q. Chen, Q. He, M. Lv, Y. Xu, H. Yang, X. Liu, F. Wei, *Appl. Surf. Sci.* **2015**, *327*, 77.

[23] M. Kim, J. F. Cahill, H. Fei, K. A. Prather, S. M. Cohen, *J. Am. Chem. Soc.* **2012**, *134*, 18082.

[24] B. Lee, J. Park, *Bull. Korean Chem. Soc.* **2021**, *42*, 290.

[25] C. Falaise, C. Volkringer, J. Facqueur, T. Bousquet, L. Gasnot, T. Loiseau, *Chem. Commun.* **2013**, *49*, 10320.

[26] M. Dan-Hardi, C. Serre, T. Frot, L. Rozes, G. Maurin, C. Sanchez, G. Férey, *J. Am. Chem. Soc.* **2009**, *131*, 10857.

[27] M. A. Nasalevich, C. H. Hendon, J. G. Santaclara, K. Svane, B. Van Der Linden, S. L. Veber, M. V. Fedin, A. J. Houtepen, M. A. Van Der Veen, F. Kapteijn, A. Walsh, J. Gascon, *Sci. Rep.* **2016**, *6*, 1.

[28] R. N. Colvile, E. J. Hutchinson, J. S. Mindell, R. F. Warren, *Atmos. Environ.* **2001**, *35*, 1537.

[29] EDF, "Le nucléaire en chiffres," can be found under https://www.edf.fr/groupe-edf/espaces-dedies/l-energie-de-a-a-z/tout-sur-l-energie/produire-de-l-electricite/le-nucleaire-en-chiffres, **2021**.

[30] G. Steinhauser, A. Brandl, T. E. Johnson, *Sci. Total Environ.* **2014**, *470–471*, 800.

[31] A. Berenjian, N. Chan, H. J. Malmiri, *Am. J. Biochem. Biotechnol.* **2012**, *8*, 220.

[32] H. Bai, A. C. Yeh, *Ind. Eng. Chem. Res.* **1997**, *36*, 2490.

[33] M. Marszewski, S. Cao, J. Yu, M. Jaroniec, *Mater. Horiz.* **2015**, *2*, 261.

[34] A. B. Albadarin, M. N. Collins, M. Naushad, S. Shirazian, G. Walker, C. Mangwandi, *Chem. Eng. J.* **2017**, *307*, 264.

[35] H. M. Ginzburg, E. Reis, *Public Health Rep.* **1991**, *106*, 32.

[36] M. Kozenko, A. E. Chudley, *Clin. Genet.* **2010**, *77*, 221—226.

[37] K. Kosaka, M. Asami, N. Kobashigawa, K. Ohkubo, H. Terada, N. Kishida, M. Akiba, *Water Res.* **2012**, *46*, 4397.

[38] P. Thakur, S. Ballard, R. Nelson, *Sci. Total Environ.* **2013**, *458–460*, 577.

[39] M. Leloire, Utilisation de Matériaux Poreux de Type Metal-Organic Framework (MOF) Pour l'adsorption de Molécules Gazeuses (I2, RuO4) Dans Le Contexte d'un Accident de Réacteur Nucléaire, Université de Lille, **2020**.

[40] H. N. Cardinal, D. W. Holdsworth, M. Drangova, B. B. Hobbs, A. Fenster, *Med. Phys.* **1993**, *20*, 15.

[41] M. Nava-Villalba, C. Aceves, *Prostaglandins Other Lipid Mediat.* **2014**, *112*, 27.

[42] M. Breugst, D. von der Heiden, *Chem. – A Eur. J.* **2018**, *24*, 9187.

[43] M. Andersson, B. de Benoist, L. Rogers, *Best Pract. Res. Clin. Endocrinol. Metab.* **2010**, *24*, 1.

[44] C. Fortin, V. Fèvre-Nollet, F. Cousin, P. Lebègue, F. Louis, *Atmos. Environ.* **2019**, *214*, 116838.

[45] G. Klopman, *J. Am. Chem. Soc.* **1968**, *90*, 223.

[46] C. Stevenson, E. Silva, G. Pineda, *J. Clin. Endocrinol. Metab.* **1974**, *38*, 390.

[47] M. B. Zimmermann, K. Boelaert, *Lancet Diabetes Endocrinol.* **2015**, *3*, 286.

[48] H. R. Chung, *Ann. Pediatr. Endocrinol. Metab.* **2014**, *19*, 8.

[49] M. A. Bhakare, K. D. Lokhande, P. S. Dhumal, M. P. Bondarde, S. Some, *Sep. Purif. Technol.* **2022**, *278*, 119490.

[50] J. Robbins, A. B. Schneider, *Rev. Endocr. Metab. Disord.* **2000**, *1*, 197.

[51] R. A. Conard, B. M. Dobyns, W. W. Sutow, *JAMA* **1970**, *214*, 316.

[52] L. Mandel, F. Liu, *J. Am. Dent. Assoc.* **2007**, *138*, 1582.

[53] L. Baugnet-Mahieu, M. Lemaire, E. D. Léonard, A. Léonard, G. B. Gerber, *Radiat. Res.* **1994**, *140*, 429.

[54] P. Verger, A. Aurengo, B. Geoffroy, B. Le Guen, *Thyroid* **2001**, *11*, 353.

[55] R. T. Jubin, **1979**, 91.

[56] R. T. Jubin, **n.d.**, DOI 10.2172/5169490.

[57] R. T. Jubin, **n.d.**, DOI 10.2172/5169490.

[58] G.-I. Park, I.-T. Kim, J.-K. Lee, S.-K. Ryu, J.-H. Kim, *Carbon Lett.* **2001**, *2*, 9.

[59] X. Yang, D. Xie, W. Wang, S. Li, Z. Tang, S. Dai, *Chem. Eng. J.* **2023**, *454*, 140365.

[60] C.-C. Chien, Y.-P. Huang, W.-C. Wang, J.-H. Chao, Y.-Y. Wei, *CLEAN – Soil, Air, Water* **2011**, *39*, 103.

[61] C.-C. Chien, Y.-P. Huang, W.-C. Wang, J.-H. Chao, Y.-Y. Wei, *CLEAN – Soil, Air, Water* **2011**, *39*, 103.

[62] K. Margeta, N. Z. Logar, M. Šiljeg, F. Anamarija, *Water Treat.* **2013**, *5*, 81.

[63] S. Chałupnik, W. Franus, M. Wysocka, G. Gzyl, *Environ. Sci. Pollut. Res.* **2013**, *20*, 7900.

[64] I. Batonneau-Gener, A. Moissette, C. Brémard, G. Buntinx, *J. Photochem. Photobiol. A Chem.* **2008**, *195*, 156.

[65] M. Hureau, A. Moissette, A. Legrand, F. Luchez, M. Sliwa, C. Bremard, *J. Phys. Chem. C* **2012**, *116*, 9092.

[66] I. Gener, G. Buntinx, A. Moissette, C. Brémard, *J. Phys. Chem. B* **2002**, *106*, 10322.

[67] K. W. Chapman, P. J. Chupas, T. M. Nenoff, *J. Am. Chem. Soc.* **2010**, *132*, 8897.

[68] B. J. Riley, J. O. Kroll, J. A. Peterson, J. Matyáš, M. J. Olszta, X. Li, J. D. Vienna, *ACS Appl. Mater. Interfaces* **2017**, *9*, 32907.

[69] S. An, X. Zhu, Y. He, L. Yang, H. Wang, S. Jin, J. Hu, H. Liu, *Ind. Eng. Chem. Res.* **2019**, *58*, 10495.

[70] Y. Yang, X. Xiong, Y. Fan, Z. Lai, Z. Xu, F. Luo, *J. Solid State Chem.* **2019**, *279*, 120979.

[71] Y. Yang, X. Xiong, Y. Fan, Z. Lai, Z. Xu, F. Luo, *J. Solid State Chem.* **2019**, *279*, 120979.

[72] N. Miyajima, T. Akatsu, T. Ikoma, O. Ito, B. Rand, Y. Tanabe, E. Yasuda, *Carbon N. Y.* **2000**, *38*, 1831.

[73] L. Yang, S. S. Saavedra, N. R. Armstrong, *Anal. Chem.* **1996**, *68*, 1834.

[74] B. Bhowmik, G. L. Jendrasiak, B. Rosenberg, *Nat. Publ. Gr.* **1967**, *216*, 615.

[75] Z.-B. Liu, J.-G. Tian, W.-P. Zang, W.-Y. Zhou, F. Song, C.-P. Zhang, J.-Y. Zheng, H. Xu, *Opt. Lett.* **2004**, *29*, 1099.

[76] C. Reid, R. S. Mulliken, *J. Am. Chem. Soc.* **1954**, *76*, 3869.

[77] L. A. Walker, S. Pullen, B. Donovan, R. J. Sension, *Chem. Phys. Lett.* **1995**, *242*, 177.

[78] H. A. Benesi, J. H. Hildebrand, *J. Am. Chem. Soc* **1949**, *71*, 2703.

[79] S. V Kireev, S. L. Shnyrev, *Laser Phys.* **2015**, *25*, 75602.

[80] A. Anderson, T. S. Sun, *Chem. Phys. Lett.* **1970**, *6*, 611.

[81] W. Kiefer, H. J. Bernstein, *J. Raman Spectrosc.* **1973**, *1*, 417.

[82] W. Guo, D. Wang, J. Hu, Z. K. Tang, S. Du, *Appl. Phys. Lett.* **2011**, *98*, 2011.

[83] P. Deplano, J. R. Ferraro, M. L. Mercuri, E. F. Trogu, *Coord. Chem. Rev.* **1999**, *188*, 71.

[84] P. Deplano, F. A. Devillanova, J. R. Ferraro, F. Isaia, V. Lippolis, M. L. Mercuri, *Appl. Spectrosc.* **1992**, *46*, 1625.

[85] A. J. Blake, F. A. Devillanova, R. O. Gould, W. S. Li, V. Lippolis, S. Parsons, C. Radek, M. Schröder, *Chem. Soc. Rev.* **1998**, *27*, 195.

[86] R. P. Cooney, P. J. Hendra, M. Fleischmann, *J. Raman Spectrosc.* **1977**, *6*, 264.

[87] P. H. Svensson, L. Kloo, *Chem. Rev.* **2003**, *103*, 1649.

[88] S. L. Hsu, A. J. Signorelli, G. P. Pez, R. H. Baughman, *J. Chem. Phys.* **1978**, *69*, 106.

[89] C. Wang, Y. Wang, R. Ge, X. Song, X. Xing, Q. Jiang, H. Lu, C. Hao, X. Guo, Y. Gao, D. Jiang, *Chem. – A Eur. J.* **2018**, *24*, 585.

[90] W. Zhang, Y. Mu, X. He, P. Chen, S. Zhao, C. Huang, Y. Wang, J. Chen, *Chem. Eng. J.* **2020**, *379*, 122365.

[91] L. B. T.-R. M. in C. Kloo Molecular Sciences and Chemical Engineering, Elsevier, **2021**.

[92] J. C. Saint Remi, A. Lauerer, C. Chmelik, I. Vandendael, H. Terryn, G. V. Baron, J. F. M. Denayer, J. Kärger, *Nat. Mater.* **2016**, *15*, 401.

[93] A. M. Wen, N. F. Steinmetz, *Chem. Soc. Rev.* **2016**, *45*, 4074.

[94] Q. L. Zhu, Q. Xu, *Chem. Soc. Rev.* **2014**, *43*, 5468.

[95] Y. Bai, Y. Dou, L. H. Xie, W. Rutledge, J. R. Li, H. C. Zhou, *Chem. Soc. Rev.* **2016**, *45*, 2327.

[96] H. Furukawa, N. Ko, Y. B. Go, N. Aratani, S. B. Choi, E. Choi, A. Ö. Yazaydin, R. Q. Snurr, M. O'Keeffe, J. Kim, O. M. Yaghi, *Science (80-.).* **2010**, *329*, 424.

[97] M. Meilikhov, K. Yusenko, D. Esken, S. Turner, G. Van Tendeloo, R. A. Fischer, *Eur. J. Inorg. Chem.* **2010**, 3701.

[98] R. Freund, O. Zaremba, G. Arnauts, R. Ameloot, G. Skorupskii, M. Dincă, A. Bavykina, J. Gascon, A. Ejsmont, J. Goscianska, M. Kalmutzki, U. Lächelt, E. Ploetz, C. S. Diercks, S. Wuttke, *Angew. Chemie - Int. Ed.* **2021**, *60*, 23975.

[99] A. J. Howarth, Y. Liu, P. Li, Z. Li, T. C. Wang, J. T. Hupp, O. K. Farha, *Nat. Rev. Mater.* **2016**, *1*, 1.

[100] P. Silva, S. M. F. Vilela, J. P. C. Tomé, F. A. Almeida Paz, *Chem. Soc. Rev.* **2015**, *44*,

6774.

[101] M. O'Keeffe, M. Eddaoudi, H. Li, T. Reineke, O. M. Yaghi, *J. Solid State Chem.* **2000**, *152*, 3.

[102] G. Férey, *J. Solid State Chem.* **2000**, *152*, 37.

[103] T. C. Wang, W. Bury, D. A. Gómez-Gualdrón, N. A. Vermeulen, J. E. Mondloch, P. Deria, K. Zhang, P. Z. Moghadam, A. A. Sarjeant, R. Q. Snurr, J. F. Stoddart, J. T. Hupp, O. K. Farha, *J. Am. Chem. Soc.* **2015**, *137*, 3585.

[104] Q. Wang, D. Astruc, *Chem. Rev.* **2020**, *120*, 1438.

[105] N. Kolobov, M. G. Goesten, J. Gascon, *Angew. Chemie - Int. Ed.* **2021**, *60*, 26038.

[106] Y. Zhu, G. Chen, X. Xu, G. Yang, M. Liu, Z. Shao, *ACS Catal.* **2017**, *7*, 3540.

[107] N.-T. Suen, S.-F. Hung, Q. Quan, N. Zhang, Y.-J. Xu, H. M. Chen, *Chem. Soc. Rev.* **2017**, *46*, 337.

[108] P. H. M. Andrade, A. L. M. Gomes, H. G. Palhares, C. Volkringer, *J. Mater. Sci.* **2022**, *57*, 4481.

[109] L. Zhou, *Renew. Sustain. Energy Rev.* **2005**, *9*, 395.

[110] U. Mueller, M. Schubert, F. Teich, H. Puetter, K. Schierle-Arndt, J. Pastré, *J. Mater. Chem.* **2006**, *16*, 626.

[111] M. Peller, K. Böll, A. Zimpel, S. Wuttke, *Inorg. Chem. Front.* **2018**, *5*, 1760.

[112] H. Yuan, J. Tao, N. Li, A. Karmakar, C. Tang, H. Cai, S. J. Pennycook, N. Singh, D. Zhao, *Angew. Chemie* **2019**, *131*, 14227.

[113] L. S. Xie, L. Sun, R. Wan, S. S. Park, J. A. DeGayner, C. H. Hendon, M. Dincă, *J. Am. Chem. Soc.* **2018**, *140*, 7411.

[114] L. G. Parratt, *Rev. Mod. Phys.* **1959**, *31*, 616.

[115] B. Lax, *Rev. Mod. Phys.* **1958**, *30*, 122.

[116] F. Heman, *Rev. Mod. Phys.* **1958**, *30*, 102.

[117] N. Ueno, in *Phys. Org. Semicond.*, **2012**, pp. 65–89.

[118] A. H. Wilson, *Proc. R. Soc. London. Ser. A. Math. Phys. Sci.* **1931**, *133*, 458.

[119] A. H. Wilson, *Proc. R. Soc. London. Ser. A. Math. Phys. Sci.* **1931**, *134*, 277.

[120] M. H. Cohen, *J. Non. Cryst. Solids* **1970**, *4*, 391.

[121] Z. G. Soos, *J. Chem. Educ.* **1978**, *55*, 546.

[122] J. Heine, K. Müller-Buschbaum, *Chem. Soc. Rev.* **2013**, *42*, 9232.

[123] C. A. Kent, D. Liu, L. Ma, J. M. Papanikolas, T. J. Meyer, W. Lin, *J. Am. Chem. Soc.* **2011**, *133*, 12940.

[124] P. Huo, T. Chen, J. Le Hou, L. Yu, Q. Y. Zhu, J. Dai, *Inorg. Chem.* **2016**, *55*, 6496.

[125] C. Xu, Y. Pan, G. Wan, H. Liu, L. Wang, H. Zhou, S. H. Yu, H. L. Jiang, *J. Am. Chem. Soc.* **2019**, *141*, 19110.

[126] Y. Li, S. Zhang, D. Song, *Angew. Chemie Int. Ed.* **2013**, *52*, 710.

[127] X. Song, L. Zhao, N. Zhang, L. Liu, X. Ren, H. Ma, C. Luo, Y. Li, Q. Wei, *Anal. Chem.* **2022**, DOI 10.1021/acs.analchem.2c03615.

[128] J. I. Deneff, K. S. Butler, L. E. S. Rohwer, C. J. Pearce, N. R. Valdez, M. A. Rodriguez, T. S. Luk, D. F. Sava Gallis, *Angew. Chemie - Int. Ed.* **2021**, *60*, 1203.

[129] J. C. Hye, P. S. Myunghyun, *J. Am. Chem. Soc.* **2004**, *126*, 15844.

[130] X. Zhang, I. Da Silva, R. Fazzi, A. M. Sheveleva, X. Han, B. F. Spencer, S. A. Sapchenko, F. Tuna, E. J. L. McInnes, M. Li, S. Yang, M. Schröder, *Inorg. Chem.* **2019**, *58*, 14145.

[131] G. Brunet, D. A. Safin, M. Z. Aghaji, K. Robeyns, I. Korobkov, T. K. Woo, M. Murugesu, *Chem. Sci.* **2017**, *8*, 3171.

[132] X. Yang, X. Liu, Y. Liu, X.-F. Wang, Z. Chen, X. Wang, *Front. Chem. Sci. Eng.* **2022**, DOI 10.1007/s11705-022-2218-3.

[133] S. Kolay, Jagannath, *J. Solid State Chem.* **2022**, *312*, 123182.

[134] Z. Meng, K. Mirica, *Nano Res.* **2021**, *14*, 369.

[135] B. Lee, Y. P. Chen, J. Park, J. Park, *ACS Appl. Mater. Interfaces* **2019**, *11*, 25817.

[136] J. Tang, S. Zhou, M. Huang, Z. Liang, S. Su, Y. Wen, Q. L. Zhu, X. Wu, *Inorg. Chem. Front.* **2022**, *9*, 3436.

[137] Y. Chen, O. Sakata, Y. Nanba, L. S. R. Kumara, A. Yang, C. Song, M. Koyama, G. Li, H. Kobayashi, H. Kitagawa, *Commun. Chem.* **2018**, *1*, 1.

[138] T. H. Noh, O. S. Jung, *Acc. Chem. Res.* **2016**, *49*, 1835.

[139] S.-T. Zheng, C. Mao, T. Wu, S. Lee, P. Feng, X. Bu, *J. Am. Chem. Soc.* **2012**, *134*, 11936.

[140] K. M. Ok, J. Sung, G. Hu, R. M. J. Jacobs, D. O'Hare, *J. Am. Chem. Soc.* **2008**, *130*, 3762.

[141] Q.-R. Fang, G.-S. Zhu, Z. Jin, Y.-Y. Ji, J.-W. Ye, M. Xue, H. Yang, Y. Wang, S.-L. Qiu, *Angew. Chemie* **2007**, *119*, 6758.

[142] S. L. James, *Chem. Soc. Rev.* **2003**, *32*, 276.

[143] D. Yan, J. Lu, J. Ma, S. Qin, M. Wei, D. G. Evans, X. Duan, *Angew. Chemie Int. Ed.* **2011**, *50*, 7037.

[144] N. Yanai, T. Uemura, M. Inoue, R. Matsuda, T. Fukushima, M. Tsujimoto, S. Isoda, S. Kitagawa, *J. Am. Chem. Soc.* **2012**, *134*, 4501.

[145] H. Yang, C. Yang, N. Zhang, K. Mo, Q. Li, K. Lv, J. Fan, L. Wen, *Appl. Catal. B Environ.* **2021**, *285*, 119801.

[146] R. Matsuda, R. Kitaura, S. Kitagawa, Y. Kubota, R. V. Belosludov, T. C. Kobayashi, H. Sakamoto, T. Chiba, M. Takata, Y. Kawazoe, Y. Mita, *Nature* **2005**, *436*, 238.

[147] P. Maniam, N. Stock, *Inorg. Chem.* **2011**, *50*, 5085.

[148] N. Yanai, T. Uemura, M. Inoue, R. Matsuda, T. Fukushima, M. Tsujimoto, S. Isoda, S. Kitagawa, *J. Am. Chem. Soc.* **2012**, *134*, 4501.

[149] S. S. Nagarkar, A. V. Desai, S. K. Ghosh, *Chem. - An Asian J.* **2014**, *9*, 2358.

[150] S.-T. Zheng, C. Mao, T. Wu, S. Lee, P. Feng, X. Bu, *J. Am. Chem. Soc.* **2012**, *134*, 11936.

[151] M. Tu, H. Reinsch, S. Rodríguez-Hermida, R. Verbeke, T. Stassin, W. Egger, M. Dickmann, B. Dieu, J. Hofkens, I. Vankelecom, N. Stock, R. Ameloot, *Angew. Chemie* **2018**, DOI 10.1002/ange.201813996.

[152] K. Khaletskaya, J. Reboul, M. Meilikhov, M. Nakahama, S. Diring, M. Tsujimoto, S. Isoda, F. Kim, K. I. Kamei, R. A. Fischer, S. Kitagawa, S. Furukawa, *J. Am. Chem. Soc.* **2013**, *135*, 10998.

[153] D. F. Sava, K. W. Chapman, M. A. Rodriguez, J. A. Greathouse, P. S. Crozier, H. Zhao, P. J. Chupas, T. M. Nenoff, *Chem. Mater.* **2013**, *25*, 2591.

[154] D. F. Sava, M. A. Rodriguez, K. W. Chapman, P. J. Chupas, J. A. Greathouse, P. S. Crozier, T. M. Nenoff, *J. Am. Chem. Soc.* **2011**, *133*, 12398.

[155] Y. Tang, H. Huang, J. Li, W. Xue, C. Zhong, *J. Mater. Chem. A* **2019**, *7*, 18324.

[156] P. Chen, X. He, M. Pang, X. Dong, S. Zhao, W. Zhang, *ACS Appl. Mater. Interfaces* **2020**, *12*, 20429.

[157] R.-X. Yao, X. Cui, X.-X. Jia, F.-Q. Zhang, X.-M. Zhang, *Inorg. Chem.* **2016**, *55*, 9270.

[158] R. J. Marshall, S. L. Griffin, C. Wilson, R. S. Forgan, *Chem. – A Eur. J.* **2016**, *22*, 4870.

[159] X. Zhang, I. da Silva, H. G. W. Godfrey, S. K. Callear, S. A. Sapchenko, Y. Cheng, I. Vitórica-Yrezábal, M. D. Frogley, G. Cinque, C. C. Tang, C. Giacobbe, C. Dejoie, S. Rudić, A. J. Ramirez-Cuesta, M. A. Denecke, S. Yang, M. Schröder, *J. Am. Chem. Soc.* **2017**, *139*, 16289.

[160] B. Guo, F. Li, C. Wang, L. Zhang, D. Sun, *J. Mater. Chem. A* **2019**, *7*, 13173.

[161] J. Maddock, X. Kang, L. Liu, B. Han, S. Yang, M. Schröder, *Chemistry (Easton).* **2021**, *3*, 525.

[162] X. Yang, X. Liu, Y. Liu, X.-F. Wang, Z. Chen, X. Wang, *Front. Chem. Sci. Eng.* **2022**, DOI 10.1007/s11705-022-2218-3.

[163] A. S. Munn, F. Millange, M. Frigoli, N. Guillou, C. Falaise, V. Stevenson, C. Volkringer, T. Loiseau, G. Cibin, R. I. Walton, *CrystEngComm* **2016**, *18*, 8108.

[164] Y.-Q. Hu, M.-Q. Li, Y. Wang, T. Zhang, P.-Q. Liao, Z. Zheng, X.-M. Chen, Y.-Z. Zheng,

Chem. – A Eur. J. **2017**, *23*, 8409.

[165] Y.-Q. Hu, M.-Q. Li, Y. Wang, T. Zhang, P.-Q. Liao, Z. Zheng, X.-M. Chen, Y.-Z. Zheng, *Chem. – A Eur. J.* **2017**, *23*, 8409.

[166] P. Mao, B. Qi, Y. Liu, L. Zhao, Y. Jiao, Y. Zhang, Z. Jiang, Q. Li, J. Wang, S. Chen, Y. Yang, *J. Solid State Chem.* **2016**, *237*, 274.

[167] B. Qi, Y. Liu, T. Zheng, Q. Gao, X. Yan, Y. Jiao, Y. Yang, *J. Solid State Chem.* **2018**, *258*, 49.

[168] Y. Guan, Y. Li, J. Zhou, T. Zhang, J. Ding, Z. Xie, L. Wang, *Inorg. Chem.* **2021**, DOI 10.1021/acs.inorgchem.1c01120.

[169] K. W. Chapman, D. F. Sava, G. J. Halder, P. J. Chupas, T. M. Nenoff, *J. Am. Chem. Soc.* **2011**, *133*, 18583.

[170] T. D. Bennett, P. J. Saines, D. A. Keen, J.-C. Tan, A. K. Cheetham, *Chem. – A Eur. J.* **2013**, *19*, 7049.

[171] D. F. Sava, T. J. Garino, T. M. Nenoff, *Ind. Eng. Chem. Res.* **2012**, *51*, 614.

[172] C. Volkringer, C. Falaise, P. Devaux, R. Giovine, V. Stevenson, F. Pourpoint, O. Lafon, M. Osmond, C. Jeanjacques, B. Marcillaud, J. C. Sabroux, T. Loiseau, *Chem. Commun.* **2016**, *52*, 12502.

[173] S. Bordiga, C. Lamberti, G. Ricchiardi, L. Regli, F. Bonino, A. Damin, K. P. Lillerud, M. Bjorgen, A. Zecchina, *Chem. Commun.* **2004**, *5*, 2300.

[174] S. Brunauer, P. H. Emmett, E. Teller, *J. Am. Chem. Soc.* **1938**, *60*, 309.

[175] I. Langmuir, *J. Am. Chem. Soc.* **1916**, *38*, 2221.

[176] M. Thommes, K. Kaneko, A. V. Neimark, J. P. Olivier, F. Rodriguez-Reinoso, J. Rouquerol, K. S. W. Sing, *Pure Appl. Chem.* **2015**, *87*, 1051.

[177] P. Kubelka, F. Munk, *Z. Tech. Phys.* **1931**, *12*, 593.

[178] S. Stoll, A. Schweiger, *J. Magn. Reson.* **2006**, *178*, 42.

[179] J. Jaumot, A. de Juan, R. Tauler, *Chemom. Intell. Lab. Syst.* **2015**, *140*, 1.

[180] S. Sircar, J. R. Hufton, *Adsorption* **2000**, *6*, 137.

[181] A. Fujishima, K. Honda, *Nature* **1972**, *238*, 37.

[182] M. A. Fox, M. T. Dulay, *Chem. Rev.* **1993**, *93*, 341.

[183] A. O. Ibhadon, P. Fitzpatrick, *Catalysts* **2013**, *3*, 189.

[184] F. Fischer, *Renew. Sustain. Energy Rev.* **2018**, *90*, 16.

[185] S. Chu, Y. Wang, Y. Guo, J. Feng, C. Wang, W. Luo, X. Fan, Z. Zou, *ACS Catal.* **2013**, *3*, 912.

[186] L. Jiao, Y. Wang, H. L. Jiang, Q. Xu, *Adv. Mater.* **2018**, *30*, 1.

[187] M. R. Hoffmann, S. T. Martin, W. Choi, D. W. Bahnemann, *Chem. Rev.* **1995**, *95*, 69.

[188] X. Deng, Z. Li, H. García, *Chem. - A Eur. J.* **2017**, *23*, 11189.

[189] R. Asahi, T. Morikawa, T. Ohwaki, K. Aoki, Y. Taga, *Science (80-.).* **2001**, *293*, 269.

[190] C. W. Jones, *JACS Au* **2022**, *2*, 1504.

[191] S. M. Moosavi, A. Nandy, K. M. Jablonka, D. Ongari, J. P. Janet, P. G. Boyd, Y. Lee, B. Smit, H. J. Kulik, *Nat. Commun.* **2020**, *11*, 1.

[192] X. Guo, L. Liu, Y. Xiao, Y. Qi, C. Duan, F. Zhang, *Coord. Chem. Rev.* **2021**, *435*, DOI 10.1016/j.ccr.2021.213785.

[193] R. Elzein, C.-M. Chang, I. Ponomareva, W.-Y. Gao, S. Ma, R. Schlaf, *ACS Appl. Mater. Interfaces* **2016**, *8*, 31403.

[194] H. Hertz, *Ann. Phys.* **1887**, *267*, 983.

[195] M. Planck, *Ann. Phys.* **1901**, *309*, 553.

[196] A. Einstein, *Ann. Phys.* **1905**, *322*, 132.

[197] R. A. Millikan, *Phys. Rev.* **1914**, *4*, 73.

[198] C. A. Mead, W. G. Spitzer, *Phys. Rev. Lett.* **1963**, *10*, 471.

[199] Z. Huang, M. Lee Tang, *J. Phys. Chem. Lett.* **2018**, *9*, 6198.

[200] C. Dette, M. A. Pérez-Osorio, C. S. Kley, P. Punke, C. E. Patrick, P. Jacobson, F. Giustino, S. J. Jung, K. Kern, *Nano Lett.* **2014**, *14*, 6533.

[201] L. M. Yang, G. Y. Fang, J. Ma, E. Ganz, S. S. Han, *Cryst. Growth Des.* **2014**, *14*, 2532.

[202] C. H. Hendon, D. Tiana, M. Fontecave, C. Sanchez, L. D'Arras, C. Sassoye, L. Rozes, C. Mellot-Draznieks, A. Walsh, *J. Am. Chem. Soc.* **2013**, *135*, 10942.

[203] L.-M. Yang, G.-Y. Fang, J. Ma, R. Pushpa, E. Ganz, *Phys. Chem. Chem. Phys.* **2016**, *18*, 32319.

[204] Q. Wang, Q. Gao, A. M. Al-Enizi, A. Nafady, S. Ma, *Inorg. Chem. Front.* **2020**, *7*, 300.

[205] C. J. H. Wort, R. S. Balmer, *Mater. Today* **2008**, *11*, 22.

[206] A. R. Zanatta, *Sci. Rep.* **2019**, *9*, 11225.

[207] V. Sarritzu, N. Sestu, D. Marongiu, X. Chang, Q. Wang, S. Masi, S. Colella, A. Rizzo, A. Gocalinska, E. Pelucchi, M. L. Mercuri, F. Quochi, M. Saba, A. Mura, G. Bongiovanni, *Adv. Opt. Mater.* **2018**, *6*, 1.

[208] G. Wang, C. Robert, M. M. Glazov, F. Cadiz, E. Courtade, T. Amand, D. Lagarde, T. Taniguchi, K. Watanabe, B. Urbaszek, X. Marie, *Phys. Rev. Lett.* **2017**, *119*, 1.

[209] W. Eberhardt, F. J. Himpsel, *Phys. Rev. B* **1980**, *21*, 5572.

[210] C. Kittel, **2005**, pp. 185–219.

[211] Y. P. Varshni, *Phys. status solidi* **1967**, *19*, 459.

[212] R. Soref, B. Bennett, *IEEE J. Quantum Electron.* **1987**, *23*, 123.

[213] S. Zwerdling, B. Lax, L. M. Roth, *Phys. Rev.* **1957**, *108*, 1402.

[214] J. Tauc, R. Grigorovici, A. Vancu, *Phys. status solidi* **1966**, *15*, 627.

[215] N. F. Mott, E. A. Davis, *Philos. Mag.* **1970**, *22*, 903.

[216] J. B. Coulter, D. P. Birnie, *Phys. Status Solidi Basic Res.* **2018**, *255*, 1.

[217] Y. Feng, S. Lin, S. Huang, S. Shrestha, G. Conibeer, *J. Appl. Phys.* **2015**, *117*, DOI 10.1063/1.4916090.

[218] B. D. Viezbicke, S. Patel, B. E. Davis, D. P. Birnie, *Phys. Status Solidi Basic Res.* **2015**, *252*, 1700.

[219] R. López, R. Gómez, *J. Sol-Gel Sci. Technol.* **2012**, *61*, 1.

[220] A. Dolgonos, T. O. Mason, K. R. Poeppelmeier, *J. Solid State Chem.* **2016**, *240*, 43.

[221] M. Meinert, G. Reiss, *J. Phys. Condens. Matter* **2014**, *26*, 115503.

[222] P. Makuła, M. Pacia, W. Macyk, *J. Phys. Chem. Lett.* **2018**, *9*, 6814.

[223] G. D. Cody, B. G. Brooks, B. Abeles, *Sol. Energy Mater.* **1982**, *8*, 231.

[224] P. Bouguer, *Traité d'optique Sur La Gradation de La Lumière*, Guerin And Delatour, Paris, **1852**.

[225] J. H. Lambert, *In Photometria, Sive de Mensura et Gradibus Luminis, Colorum et Umbrae*, Leipzig : W. Engelmann, **1760**.

[226] Beer, *Ann. Phys.* **1852**, *162*, 78.

[227] J. I. Pankove, in (Ed: I. 0-486-60275-3), Dover Publications, New York, **1971**.

[228] R. Vahalová, L. Tichý, M. Vlček, H. Tichá, *Phys. status solidi* **2000**, *181*, 199.

[229] Y. Lee, S. Kim, J. K. Kang, S. M. Cohen, *Chem. Commun.* **2015**, *51*, 5735.

[230] D. Yamashita, Y. Nakajima, A. Ishizaki, M. Uda, *J. Surf. Anal.* **2008**, *14*, 433.

[231] R. J. Davis, M. T. Lloyd, S. R. Ferreira, M. J. Bruzek, S. E. Watkins, L. Lindell, P. Sehati, M. Fahlman, J. E. Anthony, J. W. P. Hsu, *J. Mater. Chem.* **2011**, *21*, 1721.

[232] J. Jasieniak, M. Califano, S. E. Watkins, *ACS Nano* **2011**, *5*, 5888.

[233] P. Kubelka, *J. Opt. Soc. Am.* **1948**, *44*, 330.

[234] R. Alcaraz de la Osa, I. Iparragirre, D. Ortiz, J. M. Saiz, *ChemTexts* **2020**, *6*, DOI 10.1007/s40828-019-0097-0.

[235] H. G. Hecht, *J. Res. Natl. Bur. Stand. Sect. A, Phys. Chem.* **1976**, *80A*, 567.

[236] D. R. Duncan, *Proc. Phys. Soc.* **1940**, *52*, 390.

[237] R. López, R. Gómez, *J. Sol-Gel Sci. Technol.* **2012**, *61*, 1.

[238] T. Burger, J. Kuhn, R. Caps, J. Fricke, *Appl. Spectrosc.* **1997**, *51*, 309.

[239] D. J. Dahm, K. D. Dahm, *Appl. Spectrosc.* **1999**, *53*, 647.

[240] D. J. Dahm, K. D. Dahm, *J. Near Infrared Spectrosc.* **1999**, *7*, 47.

[241] T. Burger, H. J. Ploss, J. Kuhn, S. Ebel, J. Fricke, *Appl. Spectrosc.* **1997**, *51*, 1323.

[242] F. Benford, *J. Opt. Soc. Am.* **1946**, *36*, 524.

[243] G. Pracht, B. Weckler, H. D. Lutz, *Appl. Spectrosc.* **2003**, *57*, 1254.

[244] S. Landi, I. R. Segundo, E. Freitas, M. Vasilevskiy, J. Carneiro, C. J. Tavares, *Solid State Commun.* **2022**, *341*, 1.

[245] D. J. Dahm, K. D. Dahm, *J. Near Infrared Spectrosc.* **2003**, *11*, 479.

[246] M. A. Nasalevich, M. G. Goesten, T. J. Savenije, F. Kapteijn, J. Gascon, *Chem. Commun.* **2013**, *49*, 10575.

[247] L. Shen, R. Liang, M. Luo, F. Jing, L. Wu, *Phys. Chem. Chem. Phys.* **2014**, *17*, 117.

[248] Y. Horiuchi, H. Nishida, *Bunseki Kagaku* **1967**, *16*, 20.

[249] A. S. Yasin, J. Li, N. Wu, T. Musho, *Phys. Chem. Chem. Phys.* **2016**, *18*, 12748.

[250] L. M. Yang, E. Ganz, S. Svelle, M. Tilset, *J. Mater. Chem. C* **2014**, *2*, 7111.

[251] Y. Fu, D. Sun, Y. Chen, R. Huang, Z. Ding, X. Fu, Z. Li, *Angew. Chemie - Int. Ed.* **2012**, *51*, 3364.

[252] V. Barone, M. Casarin, D. Forrer, M. Pavone, M. Sambi, A. Vittadini, *J. Comput. Chem.* **2009**, *30*, 934.

[253] S. N. Kim, J. Kim, H. Y. Kim, H. Y. Cho, W. S. Ahn, *Catal. Today* **2013**, *204*, 85.

[254] M. Cabrero-Antonino, J. Albero, C. García-Vallés, M. Álvaro, S. Navalón, H. García, *Chem. - A Eur. J.* **2020**, *26*, 15682.

[255] P. Karthik, R. Vinoth, P. Zhang, W. Choi, E. Balaraman, B. Neppolian, *ACS Appl. Energy Mater.* **2018**, *1*, 1913.

[256] J. G. Santaclara, M. A. Nasalevich, S. Castellanos, W. H. Evers, F. C. M. Spoor, K. Rock, L. D. A. Siebbeles, F. Kapteijn, F. Grozema, A. Houtepen, J. Gascon, J. Hunger, M. A. Van Der Veen, *ChemSusChem* **2016**, *9*, 388.

[257] M. De Miguel, F. Ragon, T. Devic, C. Serre, P. Horcajada, H. García, *ChemPhysChem* **2012**, *13*, 3651.

[258] Y. Li, Y. Fu, B. Ni, K. Ding, W. Chen, K. Wu, X. Huang, Y. Zhang, *AIP Adv.* **2018**, *8*, DOI 10.1063/1.5021098.

[259] G. Capano, F. Ambrosio, S. Kampouri, K. C. Stylianou, A. Pasquarello, B. Smit, *J. Phys. Chem. C* **2020**, *124*, 4065.

[260] A. Y. Galashev, A. S. Vorob'ev, *J. Solid State Electrochem.* **2018**, *22*, 3383.

[261] K. Hendrickx, D. E. P. Vanpoucke, K. Leus, K. Lejaeghere, A. Van Yperen-De Deyne, V. Van Speybroeck, P. Van Der Voort, K. Hemelsoet, *Inorg. Chem.* **2015**, *54*, 10701.

[262] A. Wang, Y. Zhou, Z. Wang, M. Chen, L. Sun, X. Liu, *RSC Adv.* **2016**, *6*, 3671.

[263] J. Tu, X. Zeng, F. Xu, X. Wu, Y. Tian, X. Hou, Z. Long, *Chem. Commun.* **2017**, *53*, 3361.

[264] J. H. Cavka, S. Jakobsen, U. Olsbye, N. Guillou, C. Lamberti, S. Bordiga, K. P. Lillerud, *J. Am. Chem. Soc.* **2008**, *130*, 13850.

[265] S. Liu, Z. Ren, H. Xu, Y. Xing, X. Jin, G. Ni, Z. Wang, *Mater. Sci. Semicond. Process.* **2022**, *147*, 106708.

[266] X. Zhao, M. Xu, X. Song, X. Liu, W. Zhou, H. Wang, P. Huo, *Inorg. Chem.* **2022**, *61*, 1765.

[267] E. Flage-Larsen, A. Røyset, J. H. Cavka, K. Thorshaug, *J. Phys. Chem. C* **2013**, *117*, 20610.

[268] S. Chavan, J. G. Vitillo, D. Gianolio, O. Zavorotynska, B. Civalleri, S. Jakobsen, M. H. Nilsen, L. Valenzano, C. Lamberti, K. P. Lillerud, S. Bordiga, *Phys. Chem. Chem. Phys.* **2012**, *14*, 1614.

[269] S. Q. Wang, X. Wang, X. Y. Zhang, X. M. Cheng, J. Ma, W. Y. Sun, *ACS Appl. Mater.*

Interfaces **2021**, *13*, 61578.

[270] R. Raciti, R. Bahariqushchi, C. Summonte, A. Aydinli, A. Terrasi, S. Mirabella, *J. Appl. Phys.* **2017**, *121*, 234304.

[271] C. Rotaru, S. Nastase, N. Tomozeiu, *Phys. status solidi* **1999**, *171*, 365.

[272] B. Gu, N. H. Kwong, R. Binder, *Phys. Rev. B* **2013**, *87*, 125301.

[273] B. Jensen, *IEEE J. Quantum Electron.* **1982**, *18*, 1361.

[274] P. Hervé, L. K. J. Vandamme, *Infrared Phys. Technol.* **1994**, *35*, 609.

[275] H. Finkenrath, *Infrared Phys.* **1988**, *28*, 327.

[276] T. S. Moss, *Phys. status solidi* **1985**, *131*, 415.

[277] N. M. Ravindra, P. Ganapathy, J. Choi, *Infrared Phys. Technol.* **2007**, *50*, 21.

[278] D. R. Penn, *Phys. Rev.* **1962**, *128*, 2093.

[279] S. H. Wemple, *J. Chem. Phys.* **1977**, *67*, 2151.

[280] P. George, P. Chowdhury, *Analyst* **2019**, *144*, 3005.

[281] H. A. KRAMERS, *Nature* **1924**, *114*, 310.

[282] R. de L. Kronig, *J. Opt. Soc. Am.* **1926**, *12*, 547.

[283] A. B. Kuzmenko, *Rev. Sci. Instrum.* **2005**, *76*, 83108.

[284] E. Yablonovitch, *J. Opt. Soc. Am. B* **1993**, *10*, 283.

[285] L. Valenzano, B. Civalleri, S. Chavan, S. Bordiga, M. H. Nilsen, S. Jakobsen, K. P. Lillerud, C. Lamberti, *Chem. Mater.* **2011**, *23*, 1700.

[286] S. Jakobsen, D. Gianolio, D. S. Wragg, M. H. Nilsen, H. Emerich, S. Bordiga, C. Lamberti, U. Olsbye, M. Tilset, K. P. Lillerud, *Phys. Rev. B - Condens. Matter Mater. Phys.* **2012**, *86*, 1.

[287] S. M. J. Rogge, P. G. Yot, J. Jacobsen, F. Muniz-Miranda, S. Vandenbrande, J. Gosch, V. Ortiz, I. E. Collings, S. Devautour-Vinot, G. Maurin, N. Stock, V. Van Speybroeck, *ACS Mater. Lett.* **2020**, *2*, 438.

[288] M. H. Beyzavi, R. C. Klet, S. Tussupbayev, J. Borycz, N. A. Vermeulen, C. J. Cramer, J. F. Stoddart, J. T. Hupp, O. K. Farha, *J. Am. Chem. Soc.* **2014**, *136*, 15861.

[289] R. C. Klet, Y. Liu, T. C. Wang, J. T. Hupp, O. K. Farha, *J. Mater. Chem. A* **2016**, *4*, 1479.

[290] V. R. Bakuru, S. R. Churipard, S. P. Maradur, S. B. Kalidindi, *Dalt. Trans.* **2019**, *48*, 843.

[291] R. Wu, X. Qian, K. Zhou, H. Liu, B. Yadian, J. Wei, H. Zhu, Y. Huang, *J. Mater. Chem. A* **2013**, *1*, 14294.

[292] V. Petříček, M. Dušek, L. Palatinus, *Zeitschrift für Krist. - Cryst. Mater.* **2014**, *229*, 345.

[293] R. D. Shannon, *Acta Crystallogr. Sect. A Cryst. physics, diffraction, Theor. Gen. Crystallogr.* **1976**, *32*, 751.

[294] T. Islamoglu, D. Ray, P. Li, M. B. Majewski, I. Akpinar, X. Zhang, C. J. Cramer, L. Gagliardi, O. K. Farha, *Inorg. Chem.* **2018**, *57*, 13246.

[295] N. C. Jeong, J. S. Lee, E. L. Tae, Y. J. Lee, K. B. Yoon, *Angew. Chemie - Int. Ed.* **2008**, *47*, 10128.

[296] K. S. W. Sing, *Pure Appl. Chem.* **1982**, *54*, 2201.

[297] Z. Hu, A. Nalaparaju, Y. Peng, J. Jiang, D. Zhao, *Inorg. Chem.* **2016**, *55*, 1134.

[298] J. Tauc, *Mater. Res. Bull.* **1968**, *3*, 37.

[299] K. I. Hadjiivanov, D. A. Panayotov, M. Y. Mihaylov, E. Z. Ivanova, K. K. Chakarova, S. M. Andonova, N. L. Drenchev, *Chem. Rev.* **2021**, *121*, 1286.

[300] J. M. Gardner, M. Abrahamsson, B. H. Farnum, G. J. Meyer, *J. Am. Chem. Soc.* **2009**, *131*, 16206.

[301] P. Klaboe, *J. Am. Chem. Soc.* **1967**, *89*, 3667.

[302] S. S. Lobanov, J. A. Daly, A. F. Goncharov, X. Chan, S. K. Ghose, H. Zhong, L. Ehm, T. Kim, J. B. Parise, *J. Phys. Chem. A* **2018**, *122*, 6109.

[303] C. Morterra, E. Giamello, L. Orio, M. Volante, *J. Phys. Chem.* **1990**, *94*, 3111.

[304] M. Occhiuzzi, D. Cordischi, R. Dragone, *J. Phys. Chem. B* **2002**, *106*, 12464.

[305] J. L. Mancuso, A. M. Mroz, K. N. Le, C. H. Hendon, *Chem. Rev.* **2020**, *120*, 8641.

[306] A. Santiago Portillo, H. G. Baldoví, M. T. García Fernandez, S. Navalón, P. Atienzar, B. Ferrer, M. Alvaro, H. Garcia, Z. Li, *J. Phys. Chem. C* **2017**, *121*, 7015.

[307] A. Schaate, P. Roy, A. Godt, J. Lippke, F. Waltz, M. Wiebcke, P. Behrens, *Chem. - A Eur. J.* **2011**, *17*, 6643.

[308] F. C. N. Firth, M. W. Gaultois, Y. Wu, J. M. Stratford, D. S. Keeble, C. P. Grey, M. J. Cliffe, *J. Am. Chem. Soc.* **2021**, *143*, 19668.

[309] R. J. Marshall, C. L. Hobday, C. F. Murphie, S. L. Griffin, C. A. Morrison, S. A. Moggach, R. S. Forgan, *J. Mater. Chem. A* **2016**, *4*, 6955.

[310] M. Kaposi, M. Cokoja, C. H. Hutterer, S. A. Hauser, T. Kaposi, F. Klappenberger, A. Pöthig, J. V Barth, W. A. Herrmann, F. E. Kühn, *Dalt. Trans.* **2015**, *44*, 15976.

[311] R. D. Shannon, *Acta Crystallogr. Sect. A Cryst. physics, diffraction, Theor. Gen. Crystallogr.* **1976**, *32*, 751.

[312] I. Goodenough, V. S. D. Devulapalli, W. Xu, M. C. Boyanich, T. Y. Luo, M. De Souza, M. Richard, N. L. Rosi, E. Borguet, *Chem. Mater.* **2021**, *33*, 910.

[313] M. Sen Bishwas, M. Malik, P. Poddar, *New J. Chem.* **2021**, *45*, 7145.

[314] G. C. Shearer, S. Chavan, J. Ethiraj, J. G. Vitillo, S. Svelle, U. Olsbye, C. Lamberti, S. Bordiga, K. P. Lillerud, *Chem. Mater.* **2014**, *26*, 4068.

[315] W. Kiefer, H. J. Bernstein, *J. Raman Spectrosc.* **1973**, *1*, 417.

[316] E. M. Nour, L. H. Chen, J. Laane, *J. Raman Spectrosc.* **1986**, *17*, 467.

[317] D. P. Strommen, K. Nakamoto, *J. Chem. Educ.* **1977**, *54*, 474.

[318] H. A. Benesi, J. H. Hildebrand, *J. Am. Chem. Soc.* **1949**, *71*, 2703.

[319] C. B. Juang, L. Finzi, C. J. Bustamante, *Rev. Sci. Instrum.* **1988**, *59*, 2399.

[320] R. P. Cooney, P. J. Hendra, M. Fleischmann, *J. Raman Spectrosc.* **1977**, *6*, 264.

[321] C. Wang, Y. Wang, R. Ge, X. Song, X. Xing, Q. Jiang, H. Lu, C. Hao, X. Guo, Y. Gao, D. Jiang, *Chem. – A Eur. J.* **2018**, *24*, 585.

[322] P. Klaeboe, *J. Am. Chem. Soc.* **1967**, *89*, 3667.

[323] P. Matousek, N. Everall, D. Littlejohn, A. Nordon, M. Bloomfield, *Appl. Spectrosc.* **2011**, *65*, 724.

[324] A. Piryatinski, S. A. Ivanov, S. Tretiak, V. I. Klimov, *Nano Lett.* **2007**, *7*, 108.

[325] M. E. Portnoi, I. Galbraith, *Phys. Rev. B* **1999**, *60*, 5570.

[326] T. Takagahara, *Phys. Rev. B* **1989**, *39*, 10206.

[327] C. Chen, X. Li, W. Zou, H. Wan, L. Dong, G. Guan, *Appl. Surf. Sci.* **2021**, *553*, 149547.

[328] M. J. Katz, Z. J. Brown, Y. J. Colón, P. W. Siu, K. A. Scheidt, R. Q. Snurr, J. T. Hupp, O. K. Farha, *Chem. Commun.* **2013**, *49*, 9449.

[329] P. George, N. R. Dhabarde, P. Chowdhury, *Mater. Lett.* **2017**, *186*, 151.

[330] Y. Horiuchi, T. Toyao, M. Saito, K. Mochizuki, M. Iwata, H. Higashimura, M. Anpo, M. Matsuoka, *J. Phys. Chem. C* **2012**, *116*, 20848.

[331] P. Yang, Y. Huang, Z. W. Zhang, N. Li, Y. Fan, *Dalt. Trans.* **2020**, *49*, 10052.

[332] M. El-Shahat, A. E. Abdelhamid, R. M. Abdelhameed, *Carbohydr. Polym.* **2020**, *231*, 115742.

[333] T. Ahnfeldt, N. Guillou, D. Gunzelmann, I. Margiolaki, T. Loiseau, G. Férey, J. Senker, N. Stock, *Angew. Chemie - Int. Ed.* **2009**, *48*, 5163.

[334] Y. Sun, Y. Liu, J. Caro, X. Guo, C. Song, Y. Liu, *Angew. Chemie* **2018**, *130*, 16320.

[335] V. Muelas-Ramos, M. J. Sampaio, C. G. Silva, J. Bedia, J. J. Rodriguez, J. L. Faria, C. Belver, *J. Hazard. Mater.* **2021**, *416*, 126199.

[336] X. Zheng, S. Liu, S. Rehman, Z. Li, P. Zhang, *Chem. Eng. J.* **2020**, *389*, 123424.

[337] S. Hu, M. Liu, K. Li, Y. Zuo, A. Zhang, C. Song, G. Zhang, X. Guo, *CrystEngComm* **2014**, *16*, 9645.

[338] H. Yin, J. Wang, Z. Xie, J. Yang, J. Bai, J. Lu, Y. Zhang, D. Yin, J. Y. S. Lin, *Chem. Commun.* **2014**, *50*, 3699.

[339] N. Ahmadpour, M. H. Sayadi, S. Homaeigohar, *RSC Adv.* **2020**, *10*, 29808.

[340] N. A. Rodríguez, A. Savateev, M. A. Grela, D. Dontsova, *ACS Appl. Mater. Interfaces* **2017**, *9*, 22941.

[341] X. Zhong, W. Liang, H. Wang, C. Xue, B. Hu, *J. Hazard. Mater.* **2021**, *407*, 124729.

[342] X. Zhong, W. Liang, H. Wang, C. Xue, B. Hu, *J. Hazard. Mater.* **2021**, *407*, 124729.

[343] S. Schaack, U. Ranieri, P. Depondt, R. Gaal, W. F. Kuhs, A. Falenty, P. Gillet, F. Finocchi, L. E. Bove, *J. Phys. Chem. C* **2018**, *122*, 11159.

[344] X. Chen, X. Peng, L. Jiang, X. Yuan, H. Yu, H. Wang, J. Zhang, Q. Xia, *Chem. Eng. J.* **2020**, *395*, 125080.

[345] A. Von Mankowski, K. Szendrei-Temesi, C. Koschnick, B. V. Lotsch, *Nanoscale Horizons* **2018**, *3*, 383.

[346] H. Wang, X. Yuan, Y. Wu, G. Zeng, X. Chen, L. Leng, Z. Wu, L. Jiang, H. Li, *J. Hazard. Mater.* **2015**, *286*, 187.

[347] J. Zhang, P. Li, X. Zhang, X. Ma, B. Wang, *ACS Appl. Mater. Interfaces* **2020**, *12*, 46057.

[348] R. F. Howe, M. Grätzel, *J. Phys. Chem.* **1987**, *91*, 3906.

[349] M. A. Nasalevich, R. Becker, E. V. Ramos-Fernandez, S. Castellanos, S. L. Veber, M. V. Fedin, F. Kapteijn, J. N. H. Reek, J. I. Van Der Vlugt, J. Gascon, *Energy Environ. Sci.* **2015**, *8*, 364.

[350] E. Carter, A. F. Carley, D. M. Murphy, *J. Phys. Chem. C* **2007**, *111*, 10630.

[351] D. Sun, W. Liu, Y. Fu, Z. Fang, F. Sun, X. Fu, Y. Zhang, Z. Li, *Chem. - A Eur. J.* **2014**, *20*, 4780.

[352] O. I. Micic, Y. Zhang, K. R. Cromack, A. D. Trifunac, M. C. Thurnauer, *J. Phys. Chem.* **1993**, *97*, 7277.

[353] D. C. Hurum, A. G. Agrios, K. A. Gray, T. Rajh, M. C. Thurnauer, *J. Phys. Chem. B* **2003**, *107*, 4545.

[354] S. Furukawa, T. Shishido, K. Teramura, T. Tanaka, *ACS Catal.* **2012**, *2*, 175.

[355] K. Komaguchi, T. Maruoka, H. Nakano, I. Imae, Y. Ooyama, Y. Harima, *J. Phys. Chem. C* **2009**, *113*, 1160.

[356] M. Zeama, M. A. Morsy, M. Abdelnaby, L. Gutiérrez-Arzaluz, O. F. Mohammed, Z. H. Yamani, *Chem. - An Asian J.* **2021**, *16*, 2520.

[357] C. P. Kumar, N. O. Gopal, T. C. Wang, M.-S. Wong, S. C. Ke, *J. Phys. Chem. B* **2006**, *110*, 5223.

[358] R. F. Howe, M. Grätzel, *J. Phys. Chem.* **1985**, *89*, 4495.

[359] P. H. M. Andrade, M. Moreau, N. Henry, M. T. Bakouche, S. Duval, C. Volkringer, T. Loiseau, M. Hureau, A. Moissette, *J. Phys. Chem. C* **2022**, *2*, DOI 10.1021/acs.jpcc.2c08723.

[360] P. H. M. Andrade, H. Ahouari, C. Volkringer, T. Loiseau, H. Vezin, M. Hureau, A. Moissette, *ACS Appl. Mater. Interfaces* **2023**, *15*, 31032.

[361] J. T. Hughes, D. F. Sava, T. M. Nenoff, A. Navrotsky, *J. Am. Chem. Soc.* **2013**, *135*, 16256.

[362] R. Pénélope, L. Campayo, M. Fournier, A. Gossard, A. Grandjean, *J. Nucl. Mater.* **2022**, *563*, DOI 10.1016/j.jnucmat.2022.153635.

[363] D. Banerjee, X. Chen, S. S. Lobanov, A. M. Plonka, X. Chan, J. A. Daly, T. Kim, P. K. Thallapally, J. B. Parise, *ACS Appl. Mater. Interfaces* **2018**, *10*, 10622.

[364] G. Massasso, J. Long, J. Haines, S. Devautour-Vinot, G. Maurin, A. Grandjean, B. Onida, B. Donnadieu, J. Larionova, C. Guérin, Y. Guari, *Inorg. Chem.* **2014**, *53*, 4269.

[365] W. J. Albery, P. N. Bartlett, C. P. Wilde, J. R. Darwent, *J. Am. Chem. Soc.* **1985**, *107*, 1854.

[366] M. Hureau, A. Moissette, A. Legrand, F. Luchez, M. Sliwa, C. Bremard, *J. Phys. Chem. C* **2012**, *116*, 9092.

[367] D. J. Lavrich, S. M. Wetterer, S. L. Bernasek, G. Scoles, *J. Phys. Chem. B* **1998**, *102*, 3456.

[368] D. Rouxel, B. Weber, J. Ehrhardt, A. Thomy, *Tech. L'ingénieur* **2019**, *1*, 1.

[369] The Editors of Encyclopaedia Britannica, "X-ray diffraction," can be found under https://www.britannica.com/science/X-ray-diffraction, **2023**.

[370] "UCCS - Plateau d'analyses par diffraction des Rayons X," can be found under https://uccs.univ-lille.fr/index.php/fr/bienvenue/ressources/2-non-categorise/59-diffraction-x, **2022**.

[371] S. Cherevko, K. J. J. Mayrhofer, in (Ed: K.B.T.-E. of I.C. Wandelt), Elsevier, Oxford, **2018**, pp. 326–335.

[372] Agilent, "ICP-OES Instruments - 5110 ICP-OES," can be found under https://www.agilent.com/en/product/atomic-spectroscopy/inductively-coupled-plasma-optical-emission-spectroscopy-icp-oes/icp-oes-instruments/5110-icp-oes, **2023**.

[373] K. S. W. Sing, D. H. Everett, R. A. W. Haul, L. Moscou, R. A. Pierotti, J. Rouquerol, T. Siemieniewska, *Pure Appl. Chem.* **1985**, *57*, 603.

[374] Micromeritics, "Surface Area," can be found under https://www.micromeritics.com/particle-testing/analytical-testing/surface-area/, **2023**.

[375] Micromeritics, "ASAP 2020 PLUS," can be found under https://www.micromeritics.com/asap-2020-plus/, **2023**.

[376] B. J. Ford, D. C. Joy, S. Bradbury, "scanning electron microscope," can be found under https://www.britannica.com/technology/scanning-electron-microscope, **2023**.

[377] Hitachi High-Tech Corporation, "Schottky Field Emission Scanning Electron Microscope SU5000," can be found under https://www.hitachi-hightech.com/global/en/products/microscopes/sem-tem-stem/fe-sem/su5000.html, **2023**.

[378] Muso, "File:EDX-scheme.svg," can be found under https://commons.wikimedia.org/wiki/File:EDX-scheme.svg, **2023**.

[379] MRI, "Fourier Transform," can be found under https://mriquestions.com/fourier-

transform-ft.html, **2023**.

[380] Fulvio314, "File:ATR path-en.svg," can be found under https://en.wikipedia.org/wiki/File:ATR_path-en.svg, **2013**.

[381] PerkinElmer, "Spectrum Two FT-IR Spectrometer," can be found under https://www.perkinelmer.com.br/product/spectrum-two-ft-ir-sp10-software-l1160000a, **2023**.

[382] Edinburgh Instruments, "What is Raman Spectroscopy?," can be found under https://www.edinst.com/blog/what-is-raman-spectroscopy/, **2023**.

[383] HORIBA Scientific, "LabRAM HR Evolution," can be found under https://www.horiba.com/int/scientific/products/detail/action/show/Product/labram-hr-evolution-1083/, **2023**.

[384] Bruker, "FT-Raman Spectrometer MultiRAM," can be found under https://www.bruker.com/en/products-and-solutions/infrared-and-raman/raman-spectrometers/multiram-ft-raman-spectrometer.html, **2023**.

[385] Shimadzu, "How do you measure relative diffuse reflectance?," can be found under https://www.ssi.shimadzu.com/service-support/faq/relative-diffuse-reflectance/2/index.html, **2023**.

[386] R. Cao, X. Liu, Y. Liu, X. Zhai, T. Cao, A. Wang, J. Qiu, *Food Chem.* **2021**, *342*, 128258.

[387] IPF, "Thermogravimetric Analysis (TGA)," can be found under https://www.ipfdd.de/en/research/institute-of-macromolecular-chemistry/center-macromolecular-structure-analysis/analytical-methods/thermal-analysis/thermogravimetric-analysis-tga/, **2023**.

[388] Creative Biostructure, "Thermal Gravimetric Analysis (TGA)," can be found under https://www.creative-biostructure.com/maghelix^{TM}-thermal-gravimetric-analysis-tga-216.htm, **2023**.

Annexes

1. Characterization Techniques

1.1. X-Ray Diffraction

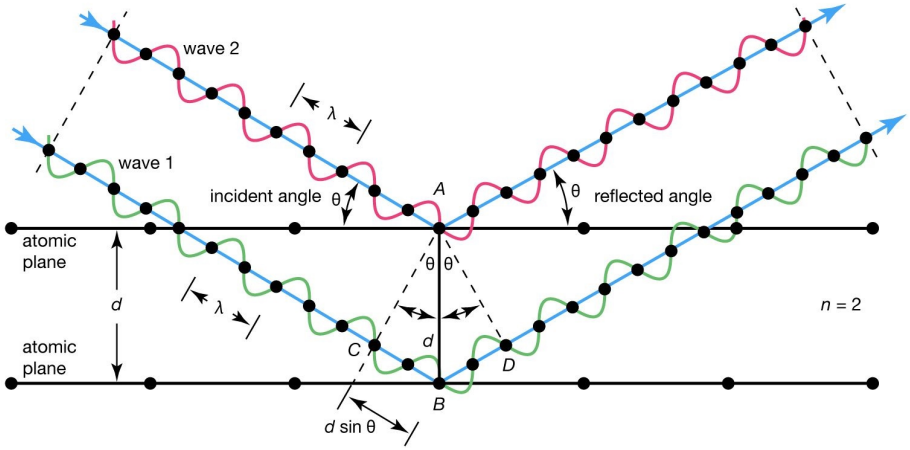

Figure A1: Scheme representing the constructive interference between elastically scattered X-ray beams with wavelength λ in a crystal with interplanar spacing d according to the Bragg's Law $n\lambda = 2d \cdot \text{sen}(\theta)$. Scheme obtained from Ref. [369].

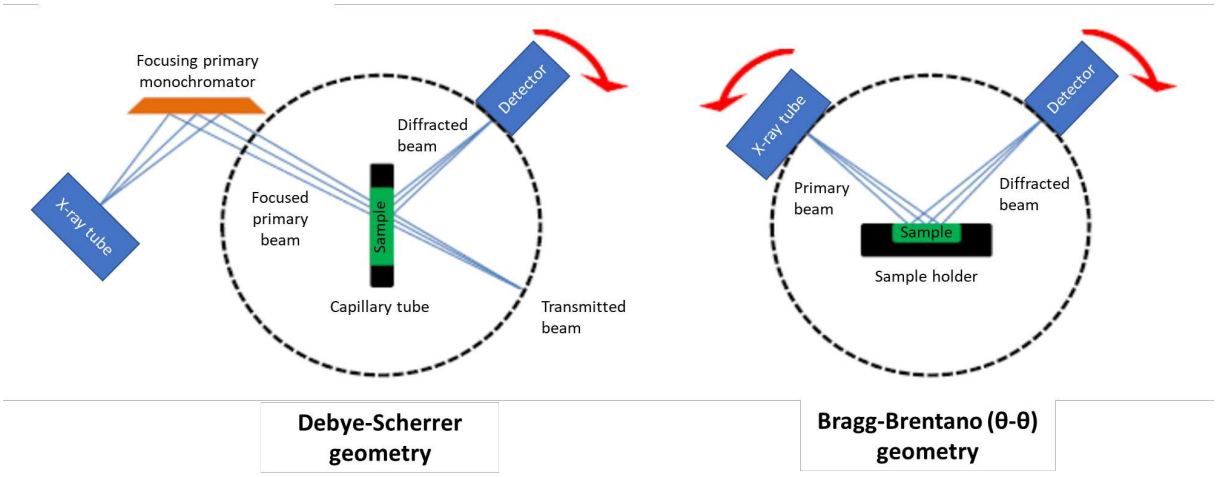

Figure A2: Scheme showing the differences between the Debye-Scherrer and Bragg-Brentano geometries for XRD equipment.

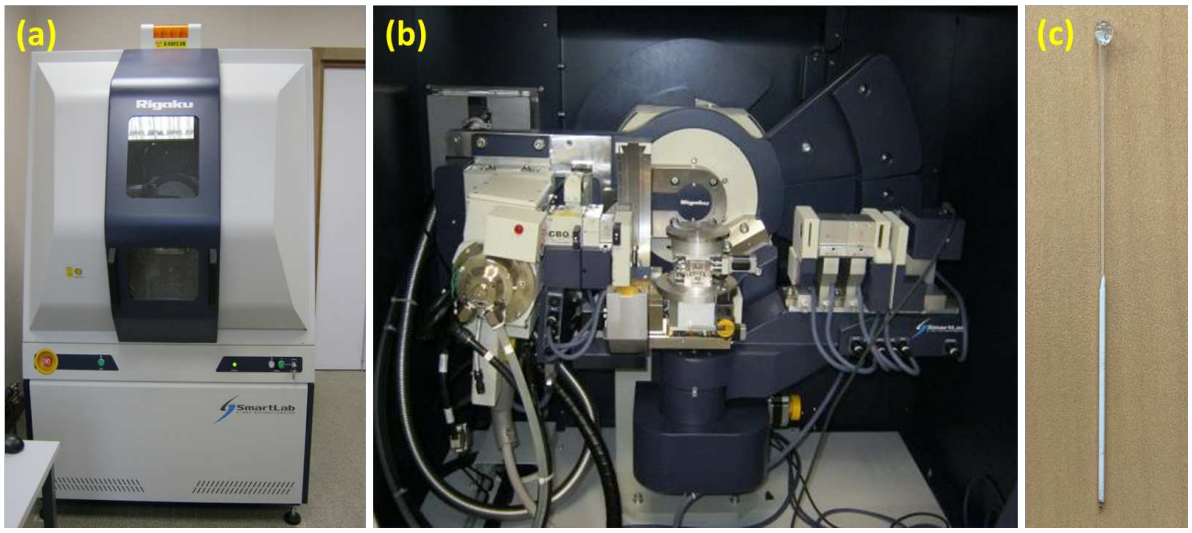

Figure A3: Picture obtained from Ref. [370] showing the (a) external and (b) internal parts of the SmartLab Rigaku diffractometer. (c) capillary filled with UiO-66(Zr) powder.

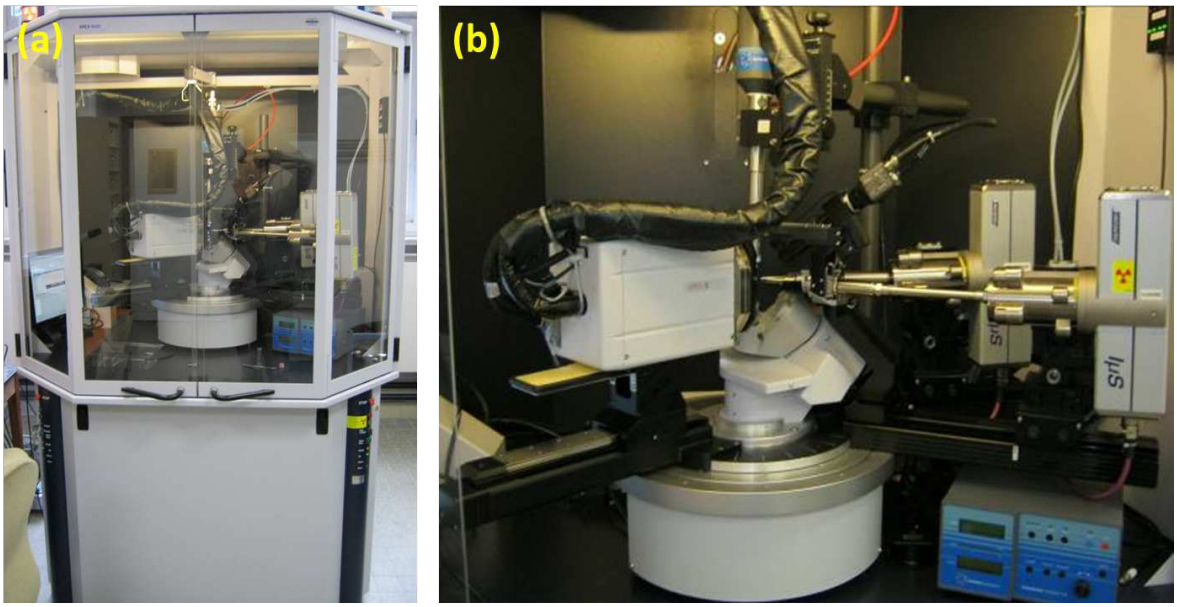

Figure A4: Picture obtained from Ref. [370] showing the (a) external and (b) internal parts of the Bruker DUO-APEX2 diffractometer.

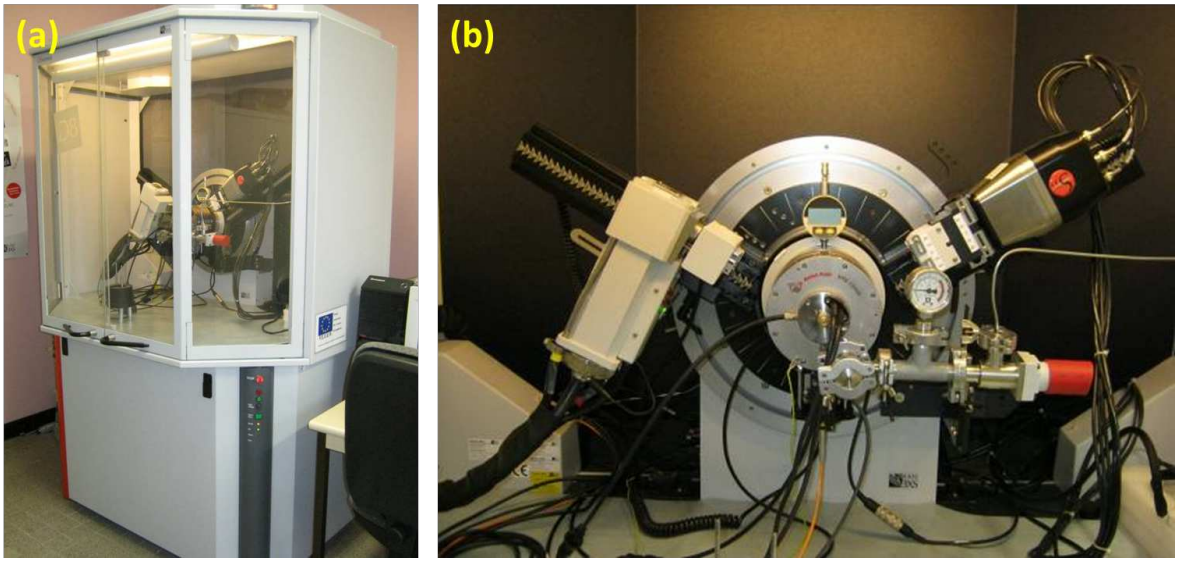

Figure A5: Picture obtained from Ref. [370] showing the (a) external and (b) internal parts of the HTK1200 Bruker diffractometer.

1.2. Inductively Coupled Plasma – Optical Emission Spectroscopy

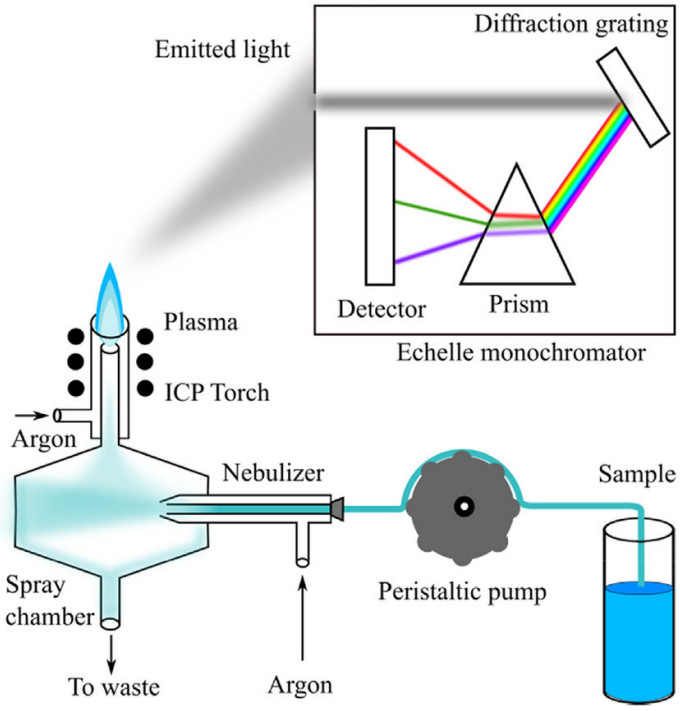

Figure A6: Image obtained from Ref. [371] showing the principle of ICP-OES technique.

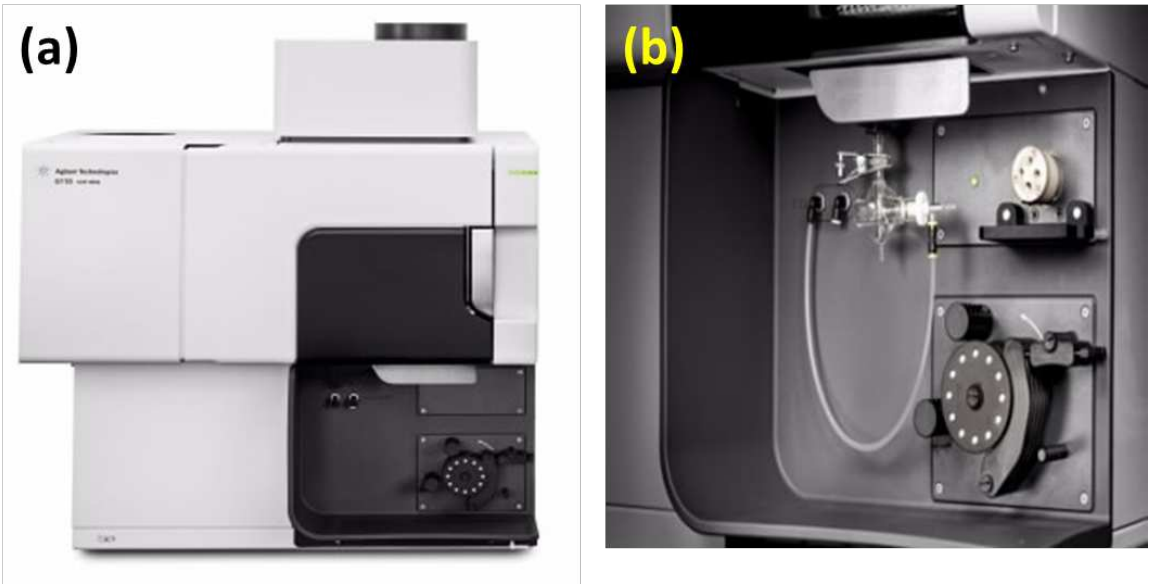

Figure A7: Image obtained from Ref. [372] showing the (a) external and (b) chamber parts of the Agilent 5110 ICP-OES spectrometer.

1.3. N_2 sorption tests

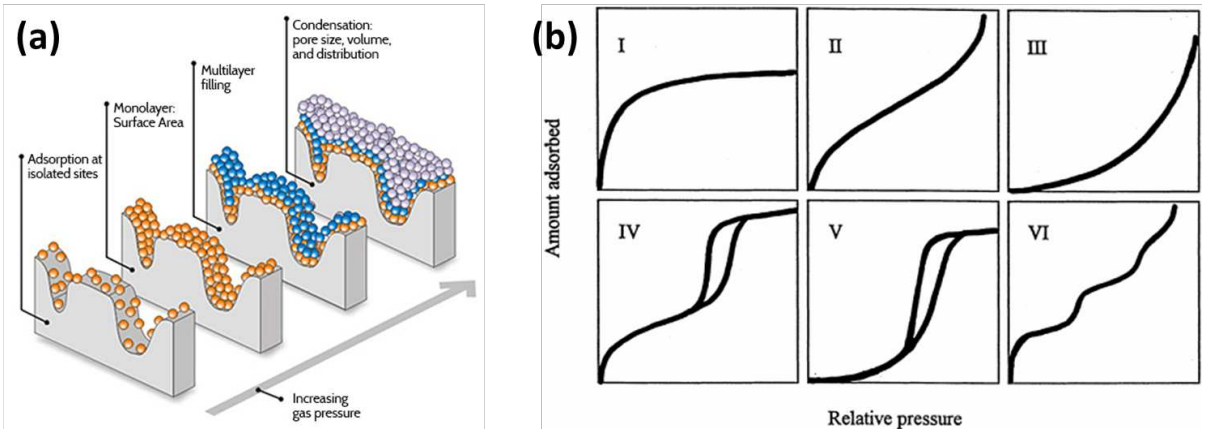

Figure A8: Scheme adapted from Ref. [373,374] showing (a) the principle of physisorption considered by the BET method and (b) the different sorption isotherms according to IUPAC.

Figure A9: Image obtained from Ref. [375] showing the Micromeritics ASAP2020 apparatus used for the nitrogen sorption experiments.

1.4. Scanning Electron Microscopy

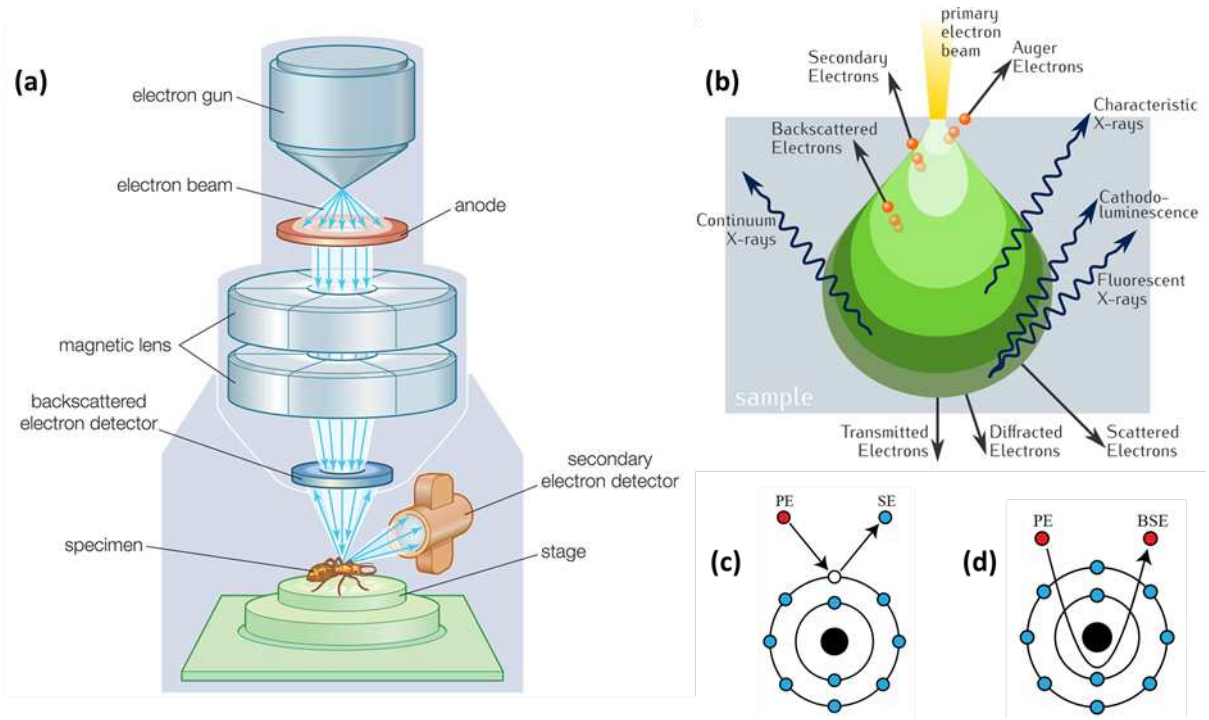

Figure A10: Image obtained from Ref. [376] showing (a) the components of a SEM equipment, (b) the interaction volume between the beam and the sample, and the mechanisms of emission for (c) secondary and (d) backscattered electrons.

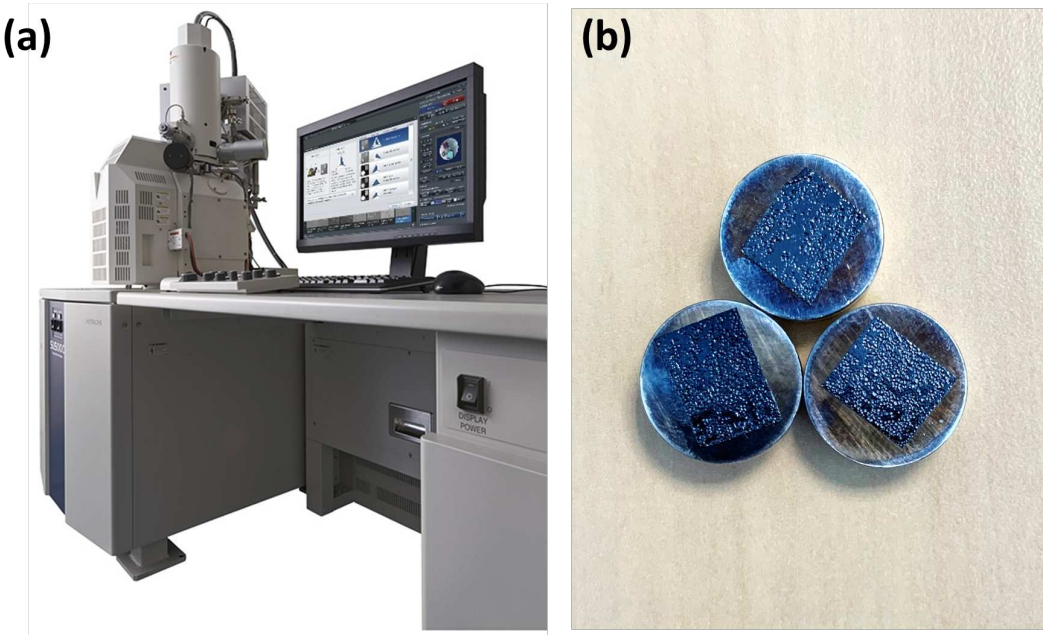

Figure A11: Image obtained from Ref. [377] showing (a) the Hitachi SU 5000 SEM equipment and (b) the prepared MOF samples placed over a carbon tape and sputter-coated with carbon.

1.5. Energy-Dispersive X-ray Spectroscopy

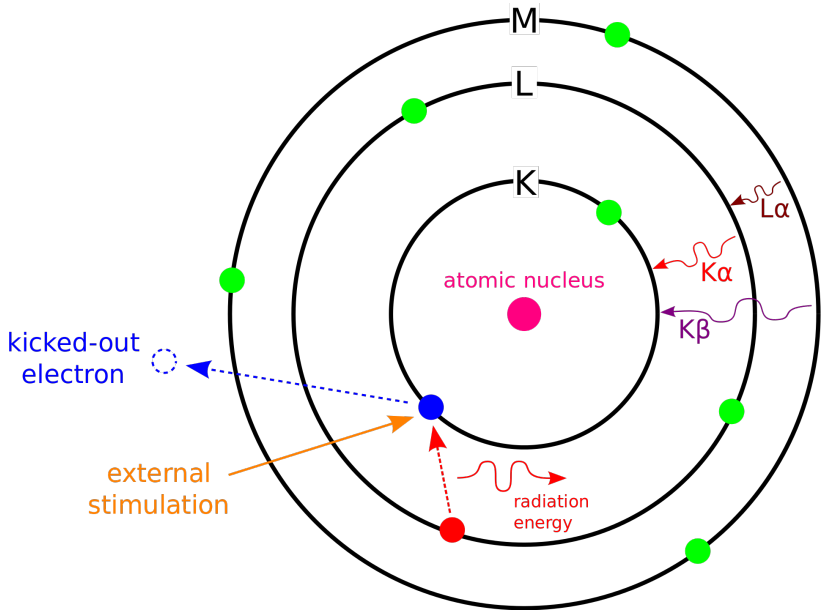

Figure A12: Image obtained from Ref. [378] showing the principle of the EDS spectroscopy.

1.6. Fourier Transform Infrared Spectroscopy

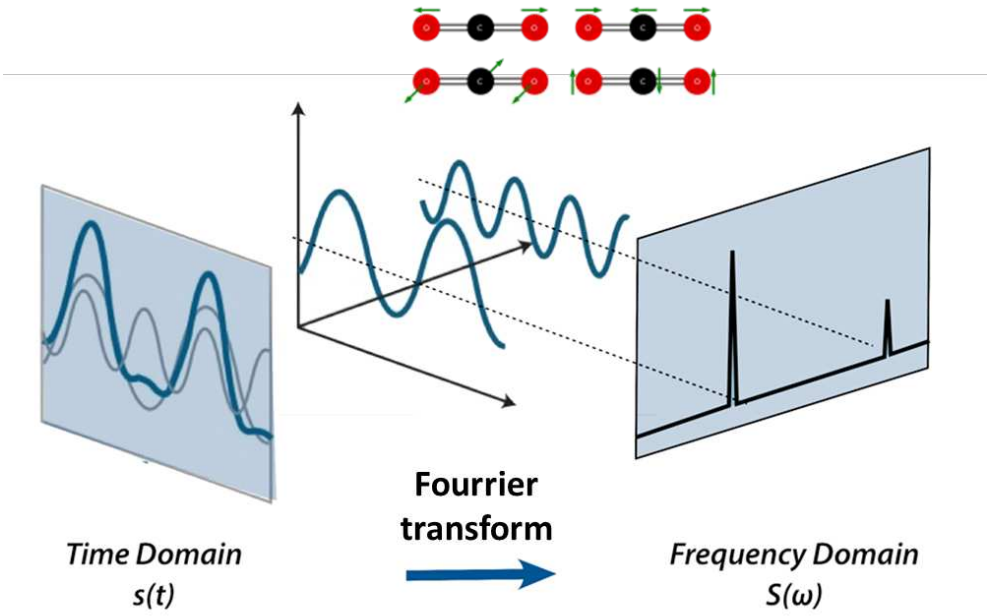

Figure A13: Image adapted from Ref. [379] showing the principle of the FTIR spectroscopy.

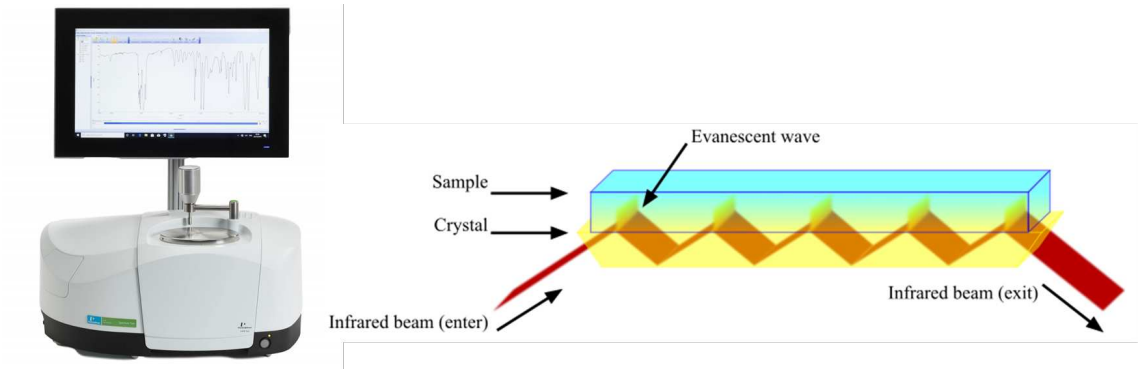

Figure A14: Image adapted from Ref. [380,381] showing the Perkin Elmer Spectrum 2 and the principle of the ATR-FTIR spectroscopy.

1.7. Raman spectroscopy

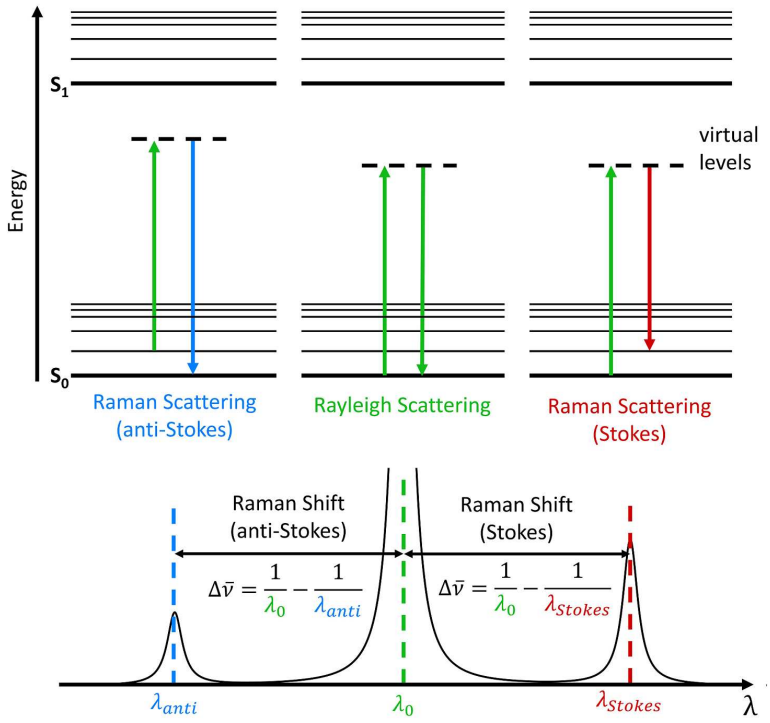

Figure A15: Image obtained from Ref. [382] showing the Jablonski Diagram of the Raman Scattering (anti-Stokes and Stokes) and Rayleigh Scattering phenomena.

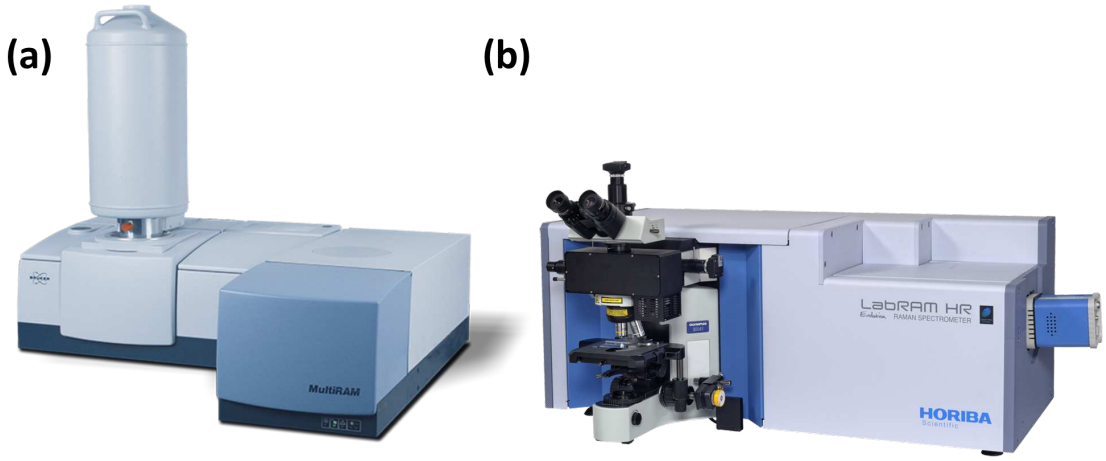

Figure A16: Image obtained from Ref. [383,384] showing (a) the Bruker RFS 100/S FT-Raman spectrometer; (b) the LabRam HR-Evolution (Horiba scientific) microspectrometer.

1.8. Ultraviolet-Visible spectroscopy

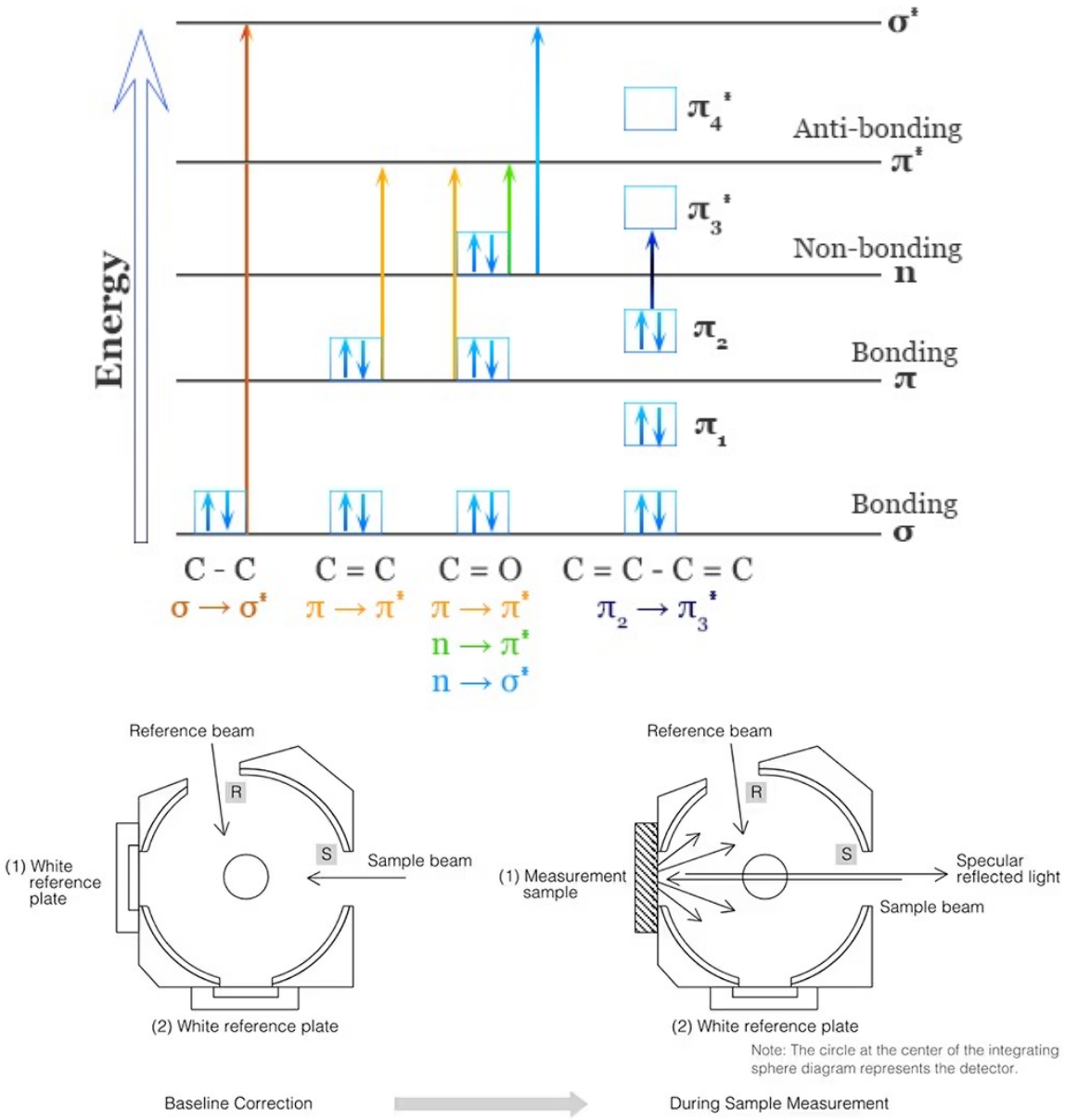

Figure A17: Image obtained from Ref. [385] showing the principle of diffuse reflectance UV-Vis spectroscopy.

1.9. Electron Paramagnetic Resonance spectroscopy

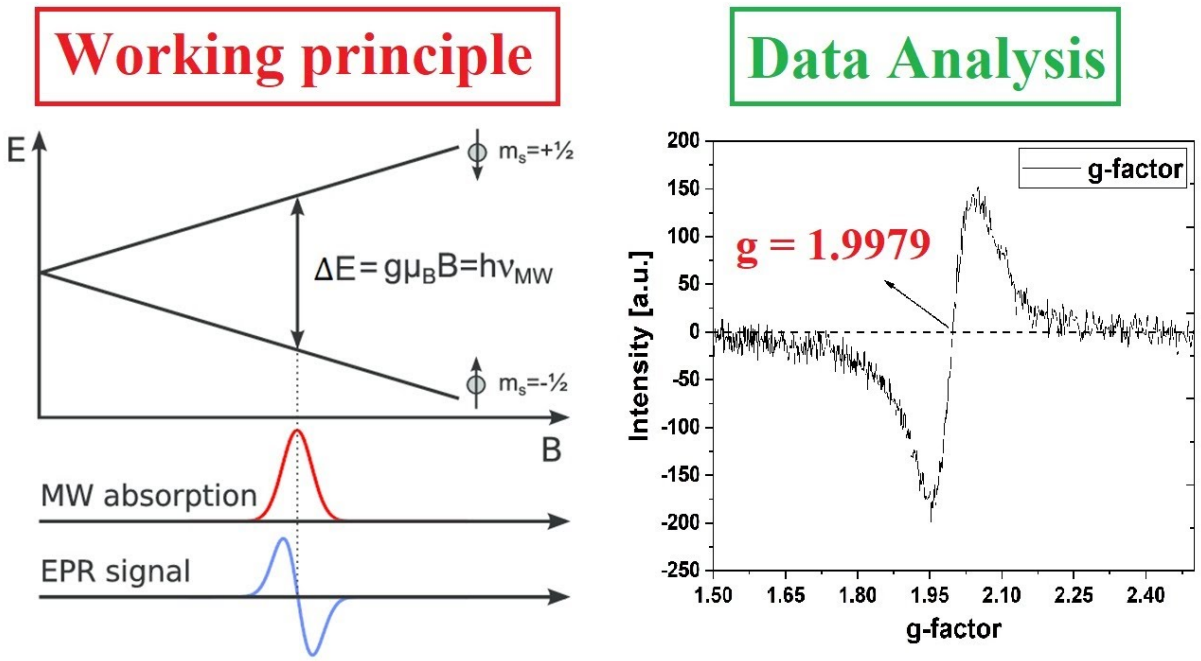

Figure A18: Image obtained from Ref. [385] showing the working principle and the data analysis of Electron Paramagnetic Resonance spectroscopy.

Table A1: Parameters used for the Electron Paramagnetic Resonance spectroscopy experiments.

MOF	Temperature	Microwave power (mW)
UiO-66(Zr,Hf)	RT	5.0
MIL-125(Ti)	RT	5.0
	120 K	1.0
MIL-125(Ti)_NH_2	RT	5.0
	120 K	1.0
CAU-1(Al)_NH_2	RT	2.0
	120 K	5.0
I_2@MIL-125(Ti)	RT	10.0
	120 K	1.0
I_2@MIL-125(Ti)_NH_2	RT	0.5
	120 K	0.5
I_2@CAU-1(Al)_NH_2	RT	2.0
	120 K	5.0

1.10. Nuclear Magnetic Resonance spectroscopy

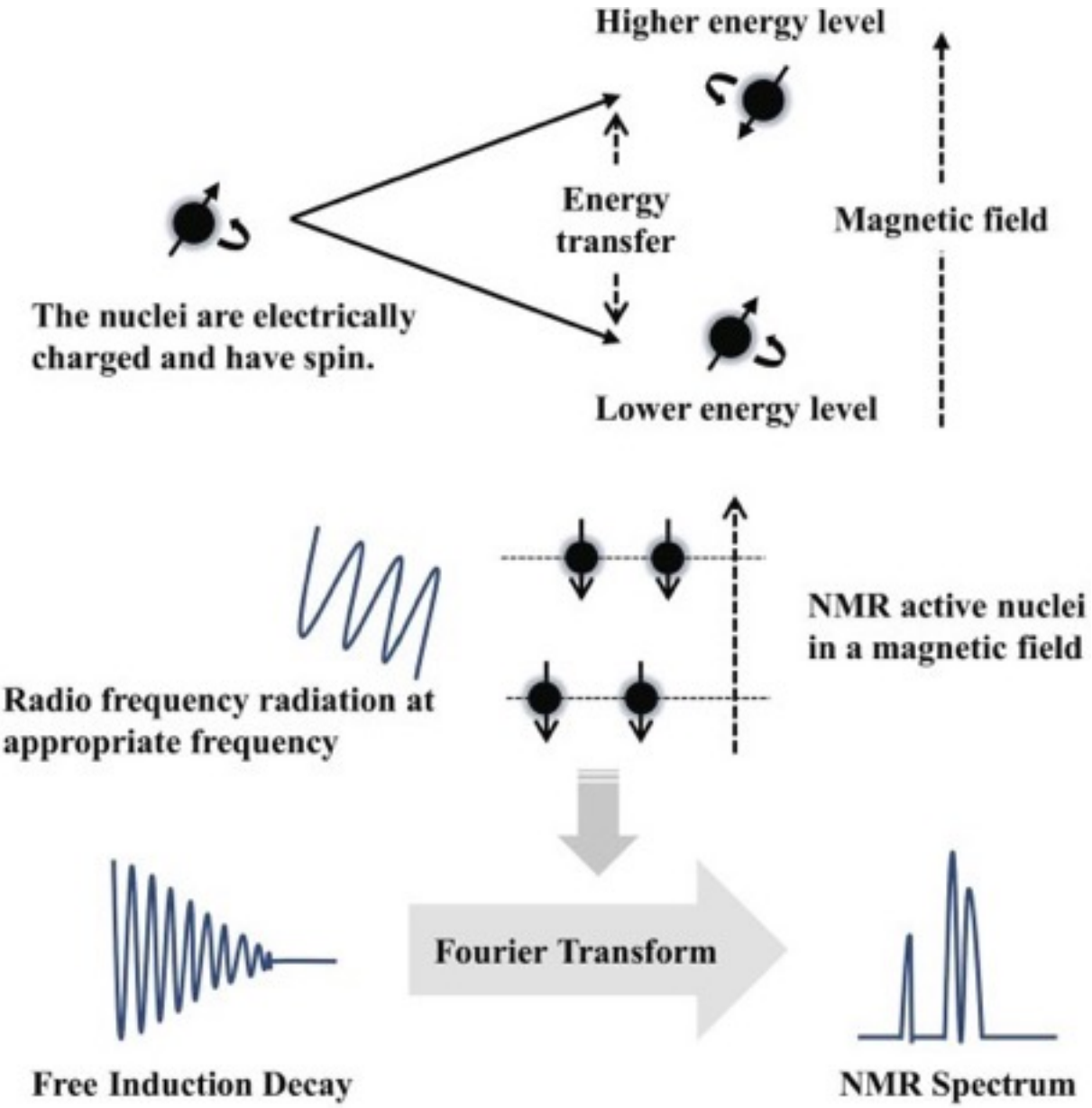

Figure A19: Image obtained from Ref. [386] showing the working principle of Nuclear Magnetic Resonance spectroscopy.

1.11. Thermogravimetric Analysis

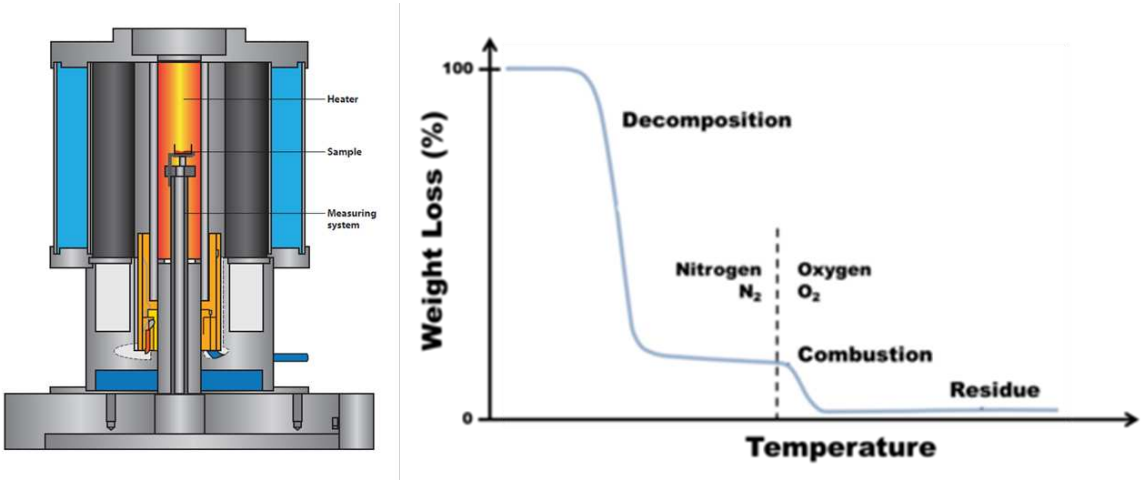

Figure A20: Image adapted from Ref. [387,388] showing the instrumentation and an example of data obtained from Thermogravimetric Analysis measurements.

1.14. Chemometrics

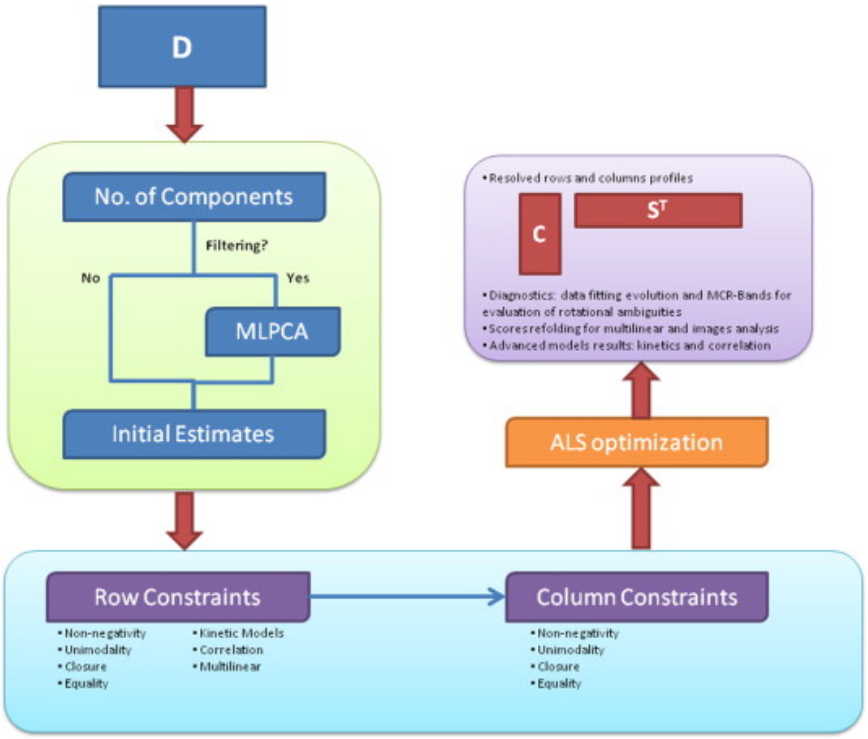

Figure A21: Scheme obtained from Ref. [179] showing the flowchart of the analysis using the MCR-ALS GUI. MLPCA = Maximum Likelihood Principal Component Analysis, ALS = Alternating Least Squares

2. NMR and XRD Data from UiO-67_NH_2 Compounds

Table A2: Chemical formula, mass of product obtained, reaction yield, ^{1}H NMR (300 MHz, $CDCl_3$) data, and ^{13}C NMR (75 MHz, $CDCl_3$) data for the products represented in Figure 2.2 of the thesis manuscript.

Chemical nomenclature	Chemical formula	Molecular weight ($g.mol^{-1}$)	Mass (g)	Yield (%)	^{1}H NMR (300 MHz, $CDCl_3$) (δ ppm)	^{13}C NMR (75 MHz, $CDCl_3$) (δ ppm)
2-nitro-[1,1'-biphenyl]-4,4'-dimethyl-dicarboxylate	$C_{16}H_{13}NO_6$	315.28	2.92	50	8.55 (d, J = 1.6 Hz, 1H); 8.29 (dd, J = 8.0, 1.7 Hz, 1H); 8.15 – 8.08 (m, 2H); 7.54 (d, J = 8.0 Hz, 1H); 7.43 – 7.36 (m, 2H); 4.00 (s, 3H); 3.95 (s, 3H).	166.56; 164.82; 149.10; 141.19; 139.61; 133.22; 132.22; 131.18; 130.64; 130.17; 128.01; 125.61; 52.97; 52.43.
2-amino-[1,1'-biphenyl]-4,4'-dimethyl-dicarboxylate	$C_{16}H_{15}NO_4$	285.30	2.0	76	δ 8.53 (d, J = 1.6 Hz, 1H); 8.27 (dd, J = 8.0, 1.7 Hz, 1H); 8.09 (d, J = 8.4 Hz, 2H); 7.52 (d, J = 8.0 Hz, 1H); 7.42 – 7.34 (m, 2H); 3.95 (d, J = 15.7 Hz, 6H).	167.15; 166.88; 143.66; 143.52; 130.90; 130.64; 130.48; 130.37; 129.61; 129.01; 119.86; 116.82; 52.36; 52.25.
2-amino-[1,1'-biphenyl]-4,4'-dicarboxylic acid	$C_{14}H_{11}NO_4$	257.25	1.65	82	8.55 (d, J = 1.6 Hz, 1H); 8.29 (dd, J = 8.0, 1.7 Hz, 1H); 8.15 – 8.08 (m, 2H); 7.54 (d, J = 8.0 Hz, 1H); 7.43 – 7.36 (m, 2H); 4.00 (s, 3H); 3.95 (s, 3H).	166.56; 164.82; 149.10; 141.19; 139.61; 133.22; 132.22; 131.18; 130.64; 130.17; 128.01; 125.61; 52.97; 52.43.

Table A3: Crystallography data and refinement parameters of UiO-67_NH_2 compounds.

	UiO-67(Zr)_NH_2	UiO-67(Zr/Hf)_NH_2	UiO-67(Hf)_NH_2
Empirical formula	$Zr_6O_{32}C_{84}N_6H_{42}$	$Hf_{3.24}Zr_{2.76}O_{32}C_{84}N_6H_{42}$	$Hf_6O_{32}C_{84}N_6H_{42}$
Formula weight ($g.mol^{-1}$)	2194.6	2476.5	2718.2
Temperature (K)	293	293	293
Crystal system	Cubic	Cubic	Cubic
Space group	F m -3 m (225)	F m -3 m (225)	F m -3 m (225)
Lattice parameter *a* (Å)	26.786(2)	26.7376(6)	26.723(2)
Lattice volume ($Å^3$)	19219(2)	19114.7(7)	19.082(2)
Z	4	4	4
Calculated density ($g.cm^{-3}$)	0.7584	0.8605	0.9462
μ (mm^{-1})	0.353	1.934	3.29
F(000)	4336	4749	5104
Crystal size (mm^3)	0.111 x 0.078 x 0.07	0.28 x 0.14 x 0.12	0.17 x 0.11 x 0.10
Radiation (Å)	0.71073 (Mo K_α)	0.71073 (Mo K_α)	0.71073 (Mo K_α)
Pattern range (2θ)	4.3 – 52.7	4.3 – 67.6	4.3 – 52.7
Index ranges	$-33 \leq h \leq 32$; $-33 \leq k \leq 33$; $-33 \leq l \leq 33$	$-40 \leq h \leq 41$; $-41 \leq k \leq 41$; $-41 \leq l \leq 35$	$-33 \leq h \leq 33$; $-33 \leq k \leq 32$; $-23 \leq l \leq 33$
Reflections collected	36264	51527	26601
Independent reflections	1041 [R_{int} = 0.1417; R_{sigma} = 0.0411]	1944 [R_{int} = 0.0867; R_{sigma} = 0.0242]	1040 [R_{int} = 0.1764; R_{sigma} = 0.0572]
Nº of constraints	9	12	9
Nº of parameters	38	37	37
Nº of independent atoms	11	12	11
Goodness-of-fit on F^2	3.84	4.54	2.43
Final R indexes [$I \geq 3\sigma$ (I)]	R_1 = 0.0588; wR_2 = 0.0975	R_1 = 0.0450; wR_2 = 0.0878	R_1 = 0.0483; wR_2 = 0.0752
Final R indexes [all data]	R_1 = 0.0727; wR_2 = 0.0982	R_1 = 0.0638; wR_2 = 0.0881	R_1 = 0.0653; wR_2 = 0.0771
Largest diffraction peak/hole (e $Å^{-3}$)	1.36/-0.55	2.44/-1.68	1.84/-1.29

Table A4: Selected distances for UiO-67_NH_2 compounds.

Atoms 1—2	Distances (Å)		
	UiO-67(Zr)_NH_2	UiO-67(Zr/Hf)_NH_2	UiO-67(Hf)_NH_2
M1—M1 [a]	N.C.	0	N.C.
M1—O2 [a]	2.128(7)	2.121(8)	2.137(14)
M1—O2^{i} [a]	2.128(7)	2.121(8)	2.137(14)
M1—O2^{ii} [a]	2.128(7)	2.121(8)	2.137(14)
M1—O2^{iii} [a]	2.128(7)	2.121(8)	2.137(14)
M1—O11 [a]	2.221(5)	2.204(5)	2.206(9)
O11—C1	1.262(9)	1.256(8)	1.273(17)
C1—C2	1.495(10)	1.511(10)	1.43(2)
C2—C3	1.257(14)	1.319(14)	1.31(2)
C2—C3^{ii}	1.257(14)	1.319(14)	1.31(2)
C3—C4	1.419(19)	1.457(19)	1.39(3)
C5—C4	1.257(16)	1.253(17)	1.29(3)
C5—C5^{iv}	1.423(12)	1.359(12)	1.35(2)
C5—C4^{ii}	1.257(16)	1.253(17)	1.29(3)
C3—H1c3	0.96	0.96	0.96
C4—H1c4	0.96	0.96	0.96
C4—N1c4	1.4	1.4	1.4
N1c4—H1c4	0.44	0.44	0.44
N1c4—N1c4^{v}	1.5044	1.3902	N.C.

[a]: M = Zr, Hf/Zr, Hf ; (i) x, -y, -z; (ii) 0.5-y, 0.5-x, -z; (iii) 0.5-y, -0.5+x, z; (iv) 0.5-x, 0.5-y, z; (v) y, x, -z; (vi) 0.5+z, 0.5-x, -y; (vii) 0.5-y, z, 0.5-x ; N.C. = Non Calculated.

Table A5: Selected angles for UiO-67_NH_2 compounds.

Atoms 1—2—3	Angle (º)		
	UiO-67(Zr)_NH_2	UiO-67(Zr/Hf)_NH_2	UiO-67(Hf)_NH_2
M1—M1—O2 [a]	N.C.	0	N.C.
M1—M1—O2^{i} [a]	N.C.	0	N.C.
M1—M1—O2^{ii} [a]	N.C.	0	N.C.
M1—M1—O2^{iii} [a]	N.C.	0	N.C.
M1—O2—M1 [a]	N.C.	0	N.C.
M1^{vii}—O2—M1^{vii} [a]	110.9(3)	0	N.C.
M1^{vi}—O2—M1^{vi} [a]	N.C.	0	N.C.
M1—O2—M1^{vi} [a]	110.9(3)	110.8(4)	N.C.
M1—O2—M1^{vii} [a]	110.9(3)	110.8(4)	N.C.
M1^{vi}—O2—M1^{vii} [a]	N.C.	110.8(4)	N.C.
O2—M1—O2^{i} [a]	106.6(3)	106.7(3)	N.C.
O2—M1—O2^{ii} [a]	69.1(3)	69.1(3)	N.C.
O2—M1—O2^{iii} [a]	69.1(3)	69.1(3)	N.C.
O2^{i}—M1—O2^{ii} [a]	69.1(3)	69.1(3)	N.C.
O2^{i}—M1—O2^{iii} [a]	69.1(3)	69.1(3)	N.C.
O2^{ii}—M1—O2^{iii} [a]	106.6(3)	106.7(3)	N.C.
C1—C2—C3	123.4(9)	120.9(8)	122.8(15)
C1—C2—C3^{ii}	123.4(9)	120.9(8)	122.8(15)
C2—C3—C4	123.1(12)	117.0(11)	120.1(19)
C3—C2—C3^{ii}	113.2(10)	118.2(10)	114.4(17)
C4—C5—C4^{ii}	112.2(11)	111.0(11)	106.9(19)
C5—C4—C3	124.2(13)	128.4(12)	129(2)
C5^{iv}—C5—C4	123.9(10)	124.5(10)	126.5(18)
C5^{iv}—C5—C4^{ii}	123.9(10)	124.5(10)	126.5(18)
O11—C1—O11^{ii}	126.6(7)	126.7(6)	122.6(13)
O11—C1—C2	116.7(6)	116.6(6)	118.7(13)
O11^{ii}—C1—C2	116.7(6)	116.6(6)	118.7(13)
C2—C3—H1c3	118.438	121.522	119.944
C3—C4—H1c4	117.92	115.783	115.4
C4—C3—H1c3	118.435	121.521	119.943
C5—C4—H1c4	117.918	115.784	115.399
C3—C4—N1c4	117.92	115.784	115.4
C5—C4—N1c4	117.918	115.783	115.4
C4—N1c4—N1c4^{v}	118.171	119.711	N.C.
C4—N1c4—H1c4	0	0	0
C4—H1c4—N1c4	180	180	180
N1c4—C4—H1c4	0	0	0
N1c4^{v}—N1c4—H1c4	118.17	119.712	N.C.

[a]: M = Zr, Hf/Zr, Hf ; (i) x, -y, -z; (ii) 0.5-y, 0.5-x, -z; (iii) 0.5-y, -0.5+x, z; (iv) 0.5-x, 0.5-y, z; (v) y, x, -z; (vi) 0.5+z, 0.5-x, -y; (vii) 0.5-y, z, 0.5-x ; N.C. = Non Calculated

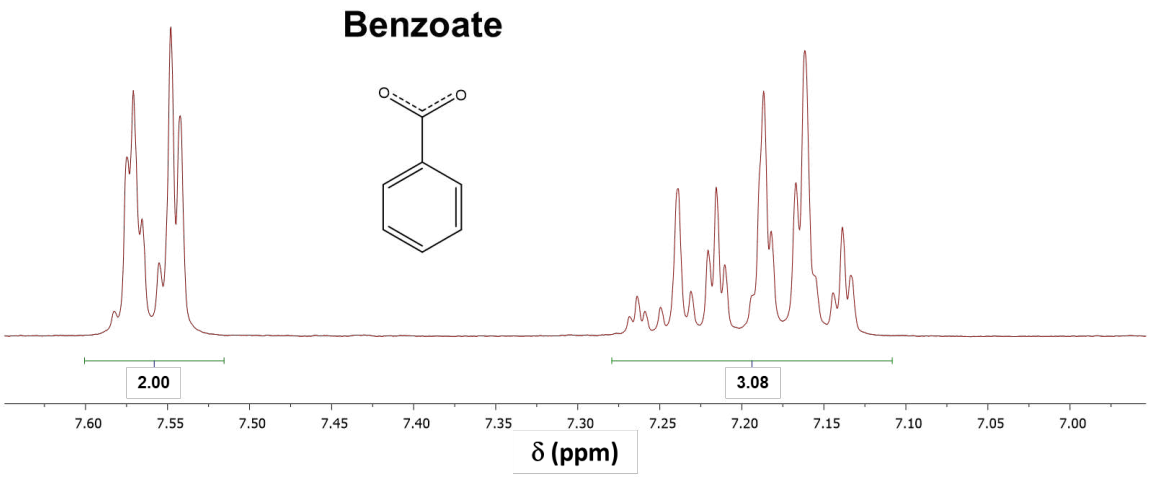

Figure A22: ^{1}H NMR spectra of the benzoate in NaOD solution. The integral values for each signal are displayed on the bottom part of the graphic.

3. Band gap evaluation

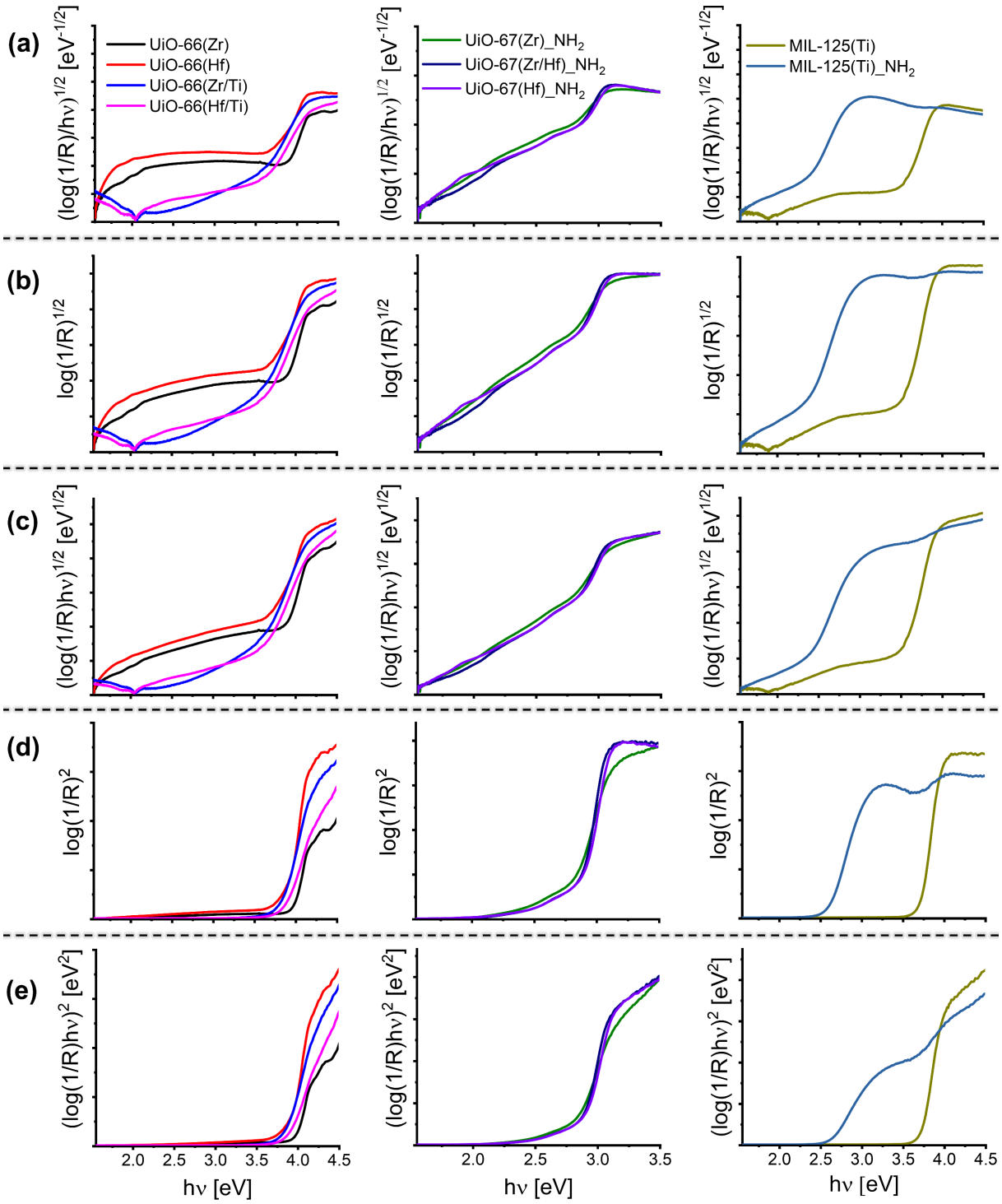

Figure A23: Band gap energies assessment using the log(1/R) function for UiO-66, UiO-67_NH_2, and MIL-125 materials. (a) Cody band gap; (b) indirect band gap; (c) Tauc indirect band gap; (d) direct band gap; (e) Tauc direct band gap.

Table A6: Band gap values assessed through the plot of R, log(1/R), $(\log(1/R)/h\nu)^{1/2}$, $\log(1/R)^{1/2}$, $(\log(1/R)h\nu)^{1/2}$, $\log(1/R)^2$, and $(\log(1/R)h\nu)^2$ against the photon energy hν.

Method	UiO-66				UiO-67_NH_2			MIL-125	
	Zr	Hf	Zr/Ti	Hf/Ti	Zr	Zr/Hf	Hf	H	NH_2
R	4.20	4.14	4.09	3.97	3.08	3.04	3.08	3.88	3.00
log(1/R)	3.88	3.79	3.67	3.71	2.81	2.76	2.76	3.63	2.47
$(\log(1/R)/h\nu)^{1/2}$	3.95	3.83	3.66	3.64	2.86	2.88	2.89	3.55	2.43
$\log(1/R)^{1/2}$	3.94	3.82	3.66	3.68	2.82	2.87	2.92	3.56	2.43
$(\log(1/R)h\nu)^{1/2}$	3.95	3.81	3.68	3.67	2.83	2.88	2.89	3.60	2.45
$\log(1/R)^2$	4.00	3.96	3.83	3.88	2.80	2.87	2.88	3.73	2.62
$(\log(1/R)h\nu)^2$	4.00	3.95	3.85	3.90	2.82	2.98	2.89	3.75	2.63

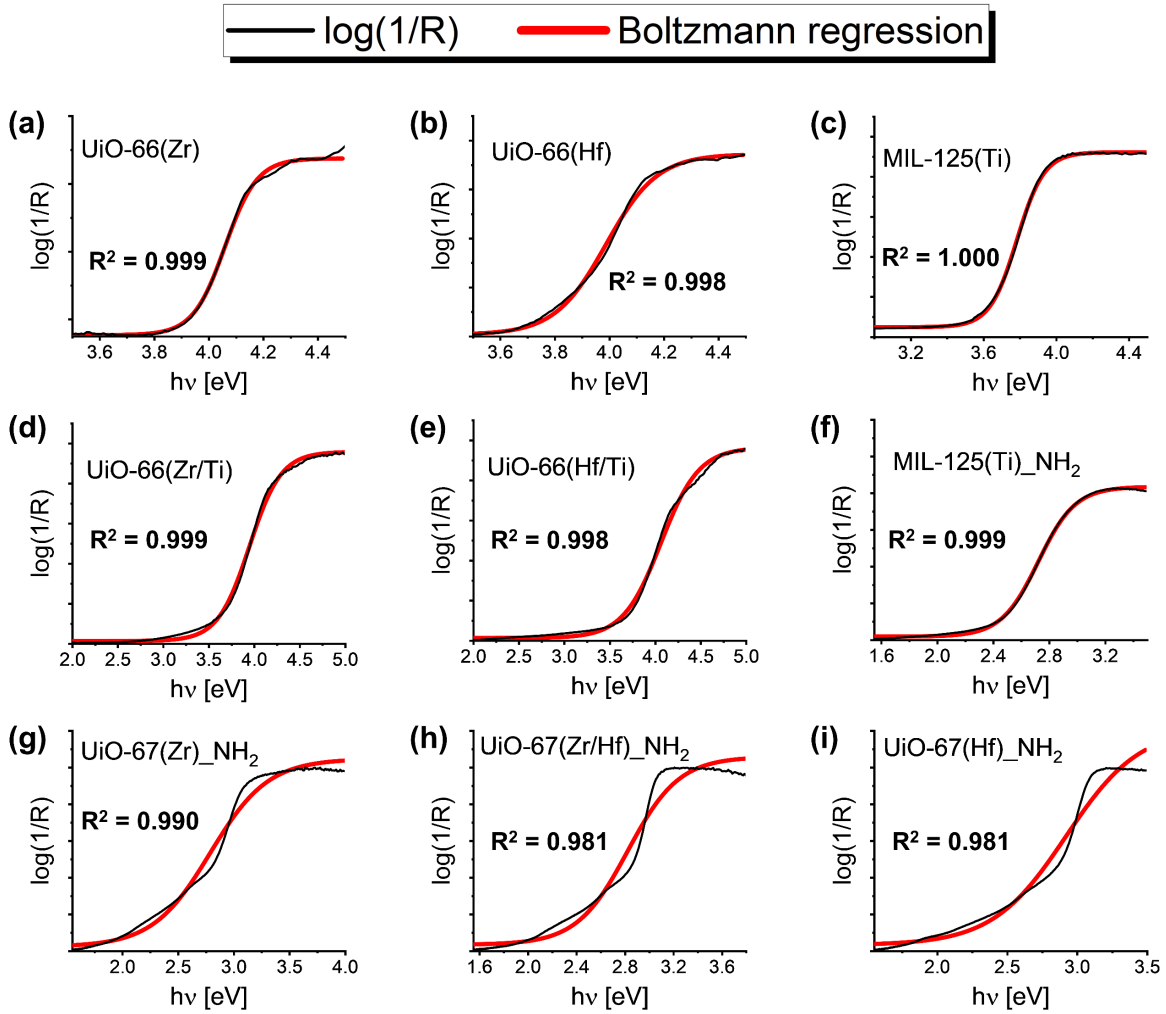

Figure A24: Optical band gap energies calculated using the Boltzmann regression according to the Equation (3.17) by means of the *log(1/R)* data for (a) UiO-66(Zr), (b) UiO-66(Hf), (c) MIL-125(Ti), (d) UiO-66(Zr/Ti), (e) UiO-66(Hf/Ti), (f) MIL-125(Ti)_NH_2, (g) UiO-67(Zr)_NH_2, (h) UiO-67(Zr/Hf)_NH_2, and (i) UiO-67(Hf)_NH_2. The black lines represent the *log(1/R)* data obtained for the MOFs and the red lines are the Boltzmann regression.

Table A7: Band gap energies calculated from Equation (3.18) considering the E_0^{Boltz} values obtained from *log(1/R)* data and using $n_{dir}^{Boltz} \approx 0.9$ and $n_{ind}^{Boltz} \approx 3.5$.

Method	UiO-66				UiO-67_NH_2			MIL-125	
	Zr	Hf	Zr/Ti	Hf/Ti	Zr	Zr/Hf	Hf	H	NH_2
E_0^{Boltz}	4.11	3.99	3.95	4.07	2.79	2.83	2.92	3.79	2.72
δE	0.059	0.094	0.174	0.209	0.260	0.211	0.264	0.075	0.133
$E_{g(dir)}^{Boltz}$	4.06	3.91	3.79	3.88	2.56	2.64	2.68	3.72	2.60
$E_{g(ind)}^{Boltz}$	3.90	3.66	3.34	3.34	1.88	2.09	2.00	3.53	2.25

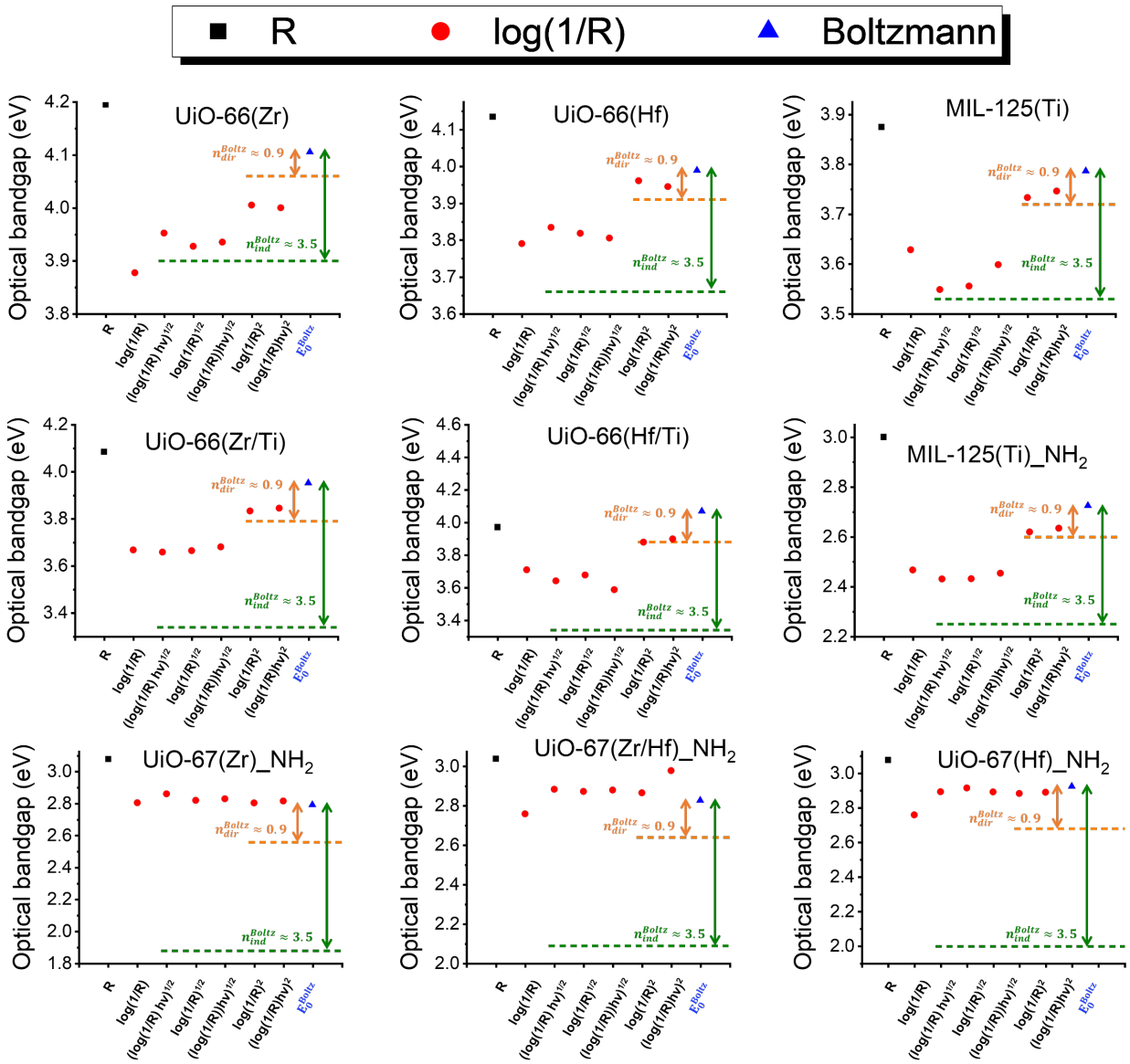

Figure A25: Optical band gap energies obtained using different methods: extrapolation of the reflectance curve (R), extrapolation of the log(1/R) curve F(R), Cody's band gap $[\log(1/R)/hv)^{1/2}]$, indirect band gap $[\log(1/R)^{1/2}]$, Tauc indirect band gap $[\log(1/R)hv)^{1/2}]$, direct band gap $[\log(1/R)^2]$, Tauc direct band gap $[\log(1/R)hv)^2]$, and Boltzmann fit of the log(1/R) spectra E_0^{Boltz}. The horizontal lines represent values obtained for the $E_{g(dir)}^{Boltz}$ (orange) and for the $E_{g(ind)}^{Boltz}$ (green) when considering $n_{dir}^{Boltz} = 0.9$ and $n_{ind}^{Boltz} = 3.5$, respectively.

Résumé :

Ce travail décrit les synthèses et les propriétés de trois familles de matériaux de type MOF (UiO-6*x*, MIL-125, CAU-1) utilisées pour capturer des molécules d'iode. Une première étude porte sur les complexes de transfert de charge entre les molécules d'iode et les MOFs, et a révélé que les composés UiO-66 à base d'hafnium présentaient une meilleure absorption et transformation de l'iode en I_3^-. Dans ce cas, un mécanisme impliquant un transfert d'électrons du ligand organique vers l'iode a été proposé. En utilisant des monocristaux de UiO-67(Zr,Hf)_NH_2 et en tirant parti de l'effet de résonance Raman, la plus grande stabilité de l'espèce I_3^- a été mise en évidence par la réalisation de cartographies Raman. Il a été démontré que la taille des cristaux affecte de manière significative la cinétique d'adsorption de l'iode. Par rapport à leur analogue structurel à base d'aluminium, les MOFs MIL-125(Ti) et MIL-125(Ti)_NH_2 présentent une cinétique d'adsorption de l'iode plus rapide en raison d'une séparation plus efficace des charges. Dans ce cas, les expériences de désorption thermique ont montré la stabilité des espèces I_3^-, en particulier en présence de groupes $–NH_2$. De plus, contrairement à ce qui est observé pour les MOF à base de zirconium et d'hafnium, l'influence du titane dans le mécanisme d'adsorption et de réduction de I_2 est mise en évidence par un changement de l'état d'oxydation des cations Ti^{4+}. L'énergie de la bande interdite des matériaux MOF ayant un effet sur les complexes de transfert de charge impliqués dans le mécanisme de réaction pour différents systèmes I_2@MOF, une combinaison de méthodologies a été proposée pour déterminer les énergies et les types de bande interdite en utilisant uniquement des données obtenues par spectroscopie UV-Vis en réflexion diffuse. L'étude souligne comment le confinement dans des matériaux poreux peut modifier les propriétés et les mécanismes de stabilisation, influençant l'adsorption et la réactivité.

Mots clés : MOFs, Iode, Spectroscopie, Bande interdite, Adsorption

Abstract:

This work describes the synthesis and properties of three families of MOF materials (UiO-6*x*, MIL-125, CAU-1) used to trap iodine molecules. A first study investigates charge transfer complexes between iodine molecules and MOF frameworks upon adsorption, finding that hafnium-based UiO-66 compounds showed enhanced iodine uptake and transformation into I_3^-. In this case, a mechanism involving electron transfer from the organic linker to iodine was proposed. Using single crystals of UiO-67(Zr,Hf)_NH_2 and taking advantage of Raman resonance effect, the higher stability of the I_3^- species was put forward by performing Raman mapping. Crystal size was shown to significantly affect iodine adsorption kinetics. In comparison to their aluminum-based structural analogue, MIL-125(Ti) and MIL-125(Ti)_NH_2 MOFs demonstrated faster iodine adsorption kinetics due to efficient charge separation. In this case, thermal desorption experiments showed the stability of I_3^- species, particularly in the presence of $–NH_2$ groups. Moreover, contrary to what is observed for zirconium and hafnium-based MOFs, the influence of titanium in the adsorption and reduction mechanism of I_2 is highlighted through a change of the Ti^{4+} cations' oxidation state. As the band gap energy of MOF materials exhibited an effect over the charge transfer complexes involved in the reaction mechanism for different I_2@MOF systems, a combination of methodologies was proposed to determine band gap energies and types using only diffuse reflectance UV-Vis data. The study emphasizes how confinement in porous materials can alter properties and stabilization mechanisms, influencing adsorption and reactivity.

Key words: MOFs, Iodine, Spectroscopy, Band gap, Adsorption